University of Glasgow

Mechanical Characterisation of Lymph Nodes and Optimisation of Needle-Tissue Interaction for Endobronchial Biopsy

Lyne Raissa Ndengue Mkoh

University of Glasgow James Watt School of Engineering

Supervisors:

Prof. Sandy Cochran & Dr Emma Henderson

A thesis submitted for the degree of Doctor of Philosophy in Ultrasonic Engineering

Abstract

Endobronchial ultrasound-guided transbronchial needle aspiration (EBUS-TBNA) is a minimally invasive biopsy technique used for lymph node sampling in lung cancer staging and for diagnosing granulomatous disease. The procedure's performance is governed by the mechanics of needle–tissue interaction, specifically needle placement accuracy, insertion mechanics, and tissue acquisition efficiency. Despite its clinical utility, reported diagnostic yields remain limited to approximately 60–80%, primarily due to inadequate tissue capture with current needle geometries. Clinical audits, including those conducted by NHS Greater Glasgow & Clyde, confirm suboptimal diagnostic performance that is consistent across multiple institutions. These limitations contribute to repeat procedures, delayed diagnosis, and increased system-level resource utilisation.

This thesis develops a combined experimental-computational framework to characterise and optimise needle insertion and tissue acquisition in lymphatic tissue. A constitutive characterisation methodology was first established to describe the nonlinear, anisotropic, quasi-incompressible, fibre-reinforced hyperelastic behaviour of lymph node tissue. Needle insertion mechanics were then quantified both experimentally and numerically across a range of controlled insertion velocities (13 mm/s, 9 mm/s, 3 mm/s, and 0.5 mm/s), and the force response was decomposed into insertion, cutting, and frictional components. Finally, parametric finite element simulations using the Coupled Eulerian–Lagrangian (CEL) formulation were employed to evaluate the influence of needle-tip geometry and cutting-plane configuration on tissue deformation, stress distribution, and sample capture efficiency.

The validated soft tissue model accurately reproduces the mechanical response of lymphatic tissue under large deformations and dynamic loading. Results indicate a strong rate-dependent response, with increasing insertion velocity leading to higher peak insertion forces (5–8 N) and cutting forces (3.62–6.14 N), while reducing frictional forces (0.5–0.4 N) and the effective coefficient of friction (1.85–1.32), consistent with velocity-dependent interfacial behaviour.

Furthermore, geometric optimisation of the needle tip significantly alters stress localisation and tissue failure mechanisms. Finite element analysis shows that a Franseen-type needle with three symmetric cutting planes enhances tissue engagement, reduces insertion forces by up to 35%

compared with conventional EBUS-TBNA needle designs, and improves specimen length while reducing tissue deformation, thereby indicating improved sampling efficiency and mechanical performance

Dedication

To my parents and my husband, thank you for your unconditional love and support throughout my adventures, especially for helping me navigate this journey.

To those who guided, helped, cared for, and loved me, thank you for making me strong and resilient.

This dissertation is dedicated to all of you.

Acknowledgements

First and foremost, I would like to give thanks and praise to the Almighty God, the Most Gracious and the Most Merciful, for His strength and blessings bestowed upon me during my studies and in completing this thesis. Indeed, to everything there is a season and a time for every purpose under heaven. “Be strong and courageous. Do not be afraid or terrified, for the Lord your God goes with you; he will never leave you nor forsake you” Deuteronomy 31:6.

My sincerest appreciation and gratitude to my supervisors, Prof. Sandy Cochran and Dr Emma Henderson, who have patiently guided and taught me over the past four years. Special thanks to Prof. Sandy Cochran, who never hesitated to devote substantial time to discussing the challenges I faced during my PhD. Thank you for genuinely caring about my PhD success. Occasionally, you even sat with me at my computer, spending hours together and brainstorming on a whiteboard.

My thanks also go to the medical physician, Steve Bicknell, and to Robin Sayer from the Medical Devices Unit for their ongoing support and guidance throughout my PhD.

A heartfelt thank you to Kevin Worrall and Helen Mulvana of Glasgow University for providing the laboratory equipment.

I am eternally grateful to my family, especially my parents, Jean Didier Mkoh and Colette Bibiane Mkoh; my husband, Dr Aristide Fabrice Nyambioh; and my sister, Dr Anne Dikao Stredy Mkoh, for their love, trust, encouragement, understanding, patience, and essential support during my most difficult times.

I would also like to thank my colleagues, including Olubunmi Onanuga, George Puthenvila, and others from FUSE, C-MIU, and CUE, for their support and assistance throughout my PhD. Special thanks to my close friends, Leslie Djouaka, Antoine Minyangadou, and Abdul Shaka, for encouraging me during the difficult periods of my PhD. The completion of my PhD would not have been possible without the help and advice of my family, husband, friends, supervisors, and colleagues.

Contents

List of Figures

List of Tables

Chapter 1: Introduction

According to Cancer Research UK, lung cancer is the second most common type of cancer in both men and women in the UK. It is estimated that approximately 49,200 new cases are diagnosed in the UK each year [1]. Lung cancer is often diagnosed using a bronchoscope, which travels through the bronchial tree to obtain high-resolution video and ultrasound images of lymph nodes. Alongside ultrasound imaging, tissue sampling techniques, also known as biopsies, play a crucial role in providing information about abnormal cells and tissue.

Early and accurate diagnosis is crucial for improving survival rates across most types of cancer. In diagnosing and staging lung cancer, Endobronchial Ultrasound-guided Transbronchial Needle Aspiration (EBUS-TBNA) is an essential tool for sampling lymph nodes for analysis. EBUS-TBNA uses hollow needles ranging from 19 gauge to 22 gauge [2-3]. The most common needle sizes used by the NHS are 21G and 22G, corresponding to outer diameters of 0.82 mm and 0.72 mm, respectively. The current procedure often requires several attempts to obtain samples for histological and cytological analysis of the lymph nodes [3]. This is because the sample may be insufficient in mass and length, or the tissue organisation may not be sufficiently defined. In either case, the result could delay or prevent a proper diagnosis.

Issues with the current EBUS-TBNA procedure include the inability to reliably obtain tissue samples. An 8-month audit by NHS Greater Glasgow and Clyde (NHS GGC) reported an EBUS-TBNA diagnostic yield of 61.22%. According to a meta-analysis of 15 studies on EBUS-TBNA, the diagnostic yield ranged from 54% to 93% [4]. A study by the American College of Chest Physicians showed that the diagnostic yield varied between 37% and 54% [5]. These studies highlight the need for an improved EBUS-TBNA system with a higher diagnostic yield, which can lead to quicker diagnosis and fewer repeat procedures [6]. This would benefit patients by enabling better treatment and avoiding additional procedures, and would also benefit healthcare providers by allowing more patients to be treated in less time and reducing the costs associated with repeated procedures.

The aim of this study is to examine EBUS-TBNA and identify factors that improve tissue sampling success rates and preserve histological integrity. Data from existing studies indicate that a larger volume can broaden the scope of pathological assessment and increase the overall diagnostic yield of the procedure. According to personal communication with Dr Steve Bicknell, a Respiratory Consultant and Interventional Bronchoscopist in 2022, larger tissue

samples enable more precise genetic profiling of cancer cells and help recognise the structural features observed in granulomatous diseases.

1.1 Lung Cancer

The lung, outlined in Figure 1.1, is a two-part, spongy, cone-shaped organ in the chest that forms part of the respiratory system, which also includes the diaphragm, windpipe, and chest wall muscles. The two lungs are separated by the mediastinum, a central structure that contains the oesophagus, lymph nodes, heart, and trachea. The right lung has three lobes and is slightly larger than the left lung, which has two lobes [7]. The primary function of the lung is to facilitate respiration by transferring oxygen from the air into the bloodstream. It also helps remove carbon dioxide from the body. When air enters the body through the nose or mouth, it passes through the trachea, which divides into tubes. These are known as bronchi, then bronchioles, ending in alveoli, which are tiny air sacs. The lungs filter harmful particles, such as bacteria, mould, and dust, that can enter through inhalation. However, inhaling toxins can lead to lung cancer [8].

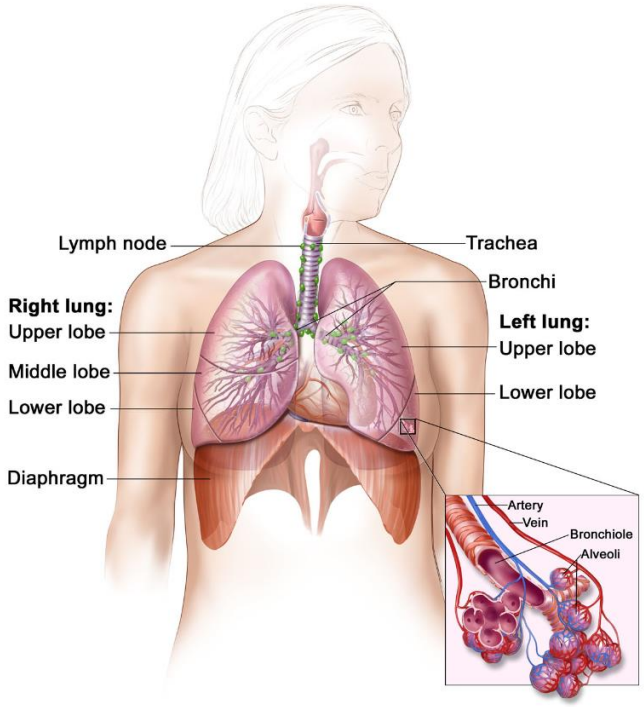

Figure 1.1: Anatomy of the respiratory system [9]. Copyright 2006 by Terese Winslow.

Since 1987, lung cancer, also known as lung carcinoma, has been recognised as the second most common type of cancer worldwide. It typically begins in the lungs, affecting the

bronchioles and alveoli. Uncontrolled division of lung cells can damage the DNA of certain airway cells, leading to lung cancer [10]. The changes affecting these genes are known as DNA modifications, which can convert genes involved in normal cell growth (proto-oncogenes) into cancer-causing (oncogenes) [11], as shown in Figure 1.2. When a cancerous tumour grows, its cells can be transported by the body's lymphatic system or bloodstream to other tissues. This process, known as metastasis and illustrated in Figure 1.3, can result in the formation of new tumours. One of the initial sites where cancer commonly spreads is the lymph nodes. The cancer can also disseminate to distant organs via the bloodstream, reaching tissues such as the liver, lungs, brain, and bones [13]. Although the cancer may grow and metastasise to distant organs, it is still classified by the primary site of origin [14].

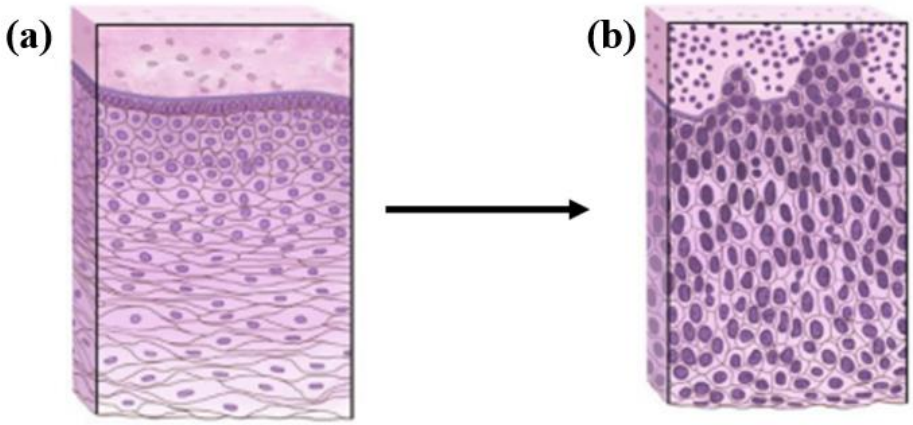

Figure 1.2: Normal cells to cancer cells. (a) normal cells, (b) cancer cells, which result from DNA changes leading to uncontrolled growth. [9]. Copyright 2014 by Terese Winslow.

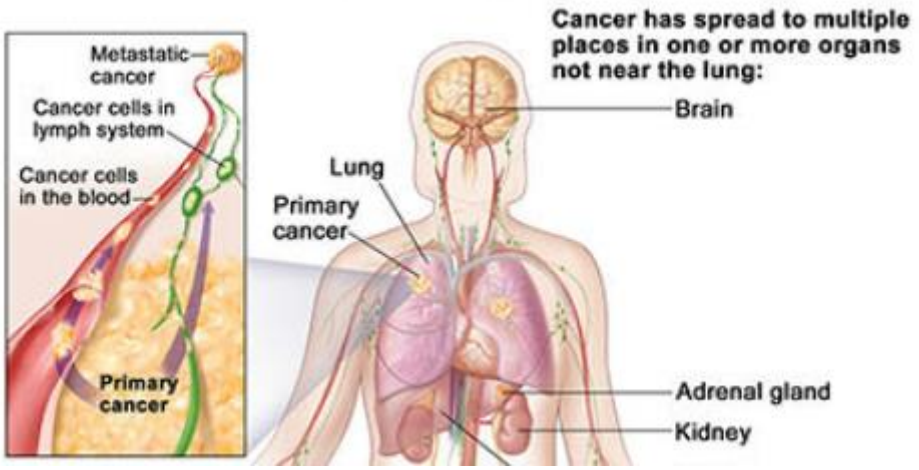

Figure 1.3: Metastasis process, which refers to cancer cells moving from one part of the body to another to form new tumours [9]. Copyright 2016 by Terese Winslow.

In the UK, lung cancer is the second most common cause of cancer-related death for both men and women, after prostate and breast cancer, respectively. It is estimated that about 49,200 new cases are diagnosed each year in the UK [1]. There are various types of lung cancer; the two main types are non-small cell lung cancer (NSCLC) and small cell lung cancer (SCLC) Figure 1.4. NSCLC accounts for more than 80% of lung cancer cases, and can be further categorised as adenocarcinoma, representing 40%; squamous cell carcinoma, ranging from 25% to 50%; and large cell carcinoma, comprising 10% to 15%. Adenocarcinoma usually arises in the outer part of the lung and is more likely to be detected before the disease spreads. The initial stage of squamous cell carcinoma is characterised by the development of flat, skin-like structures lining the airways. It is often associated with a person's smoking history and is typically found in the central part of the lung near the main airway. Any part of the lung can be affected by large cell carcinoma, which is characterised by its tendency to grow and spread uncontrollably, making it very difficult to treat. A subtype of this disease, known as large-cell neuroendocrine carcinoma, is a fast-growing tumour similar to SCLC [10].

The second type of lung cancer, SCLC, accounts for about 10% to 15% of cases. The disease tends to grow and spread more rapidly than NSCLC, and in most cases, it has already affected other parts of the body by the time of diagnosis [11].

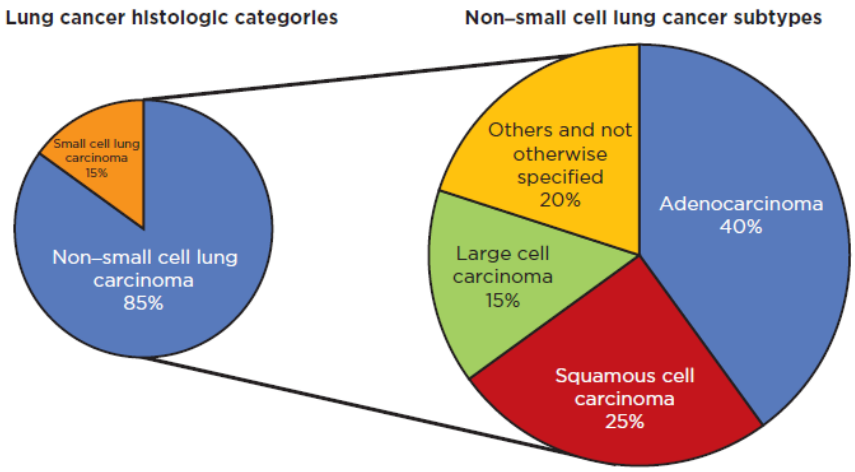

Figure 1.4: Lung cancer's distribution across different histological categories [11]. Copyright 2019 by Europe PMC.

Tobacco smoking is considered the most common and significant risk factor for lung cancer. Although only about 15% of the UK's population smokes, around 80% to 90% of new lung cancer cases in the country are linked to tobacco use [12-13]. The high prevalence of smoking is a major risk factor, but other exposures can also cause the disease. Unlike other radioactive substances, radon is odourless and tasteless, making it undetectable by soil examination. It is, however, produced by the radioactive decay of uranium and thorium in the ground [14-15]. It is estimated that radon exposure causes over 21,000 lung cancer-related deaths in the UK each year, and roughly 3% to 14% of lung cancer cases worldwide are attributed to this toxic substance [15]. Exposure to certain chemicals, such as coal tar and soot, can increase the risk of developing lung cancer; these include materials like chromium, nickel, and asbestos [16]. Heavy exposure to asbestos can raise the risk of lung cancer by about 70% [17]. Additionally, a history of respiratory illnesses like tuberculosis, pneumonia, and chronic bronchitis is known to increase the likelihood of lung cancer, as these conditions can cause inflammation in lung tissue. Individuals with a history of asthma have a 16% higher chance of developing lung cancer [18-19].

Despite significant progress in survival rates for other cancer types, lung cancer patients in the UK have seen only marginal improvements over the years. The primary reason is that they are often diagnosed at a late stage. The average five-year survival rates for NSCLC and SCLC are approximately 65% and 30%, respectively. Figure 1.5 [20-21]. Although early lung cancer

often produces no symptoms, some individuals may experience shortness of breath, chest pain, or coughing. These symptoms can vary from person to person.

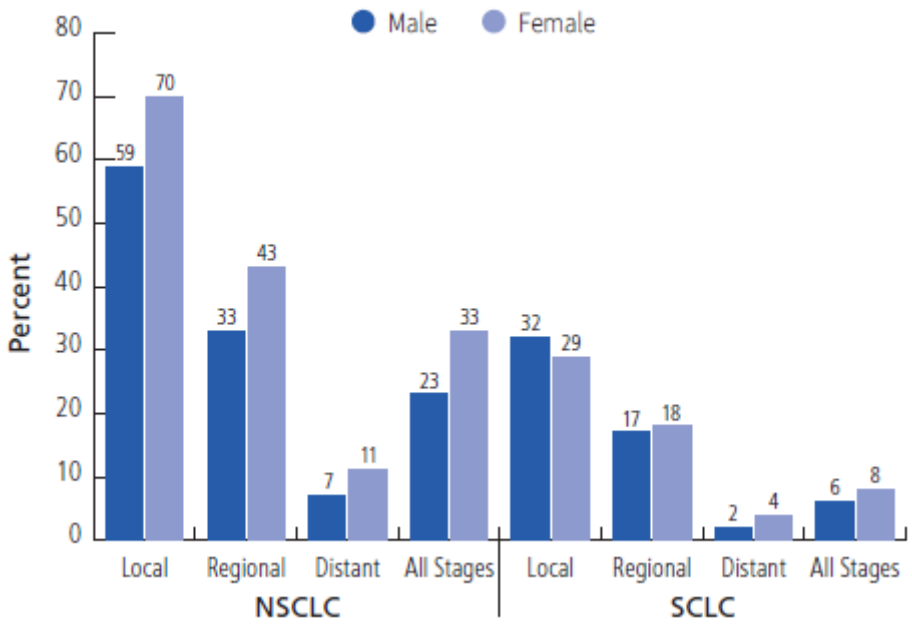

Figure 1.5: 5-year survival rate for individuals with lung cancer by stage at diagnosis, gender, and subtype [20].

1.2 Diagnosis Method of Lung Cancer: Preliminary Staging

Most cases of lung cancer are diagnosed when symptoms are linked to a specific paraneoplastic or metastatic condition. The evaluation of lung cancer involves collecting relevant samples for histological diagnosis. This process includes a physical examination and imaging techniques such as X-rays, computed tomography (CT), and positron emission tomography (PET) to obtain scans of the chest and abdomen, along with a biopsy.

X-rays, or chest radiography (Figure 1.6), use ionising radiation to visualise an individual's internal organs. They can diagnose chest wall conditions and visualise structures within the thoracic cavity, such as the heart, lungs, and great vessels. Most X-rays are not absorbed by the soft tissues of the human body, such as skin, muscles, and blood, which appear as dark grey areas. However, denser structures, such as tumours or bone, can block most X-rays from passing through [21]. In a suspected case of lung cancer, an X-ray imaging procedure might reveal a mass, visible as an enlarged mediastinum or enlarged lymph nodes, on a shadowy image [22-23].

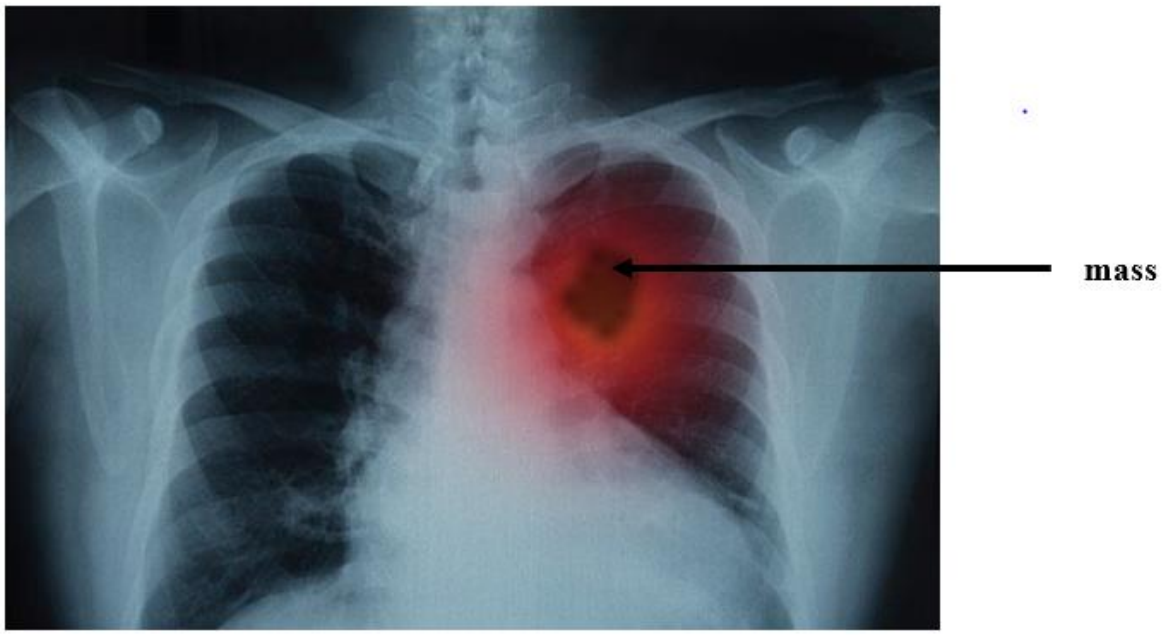

Figure 1.6: Chest radiography demonstrating a mass [7].

Unlike X-rays, which produce a flat 2D image, CT scans, as shown in Figure 1.7, reveal structures within the body by acquiring multiple X-ray measurements from different angles and reconstructing 3D cross-sectional images of the examined area [25]. CT scans are more effective than standard X-rays at detecting lung cancer. They can also determine the size, shape, and location of tumours. Additionally, they can assist in identifying lymph nodes affected by the cancer [26]. Moreover, they can be utilised to check for masses in other organs, including the liver, brain, and adrenal gland, which may indicate the spread of lung cancer [27].

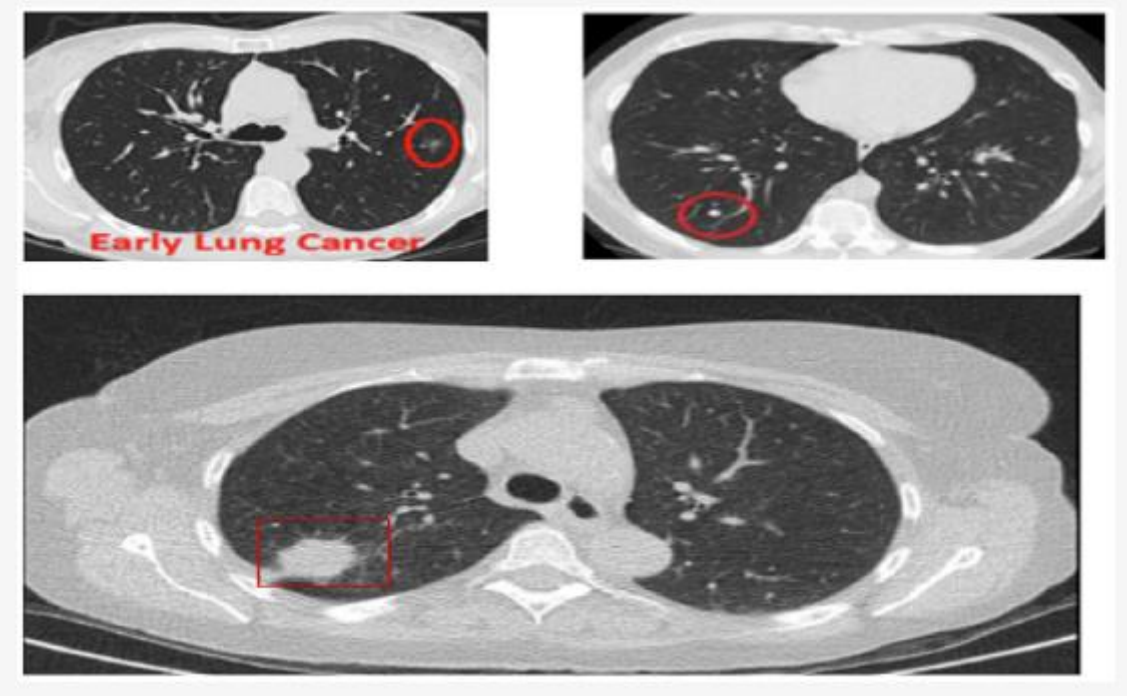

Figure 1.7: Lung CT scan showing a mass indicative of cancer [21]. Copyright 2022 by the authors.

Positron Emission Tomography (PET) is a quantitative imaging technique that visualises molecular processes in living organisms. It utilises the physical principles of gamma-ray correlation and positron emission to generate three-dimensional images of radiotracer distribution [22]. This enables the study of tissue function and metabolism, including absorption, blood flow, chemical composition, and glucose metabolism [23]. The first step in PET imaging is the intravenous injection of a radioactive substance, usually a biologically active molecule labelled with a positron-emitting radionuclide such as fluorine–18 (^18F) [24]. One of the most commonly used tracers in oncology is 18F-fluorodeoxyglucose (FDG), a glucose analogue that can enter cells via glucose transporters [25]. Unlike native glucose, which undergoes glycolysis, FDG-6-phosphate does not. It becomes trapped in cells with high glucose uptake rates. This mechanism provides a surrogate measure of cellular glucose utilisation, which is often increased in malignant tissue cells due to altered metabolic pathways. PET is a versatile imaging tool used for various applications, such as visualising cancer cells and detecting structural abnormalities. Its functional sensitivity enables it to detect changes in physiological and biochemical conditions that precede the appearance of abnormalities on MRI or CT scans. For example, increased FDG uptake can predict cancer development and the aggressiveness of cancer cells [26].

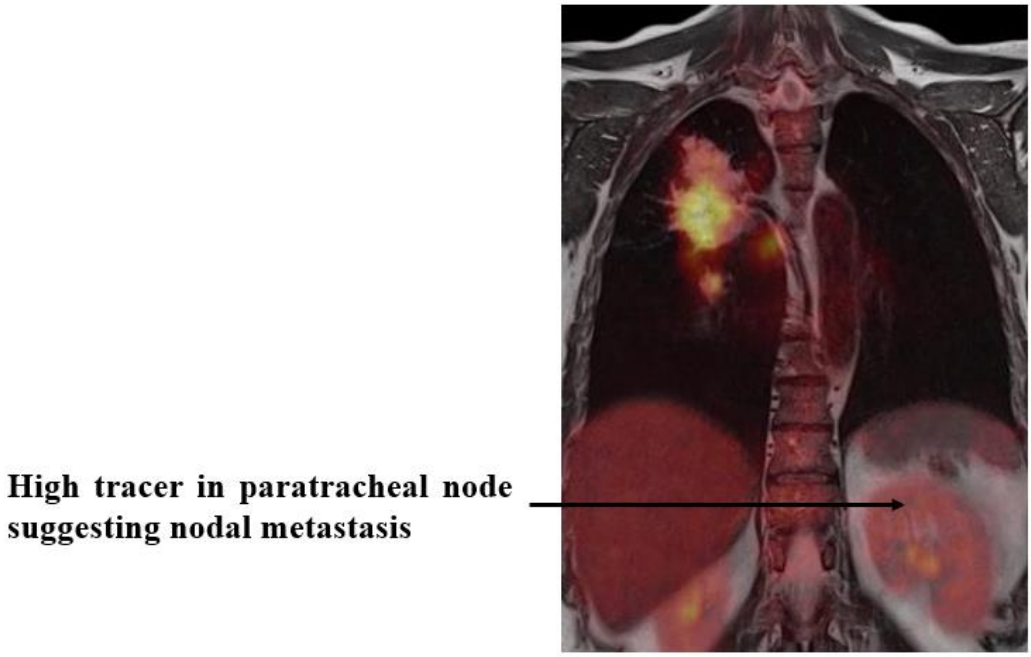

Figure 1.8: Primary tumour with high radiotracer [22] Copyright 2016 by the authors.

1.3 Aims and Objectives

Lymph nodes are small, kidney-shaped organs enclosed in a capsule of adipose tissue. They are essential for the diagnosis and staging of lung cancer. To date, little is known about how lymph nodes respond to in vivo needle insertion. To increase sample yield from EBUS-TBNA, understanding the mechanical behaviour of lymph nodes and the mechanics of needle insertion is crucial. The aims of this thesis are therefore as follows:

- To establish a comprehensive mechanical characterisation technique for measuring the nonlinear elastic properties of lung lymph nodes, and to determine their correlation with alternative soft materials: chicken breast, large pickled capers, and PVA hydrogel.
- To develop and test theoretical models of lymph nodes that are suitable for identifying the different phases, forces, and tissue deformation during needle insertion.
- To gain insights into needle-tissue interaction by modelling to predict needle deflection, tissue deformation, and the current needle-tissue sampling length.
- To investigate the effect of various needle tip geometries on tissue deformation and sampling length.

Addressing these aims and objectives can help close two significant research gaps in EBUS-TBNA needle biopsies.

(1) There is limited understanding of the physical and mechanical properties of lymph nodes.
(2) There is currently limited research on tissue samples that can be collected using common needle geometries. Additionally, the relationship between needle geometry and the tissue samples obtained, a crucial factor in cancer diagnostic accuracy, remains unknown.

1.4 Contributions to Knowledge

- Mechanical Characterisation of Lymph Nodes: To date, little is known about lymph node behaviour. Using generic soft materials and tissue-mimicking phantoms, this work has developed a methodology to characterise the non-linear elastic behaviour of lymph nodes. The loading mechanism is based on displacement-controlled relaxation testing. Using the volume-displacement method and curve fitting in Abaqus, the density and shear modulus of lymph nodes were determined to be 1.042 g/cm³ and 4.875×10^{-3} MPa, respectively.
- Understanding needle insertion mechanics into soft materials: This work adopts an experimental approach using different ex vivo soft tissues to gain a deeper understanding of how current needle designs, 21G and 22G in diameter, affect tissue deformation phases and needle forces. It is found that increasing the insertion speed decreases peak and cutting forces and increases both inner and outer friction forces, as well as the coefficient of friction. Furthermore, the forces generated by the 21G and 22G needles do not differ significantly.
- Needle-tissue interaction modelling methodology for predicting needle design insertion performance: This work develops a numerical method to model the needle-tissue interaction during insertion. A Coupled-Eulerian-Lagrangian (CEL) framework for studying tissue deformation and stress at the needle-tissue interface provides insights into needle-tissue interactions. The study shows that tissue separation at the tip affects both sample length and tissue deformation. Furthermore, the CEL model can predict the relationship between tip type and needle force, aligning with experimental results.

- Needle tip geometries and tissue sample length: In addition to the accuracy of needle deployment, the shape of the needle tip can also influence the insertion force and the length of tissue sampled. The inclination angle and the number of cutting planes determine the needle tip geometry. Based on an understanding of needle-tissue interaction, this work explores two additional needle-tip geometries, namely the double front bevel and the Franseen needle, with varying numbers of cutting planes, and compares them with the current needle tip design for precise tissue sampling length. It demonstrates that the Franseen needle, with three cutting planes, can minimise tissue damage and achieve higher tissue sampling efficiency at a medium insertion speed than the existing EBUS-TBNA needle design.

1.5 Thesis Structure

The thesis structure comprises seven further chapters: 2) Literature Review, 3) Experimental Background, 4) Mechanical Characterisation of various soft materials, 5) Analytical Methodology, 6) Needle Insertion into various soft materials, 7) Finite Element Modelling of needle insertion into various soft materials, and 8) Conclusions and Future Work.

Chapter 2 provides the background knowledge underpinning this work. The technique for diagnosing lung cancer is briefly outlined. An overview of the EBUS-TBNA system, together with the anatomy and behaviour of lymph nodes, is then presented. Finally, factors affecting diagnostic tissue yield are summarised and explained.

Chapter 3 discusses the key concepts underpinning the experimental work in this thesis. An overview of the experimental procedures, mechanical properties, and constitutive models used to characterise the nonlinear elastic properties is provided. This chapter also explains the mechanism of needle insertion into soft material.

Chapter 4 presents an experimental and analytical study of the nonlinear mechanical properties of relevant soft materials: chicken breast, large pickled capers, PVA hydrogel, and porcine lung lymph nodes. The experimental work comprises compression and nanoindentation tests conducted at a constant rate of 0.01 mm/s at strains of 5%, 10%, 15%, and 20%. Emphasis is placed on sample preparation, probe selection, calibration, measurements, and sources of

variability. The analytical work uses hyperelastic strain-energy models in Abaqus FEA software to characterise soft materials by curve fitting.

Chapter 5 examines various finite element analysis (FEA) software and the finite element method (FEM) for studying needle-tissue interaction. The benefits and limitations of these FEM techniques are discussed. Finally, the implementation of the Coupled-Eulerian-Lagrangian method is detailed.

Chapter 6 describes the stages of needle insertion into ex vivo chicken breast, large pickled capers, PVA hydrogel, and porcine lung lymph nodes. Using common needle designs, 21G and 22G needles are tested at four speeds: 13 mm/s, 9 mm/s, 3 mm/s, and 0.5 mm/s. Needle forces are recorded experimentally and compared to identify correlations between needle insertion into lymph nodes and other soft materials.

Chapter 7 explores the dynamics of needle-tissue interaction using the coupled Eulerian-Lagrangian method in FEA. It presents three needle-tip geometries: Olympus single-bevel, double-front bevel, and Acquire Franseen, and examines their effects on tissue deformation, stress, and contact. The modelling results are compared with those presented in Chapter 6, thereby establishing the link between needle-tip geometries and tissue-sample length.

Chapter 8 summarises the conclusions and limitations of the work undertaken. It also emphasises possible enhancements for future research.

1.6 Presentations Based on the Current Work

L.R. Mkoh, S. Bicknell, R. Sayer, S. Cochran, and E. Henderson. (2023) "Parameters Affecting the Re-Design of New EBUS-TBNA Needle Tips". In: 5th Doctoral School Multidisciplinary Symposium, University of Strathclyde, UK, 14th – 16th June 2023.

L.R. Mkoh, S. Bicknell, R. Sayer, S. Cochran, and E. Henderson. (2023) "Mechanical Characterisation of Soft Materials for EBUS-TBNA". In: 17th International Conference on Advances in Experimental Mechanics, University of Glasgow, UK, 30th August – 1 September 2023.

L.R. Mkoh, S. Bicknell, R. Sayer, S. Cochran, and E. Henderson. (2024) " Understanding of Lymph Nodes Behaviour and its Impact on EBUS-TBNA Diagnostic Yield". In: IEEE EMBS 46th Annual International Conference of the IEEE Engineering in Medicine and Biology Society, Orlando, USA, 15 – 19 July 2024.

L.R. Mkoh, S. Bicknell, R. Sayer, S. Cochran, and E. Henderson. (2024) " Mechanical Characterisation of Lymph Node and In-Vivo Needle Insertion for EBUS-TBNA". In: 18th International Conference on Advances in Experimental Mechanics, University of Liverpool, UK, 3 – 5 September 2024.

Chapter 2: Literature Review

2.1 Endobronchial Ultrasound-Guided Transbronchial Needle Aspiration

When analysing CT and PET scan results, physicians must first determine whether the procedure is for diagnosis or staging. They then decide which lymph nodes to sample. For diagnosis, samples are collected from the site most suitable for predictive biomarker analysis. Staging procedures involve examining every lymph node with a short-axis diameter greater than 5 mm. Although the choice of procedure in each case is usually made by the physician, EBUS-TBNA has been shown to be more accurate and to yield better diagnostic results than mediastinoscopy. EBUS-TBNA enables visualisation of structures adjacent to the central airway that are not visible during bronchoscopy. It is considered a well-tolerated, accurate, and cost-effective method for sampling lymph nodes in the hilar and mediastinal regions for the diagnosis and staging of lung cancer.

In 1949, Dr Eduardo Schieppati reported the first use of Transbronchial Needle Aspiration (TBNA), with a rigid bronchoscope, to assess lung cancer [23]. However, limited visualisation and the perception that the procedure was blind led to variability in application and diagnostic yield [24]. The development of EBUS, initially designed to sample lymph nodes near the airway walls, led to the first EBUS bronchoscope system in 1999 (Figure 2.1), enabling access to lesions in the lung parenchyma, hilum, and mediastinum. With this new technology, a flexible bronchoscope equipped with an optical viewing system was developed for use in the airways. A saline-filled balloon was placed at the tip to allow a 7.5 MHz convex ultrasound probe to visualise parabronchial structures in real time [25]. This technology enabled the operator to obtain high-quality images at depths of up to 9 cm. EBUS-TBNA devices are now manufactured by Olympus, Fuji, and Pentax, all based in Tokyo, Japan.

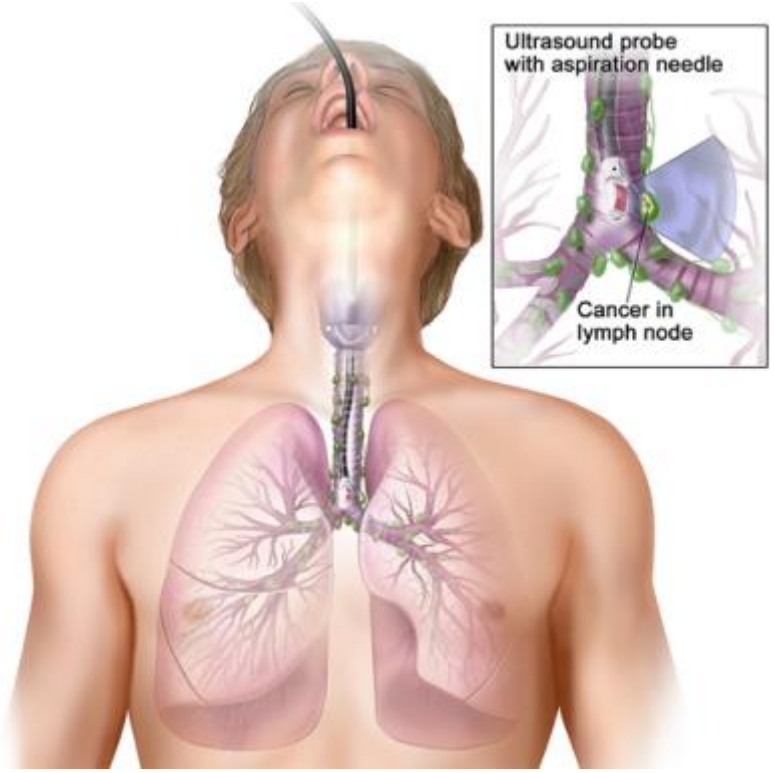

Figure 2.1: Illustration of the endobronchial ultrasound-guided transbronchial needle aspiration (EBUS-TBNA) procedure [9]. Copyright 2014 by Terese Winslow.

2.1.1 Overview of the EBUS-TBNA Device System

The EBUS-TBNA system comprises a flexible bronchoscope, an ultrasound transducer, and a needle system, which is inserted through the bronchoscope's working channel [26]. Olympus currently holds over 70% of the global market and is the leading manufacturer of EBUS-TBNA medical devices. Unlike other manufacturers, Olympus can also supply all the necessary accessories.

2.1.1.1 Bronchoscope and Ultrasound Imaging

Table 2.1 compares the various bronchoscopy models from each manufacturer.

Table 2.1: Comparison of available bronchoscopes from different manufacturers [27]

Method of Optical Image Transmission	Frequency	Field of View	Outer Diameter	Direction of View	Working Channel Diameter	Scope Index	Company
Fibreoptic	5 -12 MHz	80^0	6.9 mm	Forward oblique 35^0	2.2 mm	BF – UC180F	OLYMPUS
Charge-coupled device	5 -12 MHz	120^0	6.7 mm	Forward oblique 10^0	2.0 mm	EB – 530US	FUJI
Charge-coupled device	5 -12 MHz	100^0	7.3 mm	Forward oblique 45^0	2.2 mm	EB19 – JI0U	PENTAX
Charge-coupled device	5 -12 MHz	100^0	7.4 mm	Forward oblique 45^0	2.0 mm	EB – 1970UK	PENTAX

Bronchoscopes are mainly designed for manoeuvrability and flexibility to navigate narrow, curved sections of the bronchial tree [28]. The Olympus EBUS scope is generally stiffer and larger than a standard bronchoscope, with an external diameter of 6.2 mm and a tip size of 6.9 mm. It features a 2.2 mm instrument channel that accommodates a 22-gauge or 21-gauge TBNA needle. The primary difference between Olympus's bronchoscope and those made by Fuji and Pentax lies in the optical imaging system. While Olympus utilises an optical fibre to transmit light for imaging, the other companies use a charge-coupled device (CCD) chip [29].

The EBUS technique visualises endobronchial structures and tissues by detecting backscattered waves generated at the tissue-air interface. This bronchoscope is equipped with a miniaturised convex-array ultrasound transducer operating at 5-12 MHz. The frequency range used for the EBUS technique balances the depth and spatial resolution required to image tissues and lymph

nodes within the peri-bronchial cavity [30 - 31]. The transducer emits short ultrasound pulses through the surrounding tissues and the airway wall. It then detects echo signals, which arise as partial reflections at boundaries where the acoustic impedances of neighbouring tissues differ. The time delay between transmission and reception of echo signals is used to determine the depth of reflecting structures. The reconstructed image intensity is based on the mismatch in acoustic impedance [32].

The collected echoes are recorded as raw radiofrequency (RF) signals, which form the basis of ultrasound imaging. These signals undergo several processing stages, including pre-amplification, bandpass filtering, compensation, and depth-dependent attenuation correction. After processing, envelope detection is performed to extract amplitude information, followed by logarithmic compression to reduce the signal's dynamic range [33- 34].

A convex-probe EBUS system provides high-quality imaging of a sector–shaped field of view via electronic beam steering. Each frame comprises multiple consecutive scans. The frame rate is determined by the repetition frequency and the imaging depth of the scans [32]. Rather than providing a direct anatomical impression of tissue structure, the EBUS ultrasound image displays a detailed reconstruction of tissue echogenicity derived from the collected RF data. The image quality is affected by various factors, such as the transducer design and signal processing settings [33].

Ultrasound image quality can be degraded by poor ultrasonic coupling between the transducer and the tracheobronchial wall. This issue can be avoided by attaching a small saline-filled balloon to the bronchoscope tip. Such a device helps maintain stability and reduce stimulation of the receptors in the coughing area [34].

The most recent Olympus bronchoscope model, the BF-UC190F, is shown in Figure 2.2.

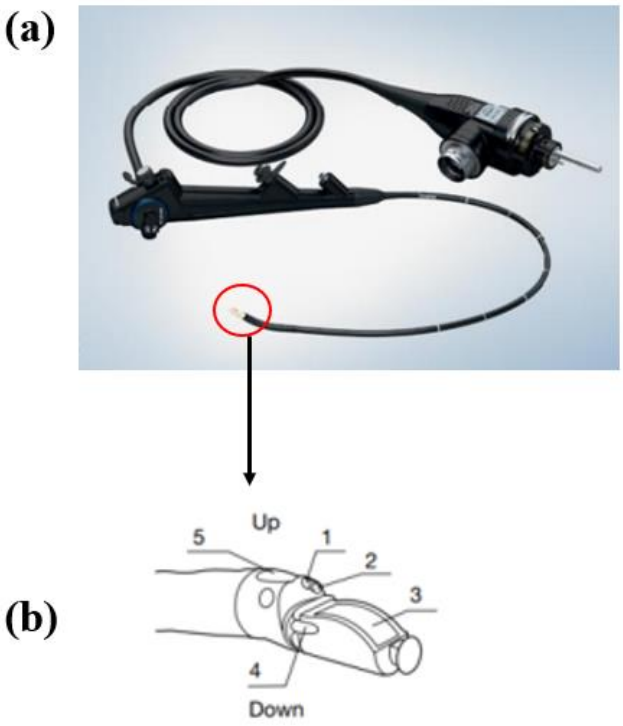

Figure 2.2: Latest Olympus bronchoscope model, BF-UC190F. (a): Overview of the full system; (b): enlarged distal end showing different features, (1) objective lens, (2) light guide lens, (3) ultrasound transducer, (4) balloon channel outlet, (5) instrument channel outlet [26]. Copyright 2021 by Olympus America.

2.1.1.2 Needle System

Some of the main companies that produce EBUS-TBNA needles include Boston Scientific, Olympus, and Cook Medical, Table 2.2. Each of these companies offers a range of designs and sizes [35].

Table 2.2: Needle systems comparison [35]

Model Name	Product Name	Needle Design	Gauge Size	Needle Material	Maximum Needle Length	Company
ViziShot	NA-201SX-4021 NA-201SX-4022	Lancet	21G / 22G	Stainless steel	40 mm	Olympus
ViziShot 2	NA-U403SX-4019 NA-U401SX-4021 NA-U401SX-4022	Backcut	19G / 21G / 22G	Stainless steel	40 mm	Olympus
Echo Tip Ultra	ECHO-HD-22 EBUS-O ECHO-HD-25-EBUS-O	Lancet	22G / 25G	Stainless steel	50 mm	Cook Medical
Echo Tip Procore	ECHO-HD-22-EBUS-O-C ECHO-HD-25-	Lancet	22G / 25G	Stainless steel	50 mm	Cook Medical
Expert Pulmonary	M00558220 M00558250	Lancet	22G / 25G	Cobalt chromium	60 mm	Boston Scientific

Depending on the intended use and the analysis to be performed on the sampled tissue, the needle size can range from 19G to 25G. The needle should be flexible enough to fit easily into the bronchoscope's working channel. It should also be strong enough to penetrate the lung wall without causing unnecessary damage. Additionally, it should be visible under ultrasound imaging; this can be achieved by adding echogenic features to the surface [36].

The needle system comprises several components. These include a handle unit, Figure 2.3 (a), label (1), an aspiration syringe, a flexible tube for bronchoscope insertion, an extendable and retractable protective sheath, Figure 2.3(a), label (2), and a stylet located inside the needle, Figure 2.3 [37]. The handle unit, Figure 2.3(b), features a locking mechanism, Figure 2.3 (b), label (5), which enables it to be secured to the bronchoscope. Additionally, it has a sliding control that allows the physician to adjust its length whenever necessary, Figure 2.3 (b), label (4). The needle is encased in a plastic tube that extends from the biopsy site to the handle. The needle's retractable stylet, Figure 2.3(b), label (1) is included to prevent blood and airway cells from entering the inner lumen, as these can compromise specimen quality. The handle unit can be operated using a small knob that is located at the tip of the needle system, Figure 2.3 (a), label (3). It can be retracted once the needle reaches the target, allowing the sample to be collected. However, this method requires the repeated insertion and removal of the stylet [38]. The entire needle system is intended for single use only and should be discarded immediately after the procedure. Nevertheless, it can still be used to repeat a procedure during the same session on the same patient.

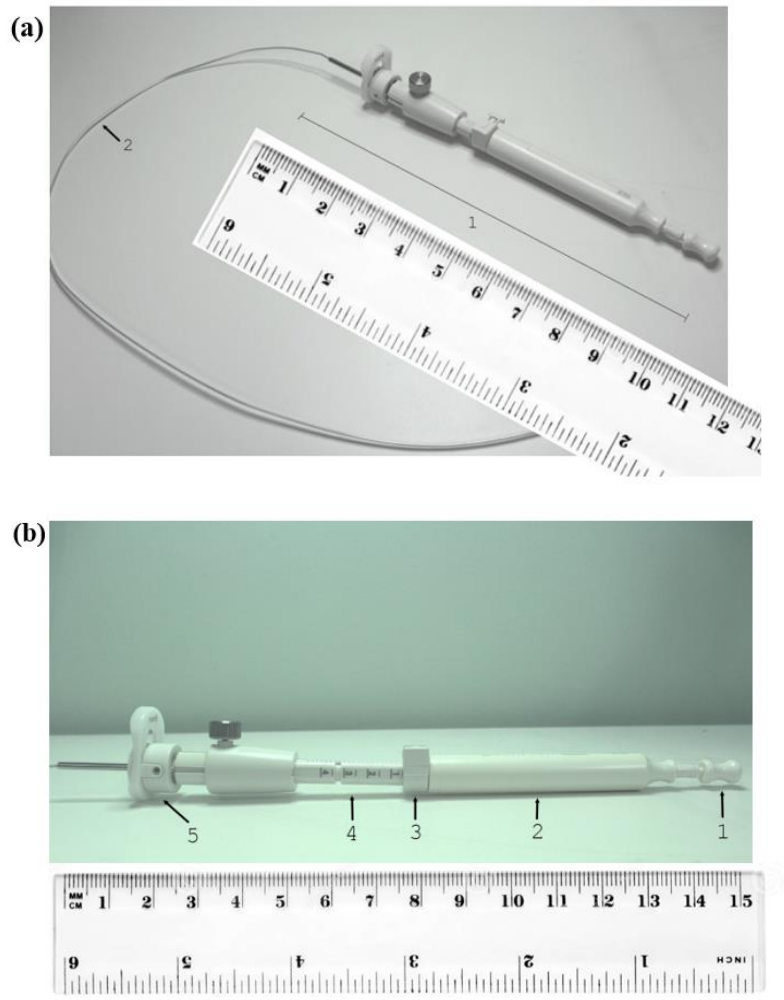

Figure 2.3: Olympus ViziShot 2 needle system diagram [37]. (a) Full needle system. Labels: (1) handle unit, (2) plastic protective sheath with the needle inside, (3) needle tip. (b) Handle unit. Labels: (1) stylet handle, (2) moving ejection mechanism, (3) ejection length lock, (4) ejection length setting area, (5) locking mechanism for connecting the bronchoscope.

2.1.1.3 Ultrasound System

The choice of ultrasound processor and instrumentation for EBUS depends on the EBUS-TBNA bronchoscope selected [42]. The latest Olympus model, the EU-ME3, provides enhanced display modes, including elastography and contrast-enhanced harmonic imaging (CHI). Elastography assesses tissue compressibility and stiffness. Malignant cells tend to be stiffer than normal tissue, which can help identify pulmonary or lymph node tumours. Both radial and linear EBUS-TBNA can be performed with Olympus ultrasound systems. The Fuji SU-1 offers similar features, including colour Doppler, elastography, and CHI. Fuji's technology includes an algorithm that calculates the optimal sound speed within the targeted

area to improve image resolution; however, this feature is limited to linear probes and cannot be used with radial probes [29]. A radial ultrasound probe has a circular array of transducers that provides a 360-degree view of the surrounding tissue. It is useful for assessing lesions in the lung periphery and airway walls. However, its resolution is lower than that of linear probes and may not resolve deeper structures. A linear probe has a narrower field of view due to its linear-array transducer. Compared with a radial probe, it offers better resolution, enabling detection of smaller lymph nodes and lesions [43].

2.1.2 EBUS-TBNA Procedure Overview

For patients undergoing EBUS-TBNA, the choice between conscious sedation and general anaesthesia depends on the expected duration of the procedure and local practice. During the initial phase, a flexible bronchoscope is used to examine the airways and identify the segments. After suctioning any secretions, 1% to 2% lidocaine is administered to minimise coughing [39].

The EBUS-TBNA procedure uses an ultrasound system to guide the bronchoscope to the target area. The transducer on the bronchoscope connects to an ultrasound machine and monitor, known as the ‘processor’ discussed earlier. The probe emits ultrasound waves into the body, which are reflected by surrounding structures. The system detects these echoes and generates an image, which is displayed on a monitor. Continuous image updates provide a clear depiction of structures and movements [40]. Once the target location is identified, the bronchoscope can be adjusted to reach it. A saline-filled balloon may be inflated at the distal end of the bronchoscope to improve stability and transducer-bronchial wall coupling, and to minimise stimulation of cough receptors. Colour Doppler imaging helps differentiate vascular from tissue structures. High vascularity can increase bleeding, potentially contaminating the sample.

After confirming the sample’s location, the needle system is adjusted and advanced through the bronchoscope’s working channel. Ultrasound imaging enables precise control of needle placement, thereby preventing damage to adjacent structures and tissues. The internal stylet is used to remove any tissue that may have entered the lumen during puncture of the lymph node wall. The aspiration syringe is attached to the needle to create negative pressure, which can be adjusted as needed. Typically, the needle is moved back and forth within the lesion of interest about 10 to 15 times over 30 to 60 seconds. Without rapid on-site evaluation (ROSE) [41], three aspiration attempts are recommended for each lymph node, with two aspirations yielding

a single tissue core. The time required to obtain a tissue sample may vary depending on the size and location of the lymph node or other tissue mass, as well as the ease of obtaining a sufficient specimen.

EBUS-TBNA is used to sample lymph nodes in Stations 1, 2, 4, 10, and 11, but cannot be used to examine lower paraesophageal stations 8 and 9, Figure 2.4 [42]. Its broad applicability makes it an ideal tool for analysing lymph nodes, compared with more invasive procedures such as mediastinoscopy. For staging purposes, it is recommended that the Station N3 lymph nodes be sampled first, followed by the N2 and N1 hilar nodes. Doing so will minimise the likelihood of false over-staging [43]. Lymph nodes that are 4 cm or less in length should also be sampled. The samples obtained can be analysed with ROSE or stored in Cytolyt. If sent to a laboratory for evaluation, the EBUS-TBNA results may be available within a few days. They can then be used to rule out various lung diseases or diagnose lung cancer. The use of ROSE can reduce the need for additional bronchoscopy and the number of punctures. It can also allow for the confirmation of adequate tissue sampling and a preliminary diagnosis where malignant cells are present [43].

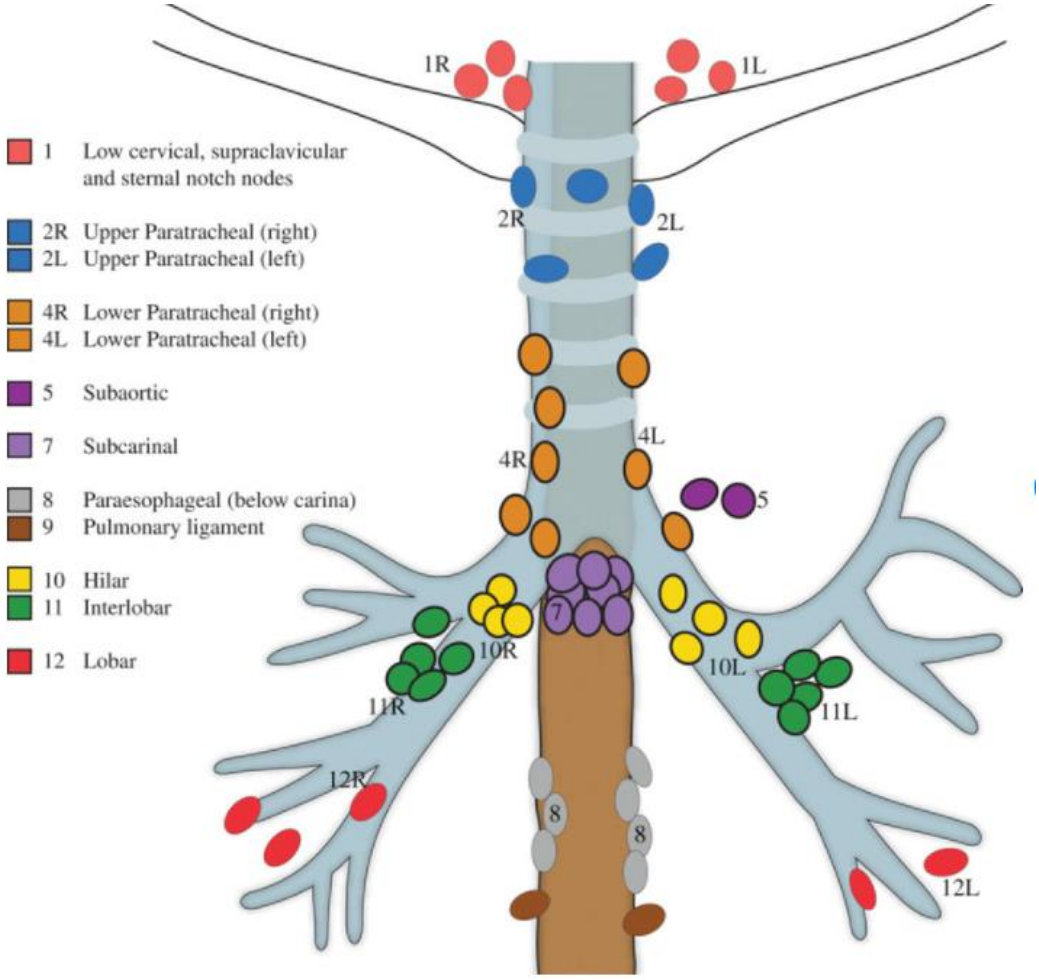

Figure 2.4: Illustration of lymph node stations; for the purpose of lung cancer staging, superior mediastinal nodes in stations 1, 2, and 4 should be sampled [42]. Copyright 2012 by the authors.

2.1.3 Sample Handling

Each needle pass should yield sufficient material to produce several slides, with enough remaining to be preserved in a solution for cell block preparation. After the needle is withdrawn from the scope, the stylet is reinserted into the TBNA needle to expel its contents onto a slide for smear preparation. Following removal of the stylet, the TBNA needle is first rinsed with 0.5 ml of saline. Compressed air is then used to flush the needle completely, removing all saline. The sample is then placed in a buffered preservative solution, Cytolyt, which helps preserve cells during transport to the laboratory. The material collected in Cytolyt is used to prepare a Thin Prep slide or a cell block, designed to minimise contamination of smears with peripheral blood [44]. After obtaining the specimen, the stylet is wiped with saline or ethanol and replaced

in the TBNA needle for the subsequent biopsy pass. If ROSE is feasible, various staining techniques can be performed immediately to assess sample adequacy. However, the results of the ROSE procedure do not constitute a definitive diagnosis. In the absence of ROSE, sufficient biopsy material must be collected to ensure the sample is representative of a lymph node. In the context of lung cancer staging, it has been recommended that three biopsy specimens be taken per lymph node. Conversely, if tissue fragments have been obtained, only two insertions should be required [45]

2.2 Lymph Node Anatomy and Behaviour

The primary target of an EBUS-TBNA biopsy is the lymph node, a key organ of the lymphatic system that maintains interstitial fluid balance, transports immune cells, and initiates adaptive immune responses. Lymph nodes act as highly organised immunological filters, removing pathogens and foreign particles, and play a pivotal role in cancer diagnosis and staging, as they are the first site of metastatic spread for many solid tumours.

Morphologically, pathological lymph nodes often exhibit a rounded geometry, heterogeneous internal echotexture, loss of the fatty hilum, and well-defined boundaries. These structural alterations reflect underlying changes in both cellular composition and tissue architecture, which are expected to influence the organ's mechanical response to external loading. Figure 2.5 illustrates the overall anatomical organisation and internal cross-sectional structure of a lymph node [45].

Anatomically, lymph nodes are encapsulated by a collagen-rich connective tissue capsule, from which trabeculae extend into the parenchyma, providing structural support and compartmentalisation. The internal structure is organised into cortical and medullary regions populated by immune cells, including lymphocytes and macrophages. These regions are supported by a specialised stromal network, including fibroblastic reticular cells (FRCs), which forms a three-dimensional reticular scaffold that guides immune cell trafficking and lymph flow. Surrounding tissues, such as adipose tissue, blood vessels, and lymphatic vessels, contribute to nutrient exchange and boundary constraints, thereby influencing the node's mechanical environment [45].

Over the past decade, considerable effort has been devoted to understanding the biomechanics of lymph nodes through both experimental investigations and computational modelling. Experimental studies have shown that lymph nodes exhibit nonlinear, viscoelastic behaviour, characterised by time-dependent deformation, strain stiffening and active mechanical regulation. Rather than behaving as homogeneous elastic bodies, lymph nodes continuously modify their mechanical properties during inflammation and immune activation through coordinated remodelling of the stromal network and the extracellular matrix.

One of the most significant advances in understanding lymph node mechanics was reported by Assen et al. [46], who combined intravital microscopy, atomic force microscopy, mechanical testing, computational image analysis, and molecular biology to investigate lymph node expansion during infection. Their results showed that lymphocyte accumulation generates outward pressure that stretches the fibroblastic reticular cell (FRC) network. Initially, the network relaxes through reduced cellular contractility; however, sustained loading stimulates remodelling and proliferation of FRCs, while the collagen-rich lymph node capsule undergoes fibrotic thickening to resist further expansion. The study proposed a multitier mechanical model in which internal connective tissue cells regulate local tissue deformation, whereas the capsule provides global mechanical resistance. The authors concluded that lymph node mechanics are controlled by distinct fibroblast populations operating across multiple spatial scales, providing one of the first comprehensive descriptions of lymph node biomechanics from the cellular to the organ level.

Additionally, the mechanical properties of lymph nodes and their surrounding structures have been investigated experimentally to improve understanding of lymphatic transport, tissue modelling, and disease progression. Experimental studies of isolated lymph node capsules have demonstrated nonlinear elastic behaviour and significant compliance, with evidence of active stress generation arising from smooth muscle and stromal cell contractility. Biological soft tissues, including lymphatic tissues, exhibit strain-stiffening behaviour due to their fibrous extracellular matrix, particularly a collagen-rich network [47]. These studies emphasise the capsule's mechanical role in controlling lymph node expansion and preventing excessive internal pressure. Changes in viscoelasticity and stiffness responses have also been observed during disease and inflammation. These modifications reflect alterations in the extracellular matrix and cellular composition [48].

These experimental findings have substantially revised the understanding of lymph node mechanics. Rather than treating lymph nodes as passive hyperelastic materials, current evidence indicates that they exhibit nonlinear viscoelastic behaviour arising from three interacting mechanisms: deformation of the collagen-rich capsule, active force generation within the fibroblastic reticular cell network, and redistribution of interstitial fluid throughout the porous tissue. This combination produces time-dependent stress relaxation and adaptive stiffness that cannot be adequately captured by purely elastic constitutive models.

The growing understanding of lymph node biomechanics has spurred the development of computational models that describe lymph transport, tissue deformation, and stromal mechanics. Recent computational work implemented in COMSOL Multiphysics coupled Navier-Stokes fluid dynamics, Darcy porous flow, and poro-elastic tissue mechanics to study lymphatic flow behaviour and tissue stress distributions under physiological conditions, including those associated with cancer and lymphoedema [48].

A comprehensive review by Jayathungage Don et al. [49] examined the development of computational fluid dynamics models of the lymphatic system and highlighted the rapid growth of lymph node-specific computational modelling over the last decade. The review identified continuum, finite element and computational fluid dynamics approaches for simulating lymph flow through anatomically reconstructed lymph nodes. Several of the reviewed studies reconstructed three-dimensional lymph node geometries from confocal microscopy and medical imaging, then solved coupled Navier-Stokes and Darcy flow equations to predict lymph transport through the subcapsular sinus and conduit network. These models consistently showed that the complex internal microarchitecture strongly influences pressure distribution and flow pathways, with approximately 90% of lymph preferentially travelling through peripheral regions of the node rather than penetrating uniformly into the parenchyma. The review concluded that future computational models should integrate fluid transport, tissue deformation and stromal remodelling within a unified multiphysics framework to improve physiological realism.

More recently, mathematical descriptions of lymph node biomechanics have incorporated porous media theory to capture interactions between solid tissue deformation and interstitial fluid flow. In these formulations, the lymph node is treated as a biphasic material comprising a deformable porous solid matrix saturated with lymphatic fluid. A representative example is the

model proposed by Giantesio et al. [50], which described pulsatile lymph flow within a lymph node by representing the organ as a porous core surrounded by a free-flowing subcapsular channel. The model combined Darcy flow within the porous tissue with the Navier-Stokes equations governing fluid motion in the surrounding sinus, and it was solved analytically and numerically using finite element methods. Simulations showed that local pressure gradients produce non-uniform tissue loading and strongly influence internal flow pathways, supporting the concept that fluid mechanics and tissue deformation are intrinsically coupled during lymph transport.

Collectively, these computational studies demonstrate a clear progression in lymph node modelling. Early investigations focused primarily on fluid transport, whereas more recent approaches incorporate anatomical reconstruction, finite element analysis, computational fluid dynamics, and multiphysics coupling to simulate interactions among lymph flow, tissue deformation, and stromal remodelling. Nevertheless, several important limitations remain. Most computational models assume homogeneous material properties despite the heterogeneous composition of lymph nodes, and relatively few incorporate experimentally measured hyperelastic and viscoelastic material parameters or active cellular contractility. Furthermore, although these models have significantly improved understanding of physiological lymph transport, they have rarely been extended to simulate externally applied mechanical loading, such as needle insertion during EBUS-TBNA procedures.

Consequently, despite substantial progress in understanding lymph node biomechanics, a significant gap remains between existing physiological models and clinically relevant mechanical simulations. Current computational studies have primarily focused on lymph flow, immune-cell migration and tissue remodelling, rather than on mechanical interactions with surgical instruments. Developing computational models that integrate experimentally validated hyperelastic constitutive behaviour, realistic anatomical geometry and needle–tissue interaction therefore represents an important next step towards improving the mechanical understanding of EBUS-TBNA biopsy procedures.

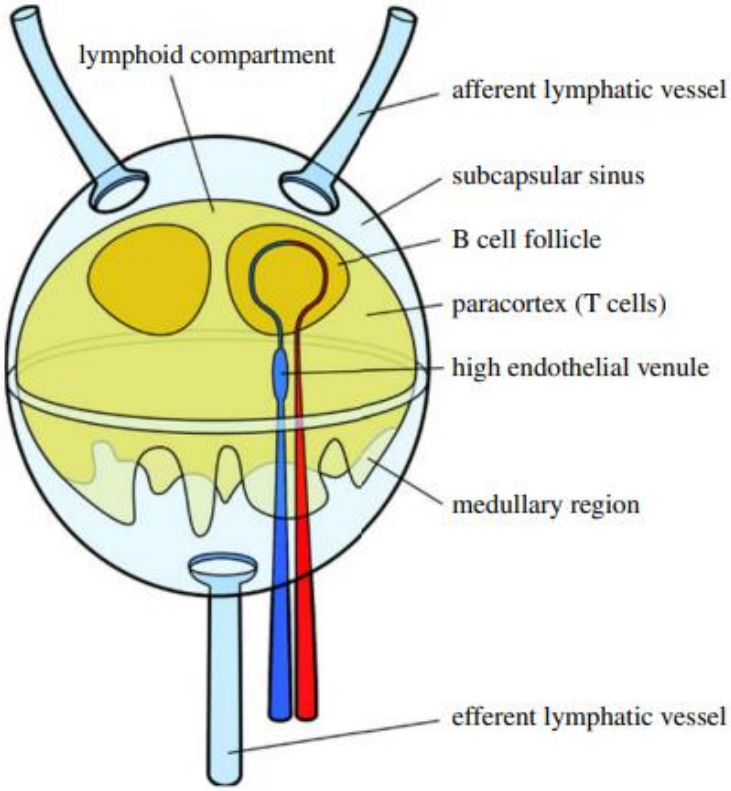

Figure 2.5: Overall structure of a lymph node [42] Copyright 2008, The Japanese Society for Immunology.

In mechanical terms, lymph nodes are best characterised by non-linear behaviour, which can be described using either a hyper-viscoelastic or a hyperelastic model [48]. The concept of hyperelastic behaviour refers to the large deformations that occur in elastic materials under stress and to their inability to return to their original shape once the stress is removed. Unlike elastic materials, which deform proportionally to applied stress, hyperelastic materials exhibit a nonlinear relationship between stress and strain [50]. This relationship can be expressed through the strain energy function in mathematical frameworks such as the Ogden, Neo-Hookean, and Mooney-Rivlin models [51]. These models can help predict the behaviour of hyperelastic materials under different loading conditions. The viscoelastic behaviour of soft tissue is characterised by the presence of both elastic and viscous properties, along with their time-dependent strain rate [52].

2.3 Other Considerations that Impact Tissue Yield

Although EBUS-TBNA offers many advantages, the quality of the tissue sample is a crucial factor that affects diagnostic yield, which reflects the likelihood of obtaining the necessary information for an accurate diagnosis. The current diagnostic yield of EBUS-TBNA ranges from about 60% to 80%, and sample size is a key issue to address to enhance the procedure's effectiveness [53]. Generally, a larger sample size results in better diagnostic accuracy, whereas an insufficient sample size reduces accuracy and can lead to delays in treatment decisions [54].

2.3.1 Needle Gauge

EBUS-TBNA is particularly useful for detecting both malignant and benign conditions. Cytological assessment involves analysing individual cells from a fluid sample, whereas histological assessment examines a tissue sample under a microscope to assess its structure and composition. For cytological procedures, 21G (0.84 mm OD, 0.61 mm ID) or 22G (0.72 mm OD, 0.55 mm ID) needles are usually employed, Figure 2.6, whereas the larger 19G (1.07 mm OD, 0.68 mm ID) needle is primarily used for histological analyses.

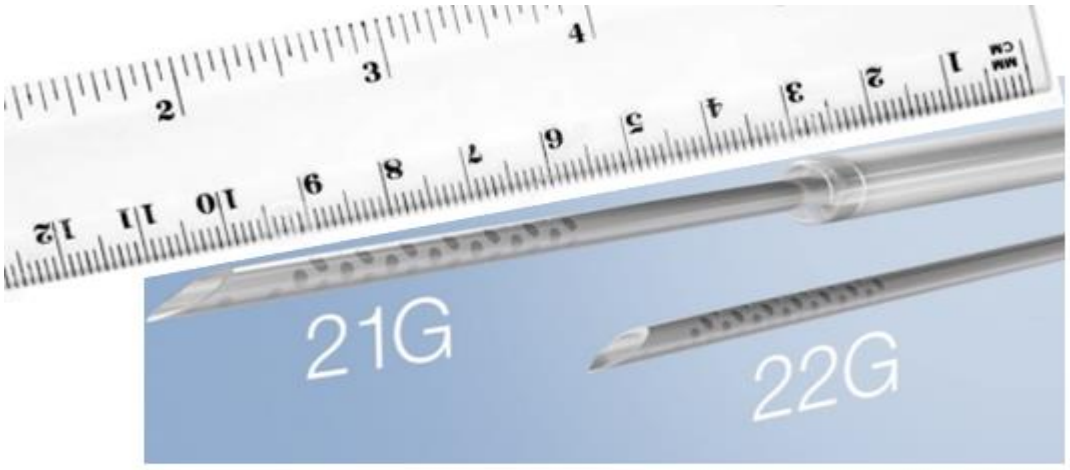

Figure 2.6: 21G and 22G Olympus Vizishot needle tip*s*. The spots visible on the needles are echogenic features on ultrasound. Copyright 2020 by Olympus America

Numerous studies have examined needle gauge size. These analyses have focused on sample adequacy and diagnostic yield. The adequacy of a biopsy sample depends on the quantity and

quality of tissue obtained during the procedure. A sample is deemed sufficient if it contains enough high-quality tissue for analysis. Diagnostic yield is the proportion of procedures or tests that result in a definitive diagnosis of a specific condition or illness in a patient. An increase in tissue yield is associated with improved diagnostic yield and sample adequacy, as higher tissue yield can enhance sample quality [54].

According to a study conducted by Dirol et al., [55] The use of 21G and 22G needles was most accurate in identifying malignancies. However, the accuracy rate of the 21G needles was higher than that of the 22G needles, indicating that fewer samples were required for a definitive diagnosis. Fewer samples could benefit a cytopathologist performing the ROSE procedure. A study conducted by Saji [56] revealed that the 21G needle was better than the 22G in terms of diagnostic yield. However, other investigations found no differences in sample adequacy or yield between the two needles.

In recent years, numerous studies have examined the use of flexible 19-gauge EBUS-TBNA needles, assuming that their larger size might enhance tissue collection [57]. Studies by Chaddha et al. [58] and Dooms et al. [59], comparing the diagnostic yields of 22G and 19G needles, found no difference in yield between the two. They also observed that the 19G needles produced fewer adequate samples.

In a study conducted by Sakai et al [60], the diagnostic capabilities of 22G and 25G needles were evaluated. Although the two needles had the same diagnostic yield, the samples obtained with the 22G needle contained more malignant cells than those obtained with the 25G needle [61]. Moreover, a study carried out by Di Felice et al. revealed that the analytical yield, sample adequacy, and diagnostic yield of 21G and 25G needles were similar [62].

Overall, tissue sampling yields inconsistent results, and the diagnostic yield with EBUS-TBNA needles varies. When choosing a needle size, consider the patient's suspected disease, the location of the lymph node station, the intended sampling method, and the desired penetration rate.

2.3.2 Suction

Although suction is commonly employed by physicians, its benefits in diagnostic yield have yet to be shown to be significant [62]. Lin et al. conducted a study on the impact of suction without a stylet on sample adequacy and diagnostic yield. It was found that those who used suction had a higher tissue core acquisition rate, but there was no notable statistical difference between the groups [63].

2.3.3 Rapid On-Site Evaluation (ROSE)

The ROSE procedure entails immediate cytopathological assessment of aspirated tissue samples during EBUS-TBNA. This allows the specialist to provide immediate feedback on the specimen's quality and adequacy. According to various studies [56], [63], [64],[65]the use of ROSE can enhance diagnostic accuracy by up to 30%, reduce the number of passes required to diagnose lung cancer, increase the specimen's adequacy, and decrease the need for a repeat procedure [66]. Moreover, ROSE can help reduce the workload of a pathology laboratory by eliminating the need to examine many slides. With that in mind, there is debate over its cost-effectiveness, given the procedure's time-consuming nature and the requirement for a dedicated cytopathologist. According to numerous studies, the use of ROSE does not have an apparent advantage in improving diagnostic yield [67], [68], [69]. The main reason for the minimal impact of this technique is that the EBUS-TBNA procedure already has a relatively high diagnostic yield, as shown by Bandiera et al [70]. In the UK, ROSE is not typically available due to logistical constraints related to the limited capacity of cytopathology services.

2.4 Current Research on Needle Tip Design

The fundamental design of needle tips depends on factors such as angle, gauge, and the number of cutting planes. The most basic type of needle tip geometry is a single-plane design.

Multi-plane designs are more complex due to varying plane angles and the choice between non-symmetric and symmetric orientations [71]. The current generation of EBUS-TBNA needle systems, Figure 2.7, utilised either a lancet or a back-cut bevel configuration; however, the exact reason for this choice remains unclear.

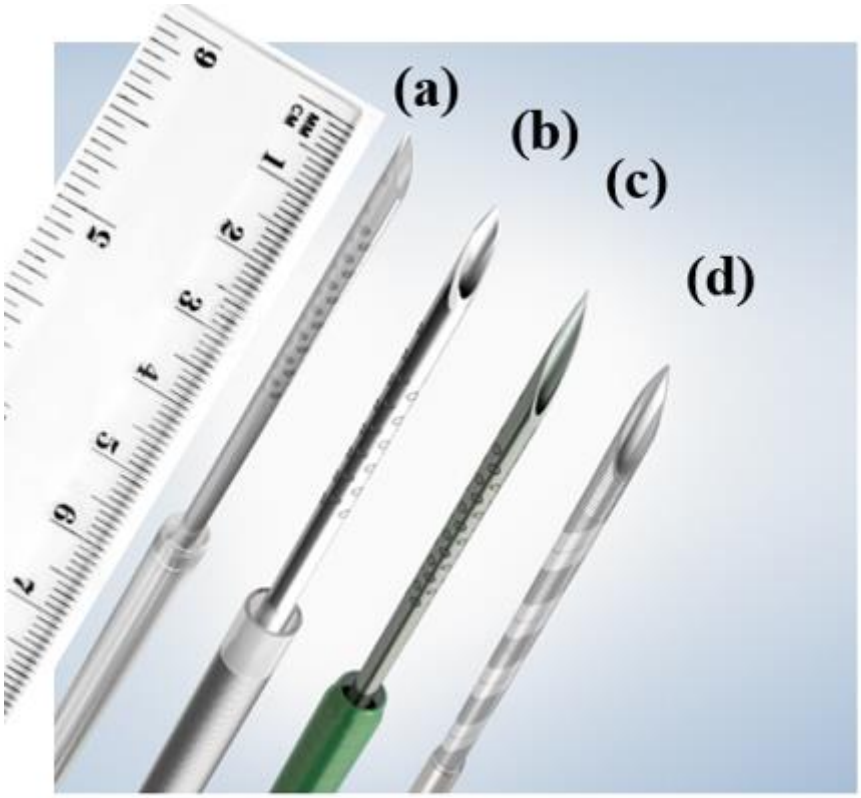

Figure 2.7: EBUS-TBNA needles. (a) 19 G, (b) 21 G, (c) 22 G, and (d) 25 G Copyright 2020 by Olympus America

When a needle is inserted into tissue, it exerts a force [72], that begins to fluctuate due to factors such as cutting and friction forces [73]. The force required to puncture tissue with a needle is referred to as the cutting force, while the stiffness force it generates results from the tissue's deformation. The cutting force comprises the plastic deformation induced by the cutting process and the force exerted by the needle on the tissue. The friction force arises from the tissue's internal structure. The tip geometry can be defined by three cutting angles: the inclination angle, λ, the induced angle, θ, and the rake angle, α [74]. The orientation angle is the angle between the tip's taper and the needle's axis. The induced angle, θ, on the other hand, is the angle between the two cutting edges. α refers to the angle between the cutting edge and the needle's direction. It determines the force required to cut the tissue. The geometry of the tip, defined by α and λ, affects the quality of the tissue obtained. A study conducted on two-plane needles revealed that those with a high λ and α can provide longer tissue samples [75]. According to Han et al., a small included angle and rake angle can reduce tissue penetration forces in the area between the tip and tissue [76].

Although few studies have specifically examined the geometry of the needle tip for EBUS-TBNA biopsy, several investigations have examined the utilisation of needles in other medical procedures. In a study by Hirsch et al., the tip of a 5-bevel needle was compared with that of a 3-bevel needle in subjects with diabetes. The study revealed that the tip of the 5-bevel needle had a 23% reduction in force when compared to the 3-bevel tip [77]. Another study, conducted by El Hajj and his team, compared the Franseen tip with a fine-needle aspiration (FNA) needle. It was discovered that the Franseen needle offers a larger specimen size and requires fewer passes than the FNA needle, but has a slightly higher risk of tissue damage [78].

2.4.1 Needle and Transducer Innovations

Significant progress has been made in transducers and needles, many of which are designed to improve tissue access and imaging guidance during minimally invasive procedures. Although many innovations aim to enhance the efficiency of these technologies, the core mechanisms governing tissue mechanical behaviour remain poorly understood.

Mechanical cutting is the primary method for performing biopsies, but a more effective and efficient way to enhance tissue-needle interaction is to incorporate ultrasonic energy. Perra et al. demonstrated that ultrasonic actuation at the needle tip, called the SonoLacet, induces highly localised nonlinear phenomena, such as cavitation, acoustic streaming, and radiation forces, which can facilitate tissue detachment and increase biopsy yield compared with passive needles of the same gauge. This technique was particularly beneficial in fine-needle biopsy procedures, as it significantly increased tissue yield, up to 3–6 times that of standard methods. This shows that ultrasonic actuation can directly influence cutting and coring mechanisms at the microscopic scale [79]. The development of these innovations demonstrates how dynamic energy input can affect the needle-tissue interaction. However, the mechanical properties of tissue, such as local stiffness, nonlinear elastic response, and energy absorption, are often assumed constant or treated as phantoms, suggesting that tissue-specific mechanical characterisation remains required.

Beyond basic actuation, advanced resonant needle designs are also being developed to manipulate vibration modes for specific clinical tasks. For example, the longitudinal-torsional needle developed by Cleary et al.[80] can penetrate deep bone. The device combines shear and axial motion through a geometric modification of the transducer-needle assembly.

Experimental and finite element analyses were used to maximise torsional displacement while preserving longitudinal amplitude. Although these methods are primarily used for bone, the principles of multimodal vibration and geometric tuning are widely applicable to needle technologies involving complex tissue structures [81]. Despite notable engineering advances in these needles, their use in soft tissues remains limited due to a lack of understanding of their mechanical properties. For instance, the performance of resonant needles in heterogeneous, nonlinear tissues such as lymph nodes remains an open question, highlighting a knowledge gap regarding how tissue properties influence needle behaviour across different scales.

Although these innovations demonstrate how dynamic needle behaviour, such as vibration mode, sensing signals, and actuation forces, can influence sampling yield, imaging guidance, and penetration efficiency, they do not replace the essential understanding of tissue mechanics, especially of lung lymph nodes, which is fundamental to accurate modelling of insertion forces, deformation, deflection, and sampling outcomes.

2.5 Summary

Since 1987, lung cancer has been the second most common cancer in both men and women worldwide. It arises from the uncontrolled division of lung cells, leading to DNA alterations. Lung cancer can spread through the bloodstream to other organs via metastasis. It is diagnosed using a bronchoscope, which is inserted into the bronchial tree to obtain high-resolution ultrasound images. For diagnosing and staging lung cancer, endobronchial ultrasound-guided transbronchial needle aspiration is a vital method for collecting and analysing mediastinal lymph node tissue samples. EBUS-TBNA employs hollow needles ranging from 19 G to 22 G. The usual target for an EBUS-TBNA biopsy is the lymph node, a small, kidney-shaped organ enclosed in a capsule of adipose tissue. Lymph nodes are soft tissues whose mechanical behaviour is best described as nonlinear and can be modelled as hyperelastic.

Ultrasonic actuation and resonant needle designs could improve the accuracy and effectiveness of percutaneous procedures by enhancing penetration, guidance, and biopsy success rates. However, studies are often limited by reliance on simplified or assumed models of tissue mechanical behaviour, particularly when interpreting sampling results and needle performance. This limitation is especially important in EBUS-TBNA, which involves multiple factors that affect biopsy success, such as controlled tissue deformation and effective sample retention.

Although lymph nodes are small, encapsulated, and mechanically heterogeneous, their nonlinear mechanical properties and response to needle insertion remain poorly understood and characterised. Therefore, existing needle innovations cannot be fully evaluated or optimised for lymph node biopsies without a deeper understanding of tissue behaviour during insertion. Additionally, while many studies have shown improvements in vibration response, needle visibility, and penetration force, little is known about how these factors affect the length of tissue sampling or the relationship between needle geometry and diagnostic tissue yield. The lack of information about how these factors affect sample properties highlights the need for foundational biomechanical research that connects tissue properties, insertion mechanics, and sampling outcomes. There is a significant gap between advanced needle and transducer technologies and the mechanical understanding needed to optimise their use in lymph node biopsy. This gap must be closed by developing a thorough understanding of the mechanical properties of lymph node tissue, validating models of needle-tissue interaction, and systematically examining how needle shape affects tissue deformation and sampling effectiveness.

Chapter 3: Experimental Background

3.1 Introduction

Any material that can bend or deform easily under external forces is referred to as ‘’ a soft material [82]. Biological soft materials, such as the brain [83], cancer cells [84], cartilage [85] and lymph nodes, exhibit varying length scales across their cellular and tissue structures. These complex structures require mechanical characterisation of their properties across the elastic modulus range and on physiologically relevant timescales, Figure 3.1.

The chapter provides an overview of the experimental techniques used in this thesis. Sections 3.2–3.3 examine experimental approaches for studying the mechanical behaviour of soft materials. Section 3.4 discusses the nonlinear elastic (hyperelastic) response of soft materials in detail, covering the implementation of common models and the underlying mathematical fundamentals. Finally, Section 3.5 provides a thorough discussion of the phenomena observed during needle-tissue interaction.

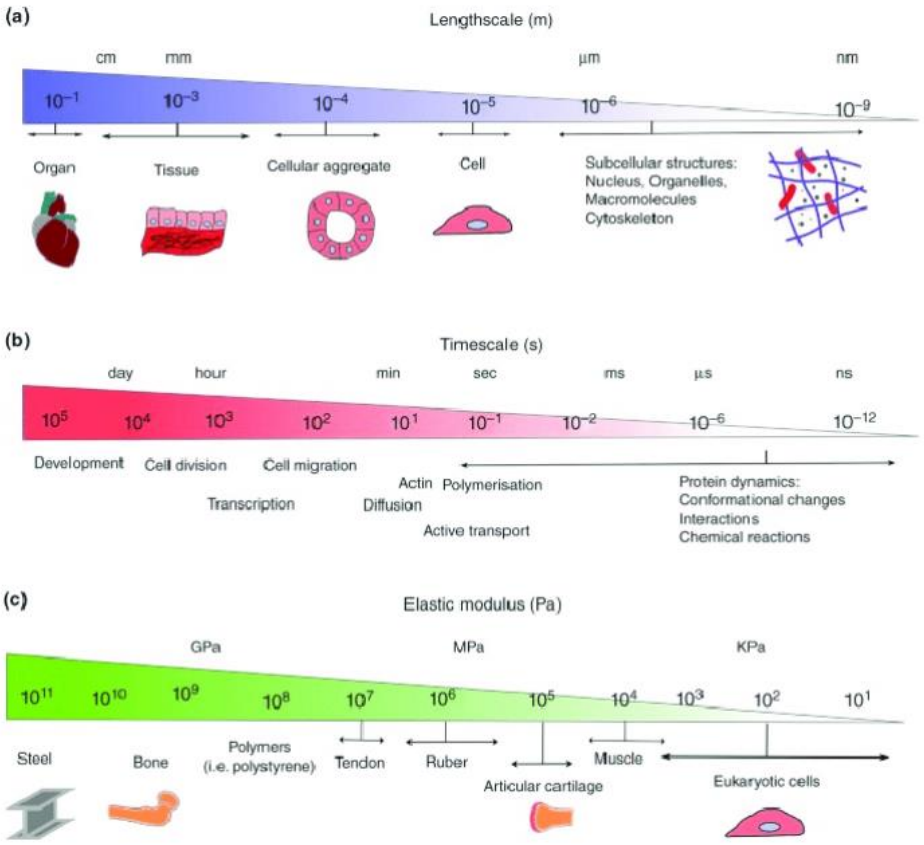

Figure 3.1: Various scales of soft biomaterials: (a) length scales from the molecular to the organ level; (b) different physiological process timescales; (c) comparison of the elastic modulus of different materials [86]. Copyright 2018 by the authors.

3.2 Soft Materials Mechanical Properties

Many constitutive models, including hyperelastic, poroelastic, viscoelastic, and linearly elastic approaches, have been utilised to study the mechanical properties of soft tissues. These models also fall into distinct categories of constitutive responses, thereby distinguishing them from typical engineering frameworks.

Several types of soft tissues and biomaterials exhibit non-linear stress-strain behaviour, characterised by an increase in stiffness with strain. Under small deformations, the relationship between stress and strain can be considered proportional, Figure 3.2(a). The elastic modulus, E, characterises the linear elastic stage of behaviour in most engineering materials. The threshold for the linear range can vary depending on the testing technique and the biomaterials used. One method for simplifying the nonlinear behaviour of materials using linear-elastic models is to decompose the stress profile into multiple components. Each component can be regarded as a linear model of mechanical behaviour [87].

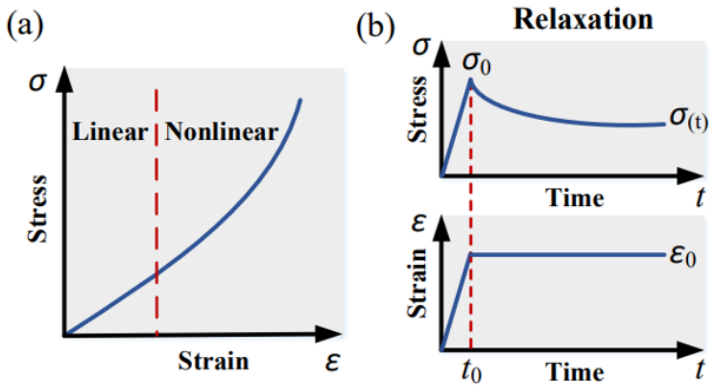

Figure 3.2: Constitutive response of soft biomaterial: (a) non-linear stress-strain behaviour model, where the stress profile can be considered linear under small strain; (b) time-dependent mechanical behaviour showing stress relaxation (top) and creep (bottom) [88]. Copyright 2018 by the authors.

The second major aspect of the properties of soft biomaterials is their time-dependent behaviour. Viscoelastic materials both store and dissipate mechanical energy when subjected to mechanical excitation. They can also exhibit stress relaxation and creep over time, Figure 3.2(b). The Prony series approximation is frequently used to describe the viscoelastic response [89]:

$$G(t) = G_\infty + \sum_j G_j . e^{-t/\tau j} \quad (3.1)$$

where the equilibrium shear modulus is G_∞, the time constant for the exponential terms is j, and the magnitude of the shear modulus is G_j. The initial shear modulus can be calculated by adding the values of G_j and G_∞. τ is the shear stress. [89].

Most soft biomaterials undergo hydration, and the poroelastic, also known as biphasic, model can be used to study the physiological effects of fluid movement through porous materials [90]. The hydraulic permeability, k, is expressed in terms of the intrinsic permeability, density, and fluid viscosity, and is a vital parameter for determining fluid-solid coupling. The shear modulus, G, and Poisson's ratio, υ, are also used to characterise the elastic behaviour of the porous skeleton [91].

The anisotropy and heterogeneity of soft materials are also important factors that influence their behaviour. Some of these characteristics exhibit direction-dependent behaviour due to their structural complexity [92], [93]. In addition to their inherent properties, external factors, such as environmental conditions, can affect the behaviour of soft materials. It is, therefore, important to study these phenomena using specific models and analysis methods [94], [95].

3.2.1 Soft Material Characterisation

The characterisation of soft tissues involves identifying the attributes that govern their mechanical properties. Knowledge of these properties enables a better understanding of how these materials respond and how they can be utilised efficiently. Mechanical properties are among the most commonly considered factors in soft-tissue characterisation. The mechanical properties of materials include Young's modulus, E, which measures elasticity in compression or tension, and shear modulus, G, which measures stiffness under elastic strain. Other properties include Poisson's ratio, υ, the ratio of longitudinal strain to transverse strain; yield strength, the stress level at which a material stops being elastic; and ultimate strength, the maximum stress a material can endure [96]. The study of soft tissues has a wide range of applications in medicine.

Characterising soft tissues can be challenging due to the complexity of the process and the many factors involved. One of the main issues is that soft tissues are fragile and smaller than

other tissues. Characterisation techniques may need to operate at the microscopic scale to study the mechanical properties of soft tissues, such as their elastic modulus, which typically ranges from tens of Pa to tens of kPa [97]. Due to the fragility of soft tissues, characterisation techniques must accurately measure and apply small-scale forces, such as micronewtons and nanonewtons, to investigate them properly. Additionally, techniques need a wide dynamic range to accommodate the various types of soft tissue. Finally, the deformation induced by forces applied to soft tissues must also be measured at smaller scales, such as micrometres and nanometres, to accurately determine their mechanical properties.

Another common issue in characterising soft tissues is sample preparation. Unlike traditional materials used in mechanical testing, which are typically rigid and dense, soft tissues are often difficult to cut and exhibit limited dimensional stability. They may also feature surface profiles with underlying architectures that follow the outlines of the constituent materials [98]. Additional challenges for characterisation methods in soft tissues include the heterogeneous, viscoelastic, and anisotropic properties previously mentioned. Water is the primary constituent of soft tissues. This means that their physiological responses to deformation can largely be attributed to the fluid flow within them [96]. Despite this, many studies, including this one, do not consider the viscoelastic behaviour and treat tissues as elastic or hyperelastic [99]. This is mainly due to the difficulty of deriving viscoelastic properties, which combine elastic and viscous characteristics. To capture these capabilities, specialised testing in the time and frequency domains is required, as well as the development of accurate mathematical models [99]. Anisotropy is a feature observed in soft tissues due to their orientation. It is important to ensure that samples are properly oriented during tests to avoid accidentally generating a bias [100].

One of the most overlooked yet vital aspects of soft tissue characterisation is how their mechanical properties change once they are outside the body. Once removed, the tissue becomes susceptible to adverse processes, including dehydration and degradation. Therefore, it is essential to test it as soon as possible to preserve its mechanical integrity. The mechanical properties of tissues can be maintained after excision; however, this requires keeping them at a specific temperature and in a hydrated environment. In some studies, tissues are temporarily frozen using liquid nitrogen. To minimise dehydration, they may instead be stored in saline solution. Regardless of the method used, it is important to preserve the tissue's natural state and characterise it as if it were being tested in vivo [103].

3.3 Mechanical Testing of Soft Tissue

Several techniques are used to mechanically test soft-tissue responses relevant to needle insertion mechanics. The mechanical characterisation techniques described in this section were selected to provide insight into tissue behaviour during needle insertion, Figure 3.3. In particular, unconfined compression testing, Figure 3.3(a), was used to evaluate the bulk mechanical response of soft tissue under compressive loading conditions analogous to needle-tissue interaction, while nanoindentation, Figure 3.3(b), enabled localised assessment of tissue stiffness and deformation behaviour at smaller length scales. These properties are key determinants of insertion force, tissue deformation, penetration resistance, and overall needle performance during intervention procedures.

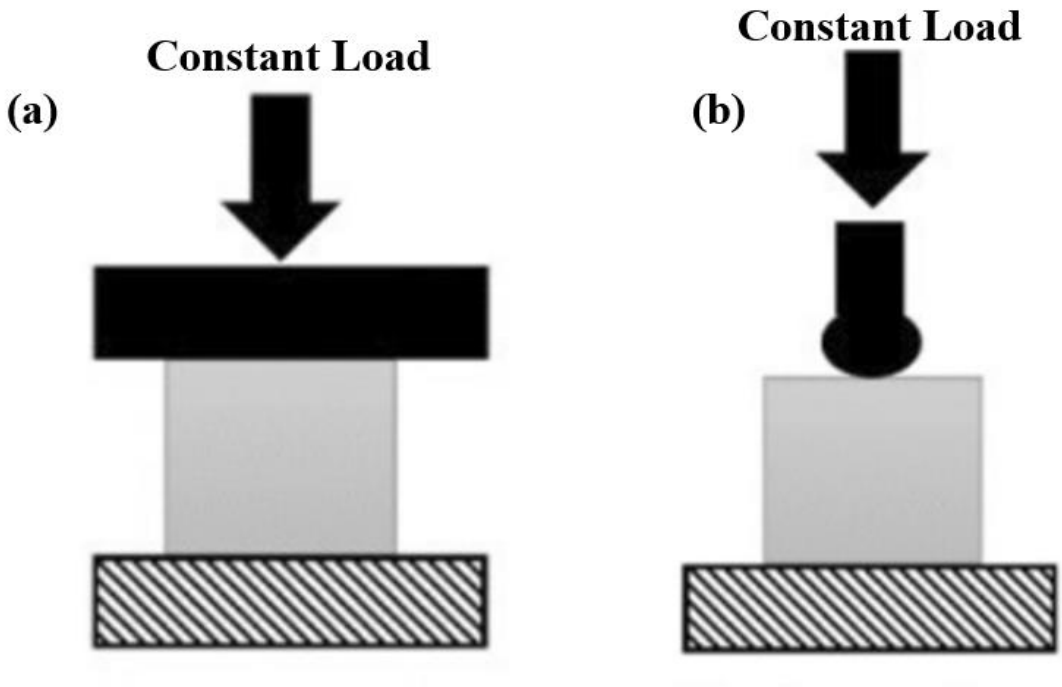

Figure 3.3: The various types of mechanical testing procedures used to assess the mechanical properties of soft tissues: (a) confined compression; and (b) nanoindentation [101]. Copyright 2014, Sage Publications.

3.3.1 Uniaxial Compression Testing

Compression testing is commonly used to characterise materials. It differs from tensile testing in that it compresses the sample rather than stretching it. The core idea of compression testing is similar to that of tensile testing: the force applied to a sample is measured to determine its stress. During the test, both strain and stress are recorded, and the resulting data are used to construct stress-strain curves. Instead of being gripped, the sample is placed between two plates and subjected to compressive loading. The two most common methods for conducting compression testing are confined compression, shown in Figure 3.4(a), and unconfined compression, shown in Figure 3.4(b) [98]. In confined compression testing (CCT), the sample is placed within an impermeable well and compressed by a platen, allowing the interior fluid to move vertically [98]. Unconfined compression testing (UCT) involves placing the sample between a non-porous plate and an impermeable base, which directs the flow of fluid radially [98].

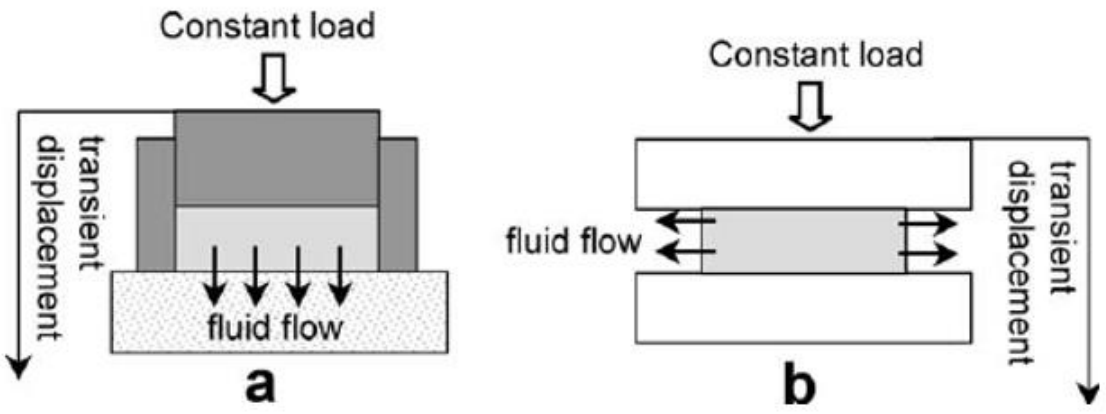

Figure 3.4: Mechanical tests for characterising soft materials: (a) confined compression, (b) unconfined compression [96]. Copyright 2023 The Authors. Published by Elsevier Ltd.

UCT allows the contact surface between a sample and the test tool to be free. The conditions under which contact between a soft tissue sample and a test tool is maintained during UCT are difficult to determine. In such cases, a small preload force is required to ensure sufficient contact between the sample and the test tool. This marks the beginning of the compression

process [105]. UCT has three contact classifications: no-contact, real-contact, and reference-contact. In the no-contact state, Figure 3.5(a), there is no strain or significant contact between the sample and the test tool. The real contact state, Figure 3.5(b), occurs when contact between the sample and the test tool is initiated and the reaction force from the tissue is negligible. It is an instantaneous state, making it difficult to define. The reference-contact state, Figure 3.5(c), occurs when the sample's reaction force reaches a set preloading threshold. The preloading force is typically used in compression testing to maintain contact between the sample and the test tool [106].

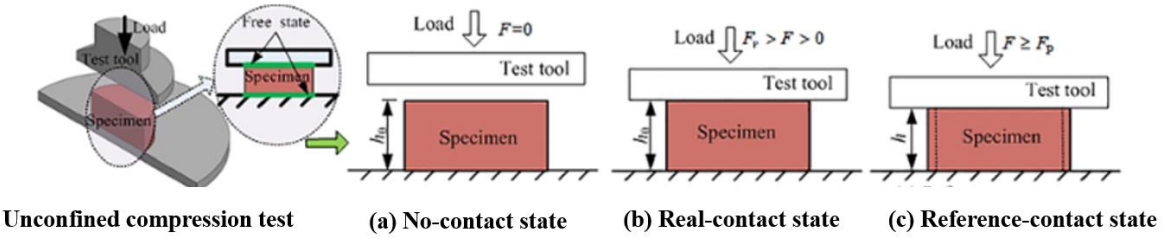

F_P: Preloading force
F: Reaction force of soft tissue
h_0: Nature height of specimen
h: Height of specimen under loading

Figure 3.5: Different contact states can be identified in biomaterials during compression tests. (a) No-contact state, characterised by the absence of contact between the tissue and the test tool and by zero strain; (b) real-contact state, in which the test tool first contacts the tissue; and (c) reference-contact state, which occurs when the tissue reaches the preloading force threshold [102]. Copyright 2021 by The Author(s).

One of the most significant advantages of compression testing is its ability to evaluate soft tissues in a hydrated environment [96]. Many load-bearing tissues in the body are subjected to compressive forces, and their mechanical properties can be measured through compression testing. Moreover, compression testing allows direct assessment of a material's properties by generating stress-strain curves. However, a disadvantage of compression testing is the difficulty of sample preparation, as samples must be cut to precise specifications and have no surface irregularities. Finally, frictional forces can affect the test's accuracy, leading to an overestimation of stress due to friction between the sample and the test tool.

During needle insertion, UCT provides insight into the bulk compressive behaviour of soft tissue and its resistance to deformation under load. The resulting stress-strain response can be used to estimate tissue stiffness and viscoelastic behaviour, both of which influence the needle insertion force and tissue displacement during penetration. Understanding these properties is important for predicting needle performance, optimising insertion parameters, and minimising tissue trauma during procedures.

3.3.2 Nanoindentation Test

Depth-sensing indentation (DSI), also known as nanoindentation, is a technique in which a load is applied, and the resulting indentation depth is measured to quantify the induced deformation (Figure 3.6). During typical DSI, the indentation depth, load P, and time t are monitored as the indenter is brought into contact with the sample surface. The sample's mechanical properties are then determined using various constitutive models.

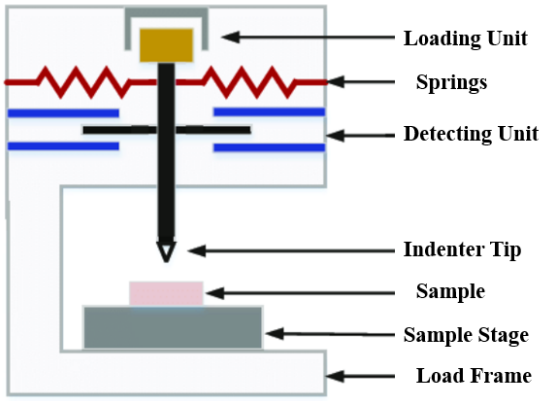

Figure 3.6: Schematic diagram showing different features of a nano-indenter instrument [103]. Copyright 2018 by the authors.

A nano-indenter has several essential components. The first is the loading unit, which can be driven by the expansion of components such as a magnetic coil or a piezoelectric element [105]. The second is the detection unit, which uses a transducer or sensor to measure the indenter's displacement. It can be used in combination with other methods to measure force, or independently [106]. The third essential component of a nano-indenter is the indenter tip. Indenter tips typically used for biomaterials are dull, such as spherical and flat indenters, rather than sharp indenters, such as the Berkovich and Vickers, to avoid penetrating the sample. The

sample stage comprises a two- or three-dimensional translational system to move the sample. A microscope is also integrated with the DSI to observe and select the indentation point on a sample during testing. The final essential component is a control system to operate the instrument, analyse the results and save the data.

Nanoindentation provides localised measurements of tissue mechanical properties, such as elastic modulus and resistance to deformation, at spatial scales relevant to needle-tip interaction. These measurements are particularly valuable for understanding the local mechanical environment encountered during needle insertion. Variations in local tissue stiffness can influence insertion force, needle deflection, penetration efficiency, and tissue damage. Therefore, nanoindentation data were used to evaluate how tissue mechanical heterogeneity may affect needle performance during insertion.

Compared with other methods, nanoindentation offers several advantages for characterising soft tissues. Firstly, it requires less effort in sample preparation than alternative techniques. This improves testing accuracy by removing constraints, such as cross-sectional dimensions, that limit comparisons between samples. Additionally, simpler sample preparation reduces damage, enabling in vivo studies of soft tissue.

3.3.3 Test Protocols

Compared with hard engineering materials, soft biomaterials are more compliant. Their elastic modulus typically ranges from MPa to kPa. Given the complexity of soft materials, it is important to consider their mechanical behaviour across multiple scales, particularly when using commercial instruments. This section provides guidelines for data collection and analysis, along with potential limitations.

3.3.3.1 Tip Selection

Tip Material

The materials used for the indenter tip are typically stiffer than the sample. This ensures that the tip's compliance is small and can be ignored. Due to the low modulus of soft materials,

indenter tips made of sapphire or diamond, which are widely used in nano-indentation, can be replaced with those made of aluminium [107], silicon [84], steel [108], and silica [109].

Tip Geometry

When characterising soft biomaterials, the force-induced indentation regime differs from that of stiff materials, as the forces generated at large displacements are smaller than those generated at relatively small displacements [101]. Compared with sharp tips, such as those made by Berkovich [104], Vickers [105], and cube corner [106], and with conical [107] geometries, the use of dull tips, such as spherical [92] and flat-ended [108] geometries, provides various advantages.

A dull tip can achieve a larger contact area, resulting in a higher force than a sharp indenter at the same indentation depth. This is ideal for testing within the instrument's resolution. Sharp tips can cause excessive stress concentrations and plastic deformation, leading to sample damage ranging from tissue penetration to membrane rupture. Due to the complexity, variability, and heterogeneity of soft biomaterials, using a sharp tip can yield inconsistent results across repeated tests. This is due to the small size and the lack of a substantial tip contact area. With a dull tip, a single measurement can be regarded as the average of multiple measurements, thereby reducing characterisation time. Despite the widespread use of spherical and flat-ended tips for characterising soft biomaterials, their advantages and disadvantages can vary with the specific conditions under which they are used. Figure 5.4 provides an overview of the different types of tips [109], [110].

Table 3.1: Comparison between spherical and flat-ended tips [111], [112].

	Typical Material types	**Advantages**	**Disadvantages**
Spherical Tips	Commonly manufactured from rigid, wear-resistant materials such as stainless steel, tungsten carbide, ruby, or diamond to maintain a constant tip radius and minimise wear during repeated indentation tests.	• Produces a smooth and gradually increasing contact area, resulting in a more uniform stress distribution. • Reduces stress concentration at the contact interface, minimising the likelihood of local tissue damage. • Better represents physiological contact conditions when testing compliant biological tissues. • Less sensitive to minor surface irregularities, providing stable and repeatable measurements on heterogeneous soft tissues.	• Contact area changes continuously with indentation depth, increasing the complexity of contact mechanics analysis. • Lower spatial resolution compared with flat-ended indenters because the contact region increases during loading. • Mechanical property calculations are highly dependent on accurate measurement of the tip radius.
Flat-Ended Tip	Typically manufactured from rigid metallic materials such as stainless steel, titanium, or aluminium, owing to their high stiffness, dimensional stability, and resistance to deformation during mechanical testing.	• Maintains a constant contact area throughout indentation, simplifying stress calculations and data interpretation. • Provides excellent positioning accuracy and high measurement repeatability. • Generates higher reaction forces than spherical tips at the same indentation depth, improving the signal-to-noise ratio of force measurements. • Well suited for quantitative mechanical characterisation,	• Produces higher stress concentrations around the contact edges, increasing the risk of localised tissue damage. • More sensitive to specimen alignment and surface roughness than spherical indenters. • Less representative of physiological contact conditions in many biological tissues due to

		where consistent contact conditions are required.	the abrupt contact geometry.

Tip Dimensions

By varying tip dimensions, indentation equipment can be used to analyse soft tissues across different length scales. Dimensions can range from the micro- and nanoscale to large-scale indentation, with tip diameters of millimetres or greater. To study the mechanical behaviour of soft tissues and avoid misinterpretation of the data, certain criteria should be applied during indentation. This is achieved by setting the tip size, R, to be five times the sample thickness and less than one-fifth of the sample width, thereby avoiding edge effects [107].

3.3.4 Choice of Mechanical Test and Indentation Tip

To evaluate the effective bulk mechanical properties of soft materials under conditions that permit lateral deformation, unconfined compression testing will be performed in Chapter 4 rather than confined compression testing. In unconfined compression, the sample can expand laterally under axial load, so the measured response reflects both axial and lateral deformation, which is influenced by the material's Poisson’s ratio. This setup is ideal for soft materials that exhibit viscoelastic behaviour and are nearly incompressible. Allowing lateral strain provides a more accurate assessment of a material's behaviour under physiological and practical loading conditions. Conversely, when confined compression is employed, lateral deformation is restricted, leading to increased apparent stiffness that may not accurately represent the mechanical behaviour of the soft material. From an experimental perspective, unconfined compression offers simpler sample preparation, reduced sensitivity to frictional and boundary conditions, and facilitates easier interpretation of the resulting stress-strain behaviour.

The shape of the indentation tip is crucial for the mechanical characterisation of soft materials, as it directly influences stress distribution, deformation patterns, and the accuracy of derived mechanical parameters. Therefore, a spherical indentation tip will be used in nanoindentation

tests for its effectiveness in characterising soft materials. Spherical indenters produce a gradually increasing contact area as indentation depth increases, resulting in a smoother stress distribution and reduced stress concentration compared with flat-ended indenters. This advantage is particularly important for soft materials, which often undergo large deformations and exhibit non-linear mechanical behaviour. By spreading deformation more evenly across a larger volume of material, spherical indentation reduces the risk of localised damage and yields a response that more accurately reflects the bulk material's properties.

Based on the theoretical considerations presented in this section, unconfined compression and spherical indentation were selected for the experimental characterisation of soft materials. These methods are described and implemented in detail in Chapter 4.

3.4 Mechanical Behaviour of Soft Material

Finding suitable constitutive laws for the complex mechanical behaviour of soft materials can be challenging; however, the mathematical analysis used to determine their mechanical properties can be very valuable. A range of non-linear models can provide a detailed understanding of the behaviour of soft materials. The most commonly used model is the hyperelastic model, which assumes that stress does not depend on the history of previous time or loading. The stiffness and stress of a material are described by the strain energy function (SEF), which depends on time [113].

3.4.1 Continuum Mechanics of Hyper-elasticity

Constitutive models for soft materials are widely used to study their nonlinear mechanical behaviour. Before describing those models, it is important to understand the two types of deformation: pure shear and volumetric deformation [114]. The SEF, ‘W’, of a hyperelastic material is expressed as [39]:

$$W = W(C) \tag{3.2}$$

where C is the right Cauchy-Green tensor. The relationship between stress and strain can be derived from (3.2) as:

$$S = 2\partial W/\partial C \quad (3.3)$$

where S denotes the second Piola-Kirchhoff stress tensor.

If the material is isotropic, then its SEF can be expressed by its principal invariants:

$$W = W(I_1, I_2, I_3) \quad (3.4)$$

where I_1, I_2, I_3 are the three invariants of the green deformation tensor, defined in terms of the principal stretch ratios λ_1, λ_2, and λ_3, as in [44]:

$$I_1 = \lambda_1^2 + \lambda_2^2 + \lambda_3^2 \quad (3.5a)$$

$$I_2 = \lambda_1^2\lambda_2^2 + \lambda_2^2\lambda_3^2 + \lambda_3^2\lambda_1^2 \quad (3.5b)$$

$$I_3 = \lambda_1^2\lambda_2^2\lambda_3^2 \quad (3.5b)$$

3.4.2 Anisotropy Structure

The mechanical response of biological soft tissues, in particular, is influenced by their structural arrangement. For instance, the presence of components with a particular spatial orientation can determine the tissue's response. This phenomenon can be captured by modifying the previous formulation to introduce new invariants related to the tissue's structural characteristics. For instance, if a single family of fibres has a specific direction in each region of the tissue structure, two additional structural invariants might be introduced [115].

$$I_4 = A.CA, I_5 = A.C^2A \quad (3.6)$$

where A indicates the fibre orientation, measured in the undeformed state. The local fibre orientation in the deformed configuration is determined by the unit vector

$$a = FA/\lambda \quad (3.7)$$

where λ is the stretch in the fibre direction. The fourth invariant equals the square of the tissue's stretch in the fibre direction, and the fifth invariant shows that the fibres' contribution to the

SEF depends on orientation and shear. Consequently, the SEF and the associated stress-strain relationship are defined as [39]:

$$W = W(I_1, I_2, I_3, I_4, I_5) \tag{3.8}$$

$$S = 2\sum_{i=1}^{5}\left[\left(\partial W/\partial I_i\right)\left(\partial I_I/\partial C\right)\right] \tag{3.9}$$

Equations (3.10) and (3.11) present a constitutive model that is isotropic and commonly used in soft tissue mechanics [116]. Equation (3.10) offers broad generality, and a simpler, more specific formulation is generally assumed [117]:

$$W = W_m(I_1, I_2, I_3) + W_f\ (I_4) \tag{3.10}$$

where the contributions of the two factors to strain-energy efficiency are usually considered separately. For instance, Equation (3.12) was justified by assuming that the tissue's isotropic ground matrix, W_m, is reinforced by fibres, W_f [118].

3.4.3 Incompressible Behaviour

It is generally believed that the presence of a significant amount of liquid in soft materials is responsible for their nearly incompressible behaviour (I3 = 1) under specific mechanical conditions, e.g., at high strain rates. This necessitates adopting a specific form of the equation, so that Equation (3.4) becomes [119]:

$$W = W(I_1 - 3, I_2 - 3) \tag{3.11}$$

3.4.3.1 Hyperelastic Models

According to Chagnon et al [120], an efficient hyperelastic model has three main characteristics. Firstly, an efficient SEF should be able to reproduce the entire soft material's response in an S-shaped manner. Secondly, the number of fitting parameters for a particular material should be minimised to reduce the number of tests required to determine them. Finally, the mathematical model should be easy to implement numerically.

In the literature, several hyperelastic models describe the hyperelastic response of soft materials, including the Neo-Hookean, full polynomial, Mooney-Rivlin, reduced polynomial, Yeoh and Ogden models [121].

Mooney-Rivlin Model

The Mooney-Rivlin (M-R) model is a polynomial model that combines two theories: large elastic deformation and the isotropic material theory developed by Mooney in 1948 and Rivlin in 1940, respectively [125]. The M-R model can be used to describe the isotropic, nearly incompressible, and nonlinear mechanical response of various soft materials through their strain-energy function (SEF) [126]. Although the M-R model is useful for studying the linear, isotropic, nonlinear, and multiphase mechanical responses of soft materials in various applications, such as shear deformation and uniaxial expansion, it cannot capture significant upturns in the force-shear-displacement and force-extension relationships.

For a compressible soft material, the M-R model takes the form [122].

$$W = C_{10}(\bar{I}_1 - 3) + C_{01}(\bar{I}_2 - 3) + \frac{1}{D_1}(J_{el} - 1)^2 \quad (3.12)$$

The strain-energy-density model function W is based on the Mooney-Rivlin hyperelastic model. The total strain energy is then decomposed into deviatoric and volumetric components. The deviatoric component depends on the first and second invariants of the isochoric right Cauchy-Green deformation tensor, $\bar{I}_1$ and $\bar{I}_2$, which are obtained by removing the volumetric component of the deformation. This ensures that these terms describe purely shear behaviour, independent of volume change.

The material constants C_{10} and C_{01} govern the material's nonlinear shear response by controlling the contributions of the first and second invariants. Subtracting 3 from each invariant ensures that the strain energy is zero in the undeformed reference configuration.

The final term represents the volumetric contribution to the strain energy, where J_{el} is the elastic volume ratio and D_1 is a material parameter related to compressibility. This term penalises deviations from incompressibility, with larger values of $1/D_1$ enforcing near-incompressible

behaviour. Together, these terms define the total strain energy stored in the material as a function of deformation.

Neo-Hookean Model

The Neo-Hookean model is regarded as the simplest theoretical model and is a special case of the M-R form with C_{01} = 0, introduced by Rivlin in 1948 [51]. It is a fundamental component of Hooke's law for large-scale deformation and is used to study the nonlinear behaviour of both compressible and incompressible materials. Mathematically, the strain energy function (SEF) of the Neo-Hookean model is expressed as:

$$W = C_{10}(\bar{I}_1 - 3) + \frac{1}{D_1}(J_{el} - 1)^2 \quad (3.13)$$

The distinguishing feature of this type of model is its constant shear modulus, which can be characterised by two parameters: the stress and the volumetric deviatoric parameter. The Neo-Hookean model is appropriate when material data is limited, but it cannot capture the upturn in the stress-strain curve.

Yeoh Model

In 1993, Yeoh proposed a phenomenological third-order polynomial based solely on the first invariant, I_1, [123]. The Yeoh model is used to study the non-linear, incompressible, and isotropic mechanical characteristics of soft materials and can capture the upturn in the stress-strain curve. For compressible materials, the Yeoh model is expressed as. [54].

$$W(C_{10}, C_{20}, C_{30}, K) = C_{10}(\bar{I}_1 - 3) + C_{20}(\bar{I_1} - 3)^2 + C_{30}(\bar{I_1} - 3)^3 + \frac{K}{2}(J_{el} - 1)^2 \quad (3.14)$$

where$C_{10}, C_{20}, \text{and } C_{30}$ are the material parameters of the deviatoric term, and K is the material's bulk modulus. In addition, volumetric deformation may be captured by higher-order terms.

In addition to being difficult to measure experimentally, the Helmholtz free energy's weak correlation with the second strain invariant (I_2) of most elastomers prompted Yeoh to exclude

I_2 from the model [124],[125]. An incompressible material can be subjected to Cauchy stress under various deformations, such as biaxial, uniaxial, and planar, which are defined as [123]:

$$\sigma_{uni} = 2[C_{10} + 2C_{20}(\bar{I}_1 - 3) + 3C_{30}(\bar{I}_1 - 3)^2](\lambda^2 - \lambda^{-1}) \quad (3.15a)$$

$$\sigma_{bi} = 2[C_{10} + 2C_{20}(\bar{I}_1 - 3) + 3C_{30}(\bar{I}_1 - 3)^2](\lambda^2 - \lambda^{-4}) \quad (3.15b)$$

$$\sigma_{pl} = 2[C_{10} + 2C_{20}(\bar{I}_1 - 3) + 3C_{30}(\bar{I}_1 - 3)^2](\lambda^2 - \lambda^{-2}) \quad (3.15c)$$

The Yeoh model is well-suited to handling large strain ranges and various deformation modes with limited data, thereby reducing the requirements for materials testing [126].

Ogden Model

In 1972, Ogden proposed a phenomenological model that uses principal stretches rather than invariants [127]. The Ogden model is widely used in applications involving biological tissues, rubber, and polymers, and is useful for describing the slightly compressed behaviour of materials.

The model's energy potential depends on the principal stretch. Unlike other models, it uses an independent variable rather than a strain tensor invariant [128].

$$W = \sum_{i=1}^{N} \frac{2\mu_i}{\alpha_i^2}\left(\overline{\lambda_1^{\alpha i}} + \overline{\lambda_2^{\alpha i}} + \lambda_3^{\alpha i} - 3\right) + \sum_{i=1}^{N} \frac{1}{D_i}(J_{el} - 1)^{2i} \quad (3.16)$$

$\bar{\lambda}_i$ is the deviatoric principal stretch, and μ_i, α_i are temperature-dependent material properties.

One advantage of the Ogden model is that it can capture the upturn in the stress-strain curve, which is useful for simulating large deformations. It is important to avoid using this model with limited test data (e.g., uniaxial tensile or compressive data only).

3.5. Needle Insertion into Soft Materials

Having considered issues relating to soft tissues, it is now necessary to consider needle insertion into these tissues.

A medical needle usually consists of a slender stainless-steel or nitinol needle tube with a plastic hub at one end and a sharp tip at the other. The hollow space inside the tube is called the "lumen," and the tip varies in cross-section. The shaft, however, maintains a constant cross-section. Needle biopsy is a minimally invasive procedure that involves taking tissue samples from organs such as the prostate, breast, and lymph nodes [129]. The precise placement of the needle and accurate tissue sampling are essential for reliable diagnosis and treatment decision-making. During the procedure, the force exerted by the needle can cause it to deform and angle away, and may also displace soft tissues and surrounding organs, resulting in false negatives or inaccurate results due to improper sampling [130].

3.5.1 Needle Insertion Phases

To accurately insert a needle into soft tissue, one should consider the needle's motion relative to its surroundings rather than its absolute motion. Figure 3.7 illustrates the various phases of needle interaction and how they can be distinguished by considering the needle's position relative to the tissue's outer boundary. These phases can recur if the needle encounters internal structures or changes in tissue properties during insertion.

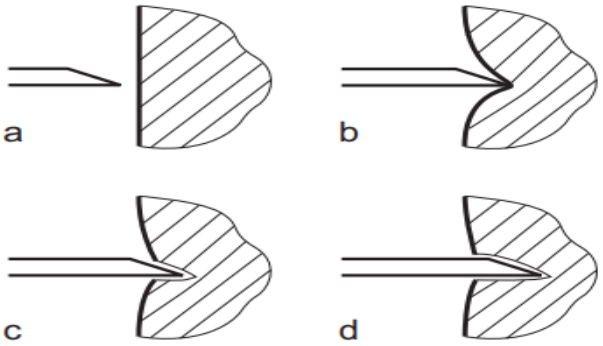

Figure 3.7: Basic phases during needle insertion: a- no interaction; b- boundary displacement; c- tip insertion; d- tip and shaft insertion [131]. Copyright 2011 by IEEE.

3.5.1.1 Phase 1: Boundary Displacement

The initial phase, shown in Figure 3.7 (b), begins when the needle contacts the tissue's outer boundary and ends when this boundary is breached. This event is known as a puncture. The displacement phase occurs when the tissue's boundary deflects under the load applied by the needle tip. However, the needle tip does not break through the tissue. This phenomenon, called "tenting", occurs when the boundary continues to move with the needle [132].

Figure 3.8 illustrates a typical force-time curve, adapted from Kobayashi et al.[133], who measured the tissue's relative velocity and displacement. The figure shows that during the displacement phase, the force increases non-linearly. The curve's shape is reminiscent of the load increase observed during thin-membrane tissue displacement, as demonstrated by Selvadurai [134]. Moreover, nearly all studies in this thesis exhibit the same non-linear axial force behaviour with respect to boundary displacement.

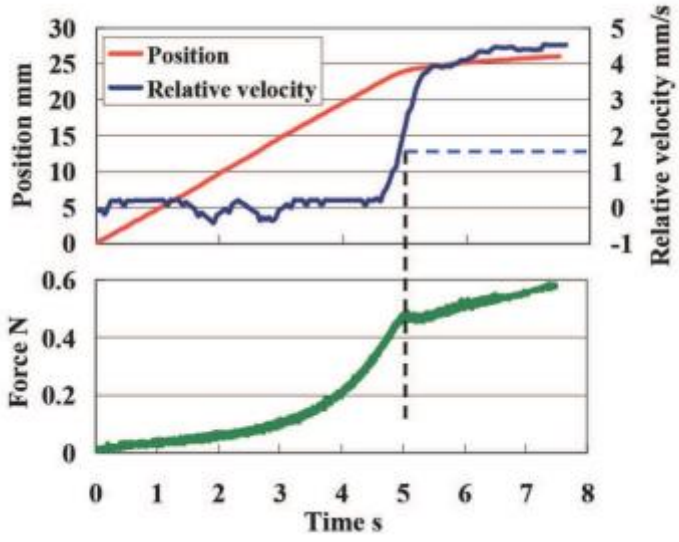

Figure 3.8: The difference between the post-puncture and pre-puncture phases during needle insertion is determined by the needle's relative velocity. For example, the position of the 17G bevelled needle is at the tissue boundary when it is inserted into a porcine liver ex vivo at 5mm/s [133]. Copyright 2009 by IEEE.

An increase in relative velocity at a specific time can indicate that a puncture has occurred. According to Mahvash and Dupont [135], Shergold and Fleck [136], Azar and Hayward [137],

and Nguyen [138], the events during the second and third stages of the procedure can be explained using fracture mechanics. When the tissue boundary is displaced by the needle, the load at the needle entry site increases, along with the stresses in the surrounding tissue. According to Kobayashi [139], if stresses exceed a threshold, a crack may form in the tissue, thereby allowing the needle to penetrate it. Based on the work of Azar and Hayward [137], and Fleck and Shergold [136], the shape of the needle tip influences crack formation. When employing conical or sharp needles, a planar crack can be initiated. Diamond-tipped needles can cause star-shaped cracks, while needles with a large bevel angle may produce ring cracks, as shown in Figure 3.9. The second phase of needle insertion begins once a crack has been initiated.

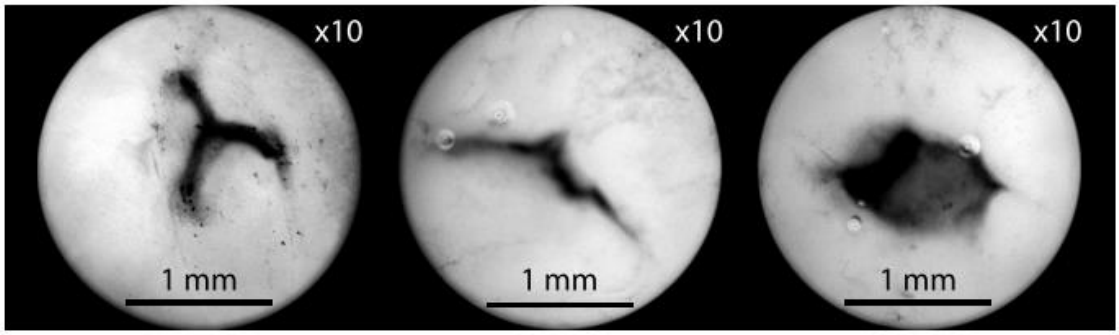

Figure 3.9: Microscopic crack pattern observed in fresh porcine tissue penetrated by three types of needles. The left image shows the geometry of the crack created with a Franseen needle, which has a triangular diamond tip, while the middle and right images show the cracks created using a standard bevel tip and a short-bevel biopsy needle, respectively [140]. Copyright 2011 by IEEE.

3.5.1.2. Phase 2: Tip Insertion

The second phase, shown in Figure 3.7 (c), begins after the tissue boundary is breached and ends when the boundary shifts from the tip to the shaft. As the needle advances, the size of the tissue-boundary crack increases. According to Mueller [147], the tip's sharp edges create a recess that is wedged open by the expanding cross-sectional area.

Depending on the tissue's properties, crack development can be categorised into two phases: a gradual process involving cutting and a sudden burst involving rupture. The tissue's properties,

such as its rupture toughness and the strain energy it stores, are also considered when determining the type of growth.

When a thin membrane is punctured, the energy stored during the displacement phase can trigger a sudden extension of the crack. This may lead to a significant decrease in force due to accumulated strain energy, an irreversible process. The increase in strain energy during deformation persists until the crack's energy becomes sufficiently low to allow stable movement.

According to Dupont and Mahvash [140], a needle passing through the internal boundary of a tissue layer can cause a rupture. This can occur when the toughness of the new tissue layer is lower than that of the existing layer. The same authors also note that the transition from the tip to the shaft can increase the axial force caused by the hole in the tissue layer's boundary. This effect can vary with the needle type, i.e., its tip geometry.

3.5.1.3 Phase 3: Tip and Shaft Insertion

The third phase, Figure 3.7 (d), begins after the transition from tip penetration to shaft penetration. It terminates when the needle stops or an internal boundary is reached. During this phase, the gap's distance, size, and shape, as well as the contact zone between the tissue and the tip, remain constant. As the needle advances, only the contact area between the shaft and the tissue increases. The needle is subjected to various forces during this phase, including rupture and cutting forces at the tip. It also experiences varying frictional forces due to the interaction between the tissue and the shaft.

In an ex vivo setting, Hing et al. observed that the cutting force in porcine liver was relatively constant [141]. However, it may vary with the degree of tissue inhomogeneity. The study's findings were based on 45 insertions of diamond-tip needles, performed at an average rate of 13 mm/s. The analysis employed a simplified force decomposition, assuming that the measured axial force is primarily governed by frictional and cutting forces. This assumption neglects secondary effects such as tissue viscoelasticity and dynamic insertion effects, which may influence force variability under different insertion conditions.

3.6 Summary

This chapter covered various principles and methodologies that will inform the experimental tests conducted in the remainder of this thesis. The experiments in this thesis will investigate the mechanical properties of various soft materials and employ needle insertion to identify the associated forces and phases.

Studies of the mechanical properties of soft biomaterials often begin with indentation and unconfined compression tests. These tests are designed to determine the stress-strain relationship. Because this relationship exhibits non-linear behaviour, it is expressed in terms of strain energy, and different hyperelastic models are analysed to identify the best-fitting model. The second part of the experimental testing will involve needle insertion, during which forces will be measured throughout Phases 1, 2, and 3. The data collected from the mechanical properties and needle insertion experiments will be crucial to achieving the aim of the thesis, as they will enable computer modelling.

Chapter 4: Mechanical Characterisation of Soft Materials

4.1 Introduction

The work presented in this chapter aimed to describe the experimental methodology used to mechanically characterise soft biological tissues and tissue-mimicking materials, and to investigate potential correlations among the measured properties of these materials. The resulting material descriptions are subsequently used as constitutive inputs for the finite element analysis (FEA) framework developed in later chapters to simulate needle-tissue interactions.

Soft tissues are widely recognised to exhibit nonlinear, anisotropic, and viscoelastic behaviour, which complicates their mechanical characterisation and modelling. Their response is also highly sensitive to environmental conditions, biological variability, and post-excision handling. These factors introduce significant challenges in obtaining consistent, representative mechanical data, particularly when the aim is to develop predictive computational models.

To address these challenges, this thesis employs a combination of experimental approaches, with unconfined compression and nanoindentation selected as the primary characterisation techniques. These methods are widely used in soft tissue mechanics but are subject to inherent limitations, including boundary effects, sample heterogeneity, and surface–probe interaction artefacts such as slip and local stress concentration.

Importantly, the selection of these two techniques is driven by their complementary relevance to the mechanics of needle–tissue interaction. Needle insertion involves deformation across multiple length scales. At the macroscopic level, tissue deformation is governed by bulk, nonlinear mechanical resistance, which determines the global force required for needle advancement. At the microscopic level, the initial interaction between the needle tip and tissue is governed by localised contact mechanics and surface-level resistance. Unconfined compression testing captures the material's global, bulk response under large deformation, while nanoindentation provides local mechanical characterisation at small length scales, representing the initial conditions of needle penetration [101].

Human soft-tissue characterisation is further constrained by ethical and regulatory limitations that restrict access to tissue samples and preclude extensive or repeated testing. In addition, biological variability arising from age, sex, pathology, and post-excision degradation

introduces further uncertainty into experimental datasets. These limitations motivate the use of both biological specimens and tissue-mimicking materials to enable systematic and reproducible mechanical characterisation.

In this study, a range of materials was selected to support this objective. Polyvinyl alcohol (PVA) hydrogel was used as a controllable and reproducible phantom material, enabling systematic variation of mechanical properties. Large pickled capers were included as a structurally heterogeneous analogue to assess the influence of internal architecture and sample handling on the measured mechanical response. Chicken breast was selected as a widely used generic soft-tissue surrogate for benchmarking. Finally, ex vivo porcine lung lymph nodes were used as the primary biological reference material, representing the target tissue of interest.

Together, this experimental framework enables the development of a multiscale mechanical characterisation strategy, forming the basis for constitutive modelling and subsequent finite element simulation of needle–tissue interaction presented in later chapters.

4.2 Summary of Development of Physical Model

The experimental workflow for characterising the mechanical behaviour of soft-tissue analogues and biological specimens is illustrated in Figure 4.1. The process began with specimen preparation using PVA hydrogel phantoms and ex vivo biological tissues selected to represent a range of low-stiffness, nonlinear elastic materials relevant to soft-tissue mechanics. Prior to mechanical testing, sample volume and mass were measured to determine density, ensuring consistent specimen preparation and enabling comparability across material groups.

Mechanical characterisation was performed using unconfined compression and nanoindentation on a Biomomentum Mach-1 V500c system equipped with flat and spherical indenters. This combination of testing modalities was selected to capture both the bulk and localised mechanical responses of the materials across different deformation scales. Unconfined compression testing was used to characterise the global, nonlinear stress–strain behaviour under large deformation, while nanoindentation provided complementary measurements of the localised surface response at small indentation depths, representing microscale tissue–contact interactions.

Load–displacement data from both experimental modalities were processed to derive stress–strain relationships, which were then used to calibrate hyperelastic constitutive models. In particular, the experimental data were fitted with Ogden-type formulations to characterise the materials' nonlinear elastic response over physiologically relevant strain ranges. The resulting material parameters were compared with published literature values to assess physiological relevance and experimental validity. Where discrepancies were observed, testing protocols were refined and measurements repeated to improve repeatability and reduce systematic error.

Beyond parameter identification, this stage of the work established the experimental basis for a multiscale mechanical description of soft-tissue behaviour. Unconfined compression captures the material's macroscopic, bulk response under large deformation, which governs global resistance during needle insertion and tissue displacement. In contrast, nanoindentation characterises localised mechanical behaviour at the microscale, reflecting the initial contact conditions between a penetrating needle tip and the heterogeneous tissue structure. Integrating these two scales provides a more complete representation of the mechanical environment encountered during needle–tissue interaction.

Importantly, the derived material parameters were not developed solely for descriptive purposes but to serve as constitutive inputs for the computational framework presented in subsequent chapters. Specifically, the experimentally calibrated hyperelastic models were implemented within a finite element (FEM) needle insertion model to simulate the mechanical response of soft tissues during needle penetration. This includes predicting force–displacement behaviour, spatial tissue deformation, and needle deflection under controlled insertion conditions. In this context, the compression-derived parameters primarily govern bulk resistance and global deformation fields, while nanoindentation-informed behaviour contributes to localised contact mechanics at the needle–tissue interface.

When agreement with literature data was insufficient, experimental conditions and modelling assumptions were refined to improve consistency and physiological relevance. This iterative approach ensured that the final constitutive parameters used in the FEM model were both experimentally grounded and mechanically representative of soft tissue behaviour.

Overall, this workflow establishes a validated multiscale experimental-to-computational pipeline, linking material characterisation directly to predictive modelling of needle–tissue interaction.

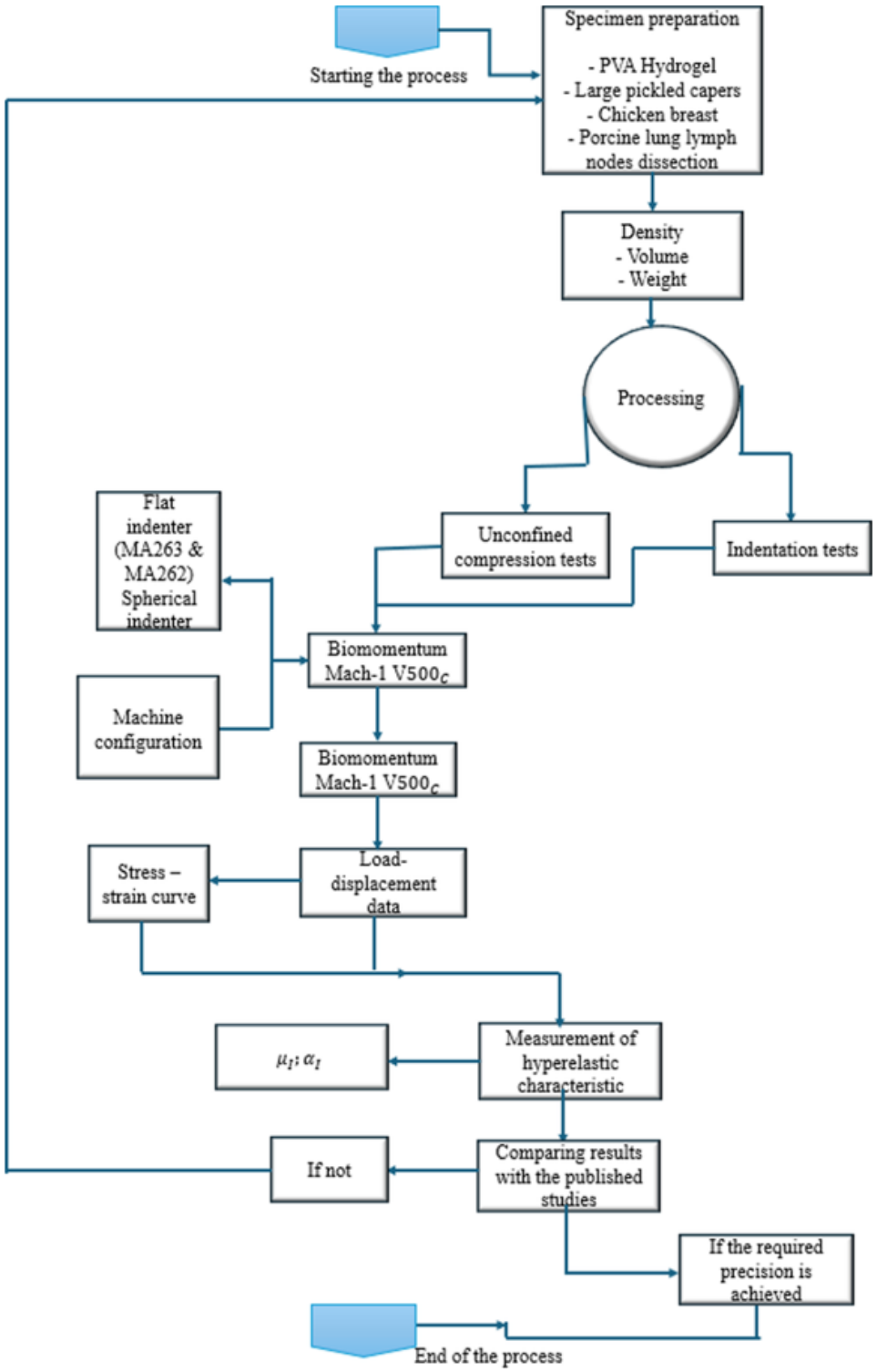

Figure 4.1: Summary of the steps involved in the mechanical characterisation of lymph nodes.

4.3 Materials and Methods

4.3.1 Materials

4.3.1.1 PVA Hydrogel

PVA hydrogels belong to the broader category of gels. They typically consist of a solvent and a polymer that forms a three-dimensional network through interactions among its macromolecular chains. This network can be stabilised by either covalent crosslinking or reversible crosslinking, arising from physical interactions such as hydrogen bonding or crystallite formation. The choice of crosslinking mechanism affects the hydrogel's responsiveness, stability, and mechanical properties [142]. The physicochemical and bio-tribological properties of polyvinyl alcohol (PVA) hydrogels make them ideal for use in the biomedical sector [149-150]. This type of gel is reported to be ideal for mimicking the mechanical behaviour of the human lung under compressive loading. This is due to the friction caused by the free flow of water between the two materials [148-151].

The production of PVA involves polymerising vinyl acetate to poly(VAc), followed by hydrolysis. Higher degrees of hydrolysis can reduce the water solubility of PVA. A preparation temperature above 70°C triggers the dissolution of PVA in water [152-153]. This occurs in products with a water concentration of 95% or higher. Physical crosslinking involves repeatedly thawing and freezing PVA solutions. This process is then utilised in a set of experiments to produce PVA-based gel structures.

The first case of physical crosslinking of PVA to create a gel was reported in 1975 [148]. Subsequent research has shown that various processing parameters and the freeze-thaw cycle affect the mechanical properties. The phase separation process plays a crucial role in the physical crosslinking of hydrated PVA gel structures, Figure 4.2(a). Exposure to sub-zero temperatures can cause the water in the solution to freeze and detach from the PVA, creating zones of high PVA hydrogel concentration, Figure 4.2(b). The proximity of the PVA chains can lead to the emergence of crystalline and hydrogen-bonding forms, Figure 4.2(c) And these structural changes can remain intact even after the solution has been thawed. As a result, these two phenomena lead to the creation of a three–dimensional network.

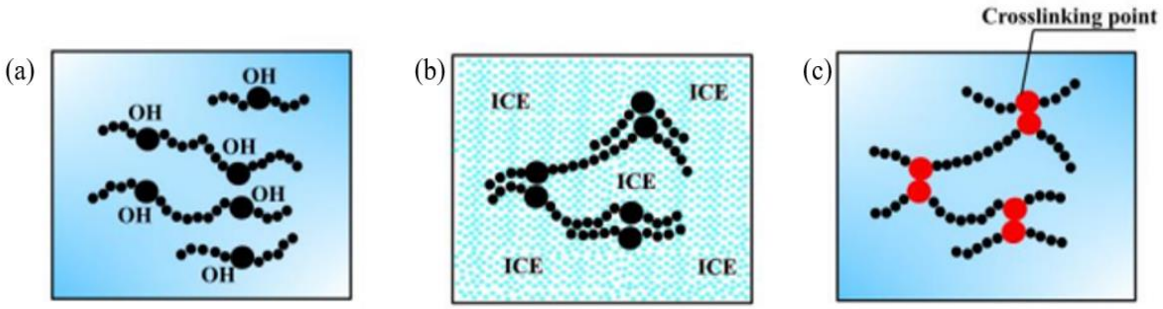

Figure 4.2: Physical crosslinking of PVA hydrogel process: (a) PVA hydrogel solution; (b) freezing process, during which water separates from the polyvinyl alcohol; (c) thawing process [149]. Copyright 2018 by Elsevier Ltd.

Sample Preparation

The PVA solution was prepared by adding 99+% hydrolysed PVA with a molecular weight (Mw) of 16400-18600 g · mol. A 6% crystalline PVA solution was prepared in a standard glass conical flask by heating, adding, and mixing 12.77 g of PVA crystal into 200 ml of distilled, degassed water. 0.01% or 0.021 ml of benzalkonium chloride was used as a preservative, Figure 4.3(b), (c). The solution was then poured into a 100 x 100 x 100 mm^3 (length x width x height) plastic cubic mould, Figure 4.3(d), and processed through three freeze-thaw cycles (FTC) between -20 °C and 20 °C. Each cycle involved freezing the solution for 12 hours at -20 °C and thawing at room temperature for another 12 hours, Figure 4.3.

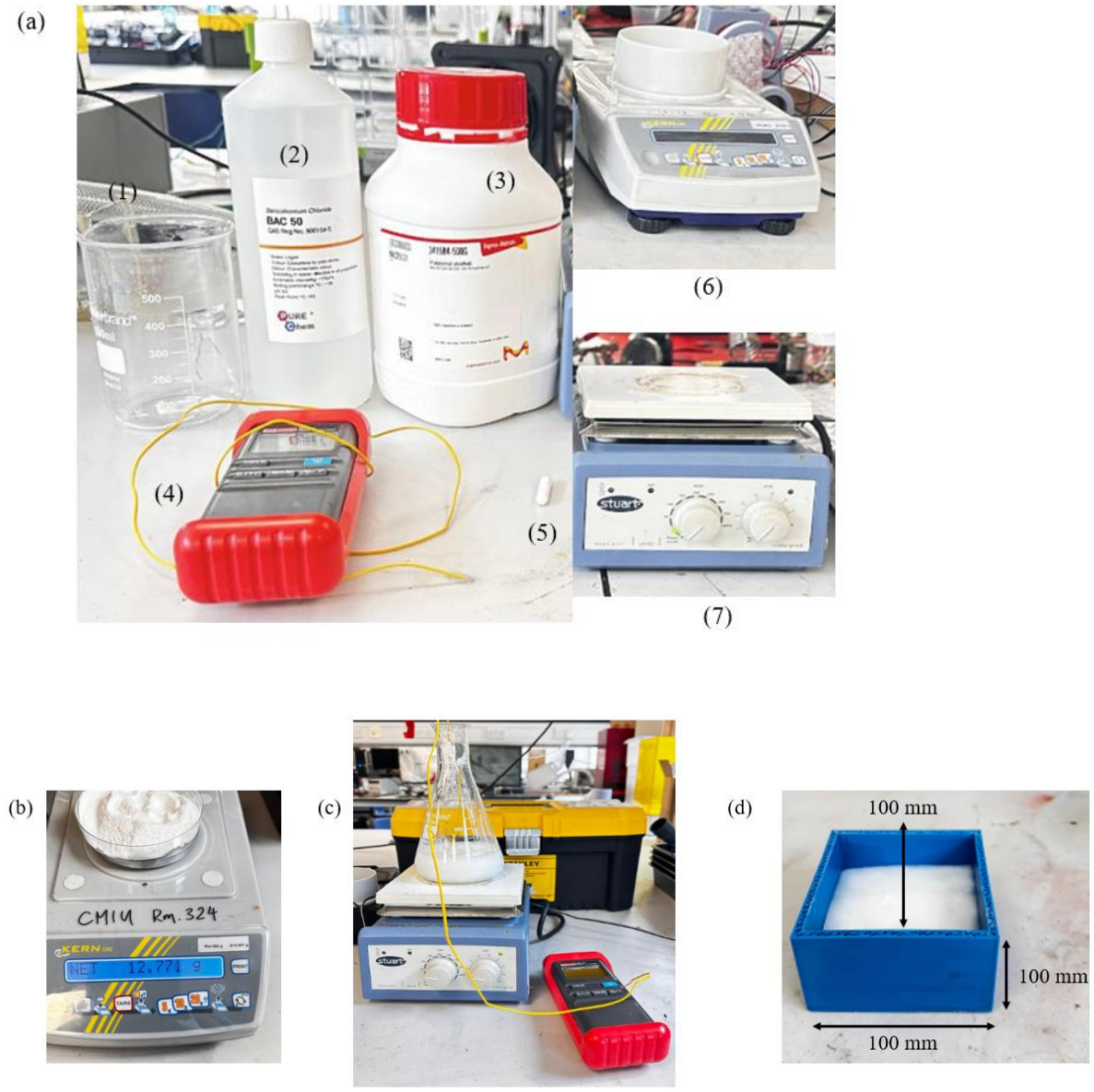

Figure 4.3: 6% PVA hydrogel preparation process. (a) ingredients and equipment comprising standard glass flask (1), benzalkonium chloride (2), 99+% hydrolysed PVA (3), temperature meter with sensor (4), magnetic mixer (5), analytical balance (6), temperature control heater (7) ; (b) mass of PVA; (c) PVA solution covered with aluminium foil to prevent evaporation; (d) PVA hydrogel in mould after freeze-thaw cycle.

$$Concentration_{PVA} = \frac{M_{PVA}}{M_{PVA}+M_{water}} * 100\%, \qquad M_{PVA} = \frac{M_{water}}{\frac{1}{PVA_{concentration}}*(100-1)} \tag{4.1}$$

The density of the PVA hydrogel used in this thesis was determined to be 1.02 g/ml using Equation 4.2.

$$\rho = \frac{M}{V} \tag{4.2}$$

where M = mass of PVA hydrogel in g and V the volume of water in ml.

4.3.1.2 Large Pickled Capers

Large pickled capers, Figure 4.4(a), are fruits of Capparis spinosa [150]. They were purchased from a local store and stored in brine at a 10% salt concentration. Each caper measures approximately 20 mm in diameter, defined as the width measured perpendicular to the caper's longitudinal axis. Large pickled capers exhibit features that resemble the internal structures and shapes of lymph nodes, thereby enabling their use in this thesis, which is based on a geometric representation of lymph nodes. Samples used for mechanical testing were obtained using a 10 mm biopsy punch, Figure 4.4(c) perpendicular to the surface of the caper. Each caper produced 4 disk-shaped samples, Figure 4.4(d). Using the volume displacement method, the density of the capers was found to be 1.2 ± 0.2 g/cm^3.

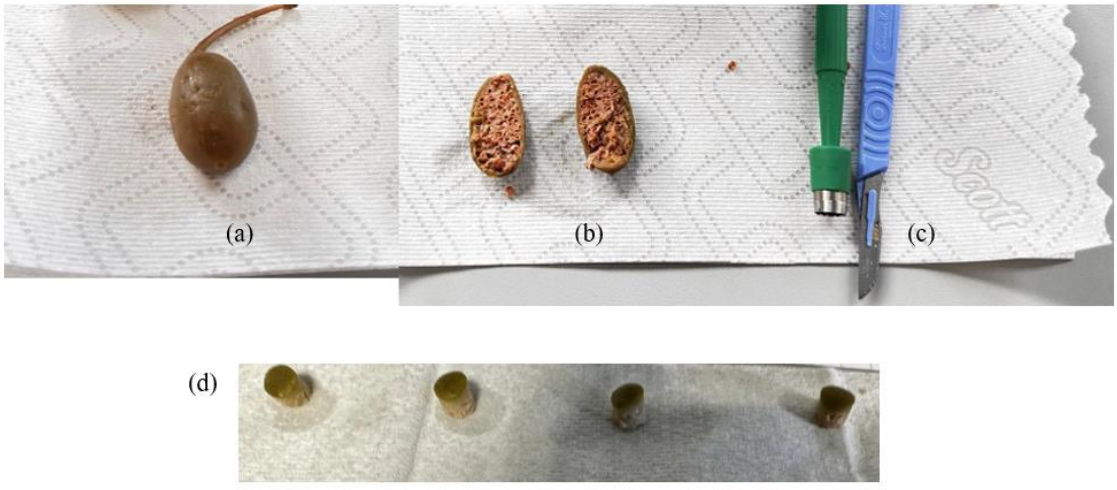

Figure 4.4: Large pickled capers sample preparation (a) whole caper; (b) cross-sectional view of the caper; (c) 10 mm biopsy punch and blades, (d) samples

4.3.1.3 Chicken Breast

Before conducting experiments on fresh lymph node tissues, it was essential to understand the testing equipment and the overall behaviour of soft tissue. This involved analysing a different

type of soft tissue to validate other measurements, thereby preventing the waste of fresh lymph node tissue samples. Additionally, it enabled verification of the effectiveness of the entire test procedure, including the test setup, safety measures, sequence of events, and the adequacy of the testing equipment. The experiments therefore began with chicken breast purchased from a local store, as it was readily available and inexpensive. Although the properties of chicken breast differ from those of lymph nodes in structure and appearance, it serves as a soft-tissue analogue that can simulate soft-tissue response.

Before testing, the chicken breast was cut into rectangular samples of uniform shape by slicing it longitudinally. Several measurements were taken with a digital calliper to ensure accuracy, and each sample was weighed on an analytical balance. Density was determined using the volume-displacement method, Figure 4.5. The density of the chicken breast was 1.1 ± 0.1 g/cm³. A summary of the measurements is provided in Table 4.1.

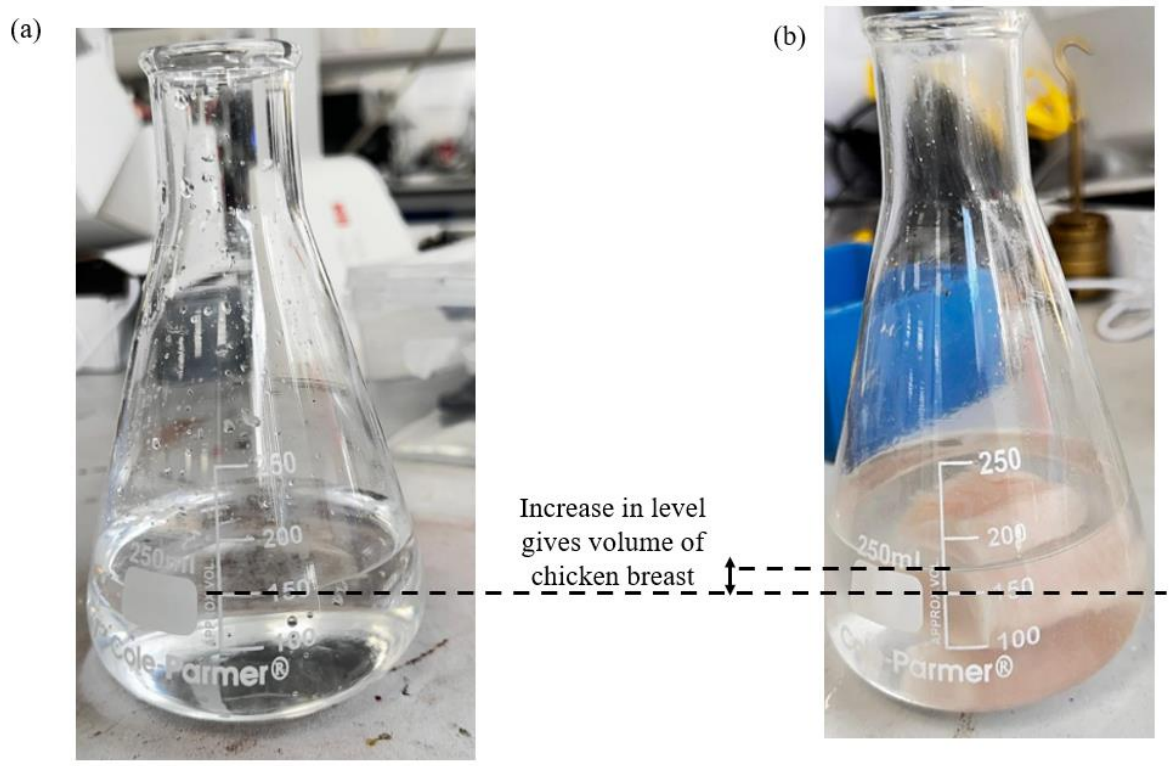

Figure 4.5: Chicken breast density calculation: (a) initial volume set to 150 ml/cm^3; (b) final volume with chicken breast. The increase in volume gives the volume of the chicken; hence, the density is obtained by dividing the mass of the chicken by its volume.

Table 4.1: Chicken breast measurements. The table shows the mean ± and standard deviation for length (L), width (W) and thickness (T).

Strain level	**20%**	**15%**	**10%**	**5%**
Mean Length (mm)	22.0 ± 0.29	22.5 ± 0.74	20.2 ± 1.26	20.4 ± 1.02
Mean Width (mm)	24.1 ± 0.82	19.6 ± 2.07	19.2 ± 2.50	18.6 ± 1.19
Mean Thickness (mm)	13.5 ± 0.83	12.0 ± 0.35	10.6 ± 0.15	8.45 ± 0.03

4.3.1.4 Porcine Lung Lymph Node

Domesticated pigs have played a vital role in improving human health over the years. They are regarded as a valuable source of therapeutic and experimental materials and serve as an ideal model for biomedical studies [157]. Pigs are similar to humans in their genetics, physiology (including the lymphatic system), and anatomy [158]. The field of respiratory medicine increasingly relies on the porcine model, which bridges the gap between human medicine and small- animal models [159]. In humans, respiratory bronchioles are usually connected to at least two or three alveolar ducts at birth, whereas in neonatal pigs, they are typically connected to paired alveolar ducts [160]. Although the morphology and distribution of porcine airways vary by breed and age, they are generally similar to those in the human lung. However, the porcine trachea is longer and more cartilaginous than the human trachea Figure 4.6(a). Both humans and pigs have highly lobulated lungs, with pulmonary lobules having well-defined interlobular septa. Additionally, the structural and anatomical features of the bronchial and lobular systems of pigs are comparable to those in humans. The pig's left lung, as shown in Figure 4.6(b), resembles the human left lung in having cranial and caudal lobes. In contrast to the human right lung, which has three lobes, the pig's right lung has four lobes Figure 4.6(d), consisting of the accessory, middle, caudal, and cranial regions. The right cranial lobe contains the cranial (tracheal) bronchus (Figure 4.6(e), which arises from the tracheal wall near the

tracheal bifurcation (Figure 4.6) [161]. The lymphatic and immune systems of pigs are well characterised and closely resemble those of humans [162], although some differences exist. The anatomy of lymph nodes differs between humans and pigs; in pigs, lymph nodes have an inverted structure, which may affect lymphocyte migration through them. Conversely, in humans, lymph nodes exhibit centripetal lymph flow [163]. Unlike humans, lymph nodes in pigs are lobulated, resulting from the fusion of three or more nodular units, each forming a functional lymph node with a specific shape and structure [164].

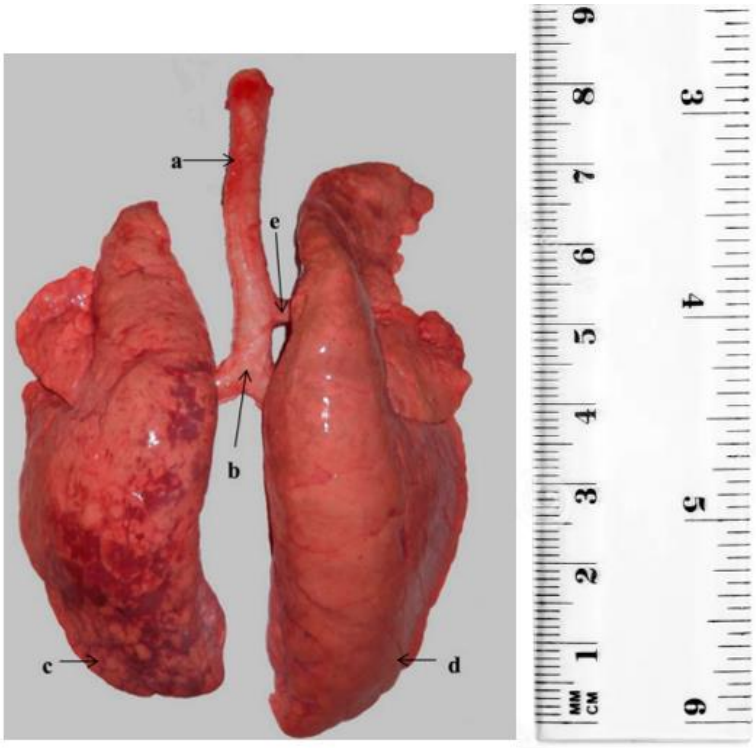

Figure 4.6: Anatomy of the porcine lung with a scale bar; (a) trachea; (b) carina; (c) left lung; (d) right lung; (e) cranial lobe bronchus [151].

Approximately 20 sets of porcine lungs used in the experiments described in this thesis were supplied by MedMeat Ltd (Rochdale, United Kingdom). They were shipped at low temperature on the same day the animals were slaughtered and received the following morning. A blunt dissection was performed with tweezers and straight forceps to harvest the highest mediastinal and lower paratracheal lymph nodes (Figure 4.7). Following the dissection, any residual fat pad tissue was gently removed from the lymph nodes, taking care not to squeeze or pierce the lymph nodes. The detachment of the fat pad around the lymph nodes was confirmed by visual inspection, and no gross disruption of lymph node structure, such as holes or incisions, was

identified after harvesting. Lymph nodes were placed in D-PBS on ice until use and between all handling steps. After harvesting, each lymph node was placed in a pre-weighed tube and weighed on an analytical balance to determine its total weight. The harvested lymph nodes varied in size, with masses ranging from 0.1 g to 3.7 g. Their mean mass was calculated to be 1.37 g ± 0.12 g and using the volume-displacement method shown in Figure 4.5, the mean density was 1.04 g/cm3 ± 0.13 g/cm3.

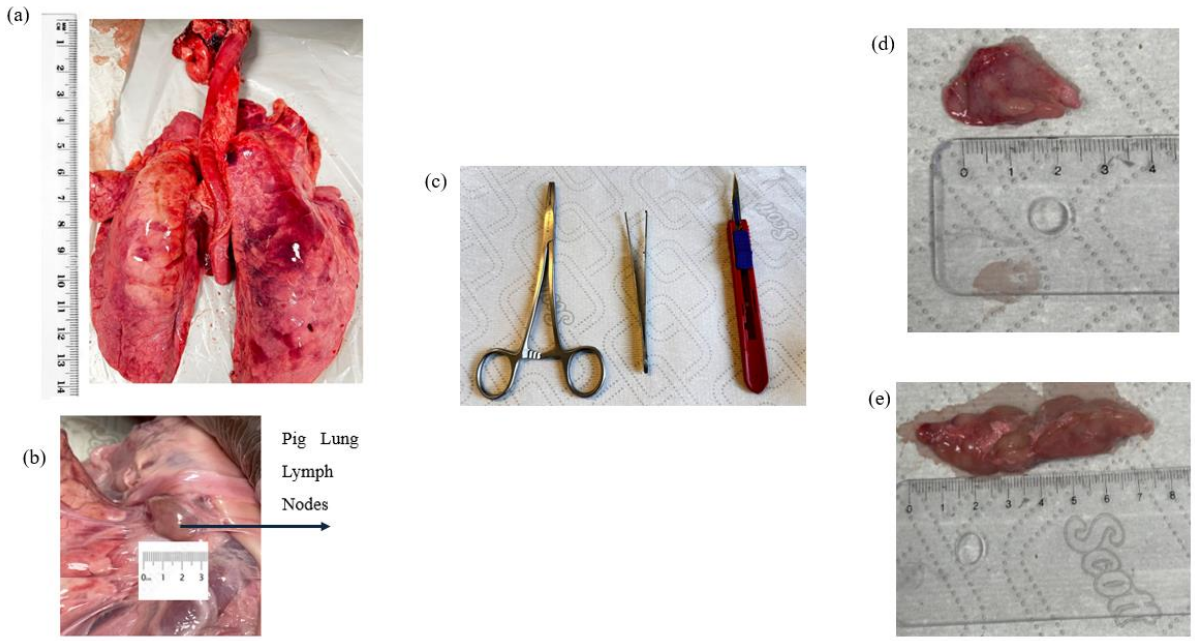

Figure 4.7: Porcine lung dissection process: (a) Fresh porcine lung; (b) mediastinal and paratracheal lymph nodes; (c) blunt dissection equipment, consisting of tweezers, blunt forceps, and a cutting blade; (d) and (e) harvested lymph nodes showing variation in shape and size.

Soft tissues, such as lymph nodes, are characterised by irregular shapes and a lack of uniform size and orientation. In this thesis, the lymph node area was determined by decomposing the organs into familiar shapes using centimetre-ruled graph paper with 2 mm x 2 mm sub-units. This method provides a practical, reproducible approach for estimating the cross-sectional area of irregular soft tissues. The areas of the shapes were then summed to determine the total area. The process for calculating the area of irregular shapes is as follows:

- Place the lymph nodes on centimetre graph paper, Figure 4.8.
- Outline the lymph nodes with a pencil, then remove them from the paper.
- Count the number of complete squares within the outline, Figure 4.9.

- Count the number of squares in the outline that are at least half within the outline.
- The total area of the lymph nodes can be calculated using equation (4.3).

$$\text{Total area of lymph node} = (\text{Number of complete squares}) + \tfrac{1}{2}(\text{Number of half / more than half squares}) \quad (4.3)$$

The numerical data extracted from the traced images are summarised in Table 4.2. The total equivalent number of rigid squares was calculated using equation 4.3

Figure 4.8: Demarcation area of porcine lung lymph nodes.

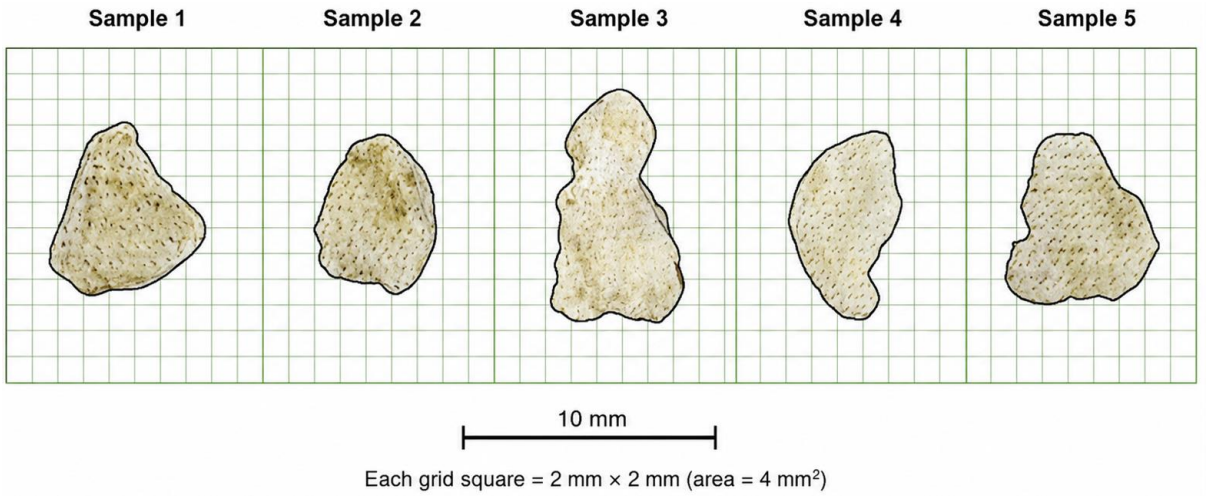

Figure 4.9: Traced cross-sectional outlines of five porcine lung lymph node samples used for image-based estimation of cross-sectional area. The outlines were superimposed on 2 mm × 2 mm graph paper, with each grid square representing an area of 4 mm².

The calculated cross-sectional areas are presented in Table 4.2.

Table 4.2: Image-based cross-sectional area estimation of porcine lung lymph node samples at 20% strain

Sample	Full squares (n)	Partial squares (n)	Area per square (mm^2)	Cross-sectional area (mm^2)
Sample 1	110	20	4	480
Sample 2	80	25	4	370
Sample 3	180	34	4	788
Sample 4	30	35	4	190
Sample 5	140	50	4	660

The densities of the materials used in this study are listed in Figure 4.3. PVA hydrogel and porcine lymph nodes have similar densities of 1.02 ± 0.1 and 1.04 ± 0.13 g/cm³, respectively, supporting the use of PVA as a tissue phantom for lymph node mechanical testing. Chicken breast is slightly denser at 1.01 ± 0.2 g/cm³, providing a general soft-tissue reference for comparison. Large pickled capers, with the highest density (1.20 ± 0.1 g/cm³), primarily serve as a geometric analogue for lymph nodes, where density matching is less critical. Overall, these density measurements confirm that the selected materials span a physiologically relevant range and are suitable for systematic mechanical characterisation and subsequent FEA.

Table 4.3: Soft materials densities

Materials	**Density (g/cm^3) ± SD**
PVA hydrogel	1.02 ± 0.1
Large pickled capers	1.2 ± 0.2
Chicken breast	1.1 ± 0.1
Lymph nodes	1.04 ± 0.13

4.3.2 Mechanical Testing Protocol

4.3.2.1 Mechanical Tester Model MACH-1 V500$_C$

Biomomentum is a medical device company that designs instruments for testing the mechanical properties of cartilage and other biological materials. The Mach-1TM (Biomomentum, Laval, Canada) is a comprehensive mechanical tester capable of performing tests such as tension, compression, friction, torsion, indentation, and indentation mapping. The micromechanical system comprises the tester frame, a motion controller, up to three motorised stages, one or more load cells, a load-cell amplifier, and a computer. It may also include accessories such as testing chambers, grips, and fixtures. The stages are used to bend, compress, or stretch the test specimen to assess its deformation, while the load cell measures the force the specimen exerts. The load-cell amplifier powers the load cell and converts the force into a digital signal, which is then sent to the computer. The stages are operated by a motion controller managed by the software. Common routines include sinusoidal, stress-relaxation, and ramp-release protocols.

Stress relaxation, the chosen mechanical testing function for this thesis, is a procedure performed by the Mach-1 V500C system (Figure 4.10) that involves applying strain or deformation to a sample to monitor the effects of stress on the sample. A test within the Mach-1 V500C motion environment consists of many repetitive actions performed in response to a given number of sequences. In turn, a sequence may consist of one or more functions, each defined by its parameter values. Before a test can be executed, all parameters of the sequence

functions should be defined. Among the many mechanical test configurations available, the one used for the compression and indentation testing of soft materials in this thesis was selected.

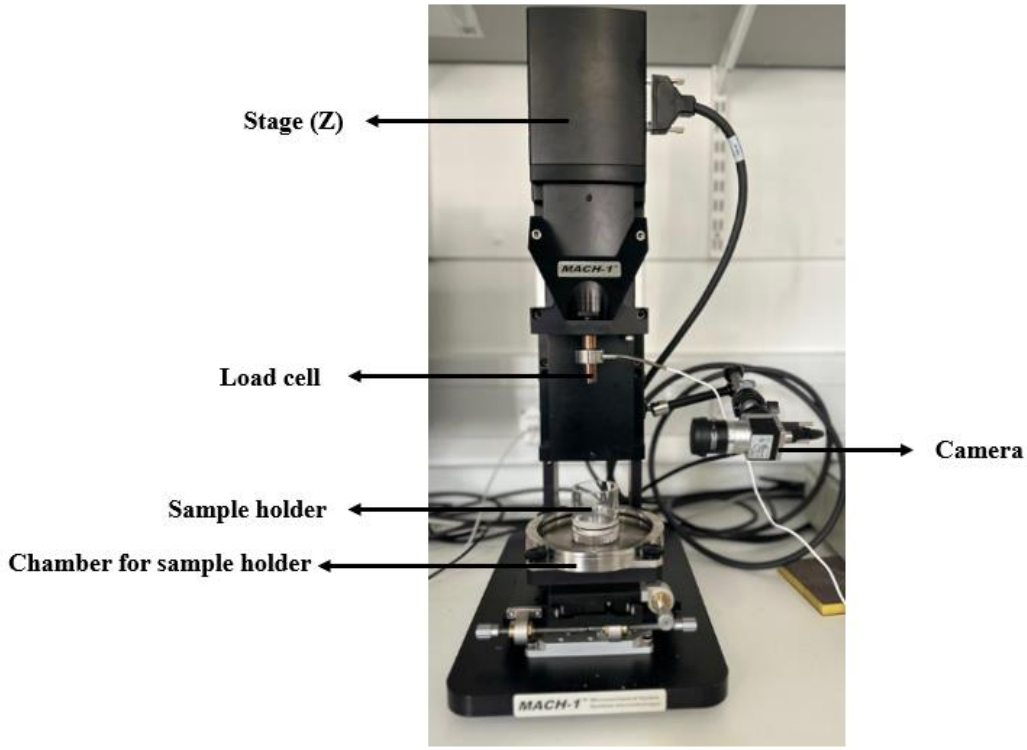

Figure 4.10: Mechanical tester model Mach-1 V500$_C$ (Laval, Canada)

4.3.2.2 Probe Selection and Usage

The V500$_C$ mechanical tester has two single-axis load cells. The high-capacity model, MA297, can output up to 250 N, while the low-capacity model, MA999, can measure force only up to 1.5 N, Figure 4.11(a) The load cells have nominal calibration weights of 500 g (MA337) and 100 g (MA336), respectively. When selecting a load cell, factors such as the material's structure, expected stiffness, and sample size should be considered. Chicken breast and PVA hydrogel were tested using a 250 N load cell, and large pickled capers were tested using a 1.5 N load cell. Depending on the size of the porcine lung lymph nodes, low- or high-capacity load cells were used.

For compression testing, the Mach-1 V500$_C$ provides two flat indenters: the 31.75 mm-diameter MA263 and the 12.5 mm-diameter MA262, Figure 4.11(b). For indentation testing, it provides a spherical indenter with tip diameters ranging from 0.3 to 5 mm, Figure 4.11(c). Two factors must be considered when selecting the appropriate indenter tip size: the tip diameter should be ≤5× the sample thickness and ≤ 1/5 of the sample width to avoid edge effects.

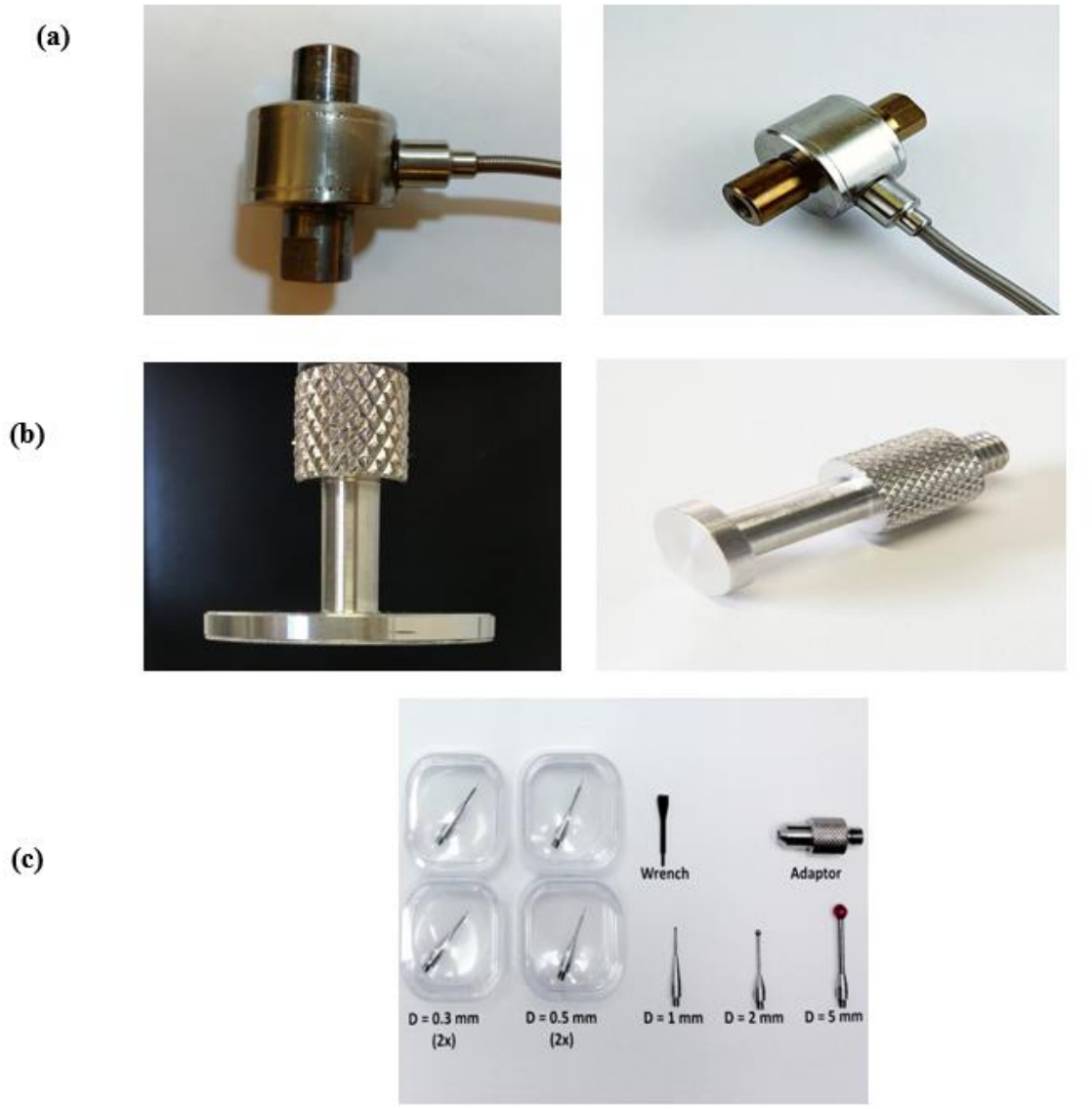

Figure 4.11: Biomomentum mechanical tester components: (a) single-axis load cell comprising a high-capacity load cell for measuring forces up to 250 N (left) and a low-capacity load cell for measuring forces up to 1.5 N (right); (b) flat compression indenters with diameters of 31.75 mm (left) and 12.5 mm (right); (c) spherical indenters for indentation tests with diameters ranging from 0.3 to 5 mm. Biomomentum (Laval, Canada).

4.3.2.3 Choice of Test Tip and Calibration

A spherical indenter tip was used for all indentation tests in this study. As discussed in Chapter 3, a spherical indenter provides a controlled, gradually increasing contact area under the applied load. Compared with sharp or flat-ended tips, spherical indentation reduces sensitivity to surface roughness and alignment errors, yields a more accurate stress distribution for soft, heterogeneous materials, and minimises surface damage during testing. This makes it particularly suitable for biological tissue and hydrogel phantoms, which exhibit non-linear behaviour and are sensitive to localised deformation.

Before mechanical testing, the load cell's integrity was verified using the instrument's calibration function. This was initiated by selecting the Load cell control label. This interface also allows a low-pass filter to be applied to reduce high-frequency noise in the measured load signal. During calibration, the system checks the load cell response by measuring its weight, displaying the corresponding mass, and calculating a calibration factor. The calibration factor indicates load cell performance and accuracy and is expected to lie within the range 0.95–1.00. Deviations exceeding ±5% from this range may indicate damage or malfunction of the load cell, in which case testing should not proceed.

4.3.2.4 Measurements

The various soft materials in this study were subjected to displacement-controlled relaxation tests, each consisting of a single indentation/compression to 10% strain, followed by a series of indentation/compression cycles at increasing strain levels of 5, 10, 15, and 20%, with intermediate unloaded dwell times of 30 s to allow baseline recovery after each indentation/compression, Figure 4.12. An indentation/compression rate of 0.1 mm/s was used in all experiments. For each strain level, 5 samples were tested, yielding 40 samples per material.

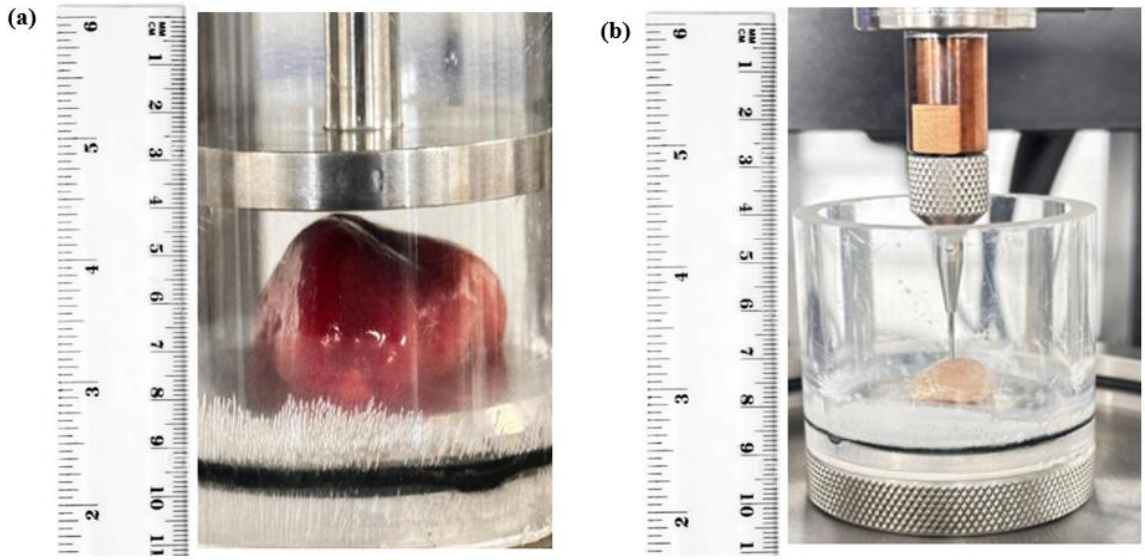

Figure 4.12: Mechanical testing of lymph nodes. (a) compression tests with a flat indenter; (b) nanoindentation test with a spherical indenter.

Before the stress relaxation test, it is essential to establish contact with the sample's surface using the "Find Contact" procedure. This allows the stage to move slowly while the probe stops, determining its exact location until the predefined load or contact criteria are met.

The stress relaxation test is performed by applying a sequence of ramps at amplitude (displacement) A and velocity V, followed by a plateau during which the position is held constant for a specified time. The ramp displacement amplitude, A, is the stage's maximum displacement at the specified strain level, and V denotes the stage's ramp execution speed.

Before stress-relaxation tests, the mean displacement amplitude of PVA hydrogel, pickled capers, chicken breast, and lymph nodes was measured under an applied strain of 5-20%. Values are presented as mean ± standard deviation to demonstrate measurement repeatability (Table 4.4, Figure 4.13). A consistent increase in displacement with strain is observed across all materials. At each strain level, PVA hydrogel and chicken breast exhibit the largest amplitudes, indicating greater deformability, whereas large pickled capers consistently show the lowest amplitudes. Lymph nodes display intermediate displacements, particularly at moderate strain levels. These initial measurements contextualise subsequent stress-relaxation experiments, ensuring that differences in hyperelastic response can be interpreted relative to each material's inherent mechanical compliance.

The complete compression and indentation test plan is set out in Appendix 5.

Table 4.4: Mean displacement amplitude measured for PVA hydrogel, capers, chicken breast, and lymph nodes at applied strains of 5-20% before stress-relaxation tests. Values are presented as mean ± standard deviation.

Strain %	PVA Hydrogel	Capers	Chicken Breast	Lymph Nodes
5	0.44 ± 0.03	0.28 ± 0.00001	0.44 ± 0.00065	0.27 ± 0.07
10	0.93 ± 0.0002	0.59 ± 0.0001	1.0 ± 0.01	1.09 ± 0.06
15	1.54 ± 0.001	0.94 ± 0.05	1.86 ± 0.09	1.47 ± 0.06
20	2.22 ± 0.01	1.39 ± 0.09	2.70 ± 0.26	2.26 ± 0.03

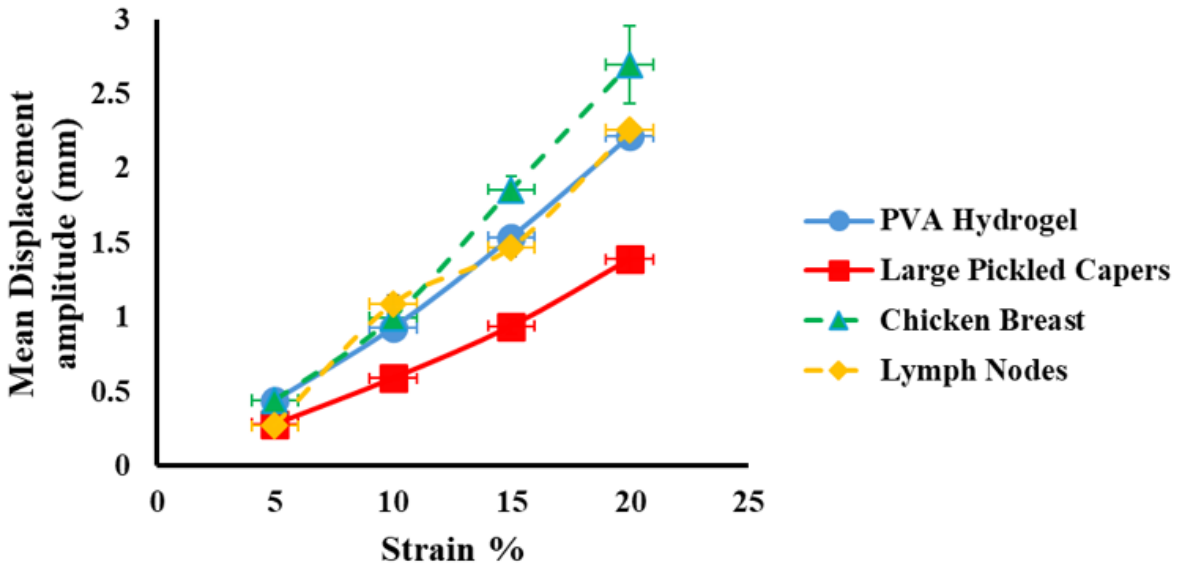

Figure 4.13: Baseline mean displacement amplitude as a function of applied strain for PVA hydrogel, capers, chicken breast, and lymph nodes, measured prior to stress-relaxation tests. Error bars indicate one standard deviation, demonstrating measurement repeatability.

4.4 Results & Discussion

4.4.1 Stress-Strain Results

To extract and compare the characteristics of the tested samples, the recorded load-displacement data from compression and nanoindentation were analysed.

The load-displacement data obtained were converted into stress-strain curves according to the principles of engineering stress, σ, which indicates the force per unit of the sample's cross-sectional area, Equation (4.4), and the engineering strain, ϵ, refers to the length change, in this case, the sample height, Equation (4.5):

$$\sigma = \frac{F}{A} \tag{4.4}$$

where σ is the engineering stress in N/mm^2 or MPa, F is the force in N, and A is the cross-sectional area of the sample in mm^2.

$$\epsilon = \frac{\Delta L}{L} \tag{4.5}$$

where ϵ is the engineering strain, ΔL is the change in length in mm, and L is the original length of the sample in mm. The calculated stress-strain curves were used for curve fitting in Section 4.4.2.

The compression and indentation stress-strain curves of various soft materials at 20% strain are shown in Figure 4.14 and the stress-strain curve data at 15%, 10%, and 5% strain can be found in Appendices 4.2 – 4.3.

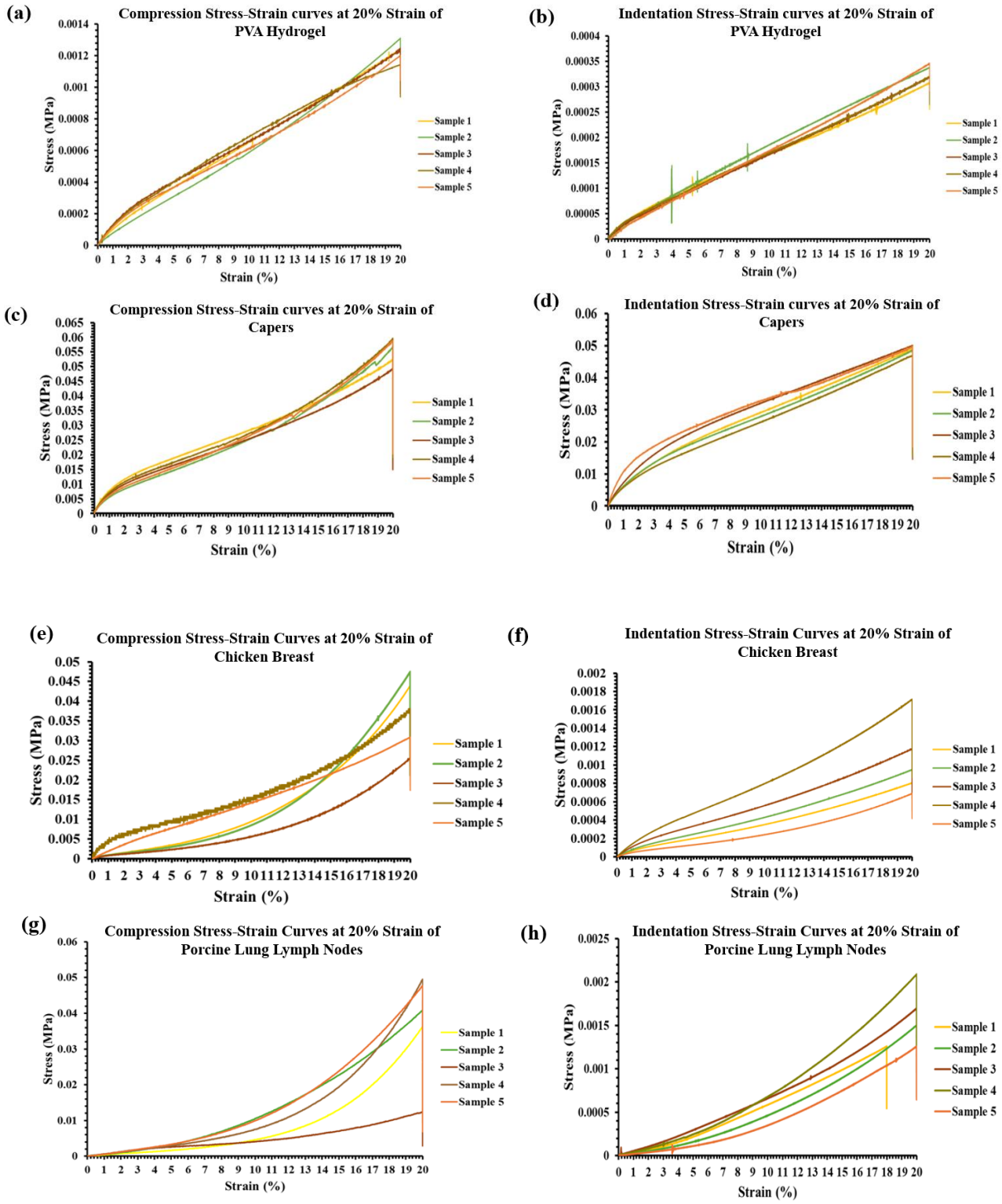

Figure 4.14: Stress-strain curves for compression and indentation at 20% strain: (a) & (b) compression and indentation stress-strain curves of PVA hydrogel; (c) & (d) compression and indentation of large pickled capers; (e) & (f) compression and indentation stress-strain curves of chicken breast; and (g) & (h) compression and indentation stress-strain curves of lymph nodes.

Table 4.5: Individual standard deviation in MPa at 20% strain for each sample during compression and indentation testing.

Materials	Tests	Sample 1	Sample 2	Sample 3	Sample 4	Sample 5
PVA Hydrogel	Compression	0.000066	0.000069	0.000064	0.000062	0.000065
	Indentation	0.000015	0.000019	0.000012	0.000102	0.000018
Large Pickled Capers	Compression	0.004846	0.004916	0.004102	0.004154	0.0041107
	Indentation	0.004252	0.004123	0.004080	0.004162	0.004053
Chicken Breast	Compression	0.009294	0.0093705	0.00993	0.00962	0.00939
	Indentation	0.000209	0.000245	0.000298	0.000188	0.000434
Porcine Lymph Nodes	Compression	0.01458	0.01584	0.01804	0.01087	0.018701
	Indentation	0.000635	0.000612	0.000641	0.000668	0.000661

Table 4.6: Summary statistics for mean stress at 20% strain during compression and indentation testing. The table also outlines the standard deviation (SD) in MPa, the coefficient of variation (CV) in %, and the confidence interval (CI) in MPa

Materials	Tests	Mean (MPa)	SD (MPa)	CV (%)	95% CI (MPa)
PVA Hydrogel	Compression	0.00123	0.0000533	4.33	± 0.00007
	Indentation	0.00033	0.000015	4.55	± 0.00002
Large Pickled Capers	Compression	0.05542	0.00443	7.98	± 0.00542
	Indentation	0.04904	0.004134	8.43	± 0.00164
Chicken Breast	Compression	0.03721	0.009521	25.59	± 0.01125
	Indentation	0.00107	0.000275	25.70	± 0.00051
Porcine Lymph Nodes	Compression	0.03944	0.015606	39.56	± 0.02009
	Indentation	0.00157	0.000643	40.95	± 0.00044

The data presented in Figure 4.14 comprise compression and indentation tests conducted on five independent specimens of each material to evaluate measurement repeatability and inter-sample variability. Individual standard deviation values at 20% strain are presented in Table 4.5, while the corresponding summary statistics are provided in Table 4.. The stress–strain curves exhibited nonlinear responses across all materials, consistent with the viscoelastic behaviour of both synthetic hydrogels and biological soft tissues. Although the overall shape of the curves was comparable among specimens, quantitative differences in stress magnitude were evident, particularly for chicken breast and porcine lymph node tissues.

The PVA hydrogel exhibited the greatest mechanical consistency across all materials tested. Under compression, the mean stress was 0.00123 ± 0.0000533 MPa (CV = 4.33%), whereas indentation yielded a mean stress of 0.00033 ± 0.000015 MPa (CV = 4.55%). The narrow

confidence intervals and low coefficients of variation indicate excellent repeatability between specimens, reflecting the uniformity of the hydrogel fabrication process. These values align with published studies on the mechanical behaviour of highly hydrated, low-crosslink-density PVA hydrogels, which typically exhibit compressive behaviour at the lower end of the reported range. For example, unconfined compression testing of PVA hydrogels has shown drained Young's modulus values of approximately 0.03–0.9 MPa, depending on water content and crosslinking density [152]. Indentation-based studies on PVA hydrogels report compressive stiffness values on the order of tens of kPa to low MPa, with a strong dependence on polymer concentration and processing method [153].

Large pickled capers also showed high repeatability, with mean compressive and indentation stresses of 0.05542 ± 0.00443 MPa (CV = 7.98%) and 0.04904 ± 0.004134 MPa (CV = 8.43%), respectively. The low variability indicates that the internal structure of the capers remained relatively homogeneous across specimens, yielding a highly reproducible mechanical response.

Chicken breast tissue exhibited substantially greater variability than either PVA hydrogel or pickled capers. The mean compressive stress was 0.03721 ± 0.00952 MPa (CV = 25.59%), whereas indentation yielded a mean stress of 0.00107 ± 0.000275 MPa (CV = 25.70%). This increased variability is consistent with the anisotropic nature of skeletal muscle, in which fibre orientation, collagen distribution, and local tissue composition influence the measured stiffness. Variations in fibre alignment relative to the loading direction are therefore expected to produce sample-to-sample differences during both compression and indentation testing [151]. This result aligns with previously reported mechanical characterisation of skeletal muscle and poultry tissue, which typically show compressive stress responses of approximately 0.01–0.1 MPa [154].

The greatest variability was observed in porcine lymph node tissue during compression, with a mean stress of 0.03944 ± 0.015606 MPa and a coefficient of variation of 39.56%. Indentation testing showed a mean stress of 0.00157 ± 0.000643 MPa with a coefficient of variation of 40.95%. This behaviour is consistent with the heterogeneous microstructure of lymphatic tissue, which comprises regions of varying cellular density, connective tissue content and capsule thickness. Consequently, local differences in tissue architecture contribute significantly to the observed mechanical dispersion.

Overall, the statistical analysis confirms that variability increases with biological complexity. The synthetic PVA hydrogel exhibited the most reproducible behaviour, followed by large pickled capers, whereas chicken breast and porcine lymph node tissues showed progressively greater variability due to their intrinsic structural heterogeneity. These findings align with previous biomechanical studies, which report greater dispersion of mechanical properties in biological tissues than in engineered hydrogel systems [155].

To facilitate constitutive model development, the stress–strain data from the five specimens of each material were averaged point-by-point to generate representative curves for hyperelastic model fitting in Abaqus. This approach preserves the characteristic nonlinear mechanical response while reducing the influence of local structural heterogeneity.

4.4.2 Curve-Fitting

Curve fitting is a process used to determine a material model's parameters by finding and fitting a best-fit curve to stress-strain measurements obtained from experimental data, with the results of the curve fitting expected to follow the test data within the range of interest. As noted in Chapter 3, there are several hyperelastic models, with the more commonly used in modelling soft materials including the Mooney-Rivlin model (N=1); reduced polynomial Neo-Hookean model (N=1); Ogden first- and third-order models (N=1 and N=3); Yeoh model (N=3); and van der Waals models. In this thesis, hyperelastic models were used to fit the stress-strain curves. Figure 4.15 compares the experimental data with the fitted responses obtained using the various hyperelastic models for each soft material. The corresponding fitted material parameters and their associated standard deviations, derived from 5 samples per material, are summarised in Table 4.5. The curve fits at 15%, 10%, and 5% strain are provided in Appendix 4.

The inter-sample variability across all materials, observed experimentally, was captured by the fitted hyperelastic model, as indicated by the standard deviation reported in Figure 4.15 and Table 4.. Such variability is expected given the heterogeneous nature of soft and biological materials. Among the models evaluated, the Ogden first-order formulation provided the most consistent and closest overall agreement with the experimental stress-strain across the full range for all four materials. While alternative formulations, particularly reduced polynomial, Neo-Hookean and Aruda-Boyce models, achieved comparable or locally improved fits for individual materials, their performance was less consistent across the dataset. The aim was not

to optimise the fit for a single case, but to adopt a constitutive model that reliably captures nonlinear strain stiffening while remaining numerically stable and comparable across materials. Therefore, the Ogden first-order model was used to characterise the mechanical properties.

Alongside fitting accuracy, the stability of each hyperelastic formulation is assessed using the Abaqus stability criterion, which evaluates the stress-strain energy function, incremental stiffness over the deformation range, and their convexity. The stability analysis showed that the Ogden first-order, Arruda-Boyce, and reduced-polynomial Neo-Hookean models remained mechanically stable within the tested strain ranges. However, some higher-order polynomial models, such as the Ogden third-order, Yeoh, and van der Waals models, exhibited instability at larger strains, consistent with the non-physical behaviour observed in the stress-strain curve. Since numerical stability is crucial for reliable finite element analysis, models exhibiting such behaviour were deemed unsuitable, despite some improvements in curve fitting.

Table 4. Provide a physically meaningful description of the material response. The shear-related parameter, μ, reflects the relative stiffness of each material, while the nonlinear exponent, C10, λM, α_0, governs the degree of strain stiffening. The variation in these parameters across materials aligns with experimentally observed differences in mechanical behaviour, and the associated standard deviation quantifies inter-sample variability.

Overall, although alternative hyperelastic models may offer marginally better fits for individual materials or strain ranges, the Ogden first-order model (N = 1) was selected to characterise the mechanical properties of all materials examined in this thesis. This decision was driven by its ability to provide a consistent, physically meaningful, and numerically stable representation of the nonlinear elastic response across a wide range of soft materials, to enable meaningful comparisons between samples, and to support reliable use in subsequent finite element analyses.

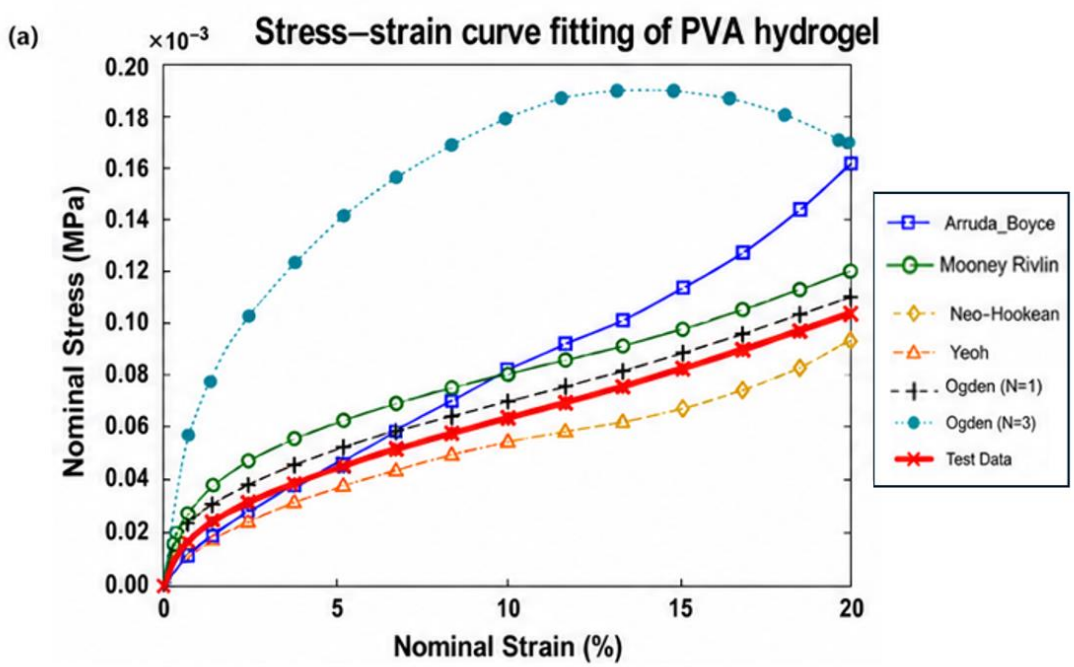
(a)
Stress–strain curve fitting of PVA hydrogel
×10⁻³
Nominal Stress (MPa)
Nominal Strain (%)
0.00
0.02
0.04
0.06
0.08
0.10
0.12
0.14
0.16
0.18
0.20
0
5
10
15
20
Arruda_Boyce
Mooney Rivlin
Neo-Hookean
Yeoh
Ogden (N=1)
Ogden (N=3)
Test Data

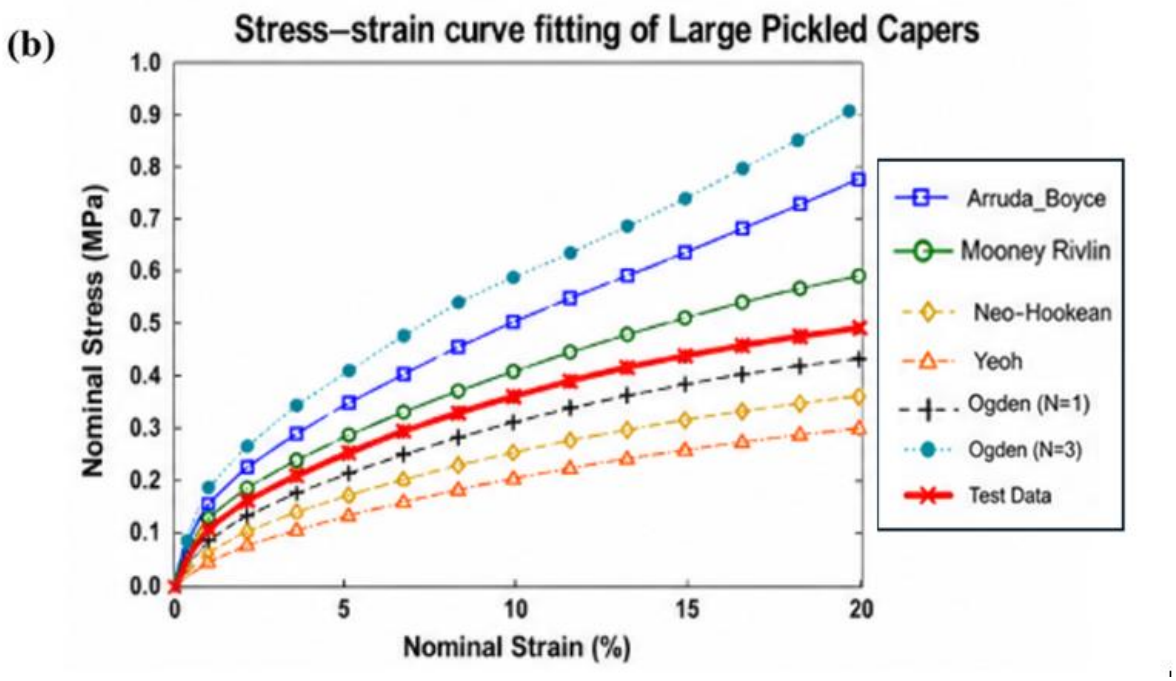
(b)
Stress–strain curve fitting of Large Pickled Capers
Nominal Stress (MPa)
Nominal Strain (%)
0.0
0.1
0.2
0.3
0.4
0.5
0.6
0.7
0.8
0.9
1.0
0
5
10
15
20
Arruda_Boyce
Mooney Rivlin
Neo-Hookean
Yeoh
Ogden (N=1)
Ogden (N=3)
Test Data

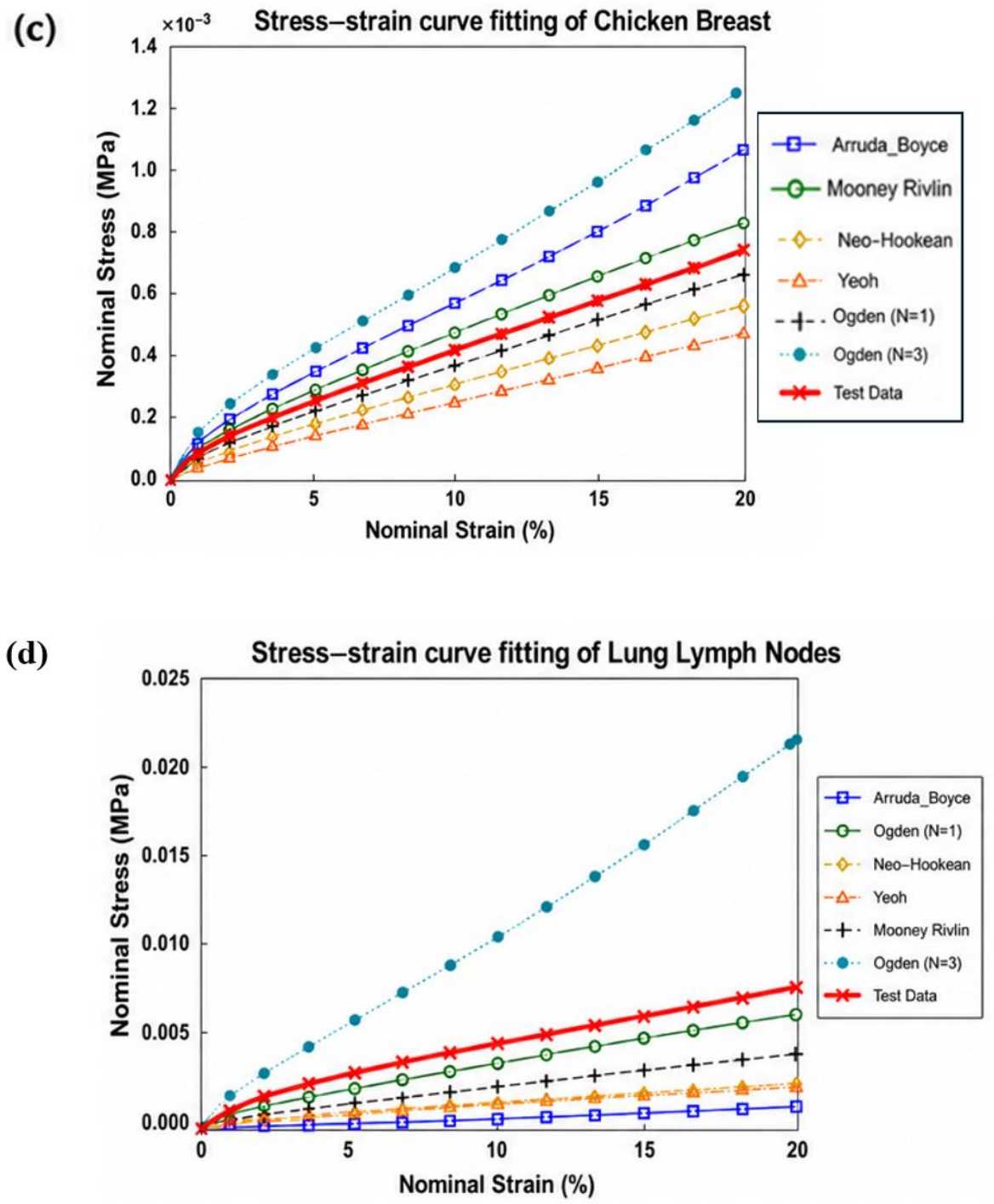

Figure 4.15: Stress-strain curve fitting for various soft materials in Abaqus (Dassault Systemès, Vélizy-Villacoublay, France). (a) PVA hydrogel, (b) large pickled capers, (c) chicken breast, and (d) pig lung lymph node.

Table 4.7: Curve fitting hyperelastic material constant of PVA hydrogel and large pickled capers.

		PVA Hydrogel		**Large Pickled Capers**		**Chicken Breast**		**Pig Lung Lymph Nodes**	
Model	**Parameters**	**Mean**	**Standard Deviation**	**Mean**	**Standard Deviation**	**Mean**	**Standard Deviation**	**Mean**	**Standard Deviation**
Neo - Hookean	C_{10} (MPa)	1.42 e-04	0.00069	2.71 e-02	0.0064	3.622 e-04	0.0002	3.74e-03	0.00383
Arruda - Boyce	μ (MPa) μ_0 (MPa) λM	2.84 e-04 2.84 e-04 456	0.00014 0.00014	5.41 e-02 5.41 e-02 725	0.0078 0.0078	3.96 e-04 3.96 e-04	0.0004 0.0004	3.136 3.1753	0.0095
Ogden_ N=1	μ_I (Mpa) α_0	2.88 e-04 11.8	0.00014	5.24 e-02 11.7	0.0039	7.74 e-04 8.50	0.00042	4.875e-03 6.03	0.0008

4.5 Summary

The primary aim of this chapter was to contribute to the first objective of this thesis: to establish a comprehensive mechanical characterisation technique for measuring the nonlinear elastic properties of lung lymph nodes and to assess their correlation with alternative soft materials, namely PVA hydrogel, large pickled capers, and chicken breast. This aim was addressed by applying unconfined compression and nanoindentation tests to both biological tissue and alternative materials.

The main findings of this chapter show that the proposed mechanical characterisation method is suitable for analysing the low-stiffness, nonlinear elastic behaviour of lymph nodes within physiologically relevant strain ranges. Displacement-controlled relaxation testing yielded consistent, repeatable load-displacement responses, and reliable surface detection was achieved across all materials. Preliminary testing of PVA hydrogel, large pickled capers, and chicken breast enabled standardisation of the experimental protocol, sample preparation, and probe selection, thereby reducing uncertainty and minimising waste of fresh porcine lung lymph node tissue.

The suitability of the experimental methodology was further validated by identifying and assessing key sources of variability in nanoindentation and unconfined-compression testing of soft materials. The results showed that variability arises from multiple factors, including acquisition methodology, the inherent heterogeneity of the materials, and probe-sample interactions. Specifically, location-dependent stress variations, assumptions of isotropic behaviour, and the use of nearly incompressible Poisson's ratio values (0.495 – 0.50) were recognised as potential sources of uncertainty. Although these assumptions have limitations, their identification offers important insights into the interpretation of the extracted material parameters and guides the design of future experimental and modelling work within this thesis.

Regarding the objective of identifying correlations between lung lymph nodes and alternative soft materials, the results were mixed. PVA hydrogel and chicken breast exhibited stress-strain responses that closely matched those of soft biological tissues and aligned with previously published data, supporting their use as reference materials for method development. In contrast, large pickled capers exhibited significantly higher compression and indentation stresses, as well as elevated Ogden hyperelastic material constants, which were attributed to their distinct internal structure and material consistency. Consequently, large pickled capers are not considered suitable mechanical or geometric mimics of lung lymph nodes. Although a clear correlation between lung lymph nodes and the remaining soft materials was not established, the results do not exclude such correlations, indicating that further refinement and investigation are required.

Hyperelastic modelling of the nonlinear stress-strain behaviour of the tested materials yielded the best overall fit. Among the models considered, the Ogden first-order (N=1) hyperelastic formulation provided the closest match to the experimental stress-strain data, capturing the

non-linear response of the soft materials across the applied strain range. This outcome supports the use of Ogden-based material formulations to represent lung lymph node mechanics in computational models, thereby enabling subsequent objectives of the thesis related to needle-tissue interaction, deformation, and needle deflection. While the modelling approach was effective, its reliance on simplifying assumptions is a limitation that should be addressed in future work.

Overall, this chapter successfully achieved the first aim of the thesis by establishing a reproducible method for the mechanical characterisation of lung lymph nodes and by critically evaluating the suitability of alternative soft materials. Key achievements include standardising protocols, identifying unsuitable surrogate materials, and extracting validated hyperelastic parameters. Limitations remain due to material heterogeneity, modelling assumptions, and the exclusive use of healthy porcine lung lymph nodes, which may not fully represent pathological tissues. Nevertheless, the findings of this chapter provide a solid mechanical foundation for developing theoretical and finite-element models of needle insertion, which are further explored in subsequent chapters to address the remaining aims of this thesis.

Chapter 5: Analytical Methodology

5.1 Introduction

Building on the continuum mechanics framework introduced in Chapter 3, Section 3.5, this chapter focuses on the numerical modelling of needle-tissue interaction. Because the governing equations for soft-tissue deformation and needle insertion involve complex material behaviour, geometries, and boundary conditions, as well as large deformations and evolving damage, analytical solutions are generally not feasible. Therefore, numerical techniques are necessary to obtain physically meaningful solutions under realistic conditions.

Finite element analysis (FEA) provides a practical means of discretising continuum formulations and solving the resulting systems of equations. This chapter first reviews numerical techniques well suited to modelling needle-tissue interaction, with particular attention to the choice of element formulations and solution schemes for large-deformation and contact problems. A comparison of implicit and explicit finite element solvers is then presented to highlight their respective advantages and limitations for highly nonlinear interaction problems. Existing finite element models reported in the literature are subsequently reviewed, covering both invasive and non-invasive needle-tissue interactions. Finally, the fundamental principles of the Coupled Eulerian-Lagrangian (CEL) techniques are introduced, along with their application to modelling tissue damage.

5.2 Finite Element Analysis Software Packages

FEA is a numerical method used to analyse physical and engineering problems. It can be used to analyse material properties and building structures, as well as to apply loads and constraints in situations where actual outcomes would not be possible [156]. FEA is commonly used in engineering fields, such as aerospace, civil, and mechanical engineering, and can perform static, dynamic, and nonlinear analyses.

A finite element is an element that forms part of a whole structure. For instance, a 3D object can be divided into smaller elements, each with a number of nodal points (nodes), depending on its complexity [158]. In FEA, the general procedure is typically divided into three main sections: preprocessing, solution, and postprocessing. The preprocessing section encompasses tasks such as geometry creation, material selection, boundary condition definition, and mesh generation and modification. It also involves applying additional parameters such as frequency,

surface roughness, and interaction. The solution section presents an algorithm for solving for an unknown number of variables in the primary field. Finally, the postprocessing section includes routines for plotting graphs and presenting results. Various software packages are used for FEA, and the most widely used for simulating mechanical needle-tissue interaction models is from Dassault Systèmes (Vélizy-Villacoublay, France).

5.2.1 Finite Element Analysis Using Abaqus

Abaqus Computer-Aided Engineering (CAE), developed by Dassault Systèmes, is a powerful finite element software package widely used for engineering simulations, including stress analysis, structural behaviour under various loading conditions, design optimisation, and static and dynamic analyses. It uses the finite element method (FEM) to address both simple linear and complex nonlinear problems.

Abaqus is particularly known for its reliable nonlinear solver, which can handle large deformations, material nonlinearity, and complex contact interactions. It also supports studies of needle-tissue interaction, dynamics, heat transfer, structural damage, fracture, and failure. The software supports both structured and unstructured meshing, including tetrahedral, hexahedral, and shell elements, and offers advanced meshing techniques such as partitioning and swept meshing to produce high-quality meshes for complex geometries. Moreover, Abaqus provides greater control over meshing parameters, enabling more precise, customised mesh options to meet specific analysis requirements.

Abaqus offers both implicit (standard) and explicit solvers. The standard implicit solver is suitable for static analyses and low-speed dynamic events, where precise stress results are critical. The explicit solver is optimised for non-linear systems with complex transient load interactions [157]. Overall, Abaqus is particularly well-suited for non-linear analysis, fracture mechanics, and simulations involving time-dependent phenomena, element failure, wave impacts, or soft tissue modelling [158].

5.3 Numerical and Mathematical Finite Element Methods

FEM is an example of an approximate procedure that involves discretising a structure or system to determine its overall response to loading. It accounts for the behaviour of the nodes within

the structure during assembly [161]. Several such methods of analysis have been developed over time and have expanded and diversified for use in various engineering and scientific studies [162]. The evolution of cheaper, faster computers has led to an increased emphasis on programming methods. Discrete element methods now provide a viable alternative to analytical methods, which can be expensive and time-consuming. The most commonly used discrete element methods are the mass-spring-damper (MSD) system, the finite element method (FEM), and the boundary element method (BEM). Among these methods, SMD and FEM are frequently used in soft tissue analysis [163].

5.3.1 Mass-Spring-Damping System

A mass-spring-damper system (MSD) is a simplified discrete mechanical model used to approximate the dynamic behaviour of deformable bodies. It combines fundamental principles from continuum mechanics and classical dynamics. The system consists of a collection of point masses connected by springs and dampers, as illustrated in Figure 5.1 [159]. This modelling approach decomposes complex geometries into interacting particles linked by elastic and dissipative elements. The system's internal energy is stored in the springs, while energy dissipation is introduced through damping terms. The MSD framework was first introduced by Miller in 1988 [160] and has since been widely applied in areas such as surgical simulation and needle–tissue interaction modelling.

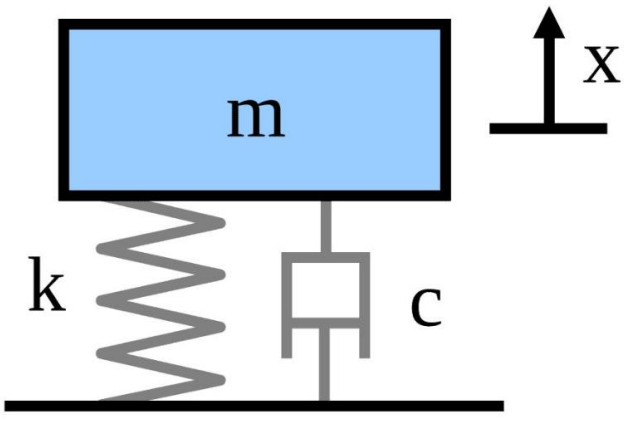

Figure 5.1: A portion of an MSD showing the forces exerted by a spring with stiffness, k, between masses, m, and damping effects, c, opposing relative motion [159].

A classical MSD model can be used to simulate the elastic behaviour of soft materials. The first step is to discretise the material into a set of particles, p_i, each with mass, m_i, connected by springs characterised by stiffness, k, and rest length, l_0. Deformation of the structure is then governed by the elongation of these springs.

The current spring length is expressed as:

$$l = l_0 + \delta \tag{5.1}$$

where δ is the spring extension. The strain energy stored in a single spring is given by:

$$W_{spring}(\delta) = \frac{1}{2}k(l - l_0)^2 \tag{5.2}$$

The corresponding restoring force is obtained by differentiating the energy with respect to the deformation:

$$F_{spring}(\delta) = -\frac{\partial W_{spring}(\delta)}{\partial \delta} = -k(l - l_0) = -k\delta \tag{5.3}$$

To incorporate energy dissipation, a damping term d is introduced between connected particles p_i and p_j. The total force acting on particle, i, due to its connection with particle, j, becomes [161]:

$$F_{ij}(\delta) = -k_{ij}\delta - d(v_j - v_i) \tag{5.4}$$

where v_i and v_j are the velocities of particles p_i and p_j, respectively.

The MSD model offers high computational efficiency and ease of implementation, making it suitable for real-time simulation. However, its accuracy and stability are strongly dependent on the spatial discretisation and the numerical integration scheme used to solve the governing equations. In particular, the choice of damping coefficient and time step size significantly influences system stability; inappropriate parameter selection may lead to numerical instability or non-physical oscillations [162].

5.3.2 Finite Element Method

A mathematical model can be constructed by making assumptions about specific physical phenomena and the laws of physics that govern their behaviour. It can be characterised by complex integral or differential equations. However, due to the complexity of the boundary conditions and the geometries of real-life problems, it is not possible to solve these equations analytically [167]. Before the advent of numerical methods, the only practical approach to solving these problems was to simplify them. However, this did not always produce an accurate solution. Nowadays, problems are solved with numerical methods. With the help of suitable mathematical and numerical models, computers can now solve many practical engineering problems. A numerical method is usually used to transform the differential equations of a continuum into a set of algebraic equations. The FEM is a widely used numerical method for solving many differential equations, including those arising in continuum mechanics [168].

The FEM is commonly used to solve problems with complex geometries, boundary conditions, and material types. It can also be used to demonstrate a more accurate method for solving continuum mechanics problems [163]. One significant difference between the MSS and FEM methods is that the MSS method accounts for energy function minimisation at the mesh nodes and the resulting equilibrium, whereas the FEM method divides the object into multiple elements. The concept of FEM involves dividing a structure into small elements. The set of these elements then produces a mesh that approximates the problem geometry. The complexity of a given engineering problem can be partly attributed to the complexity of its geometry, which makes it hard to produce an acceptable global solution. However, by subdividing the problem's domain into small elements, it becomes easier to come up with a solution [164]. The unknown variables of each finite element are approximated using known functions. These functions can be linear or higher-order polynomial expressions that depend on the geometrical nodes used to define the shape of each finite element. The integration of the governing equations of each finite element into a single solution is performed using linear algebra techniques. The resulting solution is then obtained by summing the solutions of the various elements.

5.3.3 Boundary Element Method

The boundary element method (BEM), also known as the boundary integral equation method (BIEM), is widely used in engineering to solve problems involving differential equations. The

BEM is a suitable alternative to other numerical methods for solving complex physical problems and integral boundary-value problems. In addition to actuators and electrical equipment, the BEM can be applied to other electromagnetic problems, such as antennas, waveguides, and wires. The BEM process involves discretisation only on the body surface, thereby simplifying the computational process and problem-solving. The BEM is a versatile numerical method for generating a surface mesh using discontinuous elements. It can also provide accurate solutions for structures using boundary elements [165].

An advantage of the BEM is its relative ease and flexibility in handling singularities and infinite boundaries. Secondly, data preparation is relatively simple. Thirdly, the BEM simplifies mesh generation for 3D problems and can be combined with analytical and numerical methods, such as FEM. Moreover, the BEM is regarded as an efficient technique for solving various homogeneous, linear-elastic problems. However, it is not suitable for solving complex elastoplastic problems due to the difficulty of finding appropriate governing equations [166].

To clearly differentiate between the numerical methods reviewed in the literature and the modelling approach adopted in this thesis. Table 5.1 summarises the numerical models considered, highlighting the configuration of the finite element model used for needle-insertion simulations, as described in detail in Chapter 7.

While mass-spring systems and boundary element methods have been widely applied to soft tissue, their use is generally limited to simplified geometries, linear material behaviour, or boundary-only formulations. FEM was selected over MSS and BEM for modelling the behaviour of soft materials. Finite element modelling of needle insertion into soft tissue has been widely reported in the literature, with many studies focusing on simplified material behaviour and boundary conditions. In contrast, the FEM framework developed in this thesis introduces a detailed three-dimensional model of needle-tissue interaction implemented in Abaqus, explicitly accounting for nonlinear soft-tissue behaviour, realistic contact and friction, and progressive tissue-penetration mechanisms.

The novelty of this work lies not in the use of FEM but in the model's specific configuration and parametrisation, which are designed to match experimental conditions, replicate clinical insertion mechanics, and capture the force-displacement behaviour.

Table 5.1: Comparison of numerical models

Aspect	**MSS Method**	**BEM Method**	**FEM Method**
Model purpose	Soft tissue deformation (simplified)	Boundary-value problems	Soft tissue mechanical response
Governing equations	Lumped mass-spring equations	Boundary integral equations	Continuum mechanics PDEs
Material behaviour	Linear elastic	Linear elastic	Nonlinear, non-homogeneous
Domain discretisation	Particles + springs	Boundary only	Full volumetric mesh
Element type	—	Boundary elements	tetrahedral/hexahedral
Constitutive model	Linear elastic springs	Linear elasticity	Hyperelastic/viscoelastic
Damping	Explicit (d)	Implicit	Rayleigh / material-based
Boundary conditions	Prescribed node constraints	Boundary-only	Experimentally informed BCs
Solver	Explicit time integration	Integral solver	Implicit nonlinear FEM solver

5.4 Types of Solvers in Abaqus

FEM is a widely used numerical method for solving problems across engineering disciplines. The goal of this practice is to derive equations that approximate unknown values by decomposing the problem into simpler subproblems. In the process, these sub-problems, referred to as finite elements, require either implicit or explicit analysis [167].

Implicit and explicit FEM are used to simulate dynamic linear and nonlinear problems. A comparison of implicit and explicit methods in Abaqus for nonlinear problems has been reported by ReBelo et al [168]. In all non-static and nonlinear analyses, incremental load or displacement steps are required. This suggests that solving a mathematical problem requires decomposing both the physics and the temporal relationships. To do this, time-dependent and time-independent problems need to be formulated, which are solved by implicit and explicit solvers, respectively [167]. A problem is time-dependent when the effects of acceleration cannot be ignored. For instance, in a drop test, the peak force occurs within the first few milliseconds as the object decelerates. This force must be accounted for to determine the overall effect of the deceleration. Conversely, when a load is applied slowly to a surface or structure, the response can be considered quasi-static or time-independent. This is because the loading time is insufficient for the acceleration effects to be significant.

Various explicit and implicit problems are formulated as partial differential equations (PDEs). Although computers cannot solve PDEs directly, they can solve matrix equations. These matrix equations can be either linear or nonlinear. In most structural problems, nonlinear equations can be classified into three categories. The first category comprises material nonlinearity, characterised by large deformations and strains. Secondly, geometric nonlinearity is characterised by small strains but large rotations and is usually observed in thin structures. Finally, boundary nonlinearity arises from nonlinear boundary conditions, which are commonly observed in contact problems.

5.4.1 Implicit Solver

The standard or implicit Abaqus solver is commonly used to solve problems involving both linear and nonlinear static conditions. It applies an incremental method to solve the equations of motion, efficiently addressing small-to-moderate material nonlinearity and deformation.

Nonlinear problems involving geometry, material properties, boundary, and contact conditions can be analysed by performing a series of trial solutions to establish static equilibrium within a specified tolerance for displacement and loading [175]. Each step requires iteration, and the solution from the previous step is used to determine the current iteration. Implicit solvers can also generate reaction forces, displacements, and stress and strain fields. However, they are not suitable for handling large deformations and dynamic loading, as these require multiple iterations to converge, which can be time-consuming, costly, and, on occasion, impossible. In these cases, more advanced methods are required to find a feasible solution. The standard Abaqus solver uses an implicit integration method to solve the equations of motion for a given problem. The equations of motion may include dynamic or static equilibrium equations, or a combination of both [173].

The Abaqus implicit solver derives the motion equation as a matrix equation of the form:

$$[K]\{x\} = \{F\} \tag{5.4}$$

where the stiffness matrix is denoted by [K], the displacement vector by {x}, and the nodal force vector by {F}. [K] is composed of the element's boundary conditions and stiffness matrices, and {F} is derived from the external load and the boundary conditions.

One method for determining the unknown displacement vector {x} is matrix inversion or an implicit time-stepping algorithm. The algorithm aims to make an initial estimate of the displacement vector and then iteratively solve for it using the Newton-Raphson scheme until convergence [169].

Implicit FEA solvers are best suited to problems involving slow loading, well-defined boundaries, and manageable nonlinearity. They use implicit integration, which is stable. This stability allows the time step size to be chosen independently of the problem's stiffness and size. On the other hand, for problems beyond this scope, particularly those that are significantly more complex, an explicit method might be more effective [170].

5.4.2 Explicit Solver

The use of an explicit solver can directly address acceleration issues in complex problems arising from dynamic or time-dependent effects. Explicit FEA is often used to handle high-speed events, such as impacts and crashes [171]. It is a time-based solver suited to solving the equation of motion at every stage of a problem, which makes it computationally demanding but accurate for addressing complex issues such as large deformations, contact, and material nonlinearities. An explicit solver is capable of tackling complicated boundary and geometric problems and can output data on the strain rate, deformation, and the model's overall stress state [172]. Unlike the standard implicit solver, the explicit solver uses a time-integration method to solve the equations of a given problem. The Abaqus explicit solver can generate the motion equation in a matrix equation of the form [167]:

$$[M]\{a\}+[C]\{v\}+[K]\{u\} = \{f\} \tag{5.5}$$

where [M], [C], and [K] are the mass, damping, and stiffness matrices of the elements; {a}, {u}, and {v} are the acceleration, velocity, and nodal displacement; and {f} is the nodal force vector, which accounts for contributions from external forces and boundary conditions [167].

The integration scheme used by the Abaqus explicit solver is based on a second-order method that accurately approximates central differences over the time steps and takes the following form [170]:

$$\{u\}\{t + \Delta t) = \{u\}(t) + \Delta t\{v\}\{t\} = (\Delta t^2/2)\{a\}(t) \tag{5.6}$$

$$\{v\}\{t+\Delta t) =\{v\}(t) + (\Delta t/2)\{a\}(t) + \{a\}(t+\Delta t) \tag{5.7}$$

Where $\{u\}(t+\Delta t)$ and $\{v\}(t+\Delta t)$, respectively, are the nodal displacement and velocity vectors at time $t+\Delta t$. The nodal acceleration vectors $\{a\}(t)$ and $\{a\}(t+\Delta t)$, respectively, at times t and $t+\Delta t$, are obtained by solving the equation of motion using the nodal displacement and velocity vectors [170].

5.4.3 Comparison between Implicit and Explicit Solvers

There are similarities between implicit and explicit solvers, as both account for multiple time points when calculating the model's new state. However, with the explicit solver, the new state can be computed directly from the current state, whereas with the implicit solver, both the nonlinear solution algorithm and the equations are required to obtain the solution.

In implicit FEA, equilibrium must be achieved before proceeding to the next incremental step. It is suitable for evaluating relatively slow-motion or quasi-static events, provided the system is well-restrained and stable. Moreover, standard/implicit FEA solvers can be used when there is no need to account for high-speed phenomena, such as stress-wave propagation and shock loading, within the system.

Explicit FEA is most suitable for systems that undergo rapid loading events, such as ballistic strikes. It can also be used when the system exhibits high nonlinearity or undergoes free-body motion. Additionally, an explicit FEA solver should be used when the development of stress waves and shock loads, and the transmission of loads through the system, need to be understood.

5.5 Needle-Tissue Interaction Models

Over the years, heightened interest in the diagnosis and treatment of diseases has led to an increasing number of needles used in medical applications. Their widespread use in a range of medical procedures, including blood sampling, neurosurgery, brachytherapy for cancer, and biopsy, has had a considerable impact on improving efficiency across different stages of diagnosis and treatment [180-181].

Hypodermic needles are most commonly used for drug delivery and blood sampling. Although generally safe, they can cause local tissue trauma and, if improperly placed, carry a risk of vascular or nerve injury. Rare events, such as needle breakage and embedding, have been documented, particularly during difficult punctures or repeated attempts [181]. Biopsy needles, including fine-needle aspiration and core biopsy, are used to obtain tissue samples from organs such as the breast, liver, and prostate. Misplacement or incorrect depth can result in bleeding, haematoma, injury to adjacent structures, or nondiagnostic sampling [182]. Brachytherapy

needles, used for precise delivery of radiation in cancer treatment, require accurate positioning, as misplacement can damage surrounding healthy tissue, reduce therapeutic efficacy, or expose non-target organs to radiation [183]. These examples illustrate the wide range of medical needle applications and show that the risk of tissue damage or misplacement depends strongly on needle type, anatomical target, procedural complexity, and the use of guidance techniques such as imaging.

The accuracy of cutting tissue with medical tools is affected by several factors, including the mechanical properties of the tissue, the tool material and design, and the operational mechanism [175]. This is why numerical simulation is important: modelling needle-tissue interactions helps develop new medical devices. FEA is highly effective at simulating injuries and damage in both human and animal tissues [186-187]. Studies of needle-tissue interactions have focused on a range of biological tissues, with the most common being muscle, brain, liver, and fat [188-189]. Needle-tissue interactions are typically classified into two categories, namely: non-invasive and invasive models. The first category considers needle or tissue deformation before puncture or damage occurs, whereas the second category employs a failure mechanism that allows the needle or any type of cutter to be inserted into the tissue.

5.5.1 Non-Invasive Finite Element Models

The earliest known models of needle-tissue interaction assume no crack propagation within the tissue, implying that the needle cannot penetrate it. Although some studies claim to present models that describe the penetration process, they do not provide a damage mechanism for the cutting process. These models are considered non-invasive. In these models, the needle is embedded in the tissue and cannot cause further damage. One of the main reasons for the popularity of these models is their ability to analyse tissue deformation without cutting. This provides valuable information on needle-tissue interaction, including predictions of deformation under indentation and identification of the needle reaction force before and after tissue puncture.

For example, Aoyagi et al. [190] used FM to study stress concentrations at the tips of microneedles with varying shapes, angles, and widths in the skin. The FE models employed both two- and three-dimensional representations to generate realistic, jagged, sharp microneedles that mimic a mosquito's proboscis. No failure criterion was used in the models;

instead, the microneedle was embedded in the tissue from the outset. The simulations were conducted under load control, applying a constant force along the needle's centreline to determine the stress distribution in the tissue. The needle was made of polylactic acid (PLA), and the tissue was modelled as silicone rubber with linear-elastic properties. The stress distribution within the tissue is shown in Figure 5.2, which illustrates the effects of microneedle insertion under varying loading and geometric conditions. The study found that thinner, sharper microneedles produce higher tissue stress, facilitating penetration.

The use of non-invasive FE models in the study of needle-tissue interaction can yield valuable insights into soft-tissue deformation behaviour and stress-strain characteristics. Compared with invasive models, non-invasive models are typically easier to use, enabling the study of diverse biological tissues with complex mechanical and geometric characteristics. In most cases, it is possible to incorporate viscoelastic and hyperelastic properties into tissue in non-invasive models, making them more efficient and less prone to divergence than more complex models that include damage mechanisms. Although these models can provide insight into factors affecting needle penetration, they are not suitable for all procedures, particularly those involving crack propagation. Moreover, they cannot be used in medical analyses that require a needle to penetrate tissue to a specified depth. For this reason, non-invasive FE modelling plays its most important role in studies related to the interaction between tissue and needle [180].

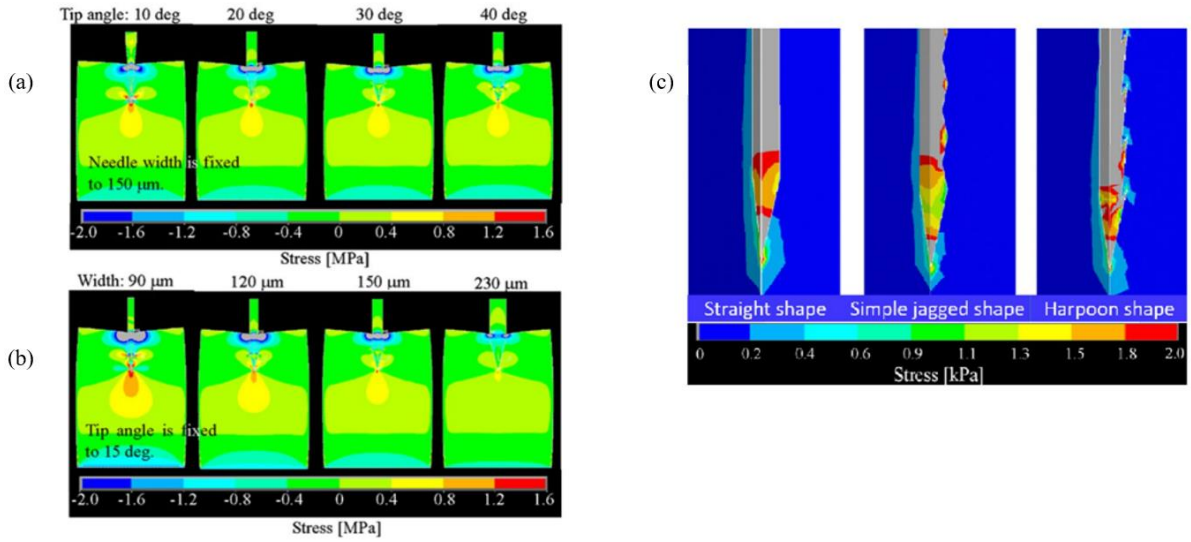

Figure 5.2: Non-invasive FE model of microneedles embedded in silicone rubber artificial skin tissue, without any damage mechanism, showing the stress distribution within the skin tissue.

(a) showing the effect of tip angle, (b) showing the effects of width, and (c) showing the effect of different microneedle shapes on the stress distribution [195]. Copyright 2023 by The Author(s) under exclusive licence to International Centre for Numerical Methods in Engineering (CIMNE).

5.5.2 Invasive Finite-Element Models

Although non-invasive models of needle-tissue interaction can provide valuable information, most medical procedures require tissue puncture and the propagation of damage. As a result, numerous groups have conducted FEA studies to model the effects of various damage mechanisms during needle insertion into soft tissues. Invasive models can be classified into five methods: nodal separation, element deletion/failure, cohesive zone, arbitrary-Lagrangian-Eulerian (ALE), and coupled Eulerian-Lagrangian (CEL).

Separation Models

Several studies have predicted damage mechanisms using algorithms that account for the displacement of nodes near the cutting zone, which underpins nodal separation models. Although the models incorporate damage, failure mechanisms have not been established for all elements, including the cutting region. Instead, the cutting force is calculated by accounting for factors such as the local effective modulus (LEM) and fracture toughness [180].

Gokgol et al. [190] conducted several experiments to test custom-made needles for penetrating bovine livers and subsequently developed an FE model based on their findings. They used a hyper-viscoelastic model to describe the mechanical properties of bovine liver. The mechanical properties were obtained from static indentation and ramp-and-hold experiments. An energy-based approach was used to model crack propagation within the tissue. The analysis was carried out using a simplified two-dimensional FE model that modelled only the region around the needle insertion point. The model was considered asymmetric with respect to the insertion-axis geometry and solution. The model shown in Figure 5.3(a) includes the two types of needles used: the cylindrical probe with a round tip (left) and the sharp-tip needle (right). The hyper-elastic properties of the tissue were defined by a five-term Mooney Rivlin strain energy function, whereas the generalised Maxwell solid model defined the viscoelastic properties. The separation of nodes at the needle tip was determined by comparing the fracture work during

insertion with the viscoelastic work. The fracture work was obtained by multiplying the crack area by its tissue fracture toughness, and the viscoelastic work was computed as the difference between the total work and the fracture work. The contact between the tissue and the needle was defined through a trial-and-error procedure that used parameters such as the coefficient of friction, the penetration tolerance factor, and the normal penalty stiffness factor. The distribution of von Mises stress levels around the needle and tissue is shown in Figure 5.3(b). Although both instances exhibited the same maximum stress, the stress in the tissue when the round-tip probe was inserted was higher than when the sharp needle was inserted.

The nodal-separation FE model has a lower computational cost than other invasive models. It does not include predefined failure mechanisms. Nonetheless, such a model typically requires several iterations to investigate and understand the needle-insertion process and trajectory. Nodal separation models generally combine the advantages and disadvantages of more complex invasive techniques with those of simpler non-invasive ones. Compared with other models, the computational cost of nodal separation models is higher than that of non-invasive methods but lower than that of invasive methods.

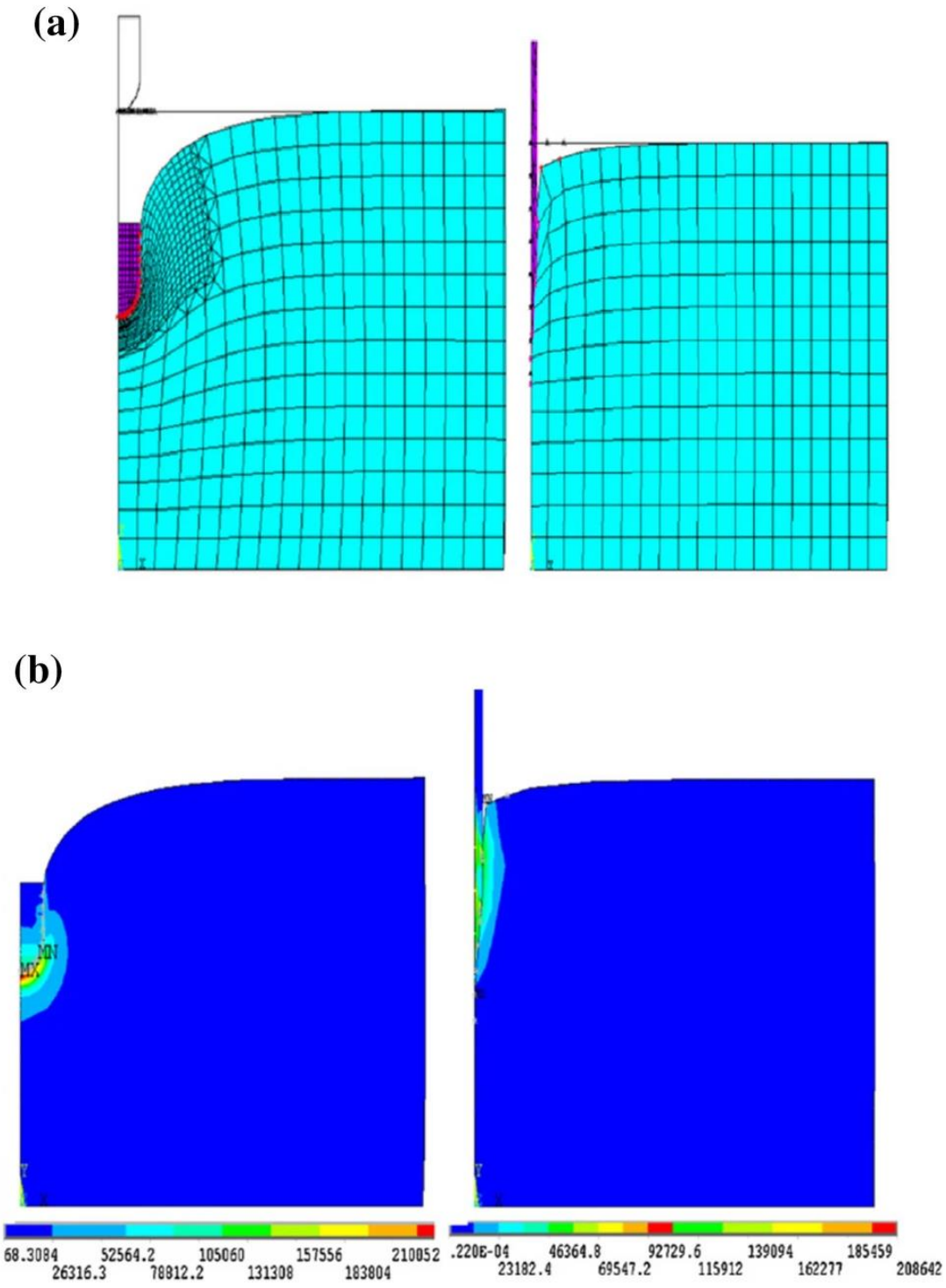

Figure 5.3: Nodal separation method used in an FE model of needle insertion into bovine liver. (a) mesh and geometry of the cylindrical probe with a round tip (left) and the needle with a sharp tip (right), (b) deformation of the bovine liver for the cylindrical probe (left) and the needle with a sharp tip (right) [181]. Copyright 2011 IPEM. Published by Elsevier Ltd.

Element Deletion/Failure Models

Invasive models require an algorithm to replicate the cutting process and maintain contact between the tissue and the needle. Among the prevalent methods used in FE models to simulate invasive approaches are element deletion and element failure. These methods each use a damage model based on parameters such as the shear strain threshold, ultimate strength, and stress failure to enable tissue cutting. Unlike the nodal separation technique, this approach applies damage mechanisms directly within the tissue's elements. The damage model is defined either across the tissue's whole domain or in a cutting zone, where the needle comes into contact with the tissue [180].

Jiang et al. [191] developed an FE model to visualise the factors that affect force, stress, and strain in the skin during hollow-needle insertion. The FE model focused on the tip angle, diameter, and insertion speed. For the study, the needle was assumed to be rigid, and the tissue's mechanical properties were set to match those of medical silicone, which has been shown to resemble human skin [192]. Figure 5.4(a) depicts the needle's insertion into a cylindrical structure, representing the skin's model configuration. The simulation was carried out in 40 iterative steps using the full Newton-Raphson method and modelled both the insertion and the extraction of the needle. Figure 5.4(b) shows the maximum strain distributions and von Mises stress levels during the various stages of the procedure, including insertion, maximum depth, and extraction. The maximum stress and strain were observed near the needle tip throughout the procedure. Stress and strain initially increased upon needle insertion, continued to increase with increasing puncture depth, and then decreased rapidly upon needle withdrawal.

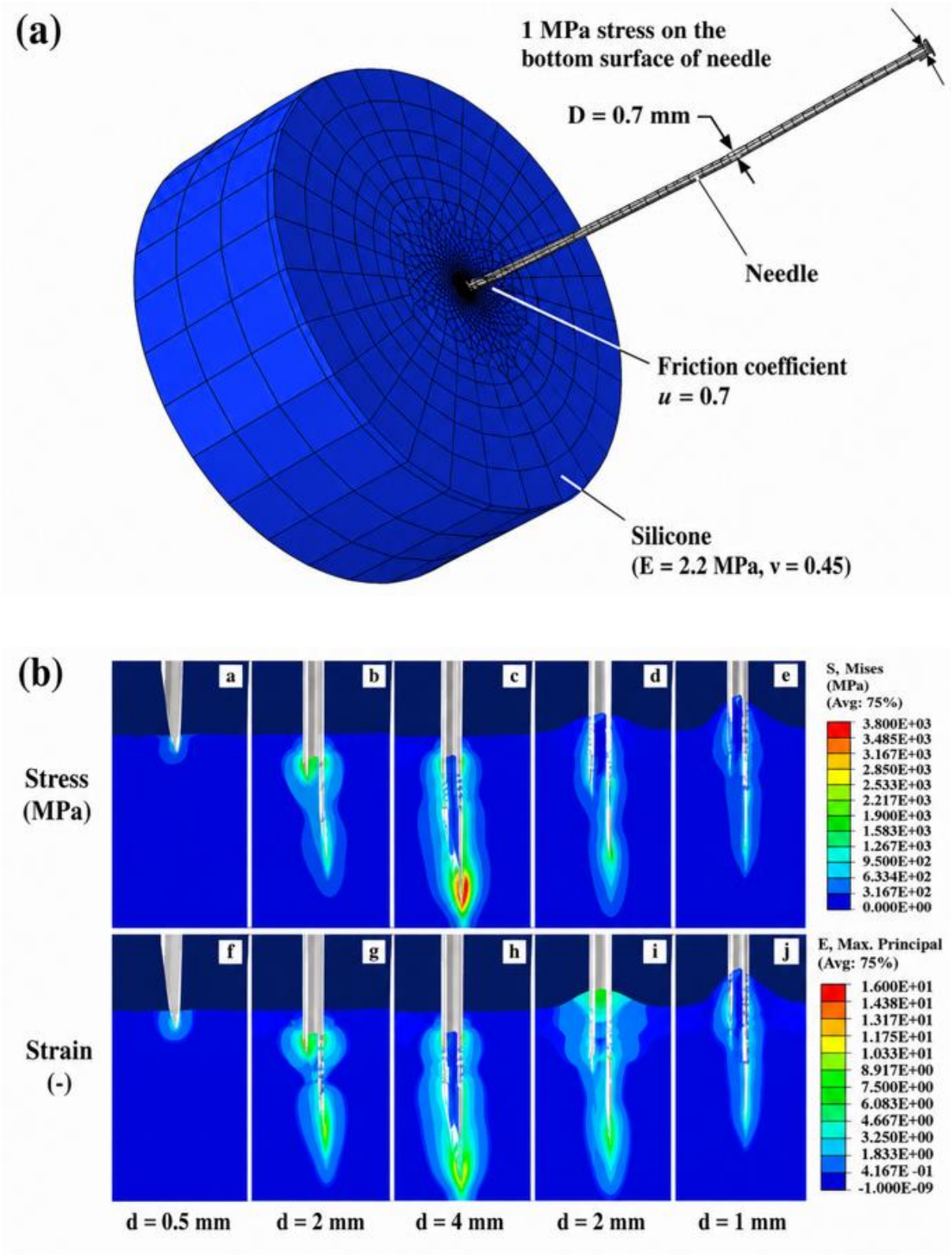

Figure 5.4: FE modelling of needle insertion into a limited area of skin tissue using the element deletion/failure method. (a) 3D mesh geometry and configuration, and (b) strain and stress in MPa fields in the skin during different stages of needle insertion and extraction [182]. Copyright 2016, the Authors. Published by Atlantis Press.

In reality, when tissue is cut, no part is removed or completely reduced in size. However, in element deletion/failure modelling, some tissue elements deteriorate and are removed during the simulation. Despite various factors that can affect the simulation, these models still provide a more realistic and valid representation of the tissue's crack propagation process. For instance, they can incorporate a crack-propagation mechanism that is similar to that observed in vitro, since the small elements in the vicinity of the crack do not affect the simulation's overall quality. Element deletion/failure models are strongly dependent on the mesh size around the crack front; therefore, a mesh study is necessary to ensure that the effects of element size on the final results are minimal. One of the main advantages of these models is that they can be applied to various tissue types and used to develop damage mechanisms specific to each model element. In addition, they provide a wide range of options for selecting the appropriate damage mechanism for a given tissue and for implementing FE packages for needle insertion.

Cohesive Zone Method

The cohesive zone model (CZM) is widely used to represent failure mechanisms in crack-propagation simulations. It allows the creation of realistic crack surfaces [183], [184]. The CZM can be defined by utilising the traction-separation law (TSL) [185], which links separation and the traction vector in the longitudinal direction. In the literature, all the models that utilise the CZM technique for needle insertion into tissue use a bilinear TSL, Figure 5.5(a), to relate the strain, ε, and the cohesive traction, t. The cohesive traction tends to increase linearly with increasing distance between the two cohesive surfaces until it reaches a critical failure traction, tc, at which damage initiates. Following this phase, increasing the distance between the two cohesive surfaces linearly decreases the cohesive traction, tc, until the surfaces separate.

Using the definition of the constitutive thickness parameter (T_c), the linking strain and separation distance, δ, are related as [186]:

$$\varepsilon_{n,s} = \frac{\delta_{n,s}}{T_c} \tag{5.7}$$

where the n and s indices denote the normal and shear directions, respectively. When T_c is set to unity, the initial traction corresponds to the separation/traction arising from the initial thickness of K, as follows [186]:

$$t = K_n \varepsilon_n e_n + K_s \varepsilon_s e_s = K_n \delta_n e_n + K_s \delta_s e_s \quad (5.8)$$

Oldfield et al. [196] used a zero-thickness cohesive component to create a two-dimensional model of needle insertion into soft tissue, enabling crack propagation. A bilinear TSL was used to define the cohesive zone within the model. A two-dimensional tissue deformation model was proposed to study the deformation process during needle insertion, analogous to the strain energy component, whereas a more complex three-dimensional strain model was introduced to investigate the entire process, including the energy components. The needle was modelled as a rigid body with a node reference, whereas the gelatine block was modelled as an elastic material. The gelatine block was meshed using three-node plane strain elements, and the cohesive zone was meshed with four plane strain elements. The mesh configuration of the proposed model is shown in Figure 5.5(b). The interaction between the needle and the gelatine block was modelled using the penalty contact algorithm, which considers either frictional or frictionless contact based on the Coulomb friction law. Figure 5.5(c) illustrates the spatial distribution of stresses within the tissue's cohesive zone and the surrounding area prior to the failure of the first cohesive elements. The material will begin to deform during this phase of insertion, which may necessitate adaptive meshing strategies, particularly when frictional forces are present.

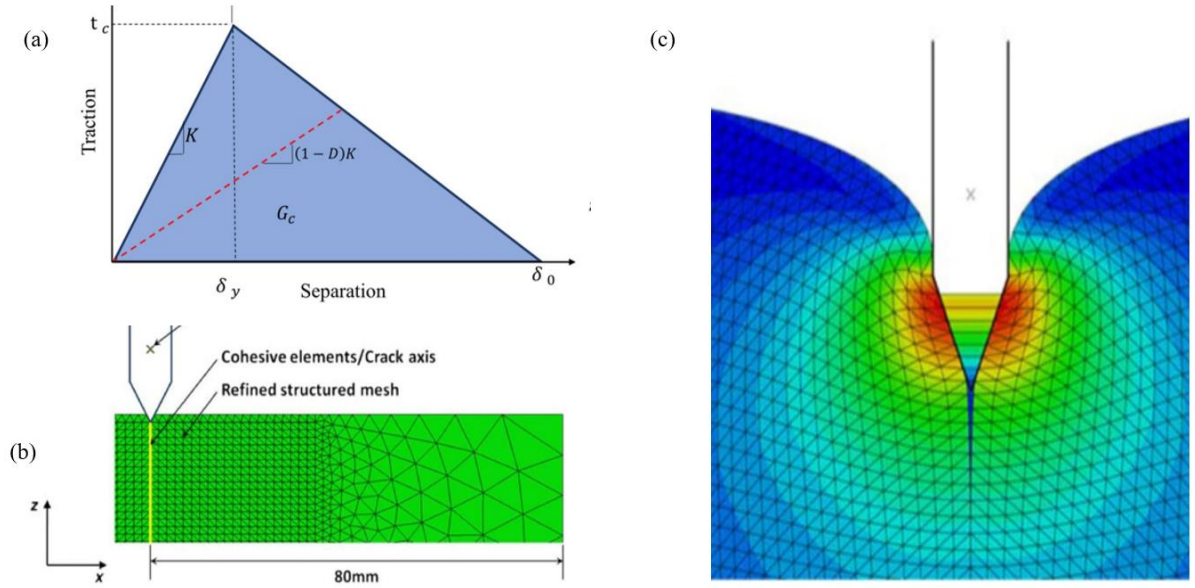

Figure 5.5: A detailed FE model of needle insertion into a gelatine phantom using a cohesive zone model (CZM). (a) bilinear traction-separation law, which is based on the strain,ε,and the

cohesive traction, t; (b) 2D model of the needle and tissue showing the mesh configuration, with the gelatine meshed using three-node plane strain elements; (c) stress and element distortion experienced by the first cohesive element before it failed during the insertion of the needle into the gelatine [186]. Copyright 2012 by Taylor & Francis.

CZM is an ideal tool for accurately depicting the cutting process in soft tissues, as it can generate realistic crack paths and accommodate the large deformations that commonly occur in these tissues. However, cohesive elements should be integrated into continuum elements to simulate needle insertion. The challenging aspects of this method are identifying the direction of crack propagation and implementing an appropriate mesh. To address this issue, the current solution employs an iterative algorithm, which complicates simulations. Incorporating such an algorithm into a three-dimensional model can be challenging due to the high computational cost and the need for numerous iterations. In certain cases, where the needle insertion and crack propagation are predictable and straight, CZM can be considered an efficient option.

Arbitrary Lagrangian-Eulerian Method

The various modelling techniques presented thus far employ a Lagrangian formulation, the earliest known and most widely used method for simulating cutting procedures such as needle insertion into soft tissues. However, due to large material deformations, elements can become distorted, leading to convergence problems and inaccurate predictions. Remeshing is an intuitive technique for compensating for element distortion in a mesh. If the mesh is distorted, a new mesh is created, and the solution from the lightly distorted mesh is mapped to the new one [187]. Generally, in a remeshing algorithm, each new mesh generation results in distinct changes to the mesh topology. The Arbitrary Lagrangian-Eulerian (ALE) formulation is a type of remeshing algorithm that involves creating the mesh through a simulation procedure that uses mesh smoothing techniques [188], [189]. In the analysis of continuum fracture models with large deformations, the ALE formulation is regarded as an efficient and powerful alternative to Lagrangian formulations [190].

As an example, Yamaguchi et al [191] presented a three-dimensional FEA of inserting copper-based needles into agar gel using the ALE technique. The FEA was implemented in Ansys LS-Dyna. The agar gel and the needle were discretised using hexahedral solid and rectangular shell elements and modelled with isotropic elastic-plastic and linear-elastic mechanical properties,

respectively (Figure .6(a). The analysis was performed for different needle tip angles, e.g. 30^0, 45^0, and 60^0. The results indicated a significant increase in the maximum shear stress with increasing tip angle. The shear stress distribution and needle deflection during the different phases of the insertion procedure for the 30° tip angle are shown in Figure .6(b). In all investigations and at every stage of the procedure, the maximum shear stress occurred in the area surrounding the needle tip.

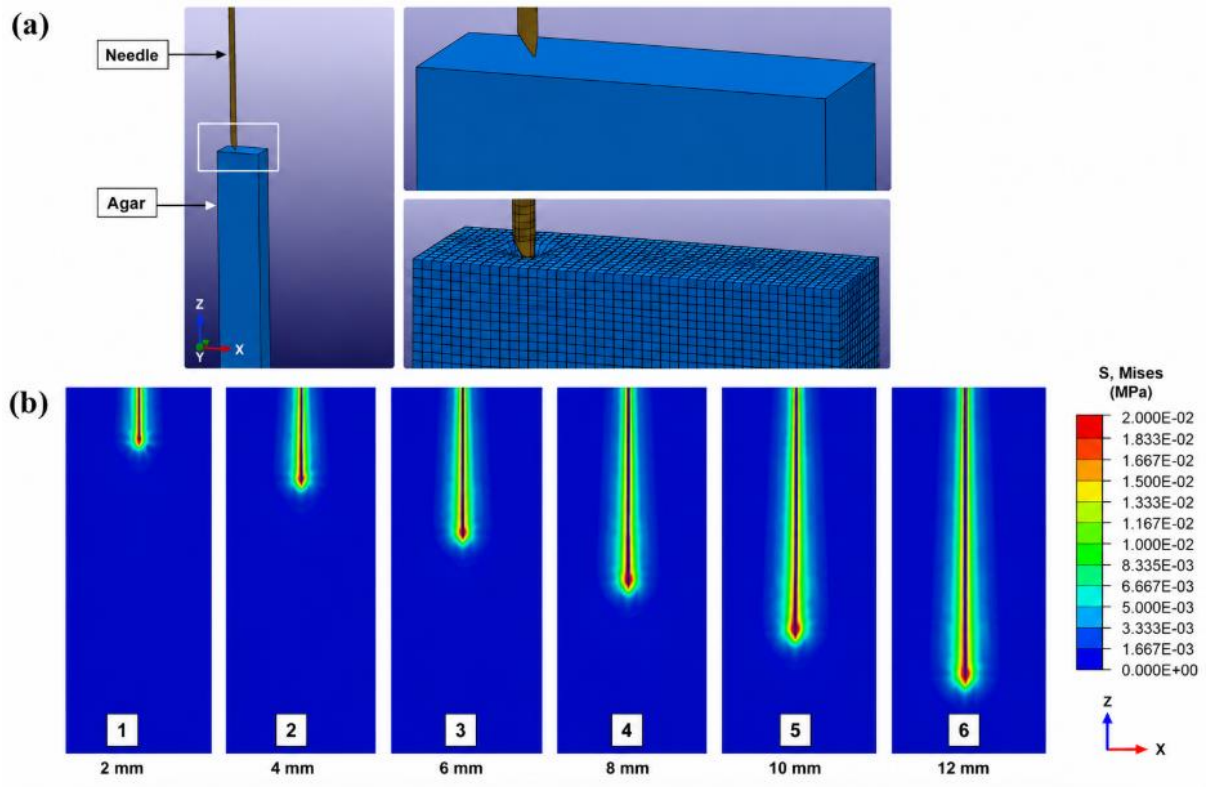

Figure 5.6: Detailed FE modelling of needle insertion into an agar gel phantom mimicking soft tissue, performed using the ALE. (a) Needle-tissue assembly and mesh configuration with the needle and tissue meshed using rectangular shell and hexahedral solid elements, respectively; (b) Shear stress and deflection of a 30^0 tip angle needle at different insertion depths [191]. Copyright 2014 by Elsevier Ltd.

The ALE method is well-suited to studying the deformation behaviour of needles during insertion into soft materials. It can also be used in path planning and optimisation studies. In addition to modelling large deformations of tissues and needles during insertion, the ALE technique enables efficient three-dimensional configuration modelling. This is a significant advantage over other models that rely solely on failure mechanics. Unfortunately, the

effectiveness of the ALE technique in generating complex tissue models, such as multi-layer tissues or tissues with visco-hyperelastic constitutive models, and in producing needles with jagged and harpoon-shaped structures has not yet been evaluated.

Coupled Eulerian-Lagrangian Method

The coupled Eulerian-Lagrangian (CEL) method is similar to the ALE technique, with the key difference that, in the CEL technique, the rezoned mesh is the original computational mesh, whereas in ALE, a new mesh is generated [190]. The CEL formulation assumes that, in the initial Lagrangian step, the mesh is treated as a temporary true node of the material deformation. Then, in the Eulerian step, deformation is suspended while the structure is remeshed, and the nodes always return to their original positions. This ensures that the mesh remains stationary during the simulation. The CEL method eliminates the distortion that occurs during the cutting process, and this does not require a conforming mesh to be produced [192].

Bushido et al. [193] performed a simulation of inserting a hollow biopsy needle into agar gel using a linear explicit dynamic CEL approach, Figure 5.7(a). Linear solid hexahedral and linear Eulerian brick elements were used to mesh the needle and the agar gel, respectively, with reduced integration and hourglass control applied to both element types. The analysis determined needle deflection and the contact stress experienced by the agar gel during insertion. The results outlined in Figure 5.7(b) revealed that the agar gel was punctured, and the maximum stress occurred at the tip of the needle shaft. It also indicated that sharper needles produced lower peak forces and greater needle deflections.

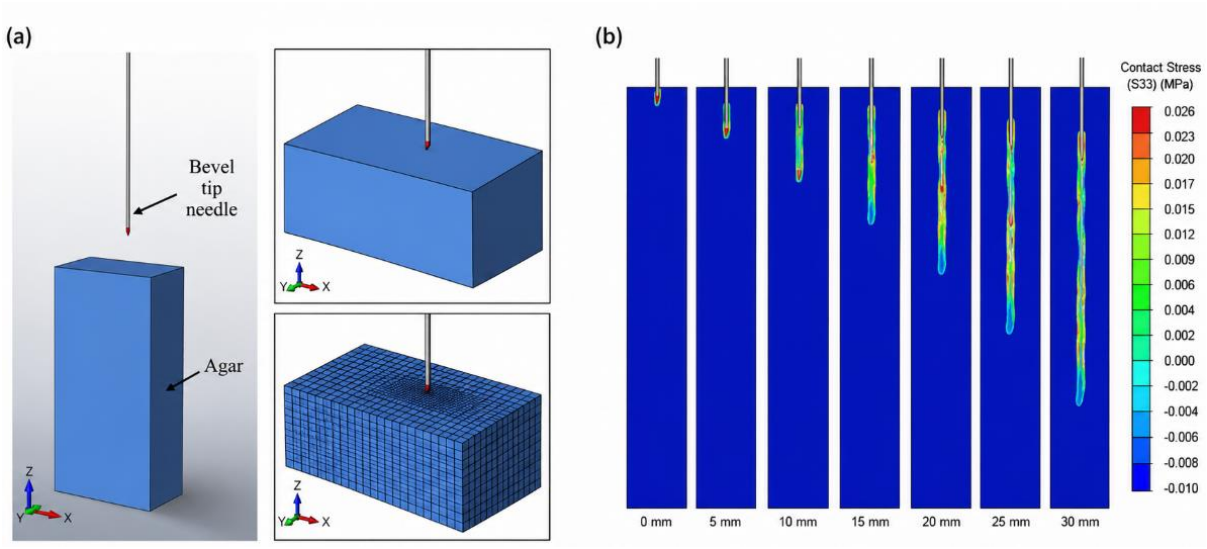

Figure 5.7: Detailed FE modelling of needle insertion into an agar gel phantom mimicking soft tissue using the CEL method. (a) Needle-tissue assembly and mesh configuration, with the needle and tissue meshed using linear-solid hexahedral and linear Eulerian brick elements, respectively; (b) contact stress distribution for a 18^0 bevel tip angle at different insertion depths, showing the maximum stress at the tip of the needle shaft [193]. Copyright 2019 by Elsevier Ltd.

The studies reviewed above show that various finite-element methods have been developed to simulate needle–tissue interactions, each with different assumptions about material behaviour, contact definitions, damage processes, and meshing techniques. To compare these approaches and emphasise the methodological differences relevant to this study, Table 5.2 summarises the key configurations and modelling features reported in the literature.

Table 5.2: Comparison of Needle-Tissue Interaction Modelling Approaches

Method	**Damage Representation**	**Mesh Distortion Handling**	**Computational Cost**	**Advantages**	**Limitations**	**Suitability for Present Study**
Non-invasive FE	No damage model	Poor under large deformation	Low	Simple implementation; useful for deformation analysis	Cannot simulate puncture or crack propagation	Limited
Nodal separation	Node release algorithms	Moderate	Moderate	Lower computational cost than other invasive methods	Requires iterative crack tracking	Moderate
Element deletion/ failure	Element-based damage criteria	Poor-moderate	Moderate	Captures crack propagation realistically	Mesh-dependent element erosion may reduce physical realism	Moderate
Cohesive zone model (CZM)	Traction-separation law	Moderate	High	Realistic crack propagation	Complex crack-path definition; high computational cost	Moderate

ALE	Remeshing/smoothing	Good	High	Handles large deformation effectively	Limited validation for complex multilayer tissues	Good
CEL	Eulerian-Lagrangian coupling	Excellent	High	Prevents mesh distortion; suitable for large deformation and multilayer interaction	Higher computational complexity	Highly suitable

Various invasive modelling techniques have been proposed to simulate needle insertion into soft materials. Each method has distinct advantages and disadvantages with respect to numerical stability, computational cost, crack propagation, and performance in large-deformation analysis. Table 5.3 summarises the properties and parameters for the models and how each is configured.

Table 5.3: Configuration of Representative Needle–Tissue Interaction FE Models

Study	Method	Tissue Model	Needle Model	Element Type	Damage Mechanism	Contact Definition
Aoyagi et al.	Non-invasive FE	Linear elastic silicone rubber	PLA microneedle	2D/3D FE	None	Embedded insertion
Gokgol et al.	Nodal separation	Hyper-viscoelastic liver	Sharp/round needle	2D FE	Energy-based node separation	Frictional contact
Jiang et al.	Element deletion	Silicone-based skin analogue	Rigid hollow needle	3D FE	Stress/strain failure	Surface contact
Oldfield et al.	CZM	Elastic gelatin	Rigid needle	Plane strain + cohesive elements	Bilinear TSL	Penalty contact
Yamaguchi et al.	ALE	Elastic-plastic agar gel	Copper needle	Hexadrehal/ shell	ALE remeshing	Contact interaction
Bushido et al.	CEL	Agar gel	Hollow biopsy needle	Eulerian brick/hexahedral	CEL coupling	General contact

To address the challenges of simulating needle insertion into soft biological tissues, including large deformations, mesh distortion, complex material behaviour, and multilayer interactions, the CEL method was selected as the primary modelling framework in this study. Unlike purely

Lagrangian methods, which suffer severe mesh distortion during large deformations, or purely Eulerian methods, which struggle to accurately track solid interfaces, CEL combines the strengths of both approaches while mitigating their respective limitations.

Compared with nodal separation and element deletion techniques, the CEL approach minimises mesh dependence and prevents artificial element erosion during crack growth. Unlike cohesive zone models, CEL doesn't require predefined crack paths or complex cohesive interface definitions, which can be challenging in intricate three-dimensional multilayer systems. Although ALE methods can reduce mesh distortion through remeshing, they may still encounter numerical instability and a higher computational load during highly localised deformation. Therefore, CEL offers a more reliable compromise among numerical stability, efficiency, and physical accuracy for simulating needle insertion into soft tissues.

Previous studies have demonstrated that CEL methods can predict needle deflection, contact stress, and insertion mechanics during needle penetration of soft materials. However, many of these studies focused primarily on simplified homogeneous tissue analogues and relatively idealised insertion conditions. The novelty of the present work lies in extending the CEL framework to investigate needle interaction with more physiologically representative soft-material structures under clinically relevant insertion conditions. Furthermore, the proposed modelling framework enables detailed evaluation of tissue deformation, stress distribution, and insertion dynamics while maintaining numerical stability throughout large deformations. This provides a more comprehensive and physically representative approach to analysing needle–tissue interaction than many existing methods reported in the literature.

5.6 Coupled-Eulerian Lagrangian Methodology

The positions of small particles within a given continuum change over time as they move through a flow or deformation, and these changes in position can be described by functions of time in the Eulerian and Lagrangian frameworks, Figure 5.8 [194].

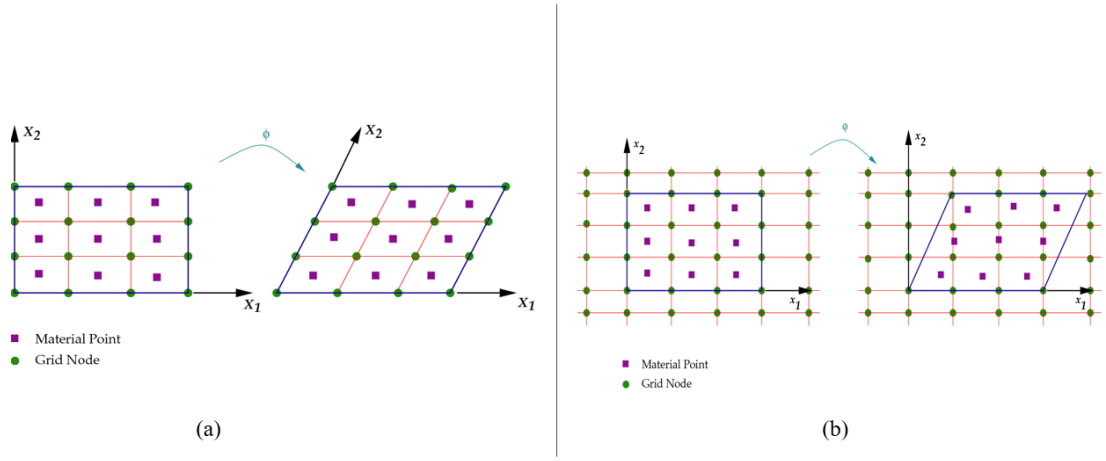

Figure 5.8: (a) Lagrangian description vs (b) Eulerian description of continuum motion [195].

In the Lagrangian formulation, the computational mesh is attached to the material, so each mesh node follows the motion of the material particles throughout the analysis. Consequently, the material coordinates remain fixed relative to the mesh, making this formulation particularly suitable for structural mechanics and solid deformation analyses where accurate tracking of material interfaces and contact boundaries is required [196]. Because the mesh deforms with the material, the Lagrangian formulation provides accurate predictions of displacement, strain and stress distributions. However, when materials undergo large deformations, such as those occurring during needle penetration of soft tissue, the finite elements may become severely distorted. Excessive mesh distortion can reduce solution accuracy, impair convergence and, in extreme cases, terminate the numerical simulation.

In contrast, the Eulerian formulation employs a fixed computational mesh through which the material flows. The mesh remains stationary throughout the analysis, while the material state within each element evolves over time. This approach is widely used in fluid mechanics and in simulations involving extremely large deformations because it effectively eliminates element distortion [197]. Within the Eulerian domain, the material state at any spatial location is characterised by field variables such as velocity, density, stress tensor and internal energy, which satisfy the conservation equations for mass, momentum and energy [195]. Although the fixed mesh prevents numerical problems associated with element distortion, the Eulerian formulation may introduce numerical diffusion at material interfaces, particularly when multiple materials occupy the same computational domain. Furthermore, because the mesh

does not move with the material, accurately tracking solid boundaries and contact interfaces is more challenging than in the Lagrangian formulation [198].

Rather than relying exclusively on either formulation, the present study employs the Coupled Eulerian–Lagrangian (CEL) approach, which combines the strengths of both methods. In the CEL formulation, the deformable tissue is represented on a fixed Eulerian mesh, allowing large deformations and material flow without element distortion, whereas the biopsy needle is modelled on a Lagrangian mesh that accurately preserves its geometry and facilitates contact detection. The interaction between the moving Lagrangian needle and the Eulerian tissue is resolved using a general contact algorithm, enabling stable simulation of needle penetration while maintaining computational accuracy.

Table 5.4 summarises how the Lagrangian and Eulerian formulations were implemented within the Coupled Eulerian–Lagrangian (CEL) model developed in this study and the rationale for assigning each component to its respective formulation.

Table 5.4: Application of the Lagrangian and Eulerian formulations in the Coupled Eulerian–Lagrangian (CEL) model developed for EBUS-TBNA needle insertion [199].

Model component	**Formulation**	**Purpose in the present Study**	**Reasons for selection**
EBUS-TBNA needle	Lagrangian	Represents the biopsy needle throughout insertion	The needle undergoes relatively small deformation and requires accurate tracking of geometry and contact
Soft tissue (lymph node or tissue phantom)	Eulerian	Represents the deformable tissue during needle penetration	Allows large deformation and material flow without mesh distortion
Needle-tissue interaction	General contact (CEL)	Simulates contact between the needle and tissue.	Maintains stable contact while permitting penetration of the Eulerian material
Overall numerical model	Coupled Eulerian-Lagrangian	Combines the advantages of both formulations	Eliminates excessive mesh distortion while accurately modelling needle motion and tissue deformation

The complementary strengths of the Lagrangian and Eulerian formulations make the CEL method particularly well suited to modelling needle insertion into soft biological tissues. By combining an accurate representation of the needle with a distortion-free description of the deforming tissue, the CEL formulation provides a robust numerical framework for simulating tissue penetration and interaction during EBUS-TBNA procedures.

5.6.1 Governing Equations between Lagrangian and Eulerian Formulations

The Eulerian and Lagrangian descriptions employ spatial and material time derivatives in their respective conservation equations. The link between the material and the space-time descriptions is defined by the chain rule as follows:

$$\frac{dy(x,t)}{dt} = \frac{\partial y(x,t)}{\partial t} + v.(\nabla_y(x,t)) \tag{5.9}$$

where y (x, t) is a tensor field with spatial coordinates, x, and time t. $\frac{dy}{dt}$ and $\frac{\partial y}{\partial t}$ are the material and time derivatives, respectively. The expression $v.(\nabla_y)$ is the constitutive term, in which v is the material velocity and ∇_y is the covariant derivative of the tensor. Equation 5.9 shows that the total change in y is proportional to the sum of the convective and local rate of change in y. In Lagrangian terms, the energy, mass, and momentum can be written as follows:

$$\frac{d\rho}{dt} + \rho\nabla.v = 0 \tag{5.10}$$

$$\rho\frac{dv}{dt} = \nabla.\sigma + \rho b \tag{5.11}$$

$$\frac{de}{dt} = \sigma : D \tag{5.12}$$

where ρ , b, e, σ, and D denote the density, body force, total energy per unit volume, Cauchy stress, and strain rate, respectively. The CEL analysis accounts for the material derivative within the Lagrangian formulation and for material meshing. Equations (5.10), (5.11), and (5.12) are then transformed to an Eulerian formulation using Equation (4.9):

$$\frac{\partial\rho}{\partial t} + \nabla.(\rho v) = 0 \tag{5.13}$$

$$\frac{\partial\rho v}{\partial t} + \nabla(\rho v \otimes v) = \nabla.\sigma + \rho b \tag{5.14}$$

$$\frac{\partial e}{\partial t} + \nabla.(ev) = \sigma : D \tag{5.15}$$

where *e* represents the internal energy. The conservation equations for the Eulerian formulation are expressed in terms of spatial derivatives, and the material moves freely within a fixed spatial mesh. The general conservation form of Equations (5.13), (5.14), and (5.15) is as follows:

$$\frac{\partial y}{\partial t} + \nabla . \emptyset = S \tag{5.16}$$

where $\emptyset$ and S are the flux function and the source term. The arbitrary variable, y, in Equation 4.16, depends on spatial orientation and varies with time. Solving the time-spatial coupling equation directly is numerically challenging. The CEL technique can address this problem by decomposing it sequentially as follows:

$$\frac{\partial y}{\partial t} = S \tag{5.17}$$

$$\frac{\partial y}{\partial t} + \nabla . \phi = 0 \tag{5.18}$$

Equations 5.17 and 5.18 refer to the Lagrangian step with the source term and the Eulerian step with the convective term, respectively. The time derivative in Equation 5.17 differs from that used in the governing equations within the Lagrangian approach. If the spatial time derivative is replaced by the material time derivative on a fixed mesh, Equation 5.17 is the same as the standard Lagrangian formulation.

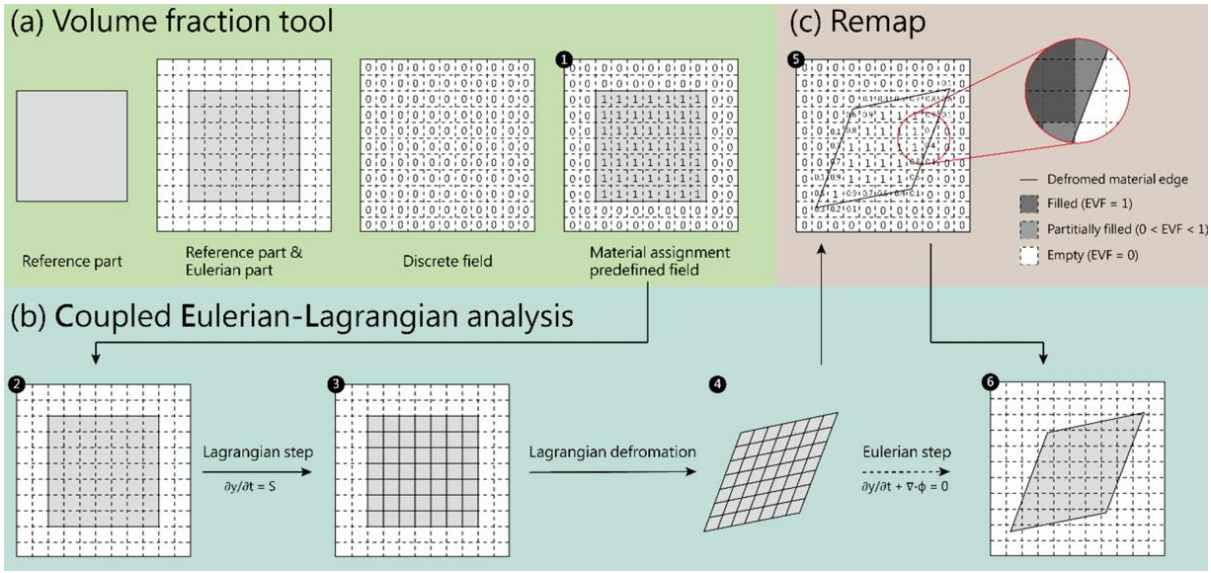

Figure 5.9: Overview of the CEL approach: (a) volume fraction tool; (b) CEL analysis; (c) remap procedure. Copyright 2020 Elsevier Ltd.

The CEL calculation procedure is shown in Figure 5.9. It shows the elements that undergo extreme deformations and their meshed state using the Eulerian method, while the Lagrangian method is used to mesh the remaining elements. In Figure 5.9(a), the volume fraction tool can create a discrete field with the help of a Boolean analysis. This method involves comparing the parts of the Eulerian principle. The Eulerian volume fraction (EVF) is computed between the Eulerian part and the reference part that intersects the Eulerian part. The EVF ranges from 0 to 1 and represents the percentage of each Eulerian element filled with a specific material. The predefined field is then used to assign materials, and the material boundaries are calculated based on the EVF of all the elements. The region not defined in the Eulerian part is treated as void. Although the material initially lacks material properties, it can still flow into and through the void during the analysis.

The data collected during the CEL analysis is stored at the nodes and then transferred to the computational mesh, Figure 5.9(b). The unknown variables are then calculated by solving the Lagrangian formulation (Equation 5.17), and the resulting displacement, velocity, and acceleration of each node are updated, Figure 5.9(b). In addition, the adopted constitutive model provides estimates of stresses and strains. The position of each node is updated after the mesh adjustment, Figure 5.10(b). In the Eulerian mesh, the Lagrangian elements can move

freely without resistance until they encounter a material-filled region (EVF = 1). General contact can facilitate interaction between Lagrangian and Eulerian materials.

To solve Equation 5.18, the deformed mesh can be remapped to the original fixed mesh, and the volume of material transferred between adjacent elements can be determined using the EVF, Figure 5.9(c). Finally, the solutions of the Lagrangian equations, such as energy, momentum, strain, and stress, are adjusted to account for material between adjacent elements [196].

5.6.2 Time Integration Scheme

For CEL analysis, the explicit-dynamic approach is employed in Abaqus/Explicit. The explicit dynamic analysis is performed over a large number of small-time increments. The unknown solution at the next time step can be computed from the previous time step without iteration or the use of a tangent stiffness matrix. Hence, compared with the direct integration rule in Abaqus/Standard, explicit dynamic analysis provides a robust and computationally efficient approach to addressing complex contact problems.

The value of the stabilisation limit for an explicit analysis, Δt_c, is computed by accounting for the critical step size of the central-difference integration. Δt_c takes into account the characteristic element lengths , L_c, and the dilatational wave speeds , C_d, which are expressed as follows:

$$\Delta t_c \approx \frac{L_c}{C_d} \tag{5.19}$$

The small distribution wave exhibited by a model across any mesh element is given in Equation 5.19 and represents the minimum transit time. For a model consisting of a single material, the value depends on the smallest element dimension in the mesh, whereas for models with numerous material descriptions, it depends on the element with the highest wave speed. A time increment of less than Δt_c can be used to achieve a stable solution in explicit dynamic analysis. However, for nonlinear problems involving significant large deformation, the highest value of the model will continuously change, resulting in Δt_c changing in every succeeding step. To ensure a stable solution, an automatic adjustment can be implemented to maintain stability during CEL simulation.

5.6.3 Contact Behaviour between Materials

The main contact problems in the CEL model involve Eulerian-to-Eulerian and Eulerian-to-Lagrangian contact. When a granular material interacts with another, the default Eulerian-to-Eulerian contact produces a "sticky" behaviour. This reflects a kinematic principle, namely that a single strain field can be applied to all materials within an element. In Eulerian-to-Eulerian contact, tensile stress can be transmitted across the contact interface, but no slip can occur at these interfaces. By contrast, an Eulerian material interacts with a Lagrangian element through Eulerian-to-Lagrangian contact.

The penalty contact method shown in Figure 5.10 is used to establish contact between Lagrangian and Eulerian materials and is less severe than the kinematic method. To establish this contact, seeds are placed on the edges and faces of the Lagrangian elements, while anchor points are created on the surfaces of the Eulerian material. The penalty contact method allows limited penetration of the Eulerian material into the Lagrangian domain. The contact force exerted between the anchor points and the seeds, denoted, Fp, is proportional to the penetration distance d_p, as described in Equation 5.20. The Lagrangian elements can move freely through the Eulerian mesh until they encounter an Eulerian element containing material [196].

$$F_P = k_p d_p \quad [196] \tag{5.20}$$

where k_p is the penalty for stiffness, which is a function of the Eulerian and Lagrangian material properties.

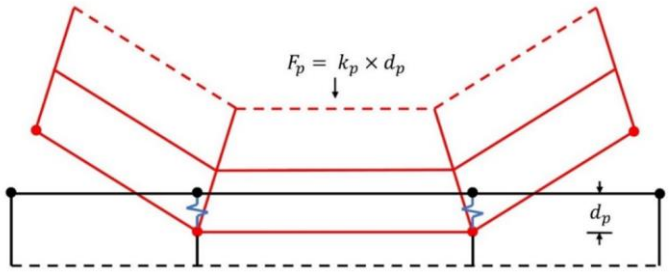

Figure 5.10: Lagrangian-Eulerian material contact definition using the penalty method [200]. Copyright 2023 by the authors.

In most cases, a Lagrangian frame is used to discretise a moving structure, and an Eulerian frame is used to represent the fluid domain. The Lagrangian boundary's velocity serves as the interface model's kinematic constraint for the Eulerian calculation using the interface models [198]. The Lagrangian domain addresses structural deformation, whereas the Eulerian domain focuses on element interactions. Since the Eulerian meshes are not constrained by mesh or element distortions, the CEL method is the most accurate for calculating the resulting loads [195].

5.7 Summary

This chapter explored the numerical modelling of needle-tissue interaction using a continuum mechanics approach. The analysis shows that FEA provides a practical method for capturing the complex, nonlinear behaviour of soft tissues during needle insertion, where analytical solutions are generally infeasible. This chapter reviewed key numerical techniques, including element formulations and solver strategies. It also compared implicit and explicit solvers in the context of large-deformation and contact problems. Existing literature on both non-invasive and invasive needle-tissue interaction was critically examined to highlight the strengths and limitations of current modelling approaches. Lastly, the potential of CEL techniques for modelling tissue damage and highly nonlinear interactions was introduced and discussed.

The assessment of different solver approaches indicates that none is universally optimal. The implicit solver excels at maintaining stable numerical performance with large time steps but may struggle with highly nonlinear behaviour. Conversely, explicit solvers are effective at handling severe nonlinearities and dynamic interactions, but they impose stricter time-step constraints. Similarly, the choice of mesh design and element formulation can significantly affect the accuracy of simulation results. According to the literature, non-invasive models focus more on guidance accuracy and tissue displacement, whereas invasive models typically focus on damage mechanics and tissue puncture. These contrasting characteristics highlight the need to develop numerical approaches that can account for specific needle-tissue interactions and predict outcomes.

This chapter also covers lessons on the models and methods used to simulate complex needle-tissue interactions. First, it is essential to balance computational cost with physical realism. Additionally, selecting suitable meshing strategies, element types, and solvers is vital to prevent

convergence issues and achieve realistic results. Second, CEL techniques, although computationally demanding, offer clear advantages for modelling tissue damage and complex interactions that are difficult to capture with standard Lagrangian FEA. Third, the review emphasises the lack of standardised validation protocols in the literature, highlighting the importance of benchmarking models against experimental data in subsequent work.

Although progress has been made, the chapter highlights several gaps and opportunities that will shape the direction of Chapter 7. Many existing models oversimplify tissue heterogeneity, anisotropy, and evolving damage, thereby limiting predictive accuracy in realistic scenarios. There is scope to improve solver strategies or to combine complementary methods to boost computational efficiency while maintaining fidelity. Lastly, additional parametric studies and experimental validation are necessary to develop robust and generalisable modelling frameworks for needle insertion, as discussed in the upcoming chapters.

In summary, Chapter 5 provides a thorough review of current numerical methods, emphasising lessons learned from their application and highlighting key gaps and opportunities to guide the experimental and modelling work discussed in the following chapters. This ensures the work progresses from a solid foundation of established techniques to address the challenges of accurate and predictive needle-tissue simulations.

Chapter 6: EBUS-TBNA Needle Insertion into Soft Materials

6.1 Introduction

This chapter examines the mechanics of tissue cutting during needle insertion, with a particular focus on rupture events at tissue-layer boundaries. Experimental force measurements are obtained using 21G and 22G EBUS-TBNA needles inserted into various soft materials. The chapter first outlines the experimental setup used to record insertion forces. It then investigates needle-tissue interactions and introduces a mechanical model to predict internal friction, force, normal stress, and the coefficient of friction. The experimental results are then presented and analysed, before concluding with a discussion of the main findings and their implications for needle deployment and tissue-sampling quality.

During needle-based procedures such as biopsies, transitions between tissue layers often lead to rupture events that involve significant tissue deformation and the formation of crack extensions [213-214]. These can occur due to tissue inhomogeneity or changes in its structure [203]. Accurate needle deployment and the quality of tissue sampling are two of the most crucial factors in making an accurate diagnosis and an individualised treatment decision. The biopsy specimen is known to significantly impact the detection rate of lung cancer. The amount of tissue obtained per needle biopsy should be increased to reduce the risk of false-negative diagnoses and delays associated with repeated EBUS-TBNA procedures.

With reference to Section 3.6, three force components are involved in inserting a needle into either biological tissue or a tissue-mimicking phantom. Figure 6.1(a) shows the cutting force, F_C, aligned with the needle trajectory and applied by the needle tip, and the inner, F_i, and outer, F_O, friction forces, aligned with the needle direction and acting on the inner and outer surfaces of the needle, respectively. Therefore, the force measured when inserting a hollow needle into a soft material is the sum of F_C, F_i and F_O, as shown in Figure 6.1(b).

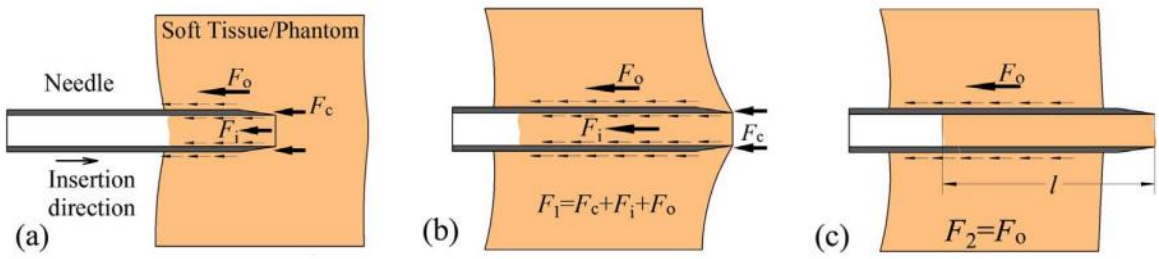

Figure 6.1: A schematic representation of the axial forces involved in inserting a needle into soft material: (a) the three axial force components during needle insertion (F_C, F_i, F_O); (b) the maximum force F_1 that the needle exerts before the tip exits the tissue; (c) the needle insertion force F_2 after the needle exits the tissue [204]. Copyright 2016 by Elsevier Ltd.

6.2 Experimental Materials and Methods

6.2.1 Experimental Setup

The monitoring and control of the forces generated during needle insertion into soft materials were carried out using a custom-built single-axis needle insertion test rig developed by Dr Kevin Worrall at the University of Glasgow, as shown in Figure 6.2.

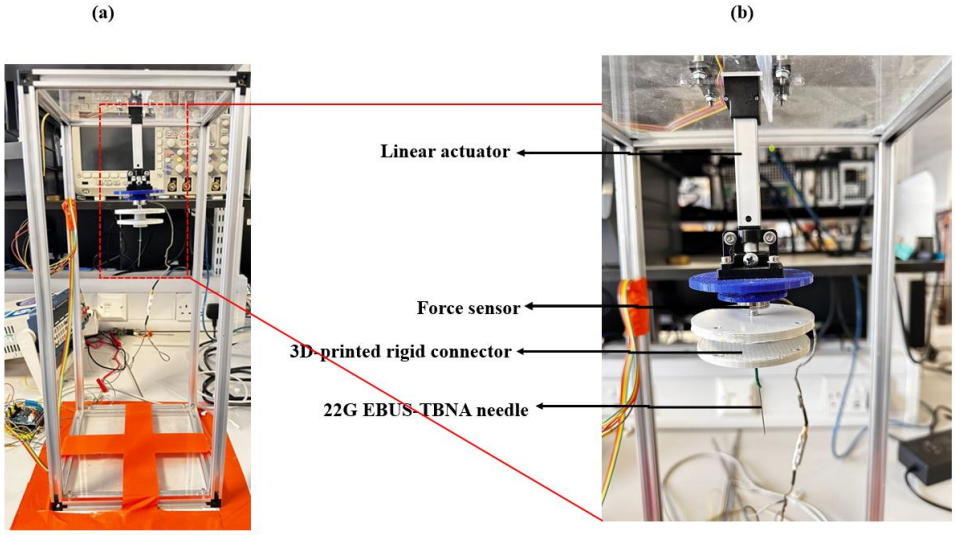

Figure 6.2: Needle insertion test rig. (a) Complete experimental setup; (b) close-up of the linear actuator, force sensor, custom 3D-printed connector, and EBUS-TBNA needle.

The test rig employed an L12 micro-linear actuator (Actuonix, Victoria, BC, Canada) to provide position-controlled vertical motion of the needle. The actuator has a maximum travel of 50 mm, and a maximum operating speed of 13 mm/s. Needle insertion forces were measured using a 100 N miniature tension/compression load cell (LCM201-100N, Omega Engineering, Stamford, CT, USA) mounted between the actuator and the needle. According to the manufacturer's specifications, the load cell has a rated capacity of 100 N and an accuracy of ±1.0% of full-scale output (Appendix 6.1). This measurement range was selected to provide sufficient sensitivity for the relatively low insertion forces generated when inserting a needle into soft materials, while maintaining an adequate safety margin against sensory overload.

The load cell and needle were mechanically coupled with a custom-designed, rigid, 3D-printed connector to ensure accurate transmission of axial insertion forces. The analogue output from the load cell was digitised using a 24-bit analogue-to-digital converter (ADC), while an Arduino Uno microcontroller interfaced with a personal computer to control actuator motion and acquire force measurements.

The actuator control signal required to achieve the prescribed needle insertion speed (mm/s) was determined using Equations 6.1 and 6.2 together with the linear-speed Arduino program provided in Appendix 6.3. The relationship between the control signal and the resulting actuator speed was experimentally verified to be linear (Appendix 6.1).

$$\text{Actuator position} = \frac{variable\ value}{1023} \text{ x maximum extension} \quad (6.1)$$

where the actuator position is expressed in mm

$$\text{Actuator speed} = \frac{Maximum\ position - Minimum\ position}{run\ time} \quad (6.2)$$

where the actuator run speed is expressed in mm/s, the maximum and minimum positions are given in mm, and the run time is expressed in s

[1]

[1] Code was first developed by Kevin-Worrall

6.2.2 Experimental Procedure

In this study, two flat-bevel needles used for EBUS-TBNA, namely the 21G (0.84 mm OD, 0.61 mm ID) and 22G (0.72 mm OD, 0.55 mm ID), as shown in Figure 6.3(a) (Vizishot, Olympus, Southend-on-Sea, UK), were inserted into four types of soft materials: PVA hydrogel, large pickled capers, chicken breast, and porcine lung lymph nodes. Needle insertion was controlled at speeds of 13 mm/s, 9 mm/s, 3 mm/s, and 0.5 mm/s. These speeds were selected to represent a range of clinically relevant insertion conditions, including rapid, intermediate, and slow. This range enabled assessment of how insertion speed affects force output while minimising dynamic effects caused by actuator inertia and vibration.

For each needle type and insertion speed, five insertions were performed into a single sample, spaced 5 mm apart to preserve tissue integrity and ensure repeatability. Because the large pickled capers and porcine lung lymph nodes are small, 5 insertions were made across 5 different samples. This resulted in 20 insertions for each soft material and each needle diameter. In each insertion, needle motion was initiated more than 1 cm from the soft material surface to ensure that needle speed remained constant from the moment the needle contacted the tissue until it emerged from the opposite side of the sample (Figure 6.3(b)). The samples were secured using a custom-designed holder that matched the tissue's shape, because excessive compression within a holder can generate additional strain energy and cause cracks to propagate. Conversely, a large clearance between the holder and the soft material will permit excessive deformation before needle puncture.

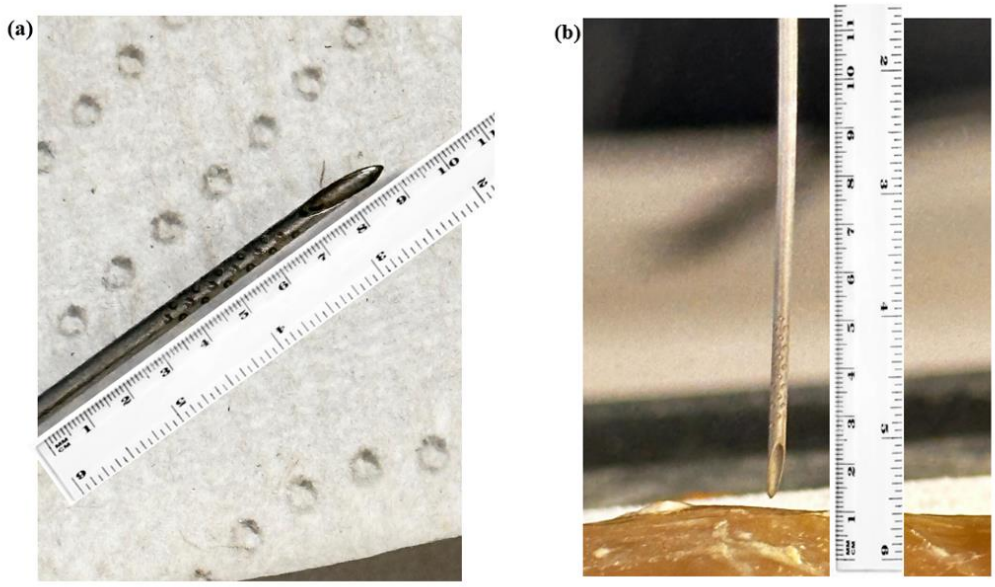

Figure 6.3: Needle insertion into the lymph node. (a) Microscopic view of the 22G EBUS-TBNA needle; (b) the predefined distance between the needle and the lymph node.

For each insertion, the force versus needle travel distance was recorded. The force acting on the needle was measured with a data recorder at 200 Hz. A low-pass filter was applied to remove high-frequency noise from the force measurements. The filter was chosen to minimise effects on deformation and force. Due to friction and potential needle-related errors, calibration was performed before each insertion to account for friction, offset, and possible drift associated with the needle and test rig. This step was especially important given the low force magnitudes involved, as small measurement errors could substantially affect the results. The calibration was performed in space, separate from the tissue, using 0.5 N and 1 N loads to determine the calibration factor for force evaluation. The needle insertion and calibration procedures were carried out using the Arduino code, which is included in Appendices 6.2–6.4.

6.3 Results

6.3.1 Force-Distance Relationship During Needle Insertion

Results of the combined force-displacement (F-D) of 21G and 22G EBUS-TBNA needles inserted into chicken breast, large pickled capers, PVA hydrogel, and porcine lung lymph nodes at 13 mm/s, 9 mm/s, 3 mm/s, and 0.5 mm/s are shown in, Figure 6.4 - Figure 6.7, respectively.

The force–displacement curves provide insight into the mechanical interaction between the needle and the soft material during penetration and advancement.

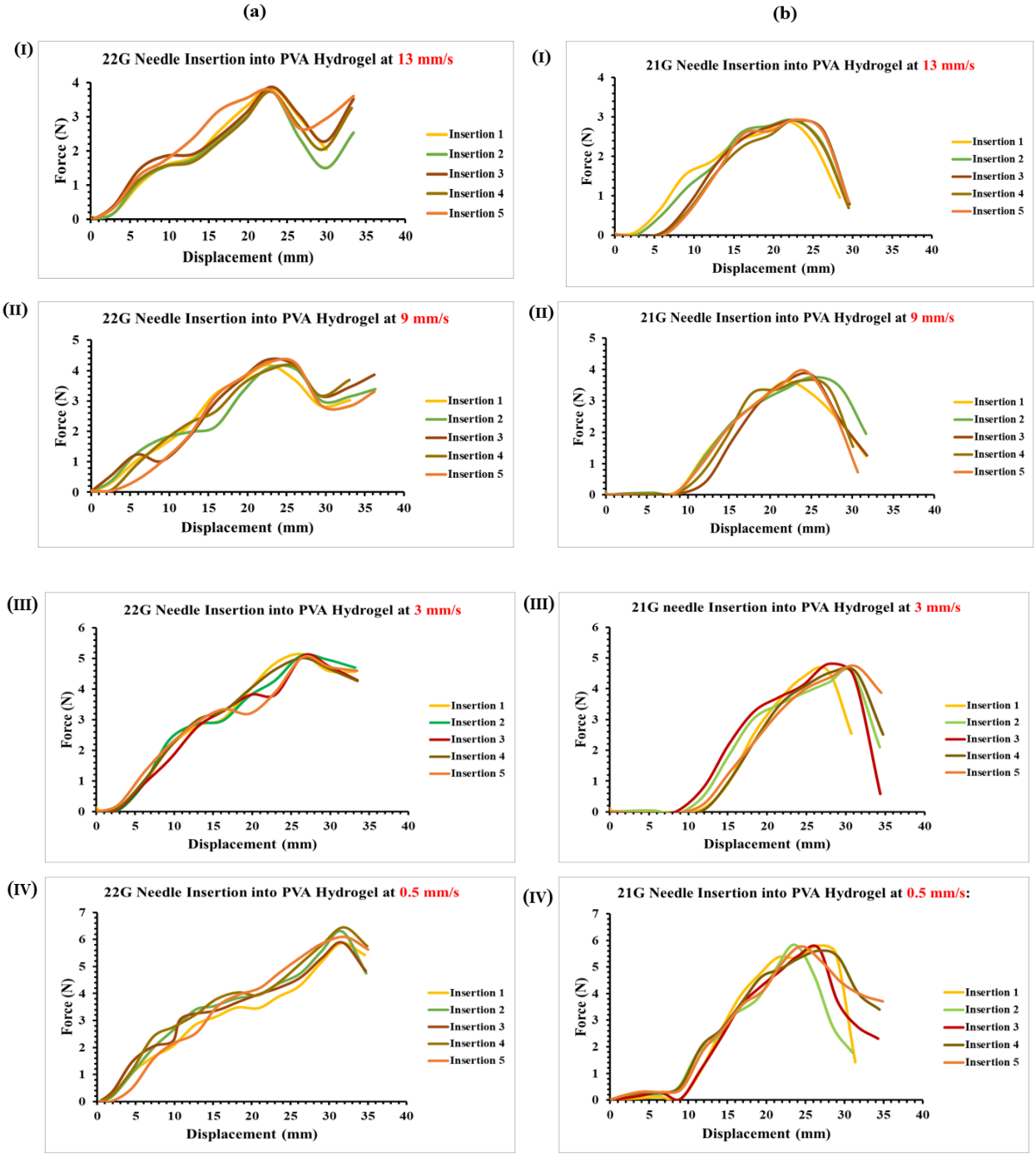

Figure 6.4: (a) 22G and (b) 21G needle insertions into a reproducible phantom material, PVA hydrogel, at speeds of 13 mm/s, 9 mm/s, 3 mm/s, and 0.5 mm/s.

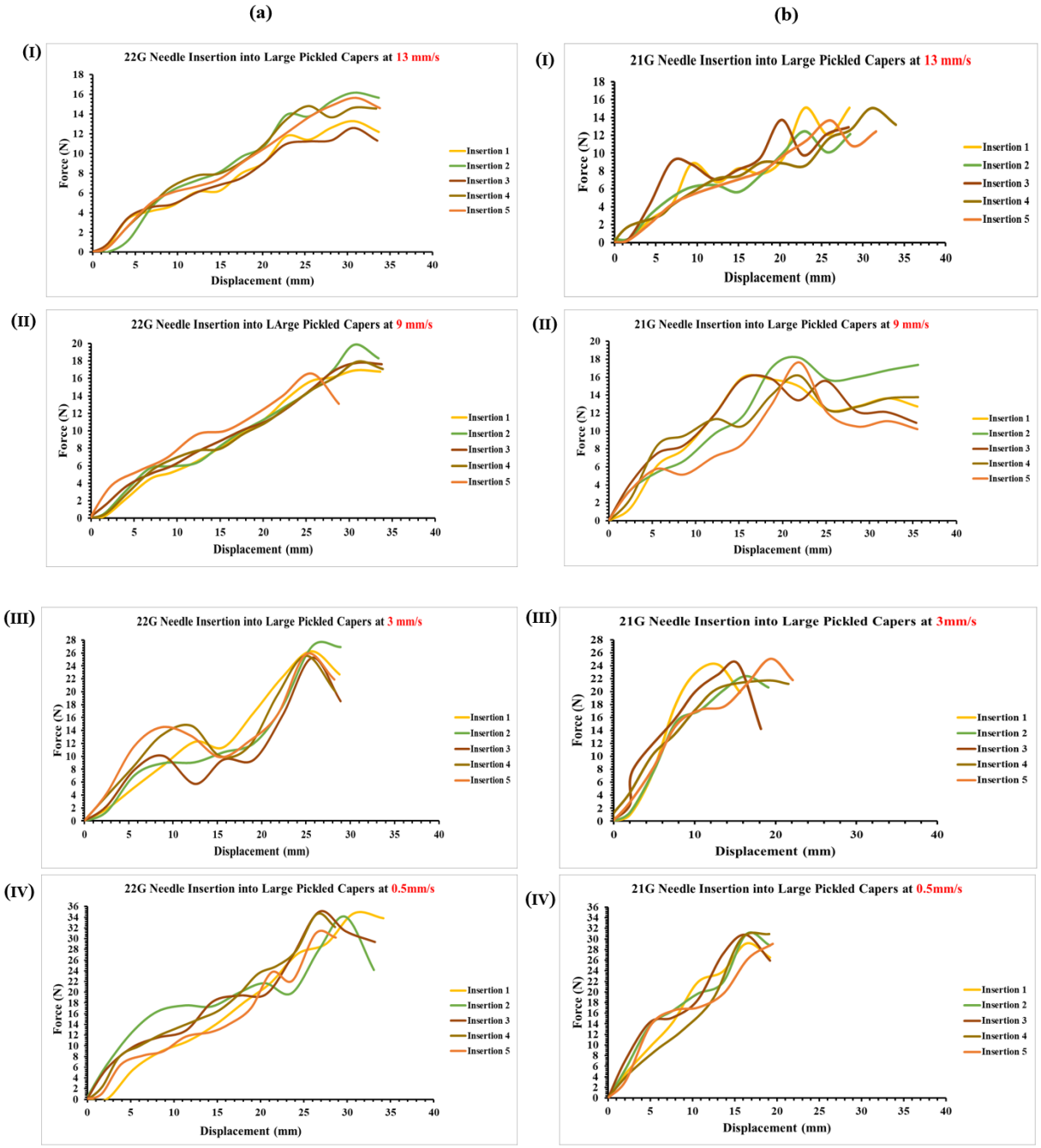

Figure 6.5: (a) 22G and (b) 21G needle insertion into large-pickled capers, a generic mimic of lymph nodes, at speeds of 13 mm/s, 9 mm/s, 3 mm/s, and 0.5 mm/s.

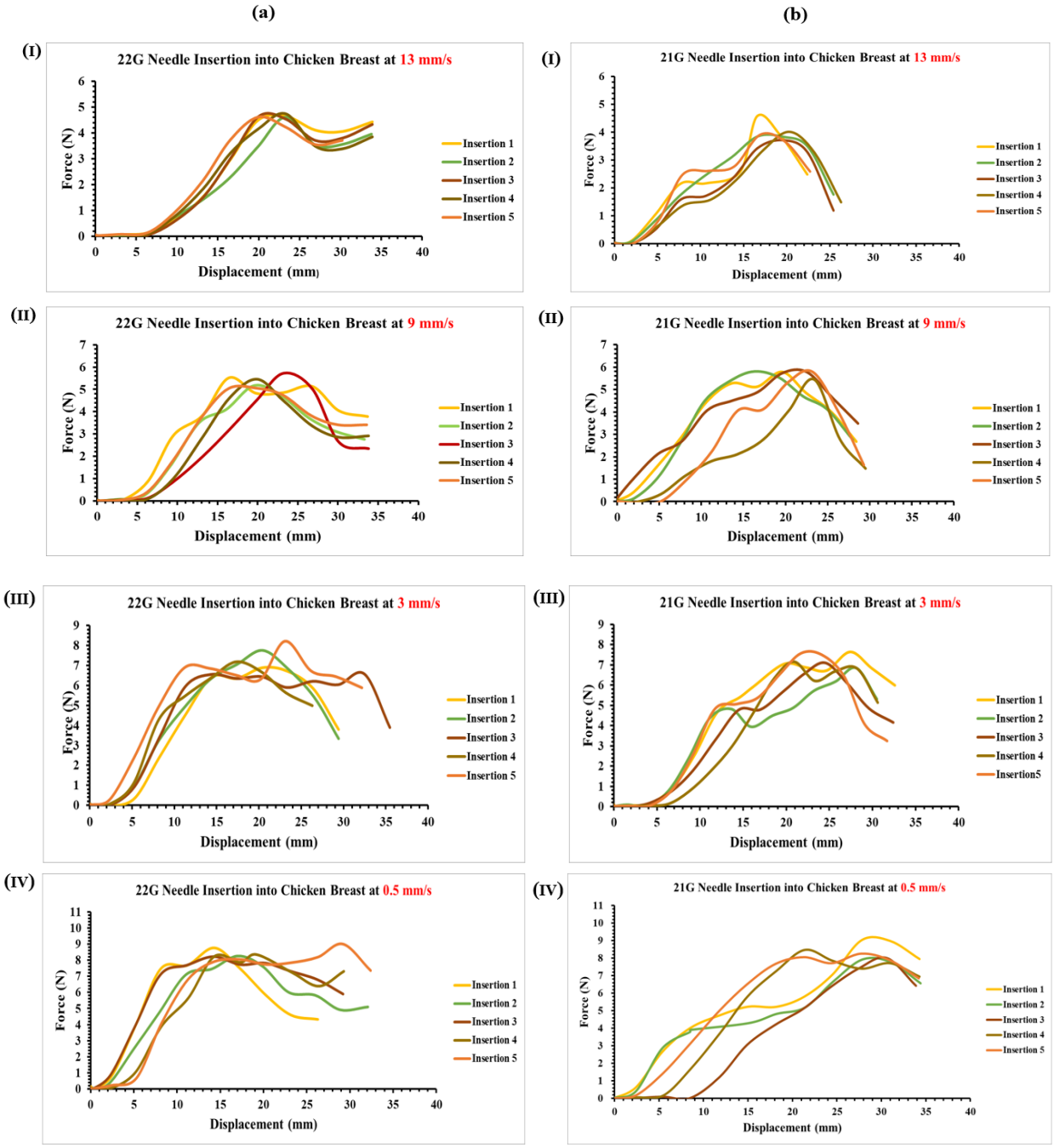

Figure 6.6: (a) 22G and (b) 21G needle insertions into a generic soft material, chicken breast, at speeds of 13 mm/s, 9 mm/s, 3 mm/s, and 0.5 mm/s.

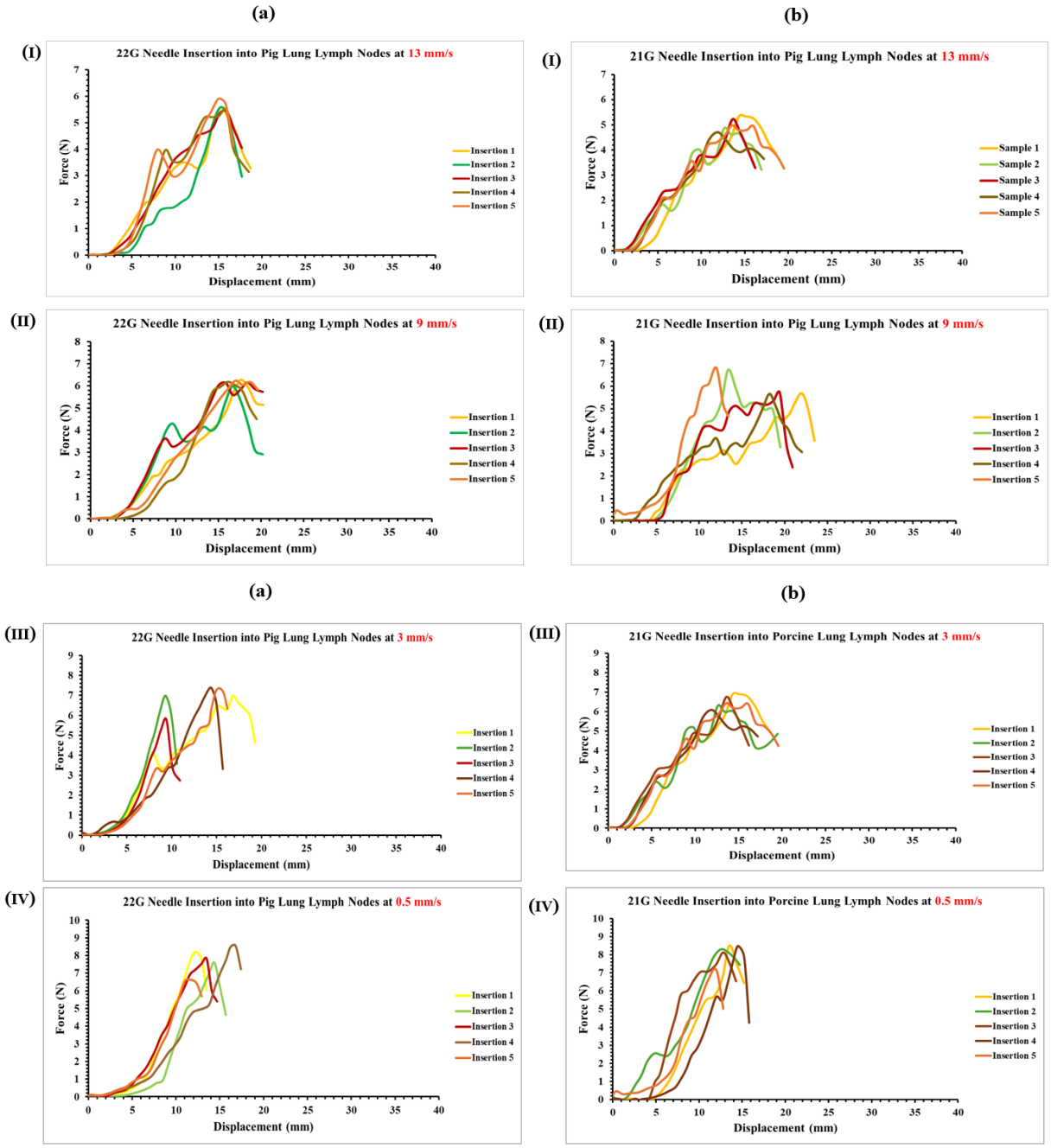

Figure 6.7: (a) 22G and (b) 21G needle insertion into porcine lung lymph nodes, at speeds of 13mm/s, 9mm/s, 3mm/s, and 0.5mm/s.

Figures 6.8–6.11 present the mean force–displacement profiles for the steady-state insertion phase (Phase III) of 21G and 22G needles inserted into different soft materials at insertion speeds of 13 mm/s, 9 mm/s, 3 mm/s, and 0.5 mm/s, respectively. These profiles were used to compare the effects of needle gauge, insertion speed, and material type on steady-state insertion mechanics.

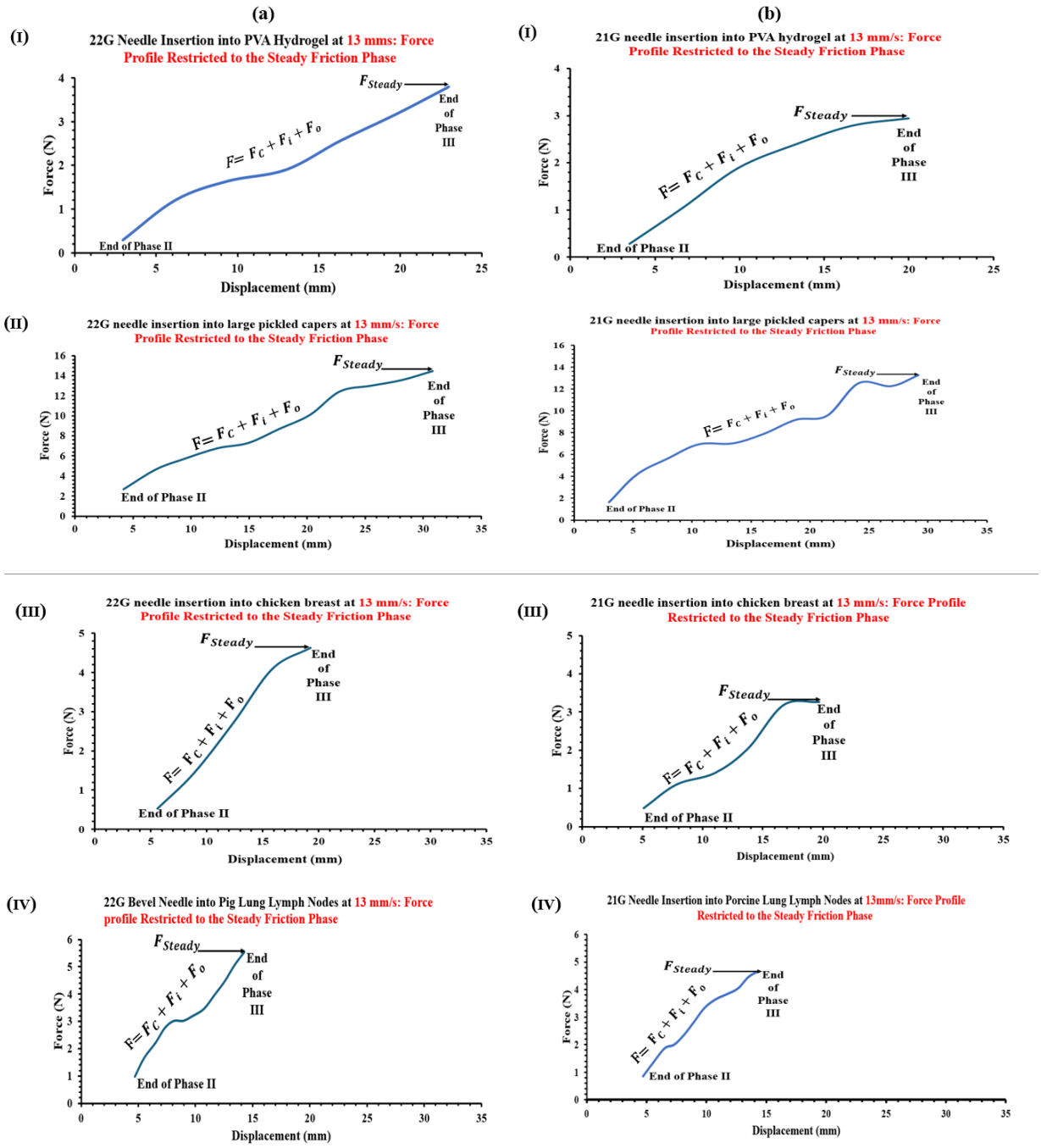

Figure 6.8: Steady-state (Phase III) force-displacement profiles for 22G (a) and 21G (b) EBUS-TBNA needle insertions into (I) PVA hydrogel, (II) chicken breast, (III) large pickled capers, and (IV) porcine lymph nodes at 13 mm/s.

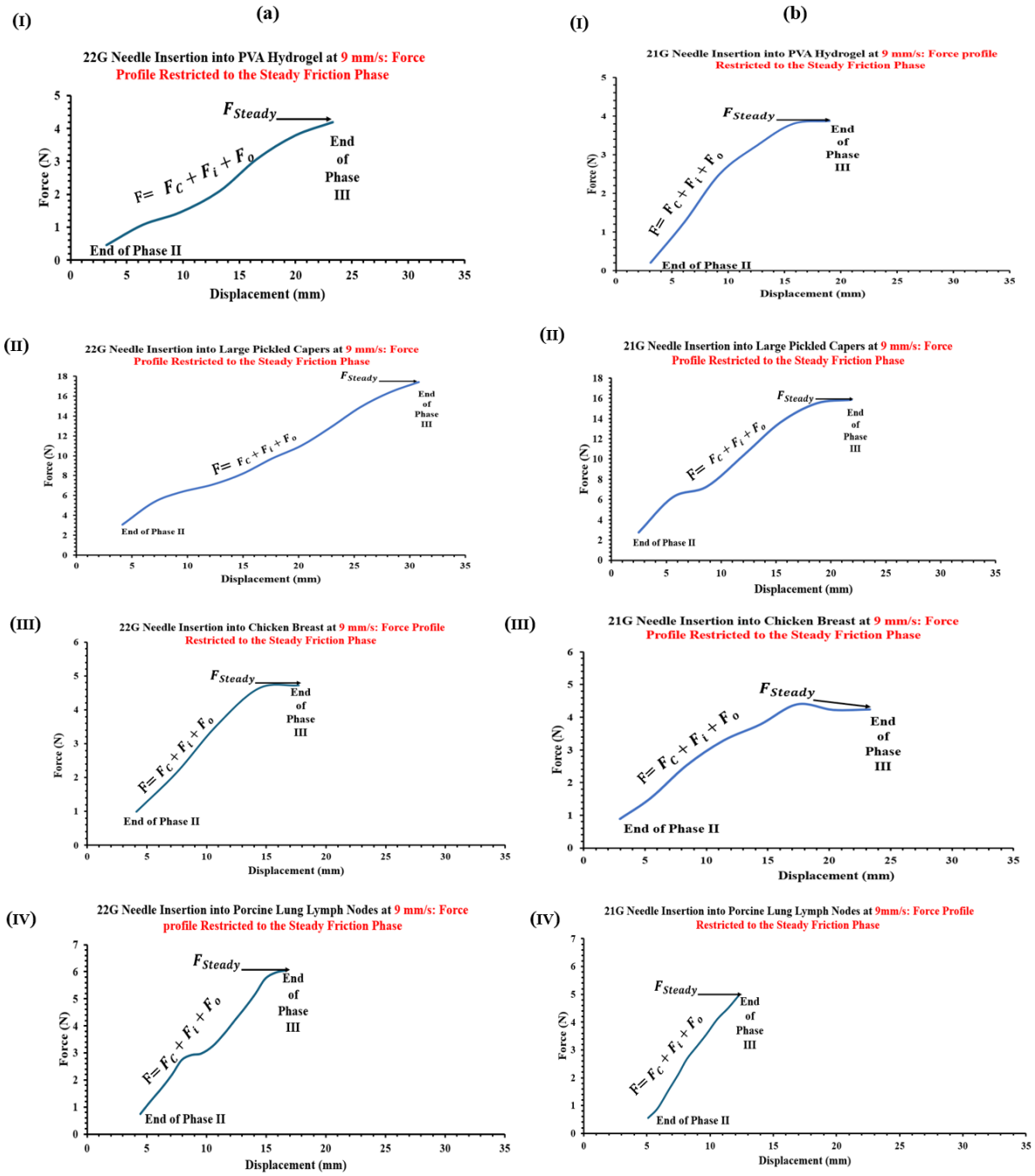

Figure 6.9: Steady-state (Phase III) force-displacement profiles for 22G (a) and 21G (b) EBUS-TBNA needle insertions into (I) PVA hydrogel, (II) chicken breast, (III) large pickled capers, and (IV) porcine lymph nodes at 9 mm/s.

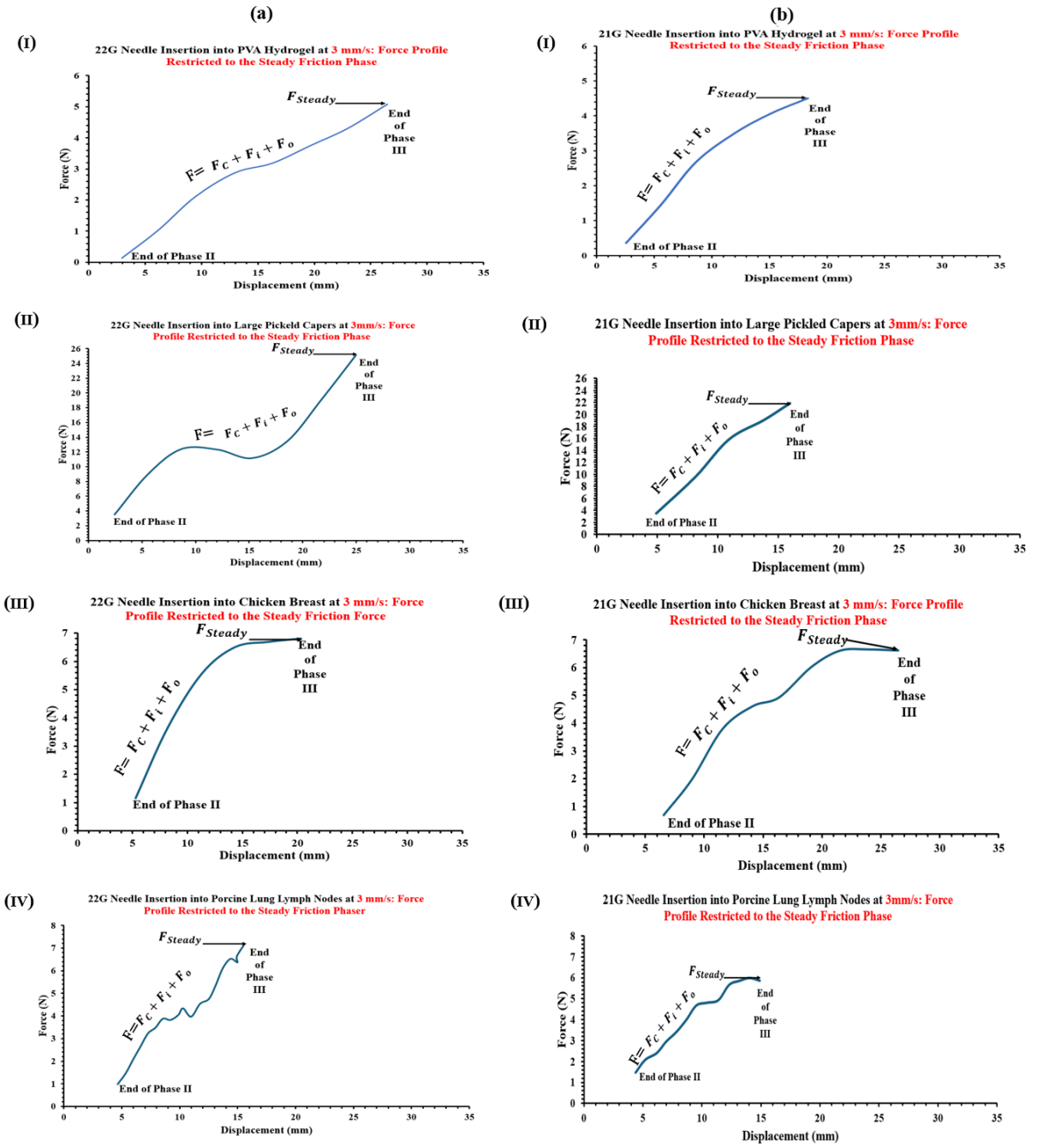

Figure 6.10: Steady-state (Phase III) force-displacement profiles for 22G (a) and 21G (b) EBUS-TBNA needle insertions into (I) PVA hydrogel, (II) chicken breast, (III) large pickled capers, and (IV) porcine lymph nodes at 3 mm/s.

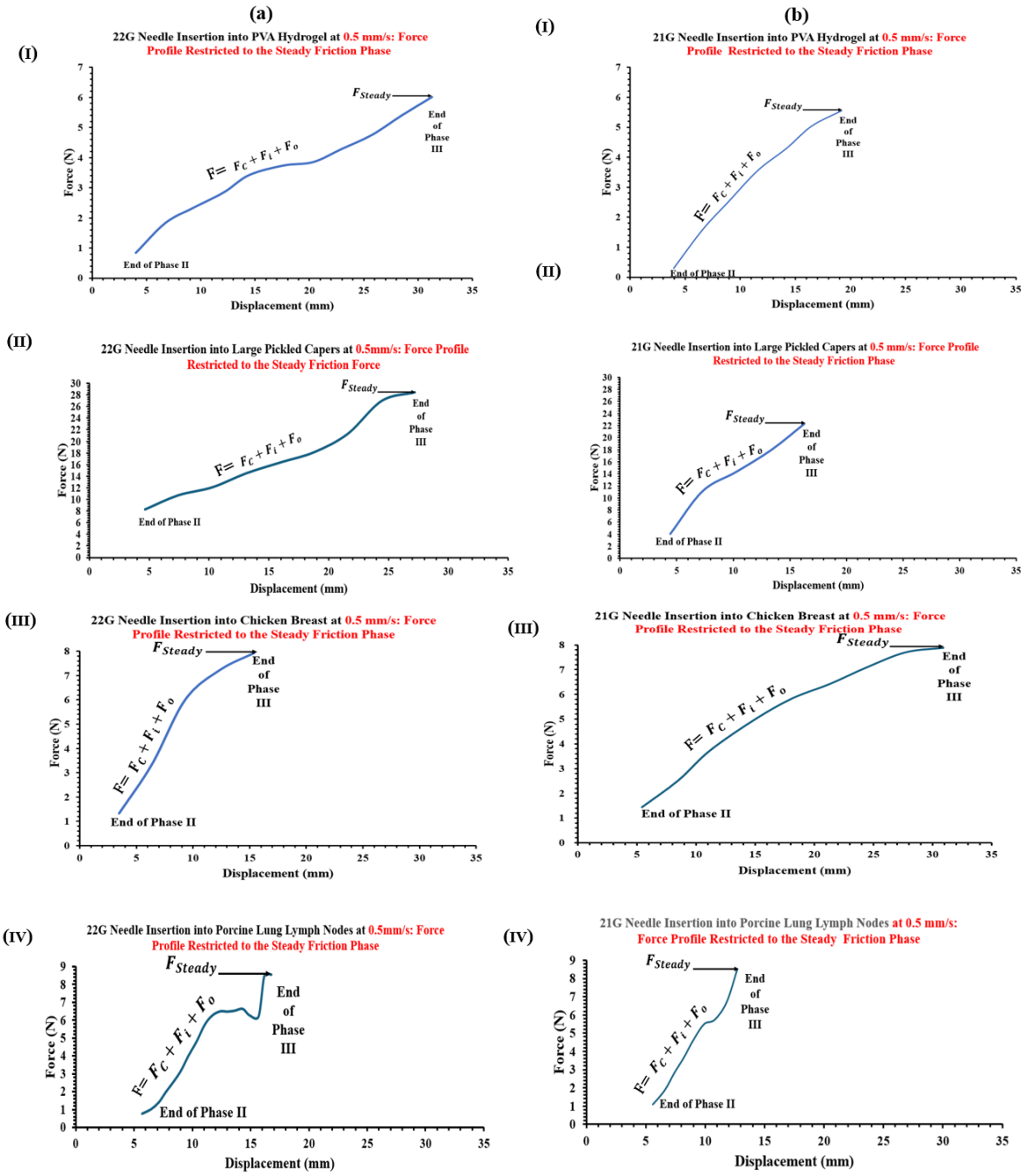

Figure 6.11: Steady-state (Phase III) force-displacement profiles for 22G (a) and 21G (b) EBUS-TBNA needle insertions into (I) PVA hydrogel, (II) chicken breast, (III) large pickled capers, and (IV) porcine lymph nodes at 0.5 mm/s.

The following figures present only the steady-state insertion phase (Phase III). During this phase, the measured insertion force comprises the cutting force (F_C), the internal friction force (F_i), and the outer friction force (F_O), reaching a maximum value F_1 at the end of Phase III.

Upon needle exit (Phase IV), the remaining force reduces to the residual outer friction force, $F_2 = F_O$.

Force–displacement (F–D) analysis was conducted to investigate the mechanical interaction between 21G and 22G EBUS-TBNA needles and a range of soft materials at controlled insertion speeds. The objectives of this analysis were to identify the characteristic phases of the needle insertion process, quantify the effects of needle gauge and insertion speed on insertion forces, and evaluate the influence of material properties on needle–tissue interaction.

Figures 6.4–6.7 present the complete F–D profiles for 21G and 22G needles inserted into PVA hydrogel, large pickled capers, chicken breast, and porcine lung lymph nodes at insertion speeds of 13, 9, 3, and 0.5 mm/s. These materials were selected to span a broad range of mechanical behaviours, from the homogeneous, reproducible properties of PVA hydrogel to the heterogeneous structure of biological tissues such as porcine lung lymph nodes. Despite differences in material properties, needle gauge, and insertion speed, the F–D profiles showed similar overall trends, allowing the needle insertion process to be divided into four distinct phases.

As the primary objective of this study was to characterise the steady-state insertion mechanics, the subsequent analysis focuses on Phase III, corresponding to the steady-state shaft insertion stage. During this phase, the measured insertion force is governed by the combined contribution of the cutting force (F_C), the internal friction force (F_i), and the outer friction force (F_O). The force increases progressively throughout Phase III and reaches the peak insertion force (F_1) at the completion of shaft advancement. Following needle exit (Phase IV), the measured force decreases to the residual force (F_2), which represents the outer friction force (F_O). Consequently, Figures 6.8–6.11 present only the steady-state insertion phase (Phase III) for insertion speeds of 13, 9, 3, and 0.5 mm/s, thereby facilitating direct comparison of the steady-state insertion behaviour across different materials and needle gauges.

Although the overall force–displacement behaviour was consistent across all experimental conditions, variations in force magnitude and force-development characteristics were observed as a function of insertion speed, needle gauge, and material type. These differences are discussed in the following sections.

Insertion Phases

The force–displacement profiles shown in Figures 6.4 – 6.7 demonstrate that needle insertion can be divided into four mechanically distinct phases. Although the magnitude of the measured force varies with needle gauge, insertion speed, and material type, the sequence of mechanical events remained consistent across all experimental conditions.

- **Phase I: Initial Contact and Pre-Penetration Deformation**
  During the initial stage of insertion, the needle tip contacts the material surface, producing local elastic deformation without penetrating. Consequently, the measured force remains relatively low because the material response is governed primarily by elastic compression rather than by cutting or frictional interactions.

- **Phase II: Penetration and Puncture:**
  As the insertion progresses, the force increases non-linearly until the stress beneath the needle tip exceeds the material's fracture resistance, resulting in puncture. The force generated during this stage is dominated by the cutting force (F_C). Immediately after penetration, a slight reduction in force is observed due to elastic recovery of the material and the transition from surface deformation to internal needle advancement.

- **Phase III: Needle Shaft Advancement**:
  After puncture, the needle shaft advances through the material while the needle tip remains fully embedded. This stage marks the steady-state insertion phase, which is considered throughout the remainder of this chapter. During Phase III, the measured insertion force arises from the combined contributions of the cutting force (F_C), the internal friction force (F_i), and the outer friction force (F_O). As insertion depth increases, the contact length between the needle shaft and the surrounding material increases, leading to a progressive rise in frictional resistance and insertion force until the peak insertion force (F_1) is reached at the end of the insertion phase.
  For the 22G needle, a distinct change in the rate of force development was consistently observed at an insertion depth of approximately 30 mm. Beyond this depth, insertion mechanics were increasingly dominated by shaft friction rather than cutting at the needle tip. This behaviour is attributed to the increasing shaft–material contact length,

viscoelastic recovery of the material surrounding the insertion track, and partial closure of the material around the needle shaft. Owing to its smaller diameter, the 22G needle appeared more sensitive to frictional effects per unit contact area than the 21G needle.

- **Phase IV: Needle Exit**:
  During withdrawal, the needle tip exits the material while part of the shaft remains embedded. Consequently, the measured force decreases to the residual force (F_2), which corresponds to the remaining outer friction force (F_O) acting on the embedded portion of the needle shaft.

Effect of Needle Gauge, Insertion Speed and Material Type on Insertion Force

The steady-state force–displacement profiles showed that needle gauge, insertion speed, and material properties all significantly affected insertion mechanics.

Across most materials and insertion conditions, the 21G needle generated higher insertion forces than the 22G needle. This behaviour is primarily attributed to its larger outer diameter, which increases both the cutting resistance at the bevel tip and the frictional interaction between the needle shaft and the surrounding material due to the greater contact surface area.

Insertion speed also had a pronounced effect on force development. Lower insertion speeds generally produced higher steady-state insertion forces and a more gradual rise in force during shaft advancement. This trend was particularly evident in chicken breast and porcine lung lymph node tissues. At lower insertion speeds, the longer interaction time between the needle and the surrounding material promotes greater viscoelastic deformation, material recovery, and adhesion around the needle shaft, thereby increasing frictional resistance. Conversely, higher insertion speeds shorten the duration of needle–sample interaction, limiting viscoelastic recovery and resulting in lower insertion forces.

These observations are consistent with the viscoelastic behaviour of soft biological materials, whose mechanical response depends on both the loading rate and the deformation history. The results therefore demonstrate that insertion speed influences both the cutting and frictional components of the insertion force during EBUS-TBNA needle insertion.

From a clinical perspective, reducing insertion force is desirable because excessive forces may increase tissue trauma, deformation, and procedural difficulty during EBUS-TBNA. Lower insertion forces are expected to improve needle controllability and targeting accuracy during lymph node sampling, while reducing deformation of the surrounding pulmonary tissue. These characteristics are particularly relevant to robot-assisted bronchoscopy and image-guided biopsy procedures, where accurate needle placement is essential.

Material properties also played a significant role in determining insertion mechanics. PVA hydrogel exhibited smooth, highly repeatable force–displacement profiles, reflecting its homogeneous and isotropic structure. By contrast, chicken breast and porcine lung lymph nodes showed greater variability, particularly during puncture and the early stages of shaft advancement, owing to differences in tissue stiffness, fibre orientation, hydration, and structural heterogeneity.

Large pickled capers exhibited behaviour intermediate between that of the homogeneous phantom material and biological tissues. Their force profiles demonstrated greater puncture resistance than those of PVA hydrogel while remaining more repeatable than those of porcine lung lymph nodes, supporting their suitability as a simplified surrogate material for preliminary needle insertion studies.

The observed differences between materials highlight the importance of selecting appropriate surrogate materials when evaluating needle insertion mechanics under controlled laboratory conditions. Variations in insertion behaviour arise from the interfacial mechanics between the needle and the surrounding material. During penetration, the bevel tip cuts and fractures the material while the advancing shaft experiences frictional sliding governed by surface roughness, contact pressure, and viscoelastic recovery around the insertion track. As insertion depth increases, partial closure of the material around the shaft generates additional normal stresses, increasing frictional resistance. Local variations in material microstructure and contact conditions further contribute to the variability observed between repeated insertions.

The greatest variability occurred during the puncture phase, reflecting sensitivity to local material properties and initial contact conditions. Following penetration, the force–displacement profiles became more consistent, indicating stable shaft–material interaction. The

excellent repeatability observed in the PVA hydrogel further confirms its suitability as a reproducible tissue-mimicking phantom for controlled needle-insertion experiments.

6.3.2 Force Calculation

For clarity, the force definitions used in this study are reiterated below:

F_1: peak insertion force during shaft advancement (end of Phase III)

F_2: residual force after needle exit representing outer friction (F_O)

F_C: cutting force at puncture (Phase II)

F_i: internal friction force during shaft insertion

At the point of penetration during Phase II and at the end of Phase III, the total insertion force, F_1, is composed of the cutting force, F_C, the internal friction force, F_i, and the outer friction force, F_O. After the needle tip exits the material during Phase IV, cutting no longer occurs ($F_C = 0$), and the tissue sample within the needle becomes stationary. Consequently, the remaining insertion force corresponds to the outer friction force only, such that:

$$F_2 = F_O \tag{6.3}$$

The difference between the peak insertion force and the residual force is therefore:

$$F_1 - F_2 = F_C + F_i \tag{6.4}$$

Since direct measurement of F_C and F_i was not experimentally feasible, a linear extrapolation method was used to estimate these force components from the insertion force profiles obtained at different sample depths. Because the tested samples had different insertion depths (d_1, d_2, d_3), the value of $F_1 - F_2$increased with increasing tissue depth due to the progressive contribution of internal friction.

Assuming the cutting force remains approximately constant during insertion, the relationship between $(F_C+F_i)$and insertion depth can be expressed as:

$$F_C + F_i = F_{C0} + f_i d \tag{6.5}$$

where the intercept at zero insertion depth represents the cutting force, F_{C0}, and the slope represents the internal friction coefficient, f_i.

Figure 6.12 illustrates the linear extrapolation method used to determine internal friction and cutting forces for PVA hydrogel, large pickled capers, chicken breast, and porcine lymph nodes from the lung.

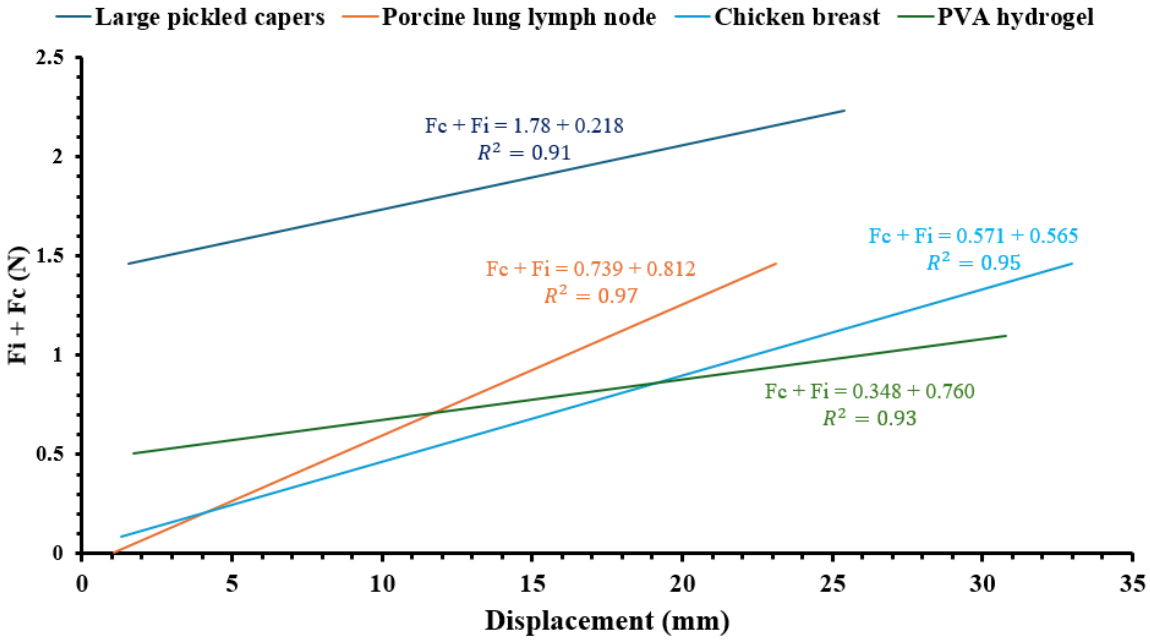

Figure 6.12: Inner friction and cutting force obtained by linear extrapolation for PVA hydrogel, large pickled capers, chicken breast and porcine lung lymph node.

The results demonstrate that the difference in insertion force after penetration (F_1-F_2)increases with insertion depth across all tested materials, indicating that internal friction becomes progressively more significant as the length of material retained within the needle increases. Conversely, the cutting force contributes a relatively constant offset throughout insertion.

Among the tested materials, large pickled capers exhibited the highest internal friction forces, indicating greater resistance to tissue motion within the needle lumen. Porcine lymph nodes exhibited the next-highest frictional behaviour, consistent with their fibrous, heterogeneous internal structure. Chicken breast exhibited intermediate behaviour, whereas the PVA hydrogel demonstrated the lowest frictional resistance, owing to its homogeneous composition and smoother internal interactions with the needle surface. The observed trends align with the peak insertion forces measured during penetration, suggesting that material microstructure strongly influences both cutting and frictional behaviour during insertion.

The linear relationships between $(F_C+F_i)$and insertion depth exhibited coefficients of determination (R^2) of approximately 0.9, indicating strong agreement between the experimental data and the proposed linear model across repeated insertions at each speed and material condition.

Values of F_1, F_2, F_i, and F_C for the 21G and 22G needles at 13 mm/s are summarised in Figure 6.13 and Table 6.1.

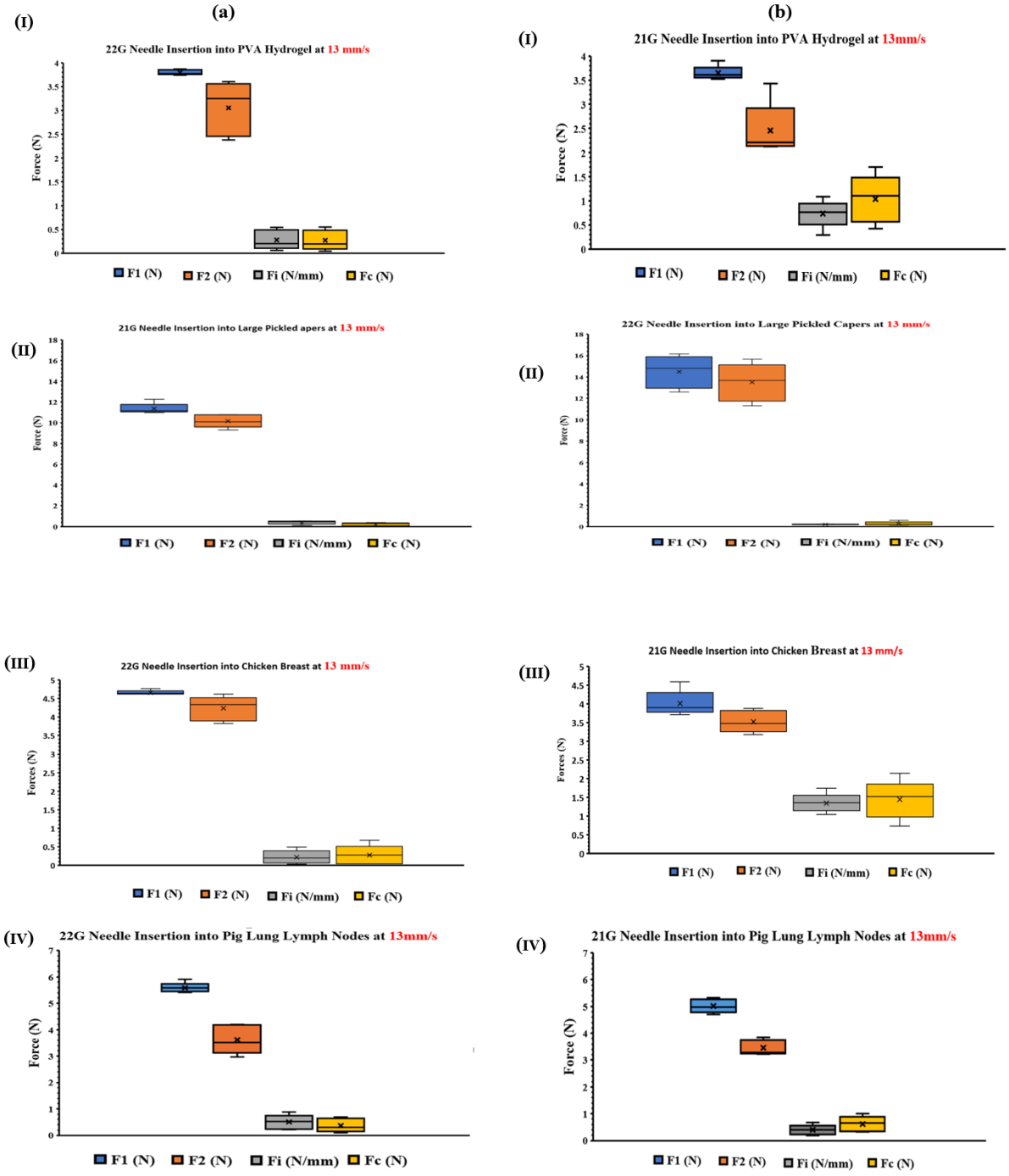

Figure 6.13: (a) 22G and (b) 21G needle insertion into four soft materials at 13 mm/s, with a comparison of the values of force F_1, F_2 (F_0), F_i, and F_C at 13 mm/s. (I) 22G and 21G needle insertion into PVA hydrogel; (II) 21G and 22G needle insertion into large pickled caper ; (III) 22G and 21G needle insertion into chicken breast; and (IV) 22G and 21G needle insertion into lymph node.

Table 6.1: Comparison of forces profile between the 21G and 22G needle insertions into PVA hydrogel, chicken breast, large pickled capers, and porcine lung lymph node at 13 mm/s, showing a higher peak force F_1 and outside friction force F_2 when using the 22G needle, and a higher inner friction F_i and cutting force F_c when using 21G needle.

Needles	Forces	PVA Hydrogel	Large Pickled Capers	Chicken Breast	Lymph Nodes
21G	**F_1 (N)**	3.79	14.51	4.66	5.59
	(STD)	(0.15)	(0.52)	(0.03)	(0.26)
	F_2 (N)	3.06	13.49	4.23	3.62
	(STD)	(0.55)	(0.62)	(0.11)	(0.27)
	F_i (N/mm)	0.581	3.3	0.73	1.35
	(STD)	(0.28)	(0.18)	(0.26)	(0.19)
	F_c (N)	1.28	0.29	1.44	0.62
	(STD)	(0.49)	(0.15)	(0.51)	(0.28)
22G	**F_1 (N)**	3.65	11.36	4.01	5.02
	(STD)	(0.06)	(0.53)	(0.06)	(0.19)
	F_2 (N)	2.46	10.15	3.53	3.46
	(STD)	(0.57)	(0.76)	(0.33)	(0.54)
	F_i (N/mm)	0.39	1.78	0.57	0.74
	(STD)	(0.20)	(0.03)	(0.18)	(0.27)
	F_c (N)	0.76	0.22	0.81	0.57
	(STD)	(0.21)	(0.17)	(0.26)	(0.26)

Overall, the 21G needle generally produced higher peak insertion forces due to its larger diameter and greater contact area with the material. However, variations in internal friction and

cutting forces depended on both material type and insertion conditions, indicating that needle–material interaction is governed by multiple mechanical factors beyond needle diameter alone.

Figure 6.14, further demonstrates the relationship between insertion speed and internal friction force across all tested materials. Across most materials, higher frictional forces were observed at lower insertion speeds, with friction decreasing progressively as insertion speed increased. Large pickled capers consistently exhibited the highest frictional forces, whereas PVA hydrogel showed the lowest values. Chicken breast and porcine lymph nodes demonstrated intermediate behaviour, although lymph nodes showed greater variability and a more pronounced reduction in friction force at higher insertion speeds.

Several force measurements (Figure 6.14-6.15) exhibited relatively large standard deviations, particularly for biological materials such as porcine lymph nodes and chicken breast. The larger error bars observed in these materials indicate substantial variability across repeated insertions. This variability is likely attributable to the heterogeneous internal structure of biological tissue, including variations in fibre orientation, local stiffness, tissue density, hydration, and internal composition.

Additional variability may arise from minor differences in insertion angle, local contact conditions, and the needle's position relative to internal tissue structures. These variations are particularly pronounced during the puncture phase, when local material failure mechanisms strongly influence the measured peak force. After penetration, the force–displacement profiles become more consistent, indicating a more stable interaction between the needle shaft and the surrounding material.

In contrast, PVA hydrogel exhibited considerably smaller error bars and greater repeatability, owing to its homogeneous and reproducible mechanical properties. The relatively low variability observed in PVA hydrogel confirms its suitability as a reproducible phantom material for controlled needle-insertion experiments.

Overall, the results demonstrate that insertion mechanics are governed by a complex interplay of needle geometry, insertion speed, and material properties. Biological tissues exhibited greater variability than phantom materials due to their heterogeneous internal structure, whereas PVA hydrogel provided highly repeatable force measurements suitable for controlled

experimental analysis. The findings further demonstrate that insertion speed significantly affects cutting and frictional behaviour, with important implications for the optimisation of EBUS-TBNA procedures, needle design, and robotic-assisted biopsy systems to reduce tissue trauma and improve procedural precision.

The maximum insertion force measured during the experiment was 14.51 N for the 21G needle inserted into large pickled capers. Although the experimental needles were manufactured from nitinol, which exhibits superelastic behaviour under sufficiently high stresses, this behaviour is typically reported to occur at approximately 300–600 MPa, depending on the alloy composition, heat treatment, and manufacturing process [205]. The measured insertion loads were considered insufficient to initiate a stress-induced martensitic transformation. Consequently, the needle was assumed to remain within its linear elastic (austenitic) regime throughout all experiments, and the effects of superelasticity were neglected. This assumption is further supported by the absence of any observable permanent deformation or residual curvature of the needle following repeated insertions. The experimentally justified assumption of linear needle behaviour was subsequently adopted in the finite element model presented in Chapter 7, where the needle was represented as a discrete rigid body.

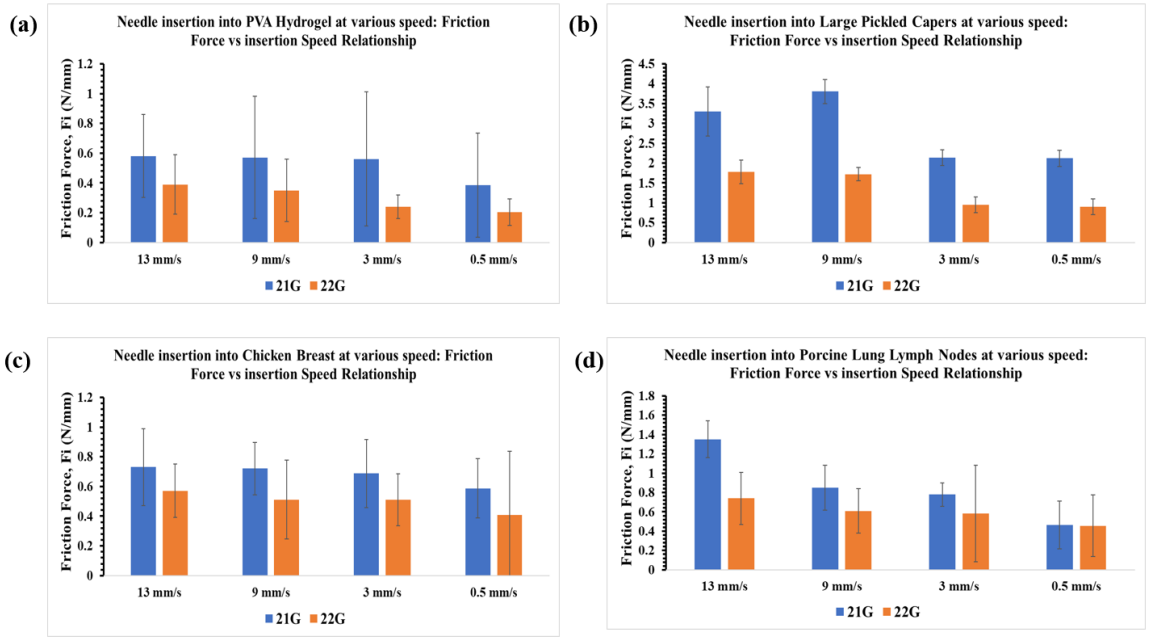

Figure 6.14: Friction force vs insertion speed relationship at various speeds: (a) PVA hydrogel; (b) large-pickled capers; (c) chicken breast; (d) porcine lung lymph node. The relationship indicates that the frictional force increases with higher insertion speeds.

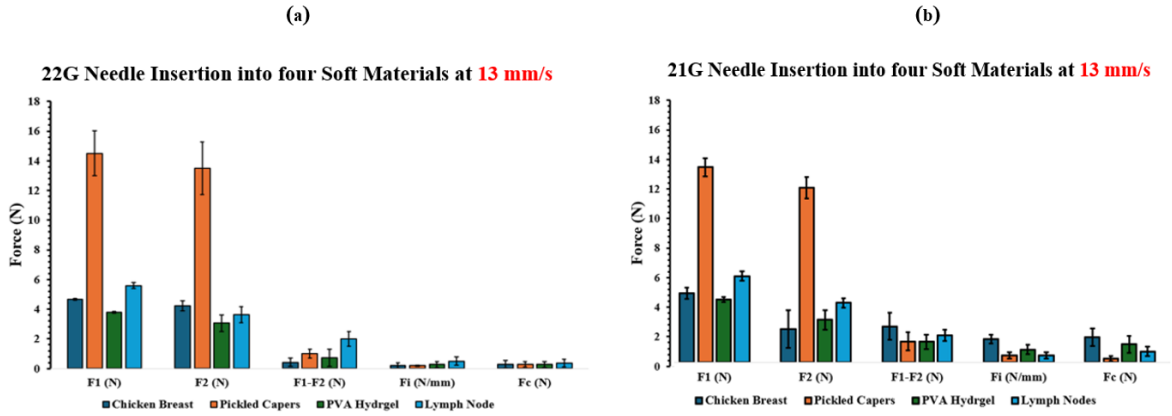

Figure 6.15: (a) 22G and (b) 21G needle insertions into four soft materials, comparing the force profiles.

6.3.3 Stress and Coefficient of Friction Calculation

The inner coefficient of friction can be defined as the ratio of friction force to the normal force, or the ratio of friction stress to normal stress, per unit length, Equation (6.4), assuming that the distributions of inner friction and normal force are uniform across the entire inner surface [206].

$$\mu = \frac{f_{fi}}{f_{Ni}} = \frac{\sigma_{fi}}{\sigma_{Ni}} \tag{6.4}$$

The inner friction stress, σ_{fi}, also known as the inner shear stress, was obtained by dividing F_i by the needle's inner circumference. The normal stress, σ_N, of the tissue was calculated by estimating the stress required to uniformly compress the tissue in the radial direction from the original core diameter, D_{co}, to the compressed core diameter, D_{cc}, under the plane stress condition [207]. The original core diameter equals the needle's outer diameter, $D_{co} = D_o$, while the compressed core diameter is its inner diameter, $D_{cc} = D_i$ [207]. The diameter of the hole, D_h, left in the soft material was assumed to equal the needle's outer diameter, $D_h = D_o$. By assuming that the radial stress was uniform throughout the domain, the normal stress would be the same as the radial stress, $\sigma_N = \sigma_r$. Hence, the general solution for σ_r in the radial direction at distance, r, from the centre is given by [208]:

$$\sigma_r = C_1 + C_2 r^{-2} \tag{6.5}$$

where C_1 and C_2 are two parameters determined by the boundary conditions.

The radial displacement, Δ, can be expressed as:

$$\Delta = \frac{1}{E}[(1-\nu)C_1 r - (1+\upsilon)C_2 r^{-1}\ ] \tag{6.6}$$

where E is Young's modulus in MPa, and ν is Poisson's ratio.

At r = $\frac{D_h}{2}$, Δ is $\frac{(D_h - D_i)}{2}$. At the centre (r = 0), Δ = 0.

Based on these two boundary conditions, C_1, the radial stress is expressed as:

$$C_1 = \frac{E(D_h - D_i)}{(1-\upsilon)D_h} \tag{6.7}$$

and $C_2 = 0$. (6.8)

Poisson's ratio was set to υ = 0.495 to reflect the incompressibility of most soft materials. Young's modulus was calculated from the shear modulus of the hyperelastic constant of the Ogden model, as given in Chapter 5, Table 5.5, using the formula:

$$E = 2G\ (1+\upsilon) \tag{6.9}$$

where G is the shear modulus in MPa.

The values of the friction stress, normal stress and the coefficient of friction of various soft materials, using the 21G needle at various speeds are presented in Table 6.

Table 6.2: Value of σ_{fi}, σ_{Ni}, and μ using the 21G needle.

Soft Materials		**13 mm/s**	**9 mm/s**	**3 mm/s**	**0.5 mm/s**
PVA	$\boldsymbol{\sigma_{fi}}$**(KPa)**	268.21	214.88	186.05	157.23
	$\boldsymbol{\sigma_{Ni}}$**(KPa)**	433.10	433.10	433.10	433.10
	$\boldsymbol{\mu}$	0.62	0.49	0.43	0.36
Large Pickled Capers	$\boldsymbol{\sigma_{fi}}$**(KPa)**	490.49	282.08	257.93	241.14
	$\boldsymbol{\sigma_{Ni}}$**(KPa)**	34.27	34.27	34.27	34.27
	$\boldsymbol{\mu}$	14.31	8.23	7.53	7.04
Chicken Breast	$\boldsymbol{\sigma_{fi}}$**(KPa)**	572.65	569.72	448.71	351.45
	$\boldsymbol{\sigma_{Ni}}$**(KPa)**	838.50	838.50	838.50	838.50
	$\boldsymbol{\mu}$	0.69	0.67	0.53	0.42
Lymph Node	$\boldsymbol{\sigma_{fi}}$**(KPa)**	440.08	384.64	348.64	314.30
	$\boldsymbol{\sigma_{Ni}}$**(KPa)**	374.92	374.92	374.92	374.92
	$\boldsymbol{\mu}$	1.17	1.02	0.93	0.84

6.4 Summary

The aim of this chapter was to examine the mechanics of needle insertion into lymph nodes, with a focus on rupture events, tissue deformation, and insertion forces. Rupture events were identified experimentally from force-displacement responses during dynamic needle insertion, enabling a qualitative assessment of crack initiation and a comparative analysis of behaviour across materials, needle gauges, and insertion speeds. Quantitative analysis of rupture was not conducted here; however, it is addressed in Chapter 7 using finite-element analysis in Abaqus.

Dynamic experiments were conducted with 21G and 22G EBUS-TBNA needles at four insertion speeds (13 mm/s, 9 mm/s, 3 mm/s, and 0.5 mm/s) in porcine lung lymph nodes and three alternative soft materials, namely PVA hydrogel, large pickled capers, and chicken breast. The results showed that rupture events significantly affect the insertion force profile. Increasing the insertion speed increased the internal frictional force per unit needle length (Fi) but reduced the peak puncture force (F1).

Among alternative materials as tissue substitutes, large pickled capers were unsuitable for lymph nodes because of their structural irregularity and significantly higher insertion forces. PVA hydrogel and chicken breast exhibited soft-tissue-like behaviour, with PVA hydrogel providing the best partial mechanical match. However, none of the materials fully replicated lymph node rupture behaviour, indicating their limited suitability as substitutes.

The experimental methodology was well-suited to addressing the objectives of this chapter, as it enabled controlled, reproducible measurements of needle insertion forces across different needles, speeds, and materials. The main advantage of this methodology is its ability to capture relative differences between frictional and peak forces, whereas its limitations include reliance on simplified loading conditions.

Overall, the main findings of this chapter include confirming the significant impact of rupture events on needle-tissue interaction, identifying insertion speed as a key factor affecting frictional and peak forces, and showing that alternative materials exhibit partial mechanical properties similar to those of lymph nodes, with no complete substitutes found. The study offers comparative insights into needle mechanics and tissue substitutes, informs the numerical

analysis in Chapter 7, and enhances understanding of needle-tissue interaction in EBUS-TBNA procedures.

Chapter 7: Finite Element Modelling of Needle Insertion into Soft Materials

7.1 Introduction

This chapter uses 3D FEA to examine how three tip geometries, namely the Olympus single-bevel, double-front-bevel, and Acquire Franseen, affect the force-displacement relationship. It also investigates tissue deformation and separation surfaces to improve force balance, thereby enabling accurate lymph node sampling during biopsy and increasing the tissue sample length within the needle.

The two common issues that can affect the performance of a needle biopsy are needle deflection and tissue deformation [209], [210]. Needle deflection can result from various factors, such as cutting force, frictional force, and tissue pressure, which create unbalanced moments that bend the needle. The cutting force is generated at the needle tip, where the tissue is cut and separated. The separated tissue's contact with the needle tip's bevel face generates a perpendicular force, which can cause needle deflection [211]. The needle-tissue interaction causes a distribution of tissue pressure across the regions of direct contact between tissue and needle, which can result in additional friction force and further exacerbate the deflection [212]. Such deflection can cause the needle to fail or under-sample the targeted lymph node, resulting in a significant impact on clinical outcomes, including lung cancer misdiagnosis and false-negative results [211], [213]

This chapter begins by describing the three needle tip designs used in this work. It then explains the components of the analysis, including the boundary conditions, meshing, and the interaction between the tissue and the needle. The results section presents the study's findings on the Olympus bevel needle and compares them with experimental results. It also compares force, stress, and tissue sample length across different needle types.

7.2 Materials and Methods

7.2.1 Materials

The results of the mechanical characterisation (Chapter 4) and needle insertion (Chapter 6) experiments showed that large pickled capers can no longer serve as geometric mimics of lymph nodes. As a result, the FEA in this chapter is performed using PVA hydrogel, chicken breast, and porcine lung lymph nodes.

7.2.2 Needle tip design

The CAD software SolidWorks (Dassault Systèmes, Vélizy-Villacoublay, France) was used to define the three needle designs studied, namely the Olympus bevel, the double front bevel, and the Acquire Franseen needles (Figure 7.1). The needle tip designs were selected to evaluate geometries proposed for use in the EBUS-TBNA procedure. Based on the results presented in Chapter 6, which showed that the 21G exhibited a higher peak force than the 22G, the three needle tips were defined as 21G to maximise potential tissue yield. The needle length and inner and outer diameters were constant across all designs at 40 mm, 0.61 mm, and 0.84 mm, respectively.

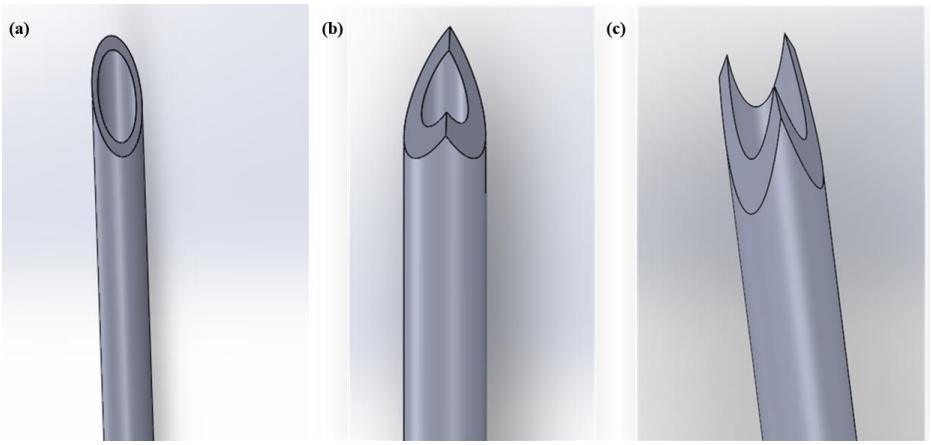

Figure 7.1*:* 21G Needle tip geometries defined in SolidWorks; (a) Olympus bevel needle, (b) double front bevel needle, (c) Acquire Franseen needle.

The bevel tip Figure 7.1(a), manufactured and commercialised by Olympus, is the most common needle tip geometry used in medical procedures, particularly in EBUS-TBNA. It features a single cutting plane, which can be oriented at various angles depending on the intended use. The bevel angle and length can influence the needle's cutting ability and penetration angle. The double-front bevel needle tip, Figure 7.1(b), features two symmetric cutting planes. The Franseen needle, Figure 7.1(c) (Boston Scientific Corporation, Marlborough, MA), is supplied by Acquire and features three symmetrical triangular cutting planes. It enables precise tissue sampling and minimises the risk of needle deflection during biopsies.

For the present study, nitinol, a nickel–titanium alloy widely used in medical devices for its shape-memory and superelastic properties, was used as the material for all experimental needles, consistent with the commercially available Olympus 21G and 22G EBUS-TBNA needles. Although nitinol exhibits nonlinear superelastic behaviour under sufficiently high stresses, the experimental results presented in Chapter 6 indicated that the insertion loads were assumed to be sufficiently low for the needle to remain within its linear-elastic (austenitic) regime. Consequently, the effects of superelasticity were neglected in the present study. As the primary objective of the finite element model was to investigate the mechanical response of the surrounding soft tissue rather than the structural deformation of the needle, the needle was represented as a discrete rigid body. This modelling assumption was considered appropriate because the expected deformation of the needle under the applied loading conditions was negligible relative to that of the surrounding tissue, thereby improving the computational efficiency and numerical stability of the simulations.

7.3 Finite Element Analysis Setup

Finite element analysis was conducted using a 3D coupled Eulerian–Lagrangian (CEL) dynamic explicit model in Abaqus to evaluate the piercing behaviour of 21G needle tip geometries. The objective of the simulation was to compare tissue deformation and insertion performance across designs under controlled and consistent boundary conditions.

The 22G needle geometries were first modelled in SolidWorks and then imported into Abaqus, where they were assembled with the tissue blocks. Two tissue geometries were used, depending on the comparison. For validation against experimental insertion results with the 21G Olympus bevel needle, a tissue block measuring 30 × 15 × 15 mm³ was used. For comparative analysis of the Olympus bevel, double front bevel, and Acquire Franseen designs, a reduced tissue domain of 15 × 10 × 10 mm³ was used to reduce computational cost while maintaining comparable boundary conditions.

To improve computational efficiency, symmetry about the XY plane was exploited, allowing the models to be reduced by half without compromising accuracy.

The soft tissue and void domains were defined using a coupled Eulerian framework. Prior to insertion, the tissue and void regions were represented as Eulerian cuboids, as shown in Figure

7.2. The initial undeformed tissue was defined by the regions BCDESTOP (23 × 15 × 15 mm³) and RSUTLKIJ (8 × 15 × 10 mm³), while the corresponding void regions BCDEFGHI (7 × 15 × 15 mm³) and RSUTPONM (2 × 15 × 10 mm³) were included to allow for material deformation during needle insertion.

The needle geometries were modelled using Lagrangian elements and positioned centrally within the tissue domain, with the tip aligned normal to the tissue surface. The needle was treated as a rigid body, while the tissue was modelled as deformable. This assumption is commonly used in insertion simulations, as it reduces computational cost while maintaining accurate predictions of tissue deformation and stress distribution.

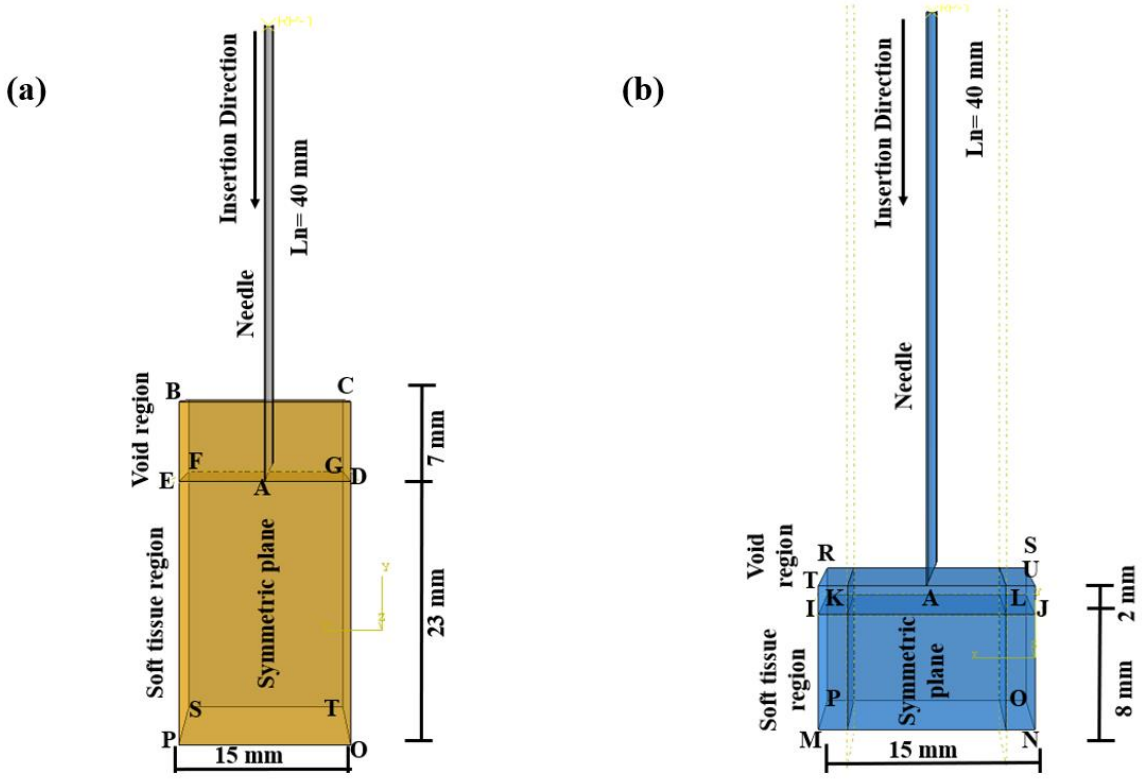

Figure 7.2: Isometric views of the 3D CEL FEA needle-tissue interaction in Abaqus; (a) geometry used for comparison with experimental results; (b) geometry used for comparison of different needle types.

7.3.1 Boundary Conditions

A symmetric boundary condition was applied to the EDOP, Figure 7.2 (a), and TUNM, Figure 7.2 (b), along the z-direction symmetry planes, while allowing deformation within the XY plane. The tissue surfaces contacted by the needle tip prior to insertion were set as free, allowing deformation in all three directions (XYZ plane). The sides and base of the tissue blocks were constrained within a fixed region, termed the "encastre" boundary condition in Abaqus, to represent the biological environment surrounding the lymph node and prevent free movement. This boundary condition allows only vertical displacement in the direction opposite to the needle insertion (positive y-direction).

The needle was constrained in the x- and z-directions while free to move in the y-direction. Needle-into-tissue simulation was conducted using a predefined needle field at translational speeds of 13 mm/s, 9 mm/s, 3 mm/s, and 0.5 mm/s, consistent with the experimental procedures. Needle insertion was modelled as a rigid motion of the assembly, beginning at the initial simulation step and continuing through the final integration step.

7.3.2 Meshing

The discretisation of the computational domain is critical to the accuracy and stability of numerical simulations, particularly for problems involving large deformation, contact, and multiphysics coupling. An insufficiently refined mesh may introduce discretisation errors, whereas an excessively fine mesh can incur prohibitive computational cost without significant improvement in solution accuracy. Therefore, a balance between numerical accuracy and computational efficiency was required in this study.

In principle, mesh convergence is achieved by systematically refining the mesh until changes in key output parameters become negligible. However, in the present work, a full mesh convergence study, including successive global refinements and quantitative convergence plots, was not conducted. This limitation stems from the high computational cost of each simulation. A single needle–tissue insertion analysis required more than 24 hours of computation time, and the study involved multiple geometries, insertion conditions, and parametric variations. Therefore, a full convergence analysis across all cases was not computationally feasible within the scope of this research.

Instead, a mesh-sensitivity-based strategy was adopted during model development to ensure numerical reliability while maintaining computational tractability. This approach focused on refining the mesh in regions where steep gradients in stress, strain, and contact interactions were expected, particularly at the needle–tissue interface.

The tissue and void regions were discretised using an 8-node linear brick element (EC3D8R) within the Abaqus Coupled Eulerian–Lagrangian (CEL) framework. This formulation is well-suited to large-deformation problems and is less sensitive to mesh distortion than purely Lagrangian approaches. As shown in Figure 7.3(a–c), a locally refined mesh with an element edge length of 0.03 mm was used in the vicinity of the needle–tissue interaction zone to accurately capture deformation gradients and contact behaviour. Away from this region, a graded mesh was employed, gradually increasing the element size to 0.1 mm towards the tissue domain boundaries to reduce computational cost while preserving local accuracy.

The puncture needle was modelled using 10-node quadratic tetrahedral elements (C3D10M) with a global element size of 0.03 mm. This element formulation provides improved accuracy for bending- and contact-dominated problems and was selected to capture needle deformation during insertion. The total number of elements in the soft tissue and needle domains was approximately 4,070,000 and 981,213, respectively.

During model development, local mesh-refinement studies were conducted in the region of interest to assess how element size affects the predicted mechanical response. Further refinement beyond the selected configuration produced negligible changes in the qualitative behaviour of key output variables, such as deformation patterns and insertion-force trends, while significantly increasing computational cost. On this basis, the final mesh was chosen as a practical compromise between numerical accuracy and efficiency.

Although a formal mesh convergence curve (e.g., solution variable versus number of elements) is not presented, the adopted refinement strategy ensures that regions with the highest gradients are sufficiently resolved. The graded mesh transition further minimises numerical artefacts arising from abrupt changes in element size. Consequently, the selected mesh is considered mesh-independent for the primary quantities of interest, and the simulation results are deemed numerically stable for comparative analysis across all cases.

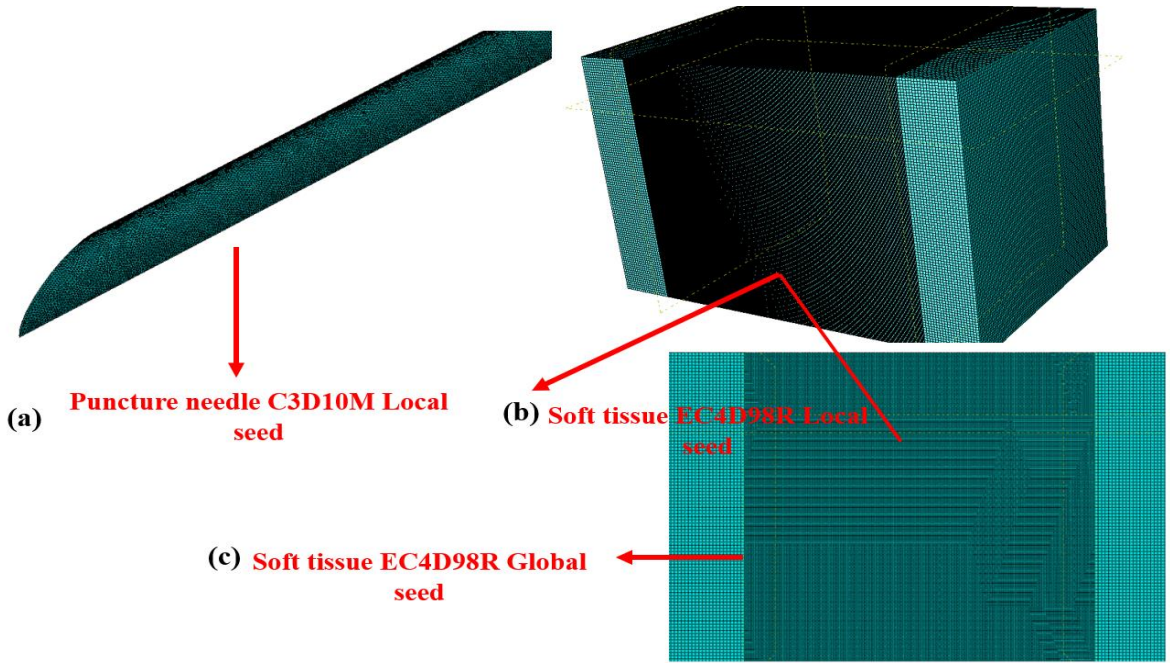

Figure 7.3: Soft tissue and needle meshing: (a) puncture needle local seed size, (b) soft tissue local seed size, (c) soft tissue global seed size.

7.3.3 Contact and Friction

The contact between meshes and bodies was modelled using the penalty contact method and a general contact algorithm, in which the Lagrangian domain of the tissue-needle assembly is treated as the master and the slave.

A coefficient of friction, μ, was applied at the needle-tissue contact in the CEL analysis. μ was derived from the needle insertion experiments described in Chapter 6, while the mechanical properties were obtained through mechanical testing and curve fitting, as described in Chapter 4. Tables 6.1 and 4.1 summarise the hyperelastic model coefficients and μ parameters for each soft material and insertion speed.

7.4 Results

Figure 7.4 outlines the steps of the 3D puncturing process and shows the contact stress between the 21G Olympus bevel and PVA hydrogel, chicken breast, and porcine lung lymph node at 13 mm/s, 9 mm/s, and 3 mm/s. As expected, the initial contact between the needle and tissue produced relatively insignificant stress, and no tissue was cut. Contact stress typically varies

between the tissue and the puncture needle. Compared with PVA hydrogel and chicken breast, porcine lung lymph nodes exhibited the highest contact stress, 30.2 kPa. Moreover, contact stress increased as the insertion speed decreased.

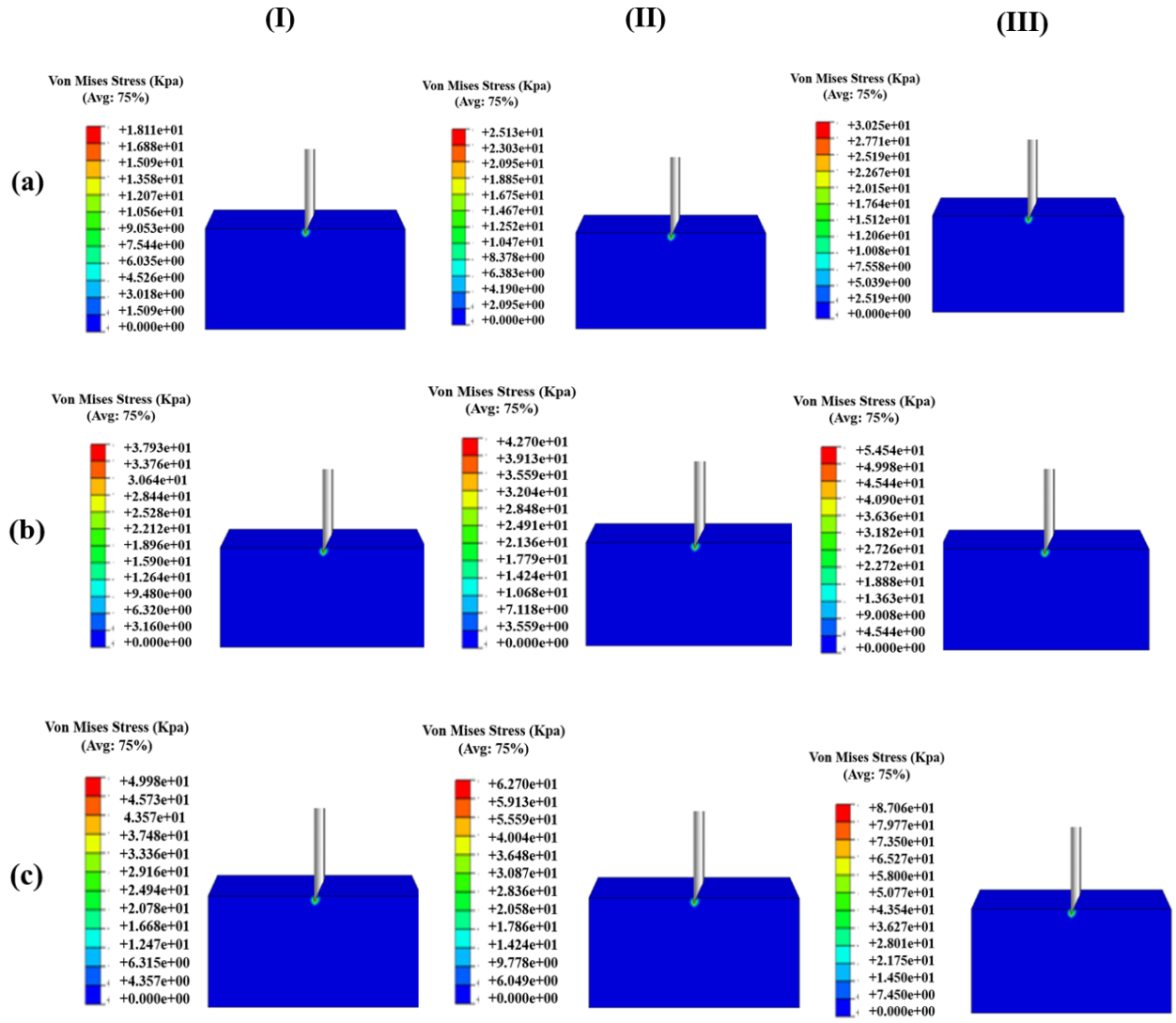

Figure 7.4: 21G Olympus single-bevel needle insertion into soft materials at (a) 13 mm/s, (b) 9 mm/s, and (c) 3 mm/s, showing the contact stress, (I) PVA hydrogel, (II) chicken breast, (III) porcine lung lymph node

The three phases of the complete needle insertion simulation are illustrated in the stress analysis across different puncture depths and needle types. The three stages comprise: the first

contact between the puncture needle and the tissue, the complete entry of the needle tip into the tissue, and the needle's penetration to a depth of 30 mm.

An example of the force-displacement characteristic of the 21G needle inserted into the porcine lung lymph node is shown in Figure 7.5. The FEA reaction force graph exhibits a characteristic multi-phase shape commonly observed in experiments on needle insertion into soft biological tissues (Chapter 6), arising from the sequential interactions between the needle tip, shaft, and tissue.

Initially, in region (a), the needle passes through a void with no assigned tissue properties, producing a negligible reaction force. Point A marks the first contact between the needle tip and the tissue surface (region (b)), after which tissue puncture begins. During this phase, stress builds at the needle tip as the tissue resists penetration, causing a rapid rise in reaction force. As insertion continues (region (c)), the reaction force increases nonlinearly due to tissue deformation ahead of the needle tip and rising friction along the outer wall of the needle shaft. The growing contact length between the needle and tissue increases frictional forces, which dominate the overall reaction force as penetration depth increases. After complete penetration of the needle tip, a local reduction in reaction force is observed; however, this drop is relatively small compared with the overall force magnitude and is therefore less visually pronounced in the force-displacement curve. Continued insertion produces a steady increase in reaction force until the peak force F_1 is reached. As the needle exits the tissue (region (d)), the contact area and frictional force decrease, reducing the reaction force to F_2. The total reaction force, therefore, comprises the force exerted by the needle tip during tissue deformation and the frictional force acting along the needle shaft.

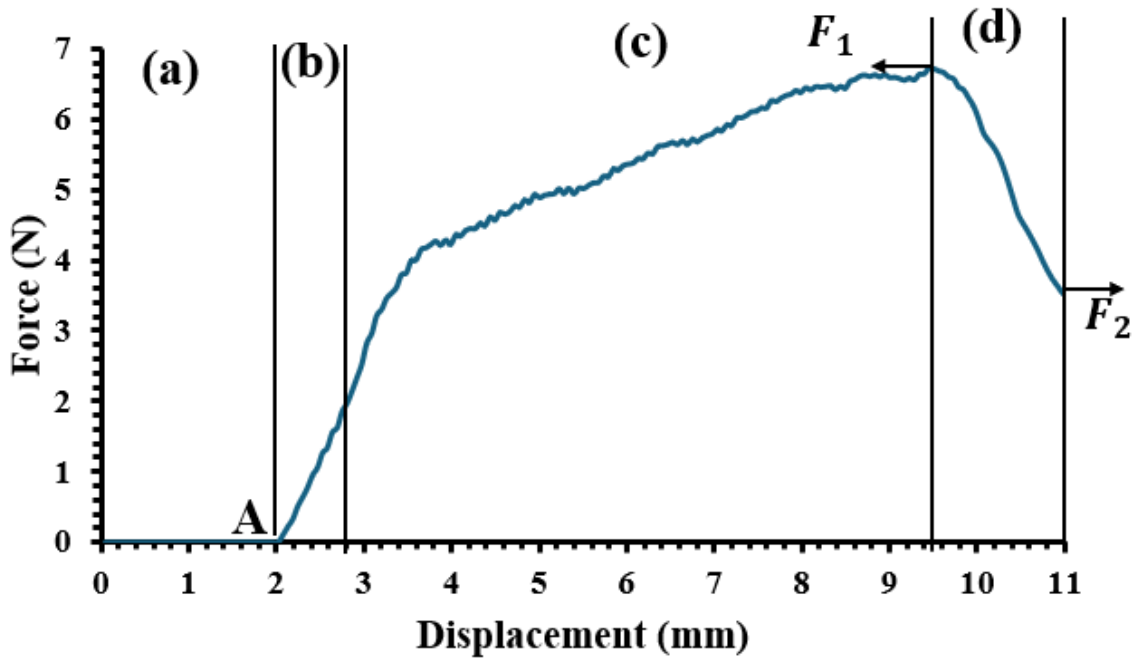

Figure 7.5: 21G bevel needle insertion into the lymph node, modelled with FEA, at different phases. (a) no contact phase, (b) first contact between the needle and the tissue, (c) needle tip travelling through the tissue until reaching the peak force F_1, (d) needle exiting the tissue and producing a force F_2.

The reaction force-puncture depth (i.e., displacement) characteristic obtained was not smooth. As the puncture depth increased, the force-depth curve exhibited multiple sudden drops. Ideally, the curve should be linear. This phenomenon is believed to arise from tissue irregularities observed during the experiments.

7.4.1 21G Olympus Bevel Needle Insertion into Soft Materials: Comparison Between FEA and Experiment

To evaluate the predictive capability of the finite element (FEA) model, simulations of 21G Olympus bevel needle insertion into PVA hydrogel, chicken breast, and porcine lung lymph node tissues were compared with experimental results reported in Chapter 6. Three insertion speeds (13 mm/s, 9 mm/s, and 3 mm/s) and three representative insertion depths (7 mm, 26.5 mm, and 28.5 mm) were analysed, as shown in Figure 7.6 and in Appendices 7.1–7.2. These depths correspond, respectively, to the initial full penetration of the needle tip, an intermediate deformation stage, and the onset of peak tissue resistance prior to needle exit.

The deformation and stress distributions were extracted directly from the finite element outputs using the von Mises stress and displacement fields. As shown, Figure 7.6, the highest deformation levels consistently occur within the needle lumen, where tissue is constrained by the inner wall of the needle. This confinement induces localised compressive deformation, leading to inward material flow into the lumen, consistent with the mechanism of tissue capture during biopsy procedures.

An axial-symmetry boundary condition was applied along the needle's longitudinal axis to reflect the system's geometric symmetry and the controlled alignment of the insertion during testing. As a result, the simulated stress and deformation fields exhibit symmetric distributions across the needle's cross-section. This assumption enables computational efficiency while maintaining sufficient fidelity for predicting macroscopic forces and deformations.

The evolution of tissue deformation is strongly influenced by insertion depth and friction between the needle and the surrounding material. At shallow penetration depths, deformation is dominated by localised compression at the needle tip. As insertion progresses, frictional forces along the needle shaft increase with the expanding contact area, promoting progressive material transport into the needle lumen. This results in greater internal deformation relative to the surrounding tissue, particularly in soft tissues.

Insertion speed was found to significantly affect both stress distribution and tissue deformation behaviour. Higher insertion speeds generally reduce the extent of stress diffusion in the surrounding tissue while promoting greater tissue entry into the needle lumen. Conversely, lower insertion speeds are associated with more pronounced stress accumulation in the surrounding matrix and reduced lumen filling. Although tissue capture volume was not directly measured, simulated lumen occupancy was used as a comparative indicator of relative tissue-capture efficiency across conditions. These results suggest that moderate insertion speeds may provide a balance between limiting excessive tissue stress and promoting effective tissue acquisition.

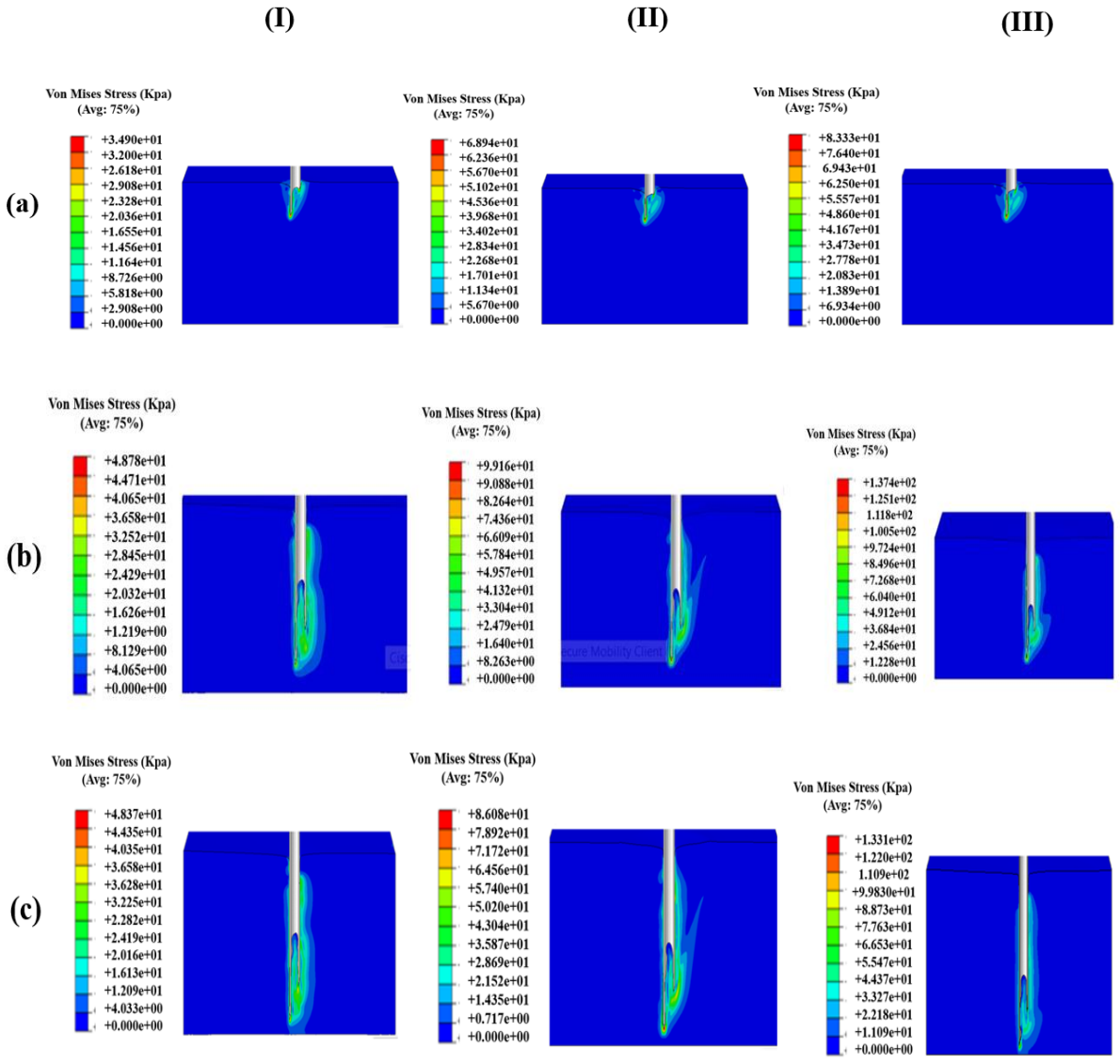

Figure 7.6: 21G needle insertion into porcine lung lymph nodes, indicating 4 stress changes and tissue yield at depths of (a) 7 mm, (b) 26.5.5 mm, and (c) 28.5 mm, and at insertion speeds of (I) 13 mm/s, (II) 9 mm/s, and (III) 3 mm/s.

The force exerted on soft tissue by the biopsy needle was difficult to measure directly; therefore, because the needle's reaction force corresponds to the force experienced by the tissue, the force on the soft tissue was analysed using the needle's reaction force. To verify model accuracy, the experimental results reported in Chapter 6 were compared with FEA predictions. The comparison of the FEA and the experimental results for the 21G Olympus bevel needle in PVA hydrogel, chicken breast, and porcine lung lymph node at 13 mm/s, 9 mm/s, and 3 mm/s is presented in Appendix 7.3, Appendix 7.4, and Figure 7.7. The blue curves represent the experimentally measured force, while the orange curve represents the force predicted by the simulation.

As shown in Figure 7.7(a-c), the experimentally measured values are consistently slightly higher than those predicted by the FEA model. Although deviations are observed in the maximum force values, the overall patterns in the displacement at which the maximum force occurs and the force-displacement curves remain in good agreement. The higher experimental forces are likely due to factors not fully captured by the FEA model, such as gravitational loading on the needle, simplified boundary conditions, small vibrations from the testing rig, and environmental effects. Additionally, real needle-tissue interactions, such as friction and adhesion, may further increase the measured reaction force during testing.

During the puncture process, the force-displacement curve shows several drops in gradient, even though the overall force increases monotonically with displacement. Two primary mechanisms were identified through experimental observation: needle vibration during insertion and interaction between the needle and the soft tissue. Force fluctuations arising from tissue-needle interaction are more pronounced than those caused by needle vibration. The interaction between the tissue and the puncture needle is analogous to a cutting process, in which tissue adhesion at the needle tip leads to the formation of a soft-tissue build-up edge. The presence of this build-up edge results in nonlinear growth of the reaction force, followed by a sudden drop when the build-up edge disappears. This process repeats throughout the puncture, with the frequency of sudden force drops corresponding to repeated formation and disappearance of build-up edges. Increasing the insertion speed leads to more frequent formation and disappearance of build-up edges, resulting in more frequent sudden force drops and reduced puncture stability.

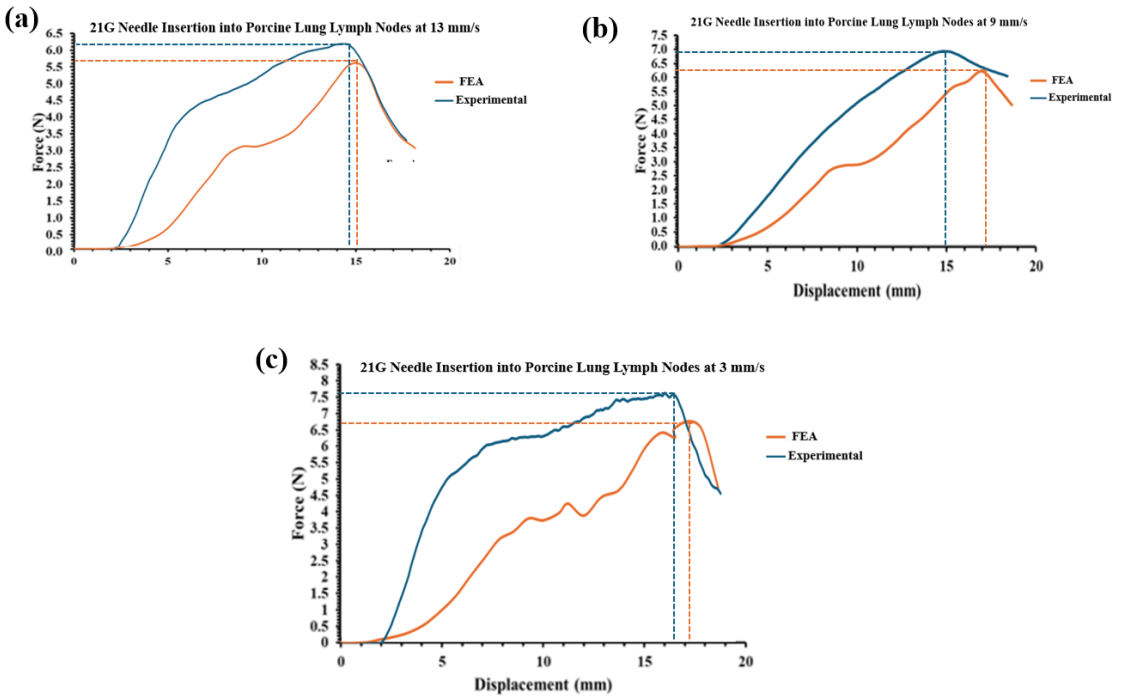

Figure 7.7: 21G single-bevel needle insertion into porcine lung lymph nodes at: (a) 13 mm/s, (b) 9 mm/s, and (c) 3 mm/s. Comparison of FEA and experimental results.

Quantitative comparison of peak insertion forces (F_1) between FEA and experimental results is summarised in Table 7.1. Overall, the model shows good predictive agreement across all tested conditions, with percentage errors ranging from below 1% to 13%, depending on material type and insertion speed. The smallest discrepancies were observed in PVA hydrogel, indicating strong model performance for homogeneous and mechanically consistent materials. In contrast, larger deviations were observed in biological tissues, particularly chicken breast and porcine lung lymph nodes, reflecting greater structural heterogeneity and nonlinear mechanical behaviour that the model's constitutive assumptions do not fully capture.

Among all materials, porcine lung lymph node tissue consistently showed the largest discrepancy between experimental and numerical results across all insertion speeds. This trend is evident in both peak force values and overall force–displacement behaviour. The increased discrepancy is attributed to the highly heterogeneous microstructure and variable mechanical response of lymphatic tissue, which introduces additional complexity not fully captured by the current modelling framework. This behaviour aligns with trends observed across the dataset, where model accuracy decreases systematically with increasing biological complexity.

Overall, the comparison between experimental data and FEA predictions shows that the developed model accurately reproduces the key mechanical features of needle–tissue interaction, while also highlighting specific limitations in capturing the full complexity of heterogeneous biological tissues. These findings validate the model for predictive simulation and identify lymph node tissue as the most challenging case for accurate numerical representation.

Table 7.1: Comparisons of peak forces: FEA vs Experimental

Insertion Speeds	**13 mm/s**		**9 mm/s**		**3 mm/s**	
Materials	FEA [Stdv]	Experimental [Stdv]	FEA [Stdv]	Experimental [Stdv]	FEA [Stdv]	Experimental [Stdv]
	3.651 (N) [1.174]	3.800 (N) [1.282]	4.383 (N) [1.311]	4.344 (N) [1.107]	4.938 (N) [1.891]	4.567 (N) [1.830]
% Differences	3.92		0.898		8.12	
Chicken Breast	5.391 (N) [1.714]	4.750 (N) [1.657]	5.687 (N) [2.073]	4.984 (N) [1.964]	5.944 (N) [2.145]	6.057 (N) [2.397]
% Differences	13.49		13.11		1,87	
Lymph Nodes	6.182 (N) [2.028]	5.587 (N) [1.936]	6.915 (N) [2.505]	6.195 (N) [2.215]	7.752 (N) [2.591]	6.879 (N) [2.471]
% Differences	10.65		11.62		12.69	

7.4.2 Comparison of 22G Needle Tip Geometries into Soft Materials

This section compares the mechanical performance of three 21G needle tip geometries, namely Olympus single bevel, double front bevel, and Acquire Franseen, during insertion into porcine lung lymph node tissue. The comparison is based on CEL FEA and focuses on tissue distribution, maximum insertion force, tissue capture, and the effect of insertion speed.

The CEL FEA model captures the full insertion process, including initial tissue indentation, fracture initiation at the cutting edges, progressive penetration, frictional sliding along the shaft, and tissue displacement into the needle lumen. Tissue behaviour is represented using large-deformation mechanics within an Eulerian framework, with von Mises stress quantifying tissue stress arising from deformation and tissue fraction within each Eulerian element. Stress concentrations develop at the cutting edges, increase with insertion depth until the maximum force is reached, and then decrease as the needle exits the tissue. This modelling framework enables direct comparison of how needle geometry influences insertion resistance, stress distributions, and tissue capture.

Figure 7.8 presents von Mises stress distributions for three needle geometries inserted into lymph node tissue at an insertion speed of 13 mm/s and a total displacement of 12 mm. The analysis begins at the initial contact point between the needle and the tissue and ends just before the needle exits. Tissue stress was calculated using von Mises stresses derived from deformation and tissue fraction within each Eulerian element. At depths of 0-2.5 mm, the tissue remained undeformed, with no stress observed, as the needle passed through a void region. The insertion of the Olympus single bevel needle is illustrated in Figure 7.8(I) - (a to d). Initial contact at 2.5 mm, Figure 7.8(I) - (a), caused local fracture and indentation with a stress of 30.2 kPa and no tissue penetration. At 4 mm, Figure 7.8 (I) - (b), the leading and trailing edges penetrated the tissue, resulting in a stress of 48.2 kPa and a small tissue displacement into the needle lumen. Maximum stress of 54.7 kPa and a force of 7.10 N occurred at a depth of 8.5 mm, Figure 7.8(I) - (c). Stress decreased slightly before the needle exited at 9.5 mm, with a stress of 54.6 kPa, Figure 7.8(I) - (d).

The insertion of the double bevel needle, which has two cutting edges, is shown in Figure 7.8(II) - (a to d). The initial contact point of the needle's first cutting edge with the tissue was established at approximately 2.5 mm, Figure 7.8(II) - (a). This caused tissue fracture and

indentation, inducing a contact stress of around 6.98 kPa, Figure 7.8(II) - (b). In comparison with the single-bevel needle, the double-bevel exhibited lower maximum stress and peak force, F_1, with values of 21.7 kPa and 5.67 N, respectively (Figure 7.8(II) - (c). A stress level of 11.5 kPa was induced by the needle just before the leading edge exited the tissue, Figure 7.8(II) - (d).

The insertion of the Acquired Franseen needle is shown in Figure 7.8(III) - (a to d). It features three symmetrical cutting edges and exhibits a distinct interaction mechanism. Tissue capture occurred during the initial contact phase, Figure 7.8(III) - (a), with a stress of 4.04 kPa at a depth of 2 -2.5 mm. At 4 mm, penetration by all three cutting edges induced a stress of 6.34 kPa and resulted in significant tissue displacement into the lumen, Figure 7.8(III) - (b). The maximum stress, 14.9 kPa, and maximum force of 4.60 N, were the lowest among the three needle tip designs, Figure 7.8(III) - (c). Just before exit at approximately 10 mm, the stress reduced to 1.456 kPa, Figure 7.8(III)- (d).

Expanded visualisation of the Franseen needle, Figure 7.9, at a depth of 8.5 mm and at the maximum stress and force of 14.9 kPa and 4.60 N, respectively, highlights the volume of tissue captured within the lumen, demonstrating that multiple cutting edges promote inward tissue displacement and improve tissue acquisition.

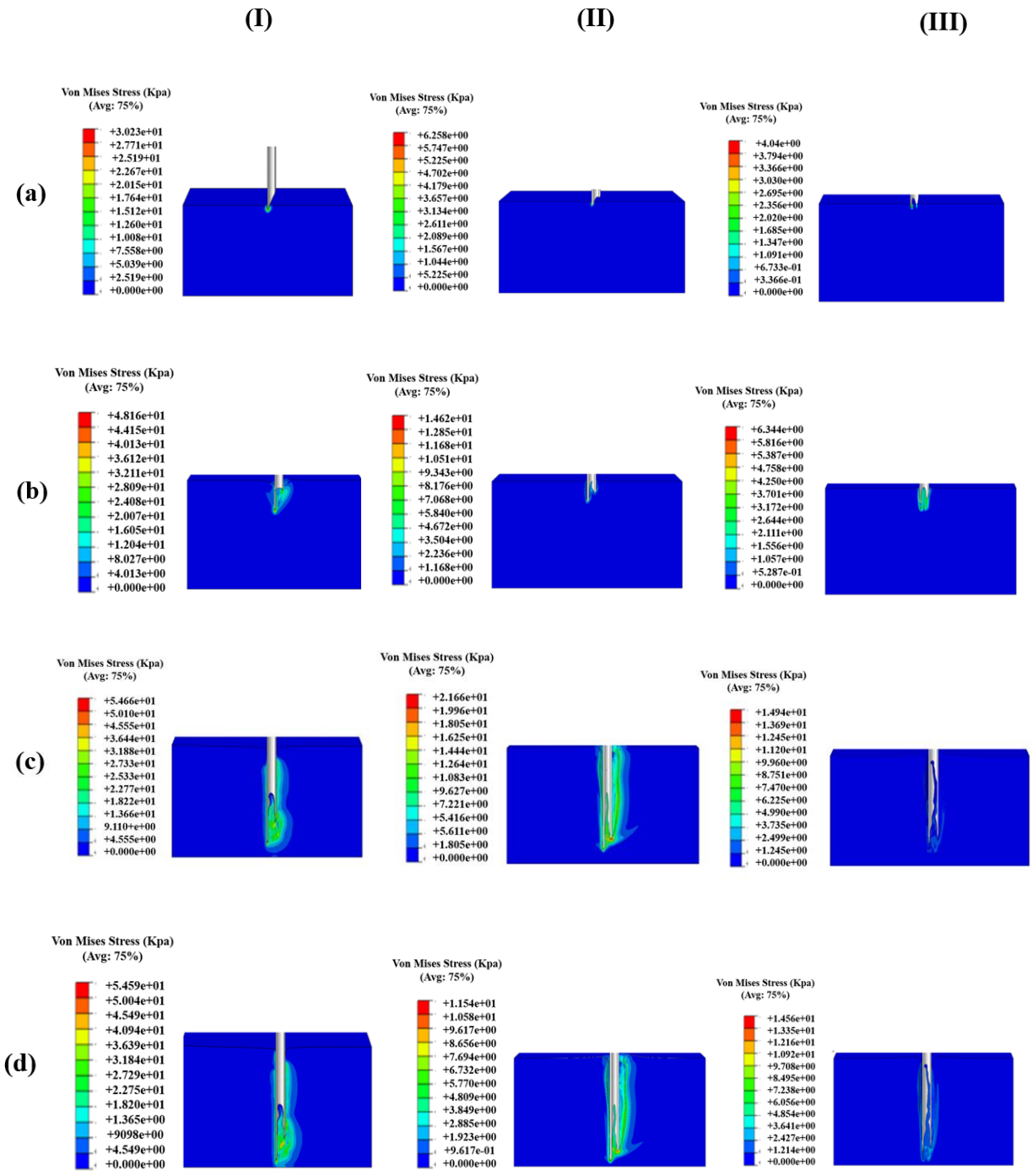

Figure 7.8: 21G needle tip geometries inserted into lymph node tissue at 13 mm/s: (I) Olympus bevel; (II) double bevel; (III) Acquire Franseen, showing tissue stress and tissue sample length at different depths; (a) 2.5 mm; (b) 4 mm; (c) 8.5 mm; and (d) 9.5 mm.

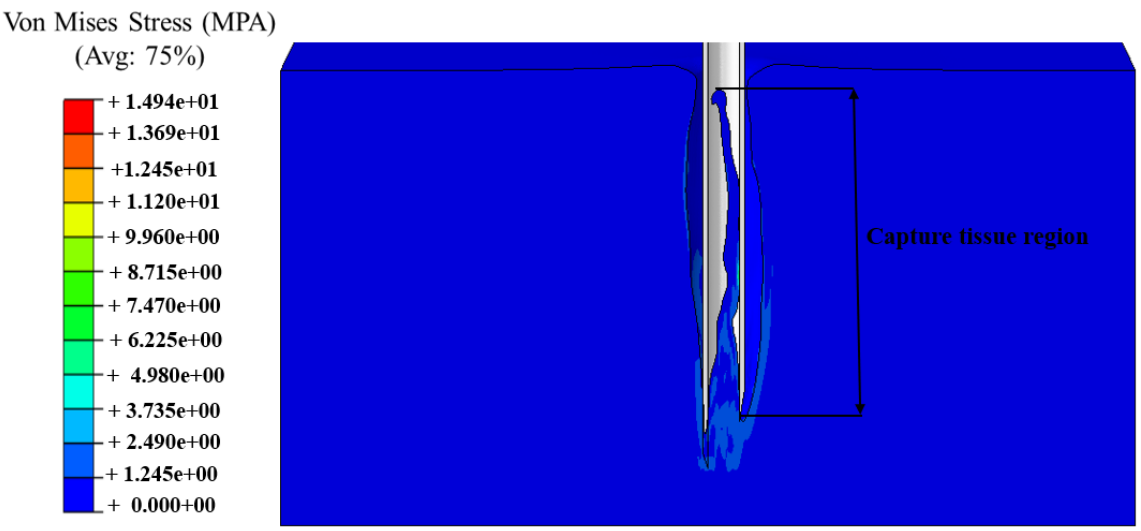

Figure 7.9: Enlarged visualisation of the Franseen needle at a depth of 8.5 mm under maximum stress and force of 14.9 kPa and 4.60 N.

While stress contour plots provide a visual representation of the stress distribution, maximum insertion forces offer a more precise quantitative basis for comparing needle performance. Figure 7.10, presents maximum force comparisons across insertion speeds for all needle-tip geometries. Across all speeds, the Acquire Franseen needle consistently showed the lowest maximum force, followed by the double bevel and single bevel needles. This confirms that increasing the number of cutting planes reduces insertion resistance and tissue stress.

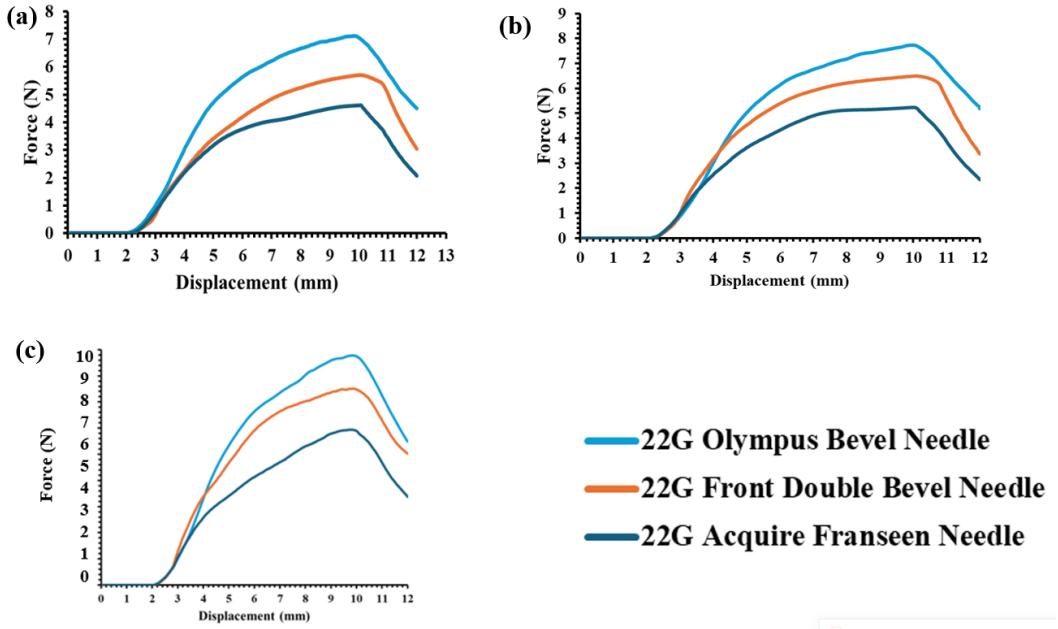

Figure 7.10: Peak force comparison of 21G single bevel, double front bevel and Franseen needle insertions into lymph nodes at different insertion speeds: (a) 13 mm/s, (b) 9 mm/s, and (c) 3 mm/s.

The differences observed between needle geometries can be explained by variations in tip-tissue interaction mechanics, which are governed primarily by the number, orientation, and distribution of cutting edges. In the single bevel geometry, the applied load is concentrated along a single dominant cutting plane, resulting in higher localised stress at the tissue interface. This increases tissue compression before puncture and leads to greater resistance during initial penetration, which is reflected in higher peak stress and force values.

In contrast, the double bevel and Acquire Franseen geometries distribute the applied load across multiple cutting edges, increasing the effective cutting perimeter and reducing stress concentrations at any single contact point. This promotes a transition from a predominantly compressive deformation mode in the tissue to a more efficient shear-dominated cutting failure, thereby reducing insertion resistance and lowering peak stresses throughout insertion.

In particular, the Acquire Franseen needle, with its three symmetrically arranged cutting edges, provides a more uniform and isotropic stress distribution at the tip. This reduces directional bias during penetration, improves path stability, and minimises localised strain accumulation. As a result, it consistently demonstrates lower insertion forces and reduced variability in stress response compared with bevel-based geometries.

Table **7.2**–7.4 summarises the relationship between insertion speed and tissue stress at initial contact, at maximum insertion depth, and just before exit. Medium insertion speeds of 13–9 mm/s consistently produced lower maximum stress and more stable force profiles than the slower 3 mm/s insertion. This behaviour reflects a balance between tissue viscoelastic relaxation at low speeds and increasing resistance associated with prolonged tissue deformation. At very low speeds, time-dependent tissue relaxation allows greater deformation before cutting, increasing stress accumulation. In contrast, at higher (medium) speeds, insertion occurs more efficiently, with less deformation time, resulting in lower peak stresses.

Based on these findings, medium insertion speeds are recommended for controlled needle insertion as they minimise tissue stress while maintaining consistent penetration behaviour.

Table 7.2: Relationship between contact stress in kPa and insertion speed into lymph nodes for different needle types.

	13 mm/s	**9 mm/s**	**3 mm/s**
Olympus Bevel	30.2	89.6	135.2
Double Bevel	6.98	23.02	68.2
Acquire Franseen	4.04	5.24	9.21

Table 7.3: Relationship between peak stress in kPa and insertion speed into lymph nodes for different needle types.

	13 mm/s	**9 mm/s**	**3 mm/s**
Olympus Bevel	54.7	111	149
Double Bevel	21.7	23.0	68.6
Acquire Franseen	14.9	21.8	31.4

Table 7.4: Relationship between stress before exit in kPa and insertion speed into lymph nodes for relationship between different needle types.

	13 mm/s	**9 mm/s**	**3 mm/s**
Olympus Bevel	55.6	89.3	386
Double Bevel	11.5	28.8	65.7
Acquire Franseen	1.46	15.0	18.3

In summary, needle tip geometries have a significant impact on insertion mechanics and tissue acquisition. Increasing the number of cutting edges reduces stress concentration at the tissue interface, promotes more uniform shear-driven cutting rather than compressive deformation, and consequently lowers insertion force and tissue stress. Among the geometries studied, the Acquire Franseen needle demonstrated superior performance, achieving the lowest peak forces and stresses across all insertion conditions. Medium insertion speeds provided optimal insertion behaviour and are therefore recommended for controlled tissue penetration and acquisition.

7.5 Summary

This chapter presented a detailed three-dimensional finite element analysis (FEA) model to investigate needle–tissue interactions during endobronchial ultrasound-guided transbronchial needle aspiration (EBUS-TBNA). The study focused on three needle tip designs: the Olympus single-bevel, the double front-bevel, and the Acquire Franseen needle. These were evaluated using representative soft-tissue models, including PVA hydrogel, chicken breast, and porcine lymph node tissue. The computational framework employed a Coupled Eulerian–Lagrangian (CEL) approach combined with dynamic fracture mechanics, enabling the simulation of large deformations and progressive tissue failure without prescribing a predefined crack path or requiring remeshing. Non-linear hyperelastic tissue behaviour was characterised using an Ogden constitutive model, with material coefficients derived in Chapter 5.

The FEA model was validated against experimental needle insertion tests described in Chapter 6. Maximum insertion forces at insertion speeds of 13, 9, and 3 mm/s were compared with simulation outputs, yielding percentage errors of 12.7%, 11.6%, and 10.6% for lymph node tissue, respectively. This level of agreement demonstrates that the model can reasonably predict insertion-force trends, tissue-deformation behaviour, and frictional interactions under the defined experimental conditions, supporting its use as a predictive tool for the comparative assessment of needle designs.

The primary findings of this chapter indicate that needle tip geometry plays a critical role in determining both mechanical performance and tissue acquisition characteristics. The Acquire Franseen needle exhibited distinct insertion behaviour, characterised by altered contact stress distribution and modified insertion resistance compared with the bevelled needle designs. It also produced longer retrieved tissue samples, suggesting improved sampling efficiency. In contrast, the Olympus single-bevel and double front-bevel needles demonstrated higher insertion forces and consistently shorter tissue samples. These results highlight that optimisation of needle tip geometry can significantly influence both mechanical loading on tissue and potential diagnostic yield in EBUS-TBNA procedures.

A key limitation of the present work is the controlled, idealised representation of biological tissue behaviour in both the experimental and numerical frameworks. Although PVA hydrogel, chicken breast, and porcine lymph node tissues provide useful approximations of soft tissue

response, real biological tissues exhibit substantial physiological variability that is not fully captured in the current model. In particular, tissue mechanical properties are strongly temperature-dependent, and deviations from physiological conditions can alter viscoelastic stiffness and fracture behaviour. Similarly, hydration and moisture content influence interfacial friction and local compliance, thereby affecting insertion resistance and force transmission during penetration. Furthermore, biological tissues are inherently heterogeneous and anisotropic, comprising layered structures and fibrous microarchitectures that govern local stress distributions and crack initiation pathways. In addition, ex vivo tissue samples may change properties due to harvesting, storage, and preparation, including dehydration, enzymatic degradation, and structural relaxation, all of which may contribute to deviations between experimental measurements and in vivo behaviour. These factors collectively introduce uncertainty when translating insertion performance from controlled laboratory conditions to clinical scenarios.

Another limitation stems from the use of shared frictional parameters across different needle designs, owing to the lack of dedicated experimental friction characterisation for the double front-bevel and Franseen geometries. While this approach enables model comparability, it may introduce minor discrepancies in predicted insertion forces and local stress fields.

In summary, this chapter demonstrates that the CEL-based FEA framework is a robust and validated tool for investigating needle–tissue interactions in EBUS-TBNA procedures. The model provides reliable predictions of insertion force and tissue deformation trends and enables comparative evaluation of needle tip geometries. The Acquire Franseen needle demonstrated favourable mechanical and tissue-acquisition performance, whereas the Olympus single-bevel and double front-bevel designs exhibited higher insertion resistance and shorter sample lengths. These findings address the thesis's overarching aims by characterising lymph node mechanical response, modelling needle insertion behaviour, and evaluating the influence of needle geometry on sampling efficiency. Collectively, the results provide a foundation for future optimisation of needle design to improve diagnostic yield in EBUS-TBNA, particularly when extended to more physiologically realistic and heterogeneous tissue environments.

Chapter 8: Conclusions and Future Work

8.1 Conclusions

This thesis explored the biomechanical behaviour of lymph nodes and the mechanics of needle–tissue interaction during Endobronchial Ultrasound-guided Transbronchial Needle Aspiration (EBUS-TBNA). The study was driven by two key gaps in existing knowledge: a limited understanding of lymph node mechanical properties and a lack of predictive models that link needle design, insertion mechanics, and tissue sampling effectiveness. To address these gaps, a hybrid experimental and computational approach was developed to analyse lymph node tissue, simulate needle insertion, and assess biopsy needle performance.

The work presented in this thesis was organised around four main objectives. The following sections summarise how each objective was achieved, the key findings, and their implications.

8.1.1 Objective 1: Mechanical characterisation of lymph nodes and comparison with surrogate materials

The first objective was to establish a comprehensive mechanical characterisation methodology for lung lymph nodes and to evaluate their correlation with alternative soft materials, including PVA hydrogel, chicken breast, and large pickled capers.

This objective was achieved through a series of displacement-controlled relaxation tests and nanoindentation experiments conducted on ex vivo porcine lung lymph nodes. The experiments were performed using a Biomomentum Mach-1 V500C mechanical testing system, enabling controlled and repeatable measurement of nonlinear soft-tissue behaviour.

The results demonstrated that lymph node tissue exhibits strongly nonlinear mechanical behaviour under compressive loading relevant to needle insertion. Constitutive model fitting showed that the first-order Ogden hyperelastic model provided the most accurate representation of the experimental stress–strain response across the strain range of interest.

The measured density and shear modulus of lymph nodes were 1.04 ± 0.13 g/cm³ and 4.88 ± 0.8 kPa, respectively. These experimentally validated parameters are suitable for use in computational modelling of needle–tissue interaction.

Comparison with surrogate materials showed that although PVA hydrogel and chicken breast exhibited partial mechanical similarity, neither fully replicated the nonlinear behaviour of lymph node tissue. Large pickled capers, despite their geometric resemblance to lymph nodes, were mechanically unsuitable as tissue analogues. These findings underscore the importance of experimentally validated tissue models and demonstrate that morphological similarity alone is insufficient for accurate biomechanical representation.

Overall, this objective established a robust experimental methodology for lymph node characterisation and yielded new quantitative insights into their mechanical properties.

8.1.2 Objective 2: Development of theoretical and computational models for needle insertion

The second objective was to develop and test theoretical and computational models capable of identifying the phases of needle insertion, including the evolution of force and tissue deformation behaviour.

This objective was achieved by developing a coupled Eulerian–Lagrangian (CEL) finite element framework to simulate needle insertion into soft biological tissue. Traditional Lagrangian formulations were found unsuitable for this application because severe mesh distortion occurs during large deformation and fracture.

The CEL approach overcame these limitations by enabling stable simulation of puncture, penetration, frictional interaction, and tissue separation, avoiding numerical instability. The model reproduced the key physical stages observed experimentally, including initial contact, tissue rupture, steady-state insertion, and needle withdrawal.

The developed framework, therefore, provides a validated computational tool for analysing needle–tissue interactions and serves as a foundation for subsequent evaluation of needle design and insertion parameters.

8.1.3 Objective 3: Experimental and modelling investigation of needle–tissue interaction

The third objective was to gain insights into needle–tissue interaction through modelling and experimentation, with a particular focus on predicting needle behaviour, tissue deformation, and tissue sampling length.

Experimental studies were conducted on various ex vivo soft tissues at clinically relevant insertion speeds (13 mm/s, 9 mm/s, 3 mm/s, and 0.5 mm/s). The results showed that needle insertion proceeds through four distinct phases: initial contact without penetration, tissue fracture and penetration, friction-dominated insertion, and needle exit.

The findings demonstrated that insertion speed significantly affects both the force response and tissue deformation. Specifically, higher insertion speeds reduced peak insertion forces, increased frictional resistance, and altered tissue deformation patterns. This suggests that dynamic effects play an important role in governing needle–tissue interaction behaviour.

The coefficient of friction was identified as a key parameter influencing both insertion force and tissue-sampling performance. Variations in friction directly affected tissue deformation and the effective length of the sampled tissue.

These results provide a more detailed mechanical understanding of tissue acquisition during EBUS-TBNA and offer experimentally validated data to improve both procedural strategies and computational models.

8.1.4 Objective 4: Influence of needle tip geometry on tissue deformation and sampling efficiency

The fourth objective was to investigate how needle tip geometry affects tissue deformation, insertion forces, and tissue sampling length.

This was achieved through numerical simulation using the validated CEL model, comparing three needle designs: a conventional single-bevel Olympus needle, a double-bevel needle, and the Acquire Franseen needle with multiple cutting planes.

The results demonstrated that needle-tip geometry plays a crucial role in determining tissue-interaction behaviour. In particular, the number and orientation of cutting planes significantly influence tissue-separation mechanisms, insertion force, and sample acquisition.

The Franseen needle, which incorporates three symmetric cutting planes, achieved higher tissue-sampling efficiency than conventional single-bevel designs. However, this improved sampling performance was associated with greater tissue disruption under certain insertion conditions. The results indicate that optimal needle performance requires a balance between sampling efficiency and tissue damage.

These findings establish a direct mechanistic relationship between needle geometry and tissue-sampling behaviour, addressing a key gap in the current understanding of biopsy needle design.

8.1.5 Overall conclusions and contribution of the thesis

Overall, this thesis demonstrates that a combined experimental and computational approach is essential for understanding the mechanics of lymph node biopsies and for improving EBUS-TBNA needle design.

The key contributions of this work are:

- A validated experimental methodology for characterising the nonlinear mechanical behaviour of lymph node tissue.
- Quantitative insight into the roles of insertion speed and friction in governing needle–tissue interaction.
- Development of a robust CEL-based computational framework capable of simulating needle insertion, tissue fracture, and sampling behaviour.
- Identification of the influence of needle tip geometry on tissue acquisition performance and tissue damage.

Collectively, these contributions provide a mechanistic and computational foundation for optimising biopsy needle design and may support improvements in diagnostic yield during EBUS-TBNA procedures.

8.2 Limitations of the Work

Several limitations should be considered when interpreting the findings of this thesis. Firstly, the mechanical characterisation and needle insertion experiments were conducted on ex vivo porcine lymph nodes collected post-mortem. Although the experimental protocols were carefully standardised, biological variability between samples, post-mortem tissue changes, storage conditions, and the time between tissue collection and testing may have influenced the measured mechanical properties and insertion responses. Such variability is inherent in soft biological tissue testing and cannot be completely eliminated.

Secondly, the study utilised healthy porcine lymph nodes rather than pathological or cancerous human lymph nodes. Diseased lymph nodes may exhibit altered structural organisation, stiffness, rupture behaviour, and tissue heterogeneity compared with healthy tissue. While pathological tissue could improve clinical relevance, obtaining and testing cancerous lymph nodes pose significant ethical, logistical, and reproducibility challenges. Consequently, this study prioritised methodological consistency and experimental repeatability to establish a reliable baseline framework for understanding lymph node biomechanics and needle–tissue interaction.

Thirdly, although several surrogate materials, including PVA hydrogel, chicken breast, and large pickled capers, were investigated as potential lymph node analogues, none fully replicated the mechanical behaviour of lymph node tissue. Therefore, caution should be exercised when extrapolating the behaviour of surrogate materials to clinical conditions. Nevertheless, the comparative evaluation provided useful insight into the suitability and limitations of commonly used tissue-mimicking materials.

Finally, the experimental evaluation of needle geometry was constrained by the availability of clinically relevant needle types, particularly the double-bevel and Acquire Franseen needles. Consequently, the range of geometries investigated was limited, and additional studies with a

broader range of needle configurations would further strengthen understanding of the relationship between needle design, tissue deformation, and sampling performance.

Despite these limitations, the experimental methodologies and computational modelling framework developed in this thesis provide a validated foundation for future investigations into lymph node biomechanics and for optimising EBUS-TBNA needle design.

8.3 Future Work

Following up on the achievement highlighted in the previous section, this section presents future directions in the short, medium and long term, through which the experimental and modelling methodologies established in this thesis can potentially be further refined and improved.

The most practical and impactful short-term extension of this research will be to conduct experimental and computational assessments of newly developed EBUS-TBNA needle designs, such as the upgraded 22G and flex19G needles, which were unavailable during this study. Testing these needles within the current framework would enable direct comparison with existing 21G and 22G needles and provide immediate insights into design enhancements without requiring substantial methodological adjustments.

The medium-term extension of this research will be to integrate viscoelastic tissue behaviour into the current modelling framework. Although the present study employed hyperelastic constitutive models, biological soft tissues also exhibit rate-dependent viscoelastic behaviour. As a result, incorporating quasilinear viscoelastic or Kelvin-Voigt models within the CEL framework would enable a more precise depiction of tissue deformation and rupture across different insertion speeds.

Long-term research will involve investigating cancerous or enlarged lymph nodes to assess pathological effects on mechanical behaviour and needle-tissue interaction. Such work requires a biologically led, ethical approval, and controlled tissue acquisition protocols. While cancerous tissue may introduce local changes in stiffness and heterogeneity, its influence on the bulk mechanical response and tissue sampling efficiency remains uncertain; further investigations beyond the scope of this thesis are warranted.

Additionally, further studies should be conducted to improve the accuracy and predictive capability of the computational models. This includes refining finite element analysis parameters, such as mesh density, element interactions, and convergence criteria. Future work could also involve direct experimental measurement of insertion force (F_i) and cutting force (F_c) to validate and refine the force estimates presented in Figure 6.13. One possible approach would be to utilise a mechanical testing system, such as an Instron universal testing machine, in combination with high-resolution imaging during needle penetration of representative soft tissue materials. By synchronising the force–displacement measurements with visual identification, such as a high-speed camera capturing penetration and insertion events, it would be possible to more accurately determine the onset of tissue penetration and to correlate these measurements with the predicted force profiles. Such an approach would provide additional experimental validation of the proposed modelling methodology and improve the reliability of force characterisation during needle insertion.

References

[1] ‘Lung cancer statistics’, Cancer Research UK. Accessed: Sep. 20, 2024. [Online]. Available: https://www.cancerresearchuk.org/health-professional/cancer-statistics/statistics-by-cancer-type/lung-cancer

[2] H. J. Kang and B. Hwangbo, ‘Technical Aspects of Endobronchial Ultrasound-Guided Transbronchial Needle Aspiration’, *Tuberc. Respir. Dis.*, vol. 75, no. 4, p. 135, 2013, doi: 10.4046/trd.2013.75.4.135.

[3] T. R. Kucklick, *The medical device R&D handbook*. CRC press, 2005. Accessed: Sep. 20, 2024. [Online]. Available: https://www.taylorfrancis.com/books/mono/10.1201/9781420038354/medical-device-handbook-theodore-kucklick

[4] R. Agarwal, A. Srinivasan, A. N. Aggarwal, and D. Gupta, ‘Efficacy and safety of convex probe EBUS-TBNA in sarcoidosis: a systematic review and meta-analysis’, *Respir. Med.*, vol. 106, no. 6, pp. 883–892, 2012.

[5] D. E. Ost *et al.*, ‘Diagnostic yield of endobronchial ultrasound-guided transbronchial needle aspiration: results of the AQuIRE Bronchoscopy Registry’, *Chest*, vol. 140, no. 6, pp. 1557–1566, 2011.

[6] P. J. Vaidya *et al.*, ‘Diagnostic value of core biopsy histology and cytology sampling of mediastinal lymph nodes using 21-gauge EBUS-TBNA needle’, *J. Cancer Res. Ther.*, vol. 12, no. 3, pp. 1172–1177, 2016.

[7] ‘Lung Cancer: Types, Stages, Symptoms, Diagnosis & Treatment’, Cleveland Clinic. Accessed: Jan. 12, 2024. [Online]. Available: https://my.clevelandclinic.org/health/diseases/4375-lung-cancer

[8] ‘What Is Lung Cancer? | Types of Lung Cancer’. Accessed: Jan. 12, 2024. [Online]. Available: https://www.cancer.org/cancer/types/lung-cancer/about/what-is.html

[9] ‘Terese Winslow LLC, Medical and Scientific Illustration’, Terese Winslow LLC, Medical and Scientific Illustration. Accessed: Jan. 14, 2024. [Online]. Available: https://www.teresewinslow.com

[10] ‘Metastatic Cancer: When Cancer Spreads - NCI’. Accessed: Sep. 23, 2024. [Online]. Available: https://www.cancer.gov/types/metastatic-cancer

[11] M. Wahbah, N. Boroumand, C. Castro, F. El-Zeky, and M. Eltorky, ‘Changing trends in the distribution of the histologic types of lung cancer: a review of 4,439 cases’, *Ann. Diagn. Pathol.*, vol. 11, no. 2, pp. 89–96, 2007.

[12] R. M. Jaber *et al.*, ‘Electronic Cigarette Use Prevalence, Associated Factors, and Pattern by Cigarette Smoking Status in the United States From NHANES (National Health and Nutrition Examination Survey) 2013–2014’, *J. Am. Heart Assoc.*, vol. 7, no. 14, p. e008178, Jul. 2018, doi: 10.1161/JAHA.117.008178.

[13] C. on H. R. of E. to R. (BEIR VI), *Health effects of exposure to radon: BEIR VI*, vol. 6. Joseph Henry Press, 1999.

[14] W. H. Organization, *WHO handbook on indoor radon: a public health perspective*. World Health Organization, 2009. Accessed: Jan. 12, 2024. [Online]. Available: https://books.google.com/books?hl=en&lr=&id=J9Bc09N1pXgC&oi=fnd&pg=PP2&dq=.+World+Health+Organization.+WHO+handbook+on+indoor+radon:+a+public+health+perspective.+Geneva,+Switzerland:+World+Health+Organization%3B+2009:1%E2%80%9394&ots=1-ViD3uKQM&sig=ALMGyZtXrpqglI-m7gJYMIgqRJg

[15] C. Garzillo, M. Pugliese, F. Loffredo, and M. Quarto, ‘Indoor radon exposure and lung cancer risk: a meta-analysis of case-control studies’, *Transl Cancer Res*, vol. 6, no. Suppl 5, pp. S934–S943, 2017.

[16] R. W. Field and B. L. Withers, ‘Occupational and environmental causes of lung cancer’, *Clin. Chest Med.*, vol. 33, no. 4, pp. 681–703, 2012.

[17] B. Järvholm and E. Åström, 'The risk of lung cancer after cessation of asbestos exposure in construction workers using pleural malignant mesothelioma as a marker of exposure', *J. Occup. Environ. Med.*, vol. 56, no. 12, p. 1297, 2014.

[18] L. Ang, P. Ghosh, and W. J. Seow, 'Association between previous lung diseases and lung cancer risk: a systematic review and meta-analysis', *Carcinogenesis*, vol. 42, no. 12, pp. 1461–1474, 2021.

[19] R. L. Siegel, K. D. Miller, and A. Jemal, 'Cancer statistics, 2019', *CA. Cancer J. Clin.*, vol. 69, no. 1, pp. 7–34, Jan. 2019, doi: 10.3322/caac.21551.

[20] M. R. Cooperberg, W. Meeks, R. Fang, F. D. Gaylis, W. J. Catalona, and D. V. Makarov, 'Time trends and variation in the use of active surveillance for management of low-risk prostate cancer in the US', *JAMA Netw. Open*, vol. 6, no. 3, pp. e231439–e231439, 2023.

[21] 'Chest X-ray (CXR): What You Should Know & When You Might Need One', Cleveland Clinic. Accessed: Jan. 12, 2024. [Online]. Available: https://my.clevelandclinic.org/health/diagnostics/10228-chest-x-ray

[22] 'Study Suggests Lung Cancer Survivors Receiving Too Many PET Scans | Imaging Technology News'. Accessed: Jan. 22, 2024. [Online]. Available: https://www.itnonline.com/content/study-suggests-lung-cancer-survivors-receiving-too-many-pet-scans

[23] E. Schieppati, 'Mediastinal lymph node puncture through the tracheal carina', *Surg. Gynecol. Obstet.*, vol. 107, no. 2, pp. 243–246, 1958.

[24] K. P. Wang, R. Brower, E. F. Haponik, and S. Siegelman, 'Flexible transbronchial needle aspiration for staging of bronchogenic carcinoma', *Chest*, vol. 84, no. 5, pp. 571–576, 1983.

[25] G. Mathis, *Atlas of chest sonography*. Springer Science & Business Media, 2003. Accessed: Jan. 20, 2026. [Online]. Available: https://books.google.com/books?hl=en&lr=&id=NhYsSKuOOJkC&oi=fnd&pg=PA1&

dq=G.+Mathis,+Atlas+of+chest+sonography.+Springer+Science+%26+Business+Media,+2003.&ots=-uOvHGg_Su&sig=MCP0-6OlFyPGjDOIhnE8i6xp9Ww

[26] 'About Us : OLYMPUS'. Accessed: Jan. 14, 2024. [Online]. Available: https://www.olympus-global.com/company/

[27] R. M. Pieterman *et al.*, 'Preoperative Staging of Non–Small-Cell Lung Cancer with Positron-Emission Tomography', *N. Engl. J. Med.*, vol. 343, no. 4, pp. 254–261, Jul. 2000, doi: 10.1056/NEJM200007273430404.

[28] 'About Us : OLYMPUS'. Accessed: Jan. 20, 2026. [Online]. Available: https://www.olympus-global.com/company/?page=company

[29] J. Yang, J. De Cardenas, M. Nobari, R. Miller, and G. Cheng, 'Narrative review of tools for endoscopic ultrasound-guided biopsy of mediastinal nodes', *Mediastinum*, vol. 4, 2020, Accessed: Jan. 14, 2024. [Online]. Available: https://www.ncbi.nlm.nih.gov/pmc/articles/PMC8794368/

[30] J. A. Jensen, *Estimation of blood velocities using ultrasound: a signal processing approach*. Cambridge University Press, 1996. Accessed: Jan. 20, 2026. [Online]. Available: https://books.google.com/books?hl=en&lr=&id=2pZOAAAAIAAJ&oi=fnd&pg=PR9&dq=Jensen+JA.+Estimation+of+blood+velocities+using+ultrasound:+A+signal+processing+approach.+Cambridge+University+Press,+1996&ots=BNaUKzHdVI&sig=F2CKpUIvFJZcl9Tf9QYQ2IewD64

[31] P. Hoskins, K. Martin, and A. Thrush, *Diagnostic ultrasound: physics and equipment*. CRC Press, 2019. Accessed: Jan. 20, 2026. [Online]. Available: https://books.google.com/books?hl=en&lr=&id=hzX3DwAAQBAJ&oi=fnd&pg=PP1&dq=Hoskins+PR,+Martin+K,+Thrush+A.+Diagnostic+Ultrasound:+Physics+and+Equipment.+3rd+ed.,+CRC+Press,+2019.&ots=g6atfi3YdB&sig=z3ibI89MZF32BtkuggXWuTl2gV8

[32] C. F. Dietrich, J. T. Annema, P. Clementsen, X. W. Cui, M. M. Borst, and C. Jenssen, 'Ultrasound techniques in the evaluation of the mediastinum, part I: endoscopic ultrasound (EUS), endobronchial ultrasound (EBUS) and transcutaneous mediastinal ultrasound (TMUS), introduction into ultrasound techniques', *J. Thorac. Dis.*, vol. 7, no. 9, p. E311, 2015.

[33] P. N. Wells, 'Ultrasound imaging', *Phys. Med. Biol.*, vol. 51, no. 13, p. R83, 2006.

[34] H. Sorger, E. F. Hofstad, T. Amundsen, T. Langø, J. B. L. Bakeng, and H. O. Leira, 'A multimodal image guiding system for Navigated Ultrasound Bronchoscopy (EBUS): A human feasibility study', *PloS One*, vol. 12, no. 2, p. e0171841, 2017.

[35] A. C. Society, *Cancer facts & figures 2014*. American Cancer Society, 2014.

[36] S. Colella *et al.*, 'Biopsy needles for mediastinal lymph node sampling by endosonography: current knowledge and future perspectives', *J. Thorac. Dis.*, vol. 10, no. 12, p. 6960, 2018.

[37] 'ViziShot 2 EBUS-TBNA Needles | Olympus America | Medical'. Accessed: Jan. 17, 2024. [Online]. Available: https://medical.olympusamerica.com/products/vizishot2-ebus-tbna-needles

[38] E. L. Scholten *et al.*, 'Stylet use does not improve diagnostic outcomes in endobronchial ultrasonographic transbronchial needle aspiration: a randomized clinical trial', *Chest*, vol. 151, no. 3, pp. 636–642, 2017.

[39] B. A. Jalil, K. Yasufuku, and A. M. Khan, 'Uses, Limitations, and Complications of Endobronchial Ultrasound', *Bayl. Univ. Med. Cent. Proc.*, vol. 28, no. 3, pp. 325–330, Jul. 2015, doi: 10.1080/08998280.2015.11929263.

[40] T. Nakajima and K. Yasufuku, 'How I do it—optimal methodology for multidirectional analysis of endobronchial ultrasound-guided transbronchial needle aspiration samples', *J. Thorac. Oncol.*, vol. 6, no. 1, pp. 203–206, 2011.

[41] C. F. Mountain and C. M. Dresler, 'Regional lymph node classification for lung cancer staging', *Chest*, vol. 111, no. 6, pp. 1718–1723, 1997.

[42] T. Ye, H. Hu, X. Luo, and H. Chen, 'The role of Endobronchial ultrasound guided transbronchial needle aspiration (EBUS-TBNA) for qualitative diagnosis of mediastinal and hilar lymphadenopathy: a prospective analysis', *BMC Cancer*, vol. 11, no. 1, p. 100, Dec. 2011, doi: 10.1186/1471-2407-11-100.

[43] J. S. W. Memoli *et al.*, 'Using endobronchial ultrasound features to predict lymph node metastasis in patients with lung cancer', *Chest*, vol. 140, no. 6, pp. 1550–1556, 2011.

[44] K. N. Margaris and R. A. Black, 'Modelling the lymphatic system: challenges and opportunities', *J. R. Soc. Interface*, vol. 9, no. 69, pp. 601–612, 2012.

[45] K. P. Arkill, J. Moger, and C. P. Winlove, 'The structure and mechanical properties of collecting lymphatic vessels: an investigation using multimodal nonlinear microscopy', *J. Anat.*, vol. 216, no. 5, pp. 547–555, May 2010, doi: 10.1111/j.1469-7580.2010.01215.x.

[46] F. P. Assen *et al.*, 'Multitier mechanics control stromal adaptations in the swelling lymph node', *Nat. Immunol.*, vol. 23, no. 8, pp. 1246–1255, 2022, doi: 10.1038/s41590-022-01257-4.

[47] C. Storm, J. J. Pastore, F. C. MacKintosh, T. C. Lubensky, and P. A. Janmey, 'Nonlinear elasticity in biological gels', *Nature*, vol. 435, no. 7039, pp. 191–194, 2005.

[48] H. Shi, *Finite element modeling of soft tissue deformation*. University of Louisville, 2007. Accessed: Jan. 18, 2024. [Online]. Available: https://search.proquest.com/openview/8ef83596920033add0a0dff5ff2ea506/1?pq-origsite=gscholar&cbl=18750

[49] T. D. Jayathungage Don, S. Safaei, G. D. Maso Talou, P. S. Russell, A. R. J. Phillips, and H. M. Reynolds, 'Computational fluid dynamic modeling of the lymphatic system: a review of existing models and future directions', *Biomech. Model. Mechanobiol.*, vol. 23, no. 1, pp. 3–22, Feb. 2024, doi: 10.1007/s10237-023-01780-9.

[50] S. Misra, K. T. Ramesh, and A. M. Okamura, 'Modeling of tool-tissue interactions for computer-based surgical simulation: A literature review', *Presence*, vol. 17, no. 5, pp. 463–491, 2008.

[51] J. Zhang, C. Jiao, D. Zou, N. Ta, and Z. Rao, 'Assigning viscoelastic and hyperelastic properties to the middle-ear soft tissues for sound transmission', *Biomech. Model. Mechanobiol.*, vol. 19, pp. 957–970, 2020.

[52] I. Bujoreanu and V. Gupta, 'Anatomy, lymph nodes', 2020, Accessed: Dec. 30, 2024. [Online]. Available: https://europepmc.org/article/nbk/nbk557717

[53] D. Feller–Kopman and A. Ernst, 'Bronchoscopic Needle Aspiration (BNA) and biopsy: Pro: BNA requires routine use of real-time imaging', *J. Bronchol. Interv. Pulmonol.*, vol. 8, no. 4, pp. 309–313, 2001.

[54] C. Chen and J.-A. Huang, 'How to increase the yield of transbronchial needle aspiration (TBNA)?', *J. Thorac. Dis.*, vol. 7, no. Suppl 4, p. S238, 2015.

[55] H. Dirol, U. Ruşen, and C. Sadullahoğlu, 'Comparison of 21 G and 22 G EBUS TBNA Needles Diagnostic Value in Mediastinal and Hilar Lymph Nodes', *Acta Medica Alanya*, vol. 4, no. 3, pp. 226–229, 2020.

[56] J. Saji *et al.*, 'Comparison of 21-gauge and 22-gauge needles for endobronchial ultrasound-guided transbronchial needle aspiration of mediastinal and hilar lymph nodes', *J. Bronchol. Interv. Pulmonol.*, vol. 18, no. 3, pp. 239–246, 2011.

[57] U. Chaddha, R. Ronaghi, W. Elatre, C.-F. Chang, and R. Mahdavi, 'Comparison of sample adequacy and diagnostic yield of 19-and 22-G EBUS-TBNA needles', *J. Bronchol. Interv. Pulmonol.*, vol. 25, no. 4, pp. 264–268, 2018.

[58] C. Dooms *et al.*, 'A randomized clinical trial of flex 19G needles versus 22G needles for endobronchial ultrasonography in suspected lung cancer', *Respiration*, vol. 96, no. 3, pp. 275–282, 2018.

[59] T. Sakai *et al.*, 'Comparison of the efficiency of endobronchial ultrasound-guided transbronchial needle aspiration using a 22G needle versus 25G needle for the diagnosis of lymph node metastasis in patients with lung cancer: a prospective randomized, crossover study', *Transl. Lung Cancer Res.*, vol. 10, no. 9, p. 3745, 2021.

[60] C. Di Felice, B. Young, and M. Matta, 'Comparison of specimen adequacy and diagnostic accuracy of a 25-gauge and 22-gauge needle in endobronchial ultrasound-guided transbronchial needle aspiration', *J. Thorac. Dis.*, vol. 11, no. 8, p. 3643, 2019.

[61] R. Sood *et al.*, 'Comparison of sample adequacy and diagnostic yield of the 21-G and 25-G EBUS TBNA needles', *J. Bronchol. Interv. Pulmonol.*, vol. 29, no. 1, pp. 34–38, 2022.

[62] X. Lin *et al.*, 'Randomized controlled trial to evaluate the utility of suction and inner-stylet of EBUS-TBNA for mediastinal and hilar lymphadenopathy', *BMC Pulm. Med.*, vol. 18, no. 1, p. 192, Dec. 2018, doi: 10.1186/s12890-018-0751-0.

[63] A. C. Griffin, L. E. Schwartz, and Z. W. Baloch, 'Utility of on-site evaluation of endobronchial ultrasound-guided transbronchial needle aspiration specimens', *Cytojournal*, vol. 8, 2011, Accessed: Jan. 18, 2024. [Online]. Available: https://www.ncbi.nlm.nih.gov/pmc/articles/PMC3229807/

[64] L. Righi *et al.*, 'Endobronchial ultrasound-guided transbronchial needle aspiration (EBUS-TBNA)—from morphology to molecular testing', *J. Thorac. Dis.*, vol. 9, no. Suppl 5, p. S395, 2017.

[65] M. Oki *et al.*, 'Rapid on-site cytologic evaluation during endobronchial ultrasound-guided transbronchial needle aspiration for diagnosing lung cancer: a randomized study', *Respiration*, vol. 85, no. 6, pp. 486–492, 2013.

[66] L. Yarmus, T. Van der Kloot, N. Lechtzin, M. Napier, D. Dressel, and D. Feller-Kopman, 'A randomized prospective trial of the utility of rapid on-site evaluation of transbronchial needle aspirate specimens', *J. Bronchol. Interv. Pulmonol.*, vol. 18, no. 2, pp. 121–127, 2011.

[67] I. S. Sehgal, S. Dhooria, A. N. Aggarwal, and R. Agarwal, 'Impact of rapid on-site cytological evaluation (ROSE) on the diagnostic yield of transbronchial needle aspiration during mediastinal lymph node sampling: systematic review and meta-analysis', *Chest*, vol. 153, no. 4, pp. 929–938, 2018.

[68] A. Bandiera and G. Arrigoni, 'The impact of pathological analysis on endobronchial ultrasound diagnostic accuracy', *Mediastinum*, vol. 4, 2020, Accessed: Jan. 18, 2024. [Online]. Available: https://www.ncbi.nlm.nih.gov/pmc/articles/PMC8794421/

[69] J. Z. Moore, Q. Zhang, C. S. McGill, H. Zheng, P. W. McLaughlin, and A. J. Shih, 'Modeling of the plane needle cutting edge rake and inclination angles for biopsy', 2010, Accessed: Jan. 21, 2024. [Online]. Available: https://asmedigitalcollection.asme.org/manufacturingscience/article-abstract/132/5/051005/456236?casa_token=yzUfcKlY3FEAAAAA:IlcIp_B-SEzZYtXuOm8Y5w6qbS17srGA85wj6HRx_VcQhwSc_TrCDouCUz9kxSqB2M_8CCC7

[70] A. M. Okamura, C. Simone, and M. D. O'leary, 'Force modeling for needle insertion into soft tissue', *IEEE Trans. Biomed. Eng.*, vol. 51, no. 10, pp. 1707–1716, 2004.

[71] M. G. Jushiddi *et al.*, 'Simulation of biopsy bevel-tipped needle insertion into soft-gel', *Comput. Biol. Med.*, vol. 111, p. 103337, 2019.

[72] M. Giovannini, J. Cao, and K. Ehmann, 'Design and models of helical needle geometries for core biopsies', *J. Mech. Behav. Biomed. Mater.*, vol. 90, pp. 113–124, 2019.

[73] J. Z. Moore, 'Tissue cutting in needle biopsy', PhD Thesis, University of Michigan, 2011. Accessed: Jan. 21, 2024. [Online]. Available: https://search.proquest.com/openview/38219283ec78bb9fe830eedf3b8a38ce/1?pq-origsite=gscholar&cbl=18750

[74] P. Han and K. Ehmann, 'Study of the effect of cannula rotation on tissue cutting for needle biopsy', *Med. Eng. Phys.*, vol. 35, no. 11, pp. 1584–1590, 2013.

[75] L. Hirsch, M. Gibney, J. Berube, and J. Manocchio, 'Impact of a Modified Needle Tip Geometry on Penetration Force as Well as Acceptability, Preference, and Perceived Pain in Subjects with Diabetes', *J. Diabetes Sci. Technol.*, vol. 6, no. 2, pp. 328–335, Mar. 2012, doi: 10.1177/193229681200600216.

[76] I. I. El Hajj *et al.*, 'Prospective assessment of the performance of a new fine needle biopsy device for EUS-guided sampling of solid lesions', *Clin. Endosc.*, vol. 51, no. 6, pp. 576–583, 2018.

[77] C. Creton and M. Ciccotti, 'Fracture and adhesion of soft materials: a review', *Rep. Prog. Phys.*, vol. 79, no. 4, p. 046601, 2016.

[78] D. B. MacManus, B. Pierrat, J. G. Murphy, and M. D. Gilchrist, 'Dynamic mechanical properties of murine brain tissue using micro-indentation', *J. Biomech.*, vol. 48, no. 12, pp. 3213–3218, 2015.

[79] E. Perra *et al.*, 'Ultrasonic actuation of a fine-needle improves biopsy yield', *Sci. Rep.*, vol. 11, no. 1, p. 8234, 2021.

[80] R. Cleary, R. Wallace, H. Simpson, G. Kontorinis, and M. Lucas, 'A longitudinal-torsional mode ultrasonic needle for deep penetration into bone', *Ultrasonics*, vol. 124, p. 106756, Aug. 2022, doi: 10.1016/j.ultras.2022.106756.

[81] R. Cleary, A. Mathieson, R. Wallace, H. Simpson, and M. Lucas, 'Design of a Slender Tuned Ultrasonic Needle for Bone Penetration', *Phys. Procedia*, vol. 70, pp. 10–13, Jan. 2015, doi: 10.1016/j.phpro.2015.08.005.

[82] C. Creton and M. Ciccotti, 'Fracture and adhesion of soft materials: a review', *Rep. Prog. Phys.*, vol. 79, no. 4, p. 046601, 2016.

[83] D. B. MacManus, B. Pierrat, J. G. Murphy, and M. D. Gilchrist, 'Dynamic mechanical properties of murine brain tissue using micro-indentation', *J. Biomech.*, vol. 48, no. 12, pp. 3213–3218, 2015.

[84] Q. S. Li, G. Y. Lee, C. N. Ong, and C. T. Lim, 'AFM indentation study of breast cancer cells', *Biochem. Biophys. Res. Commun.*, vol. 374, no. 4, pp. 609–613, 2008.

[85] D. M. Ebenstein and L. A. Pruitt, 'Nanoindentation of soft hydrated materials for application to vascular tissues', *J. Biomed. Mater. Res. A*, vol. 69A, no. 2, pp. 222–232, May 2004, doi: 10.1002/jbm.a.20096.

[86] E. Moeendarbary and A. R. Harris, 'Cell mechanics: principles, practices, and prospects', *WIREs Syst. Biol. Med.*, vol. 6, no. 5, pp. 371–388, Sep. 2014, doi: 10.1002/wsbm.1275.

[87] H. Wang, *Theory of linear poroelasticity with applications to geomechanics and hydrogeology*, vol. 2. Princeton university press, 2000. Accessed: Jan. 23, 2026. [Online]. Available: https://books.google.com/books?hl=en&lr=&id=S5MAg7VrAukC&oi=fnd&pg=PR3&dq=H.+Wang,+Theory+of+linear+poroelasticity+with+applications+to+geomechanics+and+hydrogeology,+vol.+2.+Princeton+university+press,+2000.+Accessed:+Mar.+27,+2024.+%5BOnline%5D.+Available:+https://books.google.com/books%3Fhl%3Den%26lr%3D%26id%3DS5MAg7VrAukC%26oi%3Dfnd%26pg%3DPR3%26dq%3DWang,%2BH.F.%2BTheory%2Bof%2BLinear%2BPoroelasticity%2Bwith%2BApplications%2Bto%2BGeomechanics%2Band%2BHydrogeology%253B%2BPrinceton%2BUniversity%2BPress:%2BPrinceton,%2BNJ,%2BUSA,%2B2017%26ots%3Dh4AsKqF7Hd%26sig%3DZiJ1Yyb8WHHlxPzXLSTpMIjQJkM&ots=h4FAGwA7zb&sig=31RHZLIX4mz0j7VI_XhBONZQ_yM

[88] L. Falland-Cheung, M. Scholze, N. Hammer, J. N. Waddell, D. C. Tong, and P. A. Brunton, 'Elastic behavior of brain simulants in comparison to porcine brain at different loading velocities', *J. Mech. Behav. Biomed. Mater.*, vol. 77, pp. 609–615, 2018.

[89] M. L. Crichton, X. Chen, H. Huang, and M. A. Kendall, 'Elastic modulus and viscoelastic properties of full thickness skin characterised at micro scales', *Biomaterials*, vol. 34, no. 8, pp. 2087–2097, 2013.

[90] H. Wang, *Theory of linear poroelasticity with applications to geomechanics and hydrogeology*, vol. 2. Princeton university press, 2000. Accessed: Mar. 27, 2024. [Online]. Available: https://books.google.com/books?hl=en&lr=&id=S5MAg7VrAukC&oi=fnd&pg=PR3&dq=Wang,+H.F.+Theory+of+Linear+Poroelasticity+with+Applications+to+Geomechanics+and+Hydrogeology%3B+Princeton+University+Press:+Princeton,+NJ,+USA,+2017&ots=h4AsKqF7Hd&sig=ZiJ1Yyb8WHHlxPzXLSTpMIjQJkM

[91] M. L. Oyen, T. A. Shean, D. G. Strange, and M. Galli, 'Size effects in indentation of hydrated biological tissues', *J. Mater. Res.*, vol. 27, no. 1, pp. 245–255, 2012.

[92] Q. Li *et al.*, 'Micromechanical anisotropy and heterogeneity of the meniscus extracellular matrix', *Acta Biomater.*, vol. 54, pp. 356–366, 2017.

[93] A. T. Anderson *et al.*, 'Observation of direction-dependent mechanical properties in the human brain with multi-excitation MR elastography', *J. Mech. Behav. Biomed. Mater.*, vol. 59, pp. 538–546, 2016.

[94] P. Duan *et al.*, 'How cell culture conditions affect the microstructure and nanomechanical properties of extracellular matrix formed by immortalized human mesenchymal stem cells: An experimental and modelling study', *Mater. Sci. Eng. C*, vol. 89, pp. 149–159, 2018.

[95] Y. Feng, R. J. Okamoto, R. Namani, G. M. Genin, and P. V. Bayly, 'Measurements of mechanical anisotropy in brain tissue and implications for transversely isotropic material models of white matter', *J. Mech. Behav. Biomed. Mater.*, vol. 23, pp. 117–132, 2013.

[96] M. Griffin, Y. Premakumar, A. Seifalian, P. E. Butler, and M. Szarko, 'Biomechanical characterization of human soft tissues using indentation and tensile testing', *JoVE J. Vis. Exp.*, no. 118, p. e54872, 2016.

[97] M. Scholze *et al.*, 'Utilization of 3D printing technology to facilitate and standardize soft tissue testing', *Sci. Rep.*, vol. 8, no. 1, p. 11340, 2018.

[98] R. Akhtar, M. J. Sherratt, J. K. Cruickshank, and B. Derby, 'Characterizing the elastic properties of tissues', *Mater. Today*, vol. 14, no. 3, pp. 96–105, 2011.

[99] Y. M. Efremov, T. Okajima, and A. Raman, 'Measuring viscoelasticity of soft biological samples using atomic force microscopy', *Soft Matter*, vol. 16, no. 1, pp. 64–81, 2020.

[100] M. Scholze *et al.*, 'Utilization of 3D printing technology to facilitate and standardize soft tissue testing', *Sci. Rep.*, vol. 8, no. 1, p. 11340, 2018.

[101] M. L. Oyen, 'Mechanical characterisation of hydrogel materials', *Int. Mater. Rev.*, vol. 59, no. 1, pp. 44–59, Jan. 2014, doi: 10.1179/1743280413Y.0000000022.

[102] J. Yang, M. Hu, Z. Han, D. Zhao, and T. Qin, 'A novel elimination method of preloading force on the unconfined compression tests of soft tissue', *Adv. Mech. Eng.*, vol. 13, no. 4, p. 168781402110106, Apr. 2021, doi: 10.1177/16878140211010645.

[103] L. Qian and H. Zhao, 'Nanoindentation of soft biological materials', *Micromachines*, vol. 9, no. 12, p. 654, 2018.

[104] T. Chudoba, P. Schwaller, R. Rabe, J.-M. Breguet, and J. Michler, 'Comparison of nanoindentation results obtained with Berkovich and cube-corner indenters', *Philos. Mag.*, vol. 86, no. 33–35, pp. 5265–5283, Nov. 2006, doi: 10.1080/14786430600746424.

[105] J. J. Kruzic, D. K. Kim, K. J. Koester, and R. O. Ritchie, 'Indentation techniques for evaluating the fracture toughness of biomaterials and hard tissues', *J. Mech. Behav. Biomed. Mater.*, vol. 2, no. 4, pp. 384–395, 2009.

[106] J. Chen, 'On the determination of coating toughness during nanoindentation', *Surf. Coat. Technol.*, vol. 206, no. 13, pp. 3064–3068, 2012.

[107] P. Duan, S. Bull, and J. Chen, 'Modeling the nanomechanical responses of biopolymer composites during the nanoindentation', *Thin Solid Films*, vol. 596, pp. 277–281, 2015.

[108] L. Qian *et al.*, 'Influence of strain rate on indentation response of porcine brain', *J. Mech. Behav. Biomed. Mater.*, vol. 82, pp. 210–217, 2018.

[109] A. D. Ozkan, A. E. Topal, F. B. Dikecoglu, M. O. Guler, A. Dana, and A. B. Tekinay, 'Probe microscopy methods and applications in imaging of biological materials', in *Seminars in cell & developmental biology*, Elsevier, 2018, pp. 153–164. Accessed: Apr. 28, 2024. [Online]. Available: https://www.sciencedirect.com/science/article/pii/S1084952117301921

[110] J. Chen, 'Nanobiomechanics of living cells: a review', *Interface Focus*, vol. 4, no. 2, p. 20130055, Apr. 2014, doi: 10.1098/rsfs.2013.0055.

[111] W. C. Oliver and G. M. Pharr, 'Measurement of hardness and elastic modulus by instrumented indentation: Advances in understanding and refinements to methodology', *J. Mater. Res.*, vol. 19, no. 1, pp. 3–20, 2004.

[112] J. Hay, 'INTRODUCTION TO INSTRUMENTED INDENTATION TESTING', *Exp. Tech.*, vol. 33, no. 6, pp. 66–72, Nov. 2009, doi: 10.1111/j.1747-1567.2009.00541.x.

[113] A. J. M. Spencer, 'Constitutive Theory for Strongly Anisotropic Solids', in *Continuum Theory of the Mechanics of Fibre-Reinforced Composites*, A. J. M. Spencer, Ed., Vienna: Springer Vienna, 1984, pp. 1–32. doi: 10.1007/978-3-7091-4336-0_1.

[114] A. Ali, M. Hosseini, and B. B. Sahari, 'A review of constitutive models for rubber-like materials', *Am. J. Eng. Appl. Sci.*, vol. 3, no. 1, pp. 232–239, 2010.

[115] A. J. M. Spencer, 'Constitutive Theory for Strongly Anisotropic Solids', in *Continuum Theory of the Mechanics of Fibre-Reinforced Composites*, A. J. M. Spencer, Ed., Vienna: Springer Vienna, 1984, pp. 1–32. doi: 10.1007/978-3-7091-4336-0_1.

[116] G. Limbert and M. Taylor, 'On the constitutive modeling of biological soft connective tissues: a general theoretical framework and explicit forms of the tensors of elasticity for strongly anisotropic continuum fiber-reinforced composites at finite strain', *Int. J. Solids Struct.*, vol. 39, no. 8, pp. 2343–2358, 2002.

[117] J. A. Weiss, B. N. Maker, and S. Govindjee, 'Finite element implementation of incompressible, transversely isotropic hyperelasticity', *Comput. Methods Appl. Mech. Eng.*, vol. 135, no. 1–2, pp. 107–128, 1996.

[118] A. Natali, P. Pavan, and E. L. Carniel, 'Damage phenomena in anisotropic soft biological tissues: a constitutive formulation', *Russ. J. Biomech.*, vol. 8, pp. 43–60, 2004.

[119] M. Shahzad, A. Kamran, M. Z. Siddiqui, and M. Farhan, 'Mechanical characterization and FE modelling of a hyperelastic material', *Mater. Res.*, vol. 18, pp. 918–924, 2015.

[120] G. Chagnon, G. Marckmann, and E. Verron, 'A comparison of the Hart-Smith model with Arruda-Boyce and Gent formulations for rubber elasticity', *Rubber Chem. Technol.*, vol. 77, no. 4, pp. 724–735, 2004.

[121] P. Dolwichai, J. Limtragool, S. Inban, and S. Piyasin, 'Hyperelastic Material Models for Finite Element Analysis with Commercial Rubber', in *Technology and Innovation for Sustainable Development Conference (TISD2006)*, 2006, pp. 25–26.

[122] 'Large elastic deformations of isotropic materials. I. Fundamental concepts', *Philos. Trans. R. Soc. Lond. Ser. Math. Phys. Sci.*, vol. 240, no. 822, pp. 459–490, Jan. 1948, doi: 10.1098/rsta.1948.0002.

[123] O. H. Yeoh, 'Some forms of the strain energy function for rubber', *Rubber Chem. Technol.*, vol. 66, no. 5, pp. 754–771, 1993.

[124] J. S. Bergstrom, *Mechanics of solid polymers: theory and computational modeling*. William Andrew, 2015. Accessed: Mar. 09, 2024. [Online]. Available: https://books.google.com/books?hl=en&lr=&id=DfucBAAAQBAJ&oi=fnd&pg=PP1&dq=Bergstrom,+J.+(2015).+Mechanics+of+solid+polymers:+Theory+and+computational+modeling.+Elsevier.&ots=SVXXrUUSHC&sig=lcvmH51NLnb9Sgca2OXBuNFvzi4

[125] S. Kawabata, Y. Yamashita, H. Ooyama, and S. Yoshida, 'Mechanism of carbon-black reinforcement of rubber vulcanizate', *Rubber Chem. Technol.*, vol. 68, no. 2, pp. 311–329, 1995.

[126] C. Renaud, J.-M. Cros, Z.-Q. Feng, and B. Yang, 'The Yeoh model applied to the modeling of large deformation contact/impact problems', *Int. J. Impact Eng.*, vol. 36, no. 5, pp. 659–666, 2009.

[127] ‘Large deformation isotropic elasticity – on the correlation of theory and experiment for incompressible rubberlike solids’, *Proc. R. Soc. Lond. Math. Phys. Sci.*, vol. 326, no. 1567, pp. 565–584, Feb. 1972, doi: 10.1098/rspa.1972.0026.

[128] M. Sasso, G. Palmieri, G. Chiappini, and D. Amodio, ‘Characterization of hyperelastic rubber-like materials by biaxial and uniaxial stretching tests based on optical methods’, *Polym. Test.*, vol. 27, no. 8, pp. 995–1004, 2008.

[129] D. J. van Gerwen, J. Dankelman, and J. J. van den Dobbelsteen, ‘Needle–tissue interaction forces–A survey of experimental data’, *Med. Eng. Phys.*, vol. 34, no. 6, pp. 665–680, 2012.

[130] H. M. Langevin, D. L. Churchill, J. R. Fox, G. J. Badger, B. S. Garra, and M. H. Krag, ‘Biomechanical response to acupuncture needling in humans’, *J. Appl. Physiol.*, vol. 91, no. 6, pp. 2471–2478, Dec. 2001, doi: 10.1152/jappl.2001.91.6.2471.

[131] D. J. van Gerwen, J. Dankelman, and J. J. van den Dobbelsteen, ‘Needle–tissue interaction forces–A survey of experimental data’, *Med. Eng. Phys.*, vol. 34, no. 6, pp. 665–680, 2012.

[132] A. P. S. Selvadurai, ‘Deflections of a rubber membrane’, *J. Mech. Phys. Solids*, vol. 54, no. 6, pp. 1093–1119, 2006.

[133] Y. Kobayashi, T. Sato, and M. G. Fujie, ‘Modeling of friction force based on relative velocity between liver tissue and needle for needle insertion simulation’, in *2009 Annual International Conference of the IEEE Engineering in Medicine and Biology Society*, IEEE, 2009, pp. 5274–5278. Accessed: Mar. 14, 2024. [Online]. Available: https://ieeexplore.ieee.org/abstract/document/5334078/

[134] A. P. S. Selvadurai, ‘Deflections of a rubber membrane’, *J. Mech. Phys. Solids*, vol. 54, no. 6, pp. 1093–1119, 2006.

[135] M. Mahvash and P. E. Dupont, ‘Fast needle insertion to minimize tissue deformation and damage’, in *2009 IEEE International Conference on Robotics and Automation*, IEEE,

2009, pp. 3097–3102. Accessed: Jan. 28, 2026. [Online]. Available: https://ieeexplore.ieee.org/abstract/document/5152617/

[136] O. A. Shergold and N. A. Fleck, 'Experimental investigation into the deep penetration of soft solids by sharp and blunt punches, with application to the piercing of skin', 2005, Accessed: Jan. 28, 2026. [Online]. Available: https://asmedigitalcollection.asme.org/biomechanical/article-abstract/127/5/838/447096

[137] T. Azar and V. Hayward, 'Estimation of the Fracture Toughness of Soft Tissue from Needle Insertion', in *Biomedical Simulation*, vol. 5104, F. Bello and P. J. E. Edwards, Eds., in Lecture Notes in Computer Science, vol. 5104. , Berlin, Heidelberg: Springer Berlin Heidelberg, 2008, pp. 166–175. doi: 10.1007/978-3-540-70521-5_18.

[138] C. T. Nguyen, T. Vu-Khanh, P. I. Dolez, and J. Lara, 'Puncture of elastomer membranes by medical needles. Part I: Mechanisms', *Int. J. Fract.*, vol. 155, no. 1, pp. 75–81, Jan. 2009, doi: 10.1007/s10704-009-9326-7.

[139] Y. Kobayashi, A. Onishi, T. Hoshi, K. Kawamura, and M. G. Fujie, 'Modeling of conditions where a puncture occurs during needle insertion considering probability distribution', in *2008 IEEE/RSJ International Conference on Intelligent Robots and Systems*, IEEE, 2008, pp. 1433–1440. Accessed: Jan. 28, 2026. [Online]. Available: https://ieeexplore.ieee.org/abstract/document/4650874/

[140] T. Azar and V. Hayward, 'Estimation of the Fracture Toughness of Soft Tissue from Needle Insertion', in *Biomedical Simulation*, vol. 5104, F. Bello and P. J. E. Edwards, Eds., in Lecture Notes in Computer Science, vol. 5104. , Berlin, Heidelberg: Springer Berlin Heidelberg, 2008, pp. 166–175. doi: 10.1007/978-3-540-70521-5_18.

[141] J. T. Hing, A. D. Brooks, and J. P. Desai, 'A biplanar fluoroscopic approach for the measurement, modeling, and simulation of needle and soft-tissue interaction', *Med. Image Anal.*, vol. 11, no. 1, pp. 62–78, 2007.

[142] L. E. Millon, H. Mohammadi, and W. K. Wan, 'Anisotropic polyvinyl alcohol hydrogel for cardiovascular applications', *J. Biomed. Mater. Res. B Appl. Biomater.*, vol. 79B, no. 2, pp. 305–311, Nov. 2006, doi: 10.1002/jbm.b.30543.

[143] A. S. Maiolo, M. N. Amado, J. S. Gonzalez, and V. A. Alvarez, 'Development and characterization of poly (vinyl alcohol) based hydrogels for potential use as an articular cartilage replacement', *Mater. Sci. Eng. C*, vol. 32, no. 6, pp. 1490–1495, 2012.

[144] W. Li, D. Wang, W. Yang, and Y. Song, 'Compressive mechanical properties and microstructure of PVA–HA hydrogels for cartilage repair', *RSC Adv.*, vol. 6, no. 24, pp. 20166–20172, 2016.

[145] J. Y. Chang *et al.*, *Biopolymers· PVA hydrogels anionic polymerisation Nanocomposites*, vol. 153. Springer, 2003. Accessed: Jan. 29, 2026. [Online]. Available: https://books.google.com/books?hl=en&lr=&id=MwdqCQAAQBAJ&oi=fnd&pg=PR3&dq=J.+Y.+Chang+et+al.,+Biopolymers%C2%B7+PVA+hydrogels+anionic+polymerisation+Nanocomposites,+vol.+153.+Springer+Science+%26+Business+Media,+2000.+Accessed:+Nov.+22,+2024.+%5BOnline%5D.+Available:+https://books.google.com/books%3Fhl%3Den%26lr%3D%26id%3DlI1FWBPNSJ8C%26oi%3Dfnd%26pg%3DPR3%26dq%3DChang,%2BC.%2B(Ed.).%2B(2000).%2BBiopolymers,%2BPVA%2Bhydrogels,%2Banionic%2Bpolymerisation,%2Bnanocomposites.%2B%2BSpringer%26ots%3D0kKLmZuiqE%26sig%3DHhmBj37JhTJjLgCTAN9GAUUOEMQ&ots=q4zmYOYqu3&sig=mVBG0ksyjgm4d5D_q-KqO7al6Xs

[146] R. Ricciardi, F. Auriemma, C. Gaillet, C. De Rosa, and F. Lauprêtre, 'Investigation of the Crystallinity of Freeze/Thaw Poly(vinyl alcohol) Hydrogels by Different Techniques', *Macromolecules*, vol. 37, no. 25, pp. 9510–9516, Dec. 2004, doi: 10.1021/ma048418v.

[147] N. A. Peppas, 'Turbidimetric studies of aqueous poly(vinyl alcohol) solutions', *Makromol. Chem.*, vol. 176, no. 11, pp. 3433–3440, Nov. 1975, doi: 10.1002/macp.1975.021761125.

[148] N. A. Peppas, ‘Turbidimetric studies of aqueous poly(vinyl alcohol) solutions’, *Makromol. Chem.*, vol. 176, no. 11, pp. 3433–3440, Nov. 1975, doi: 10.1002/macp.1975.021761125.

[149] R. Ricciardi, F. Auriemma, C. Gaillet, C. De Rosa, and F. Lauprêtre, ‘Investigation of the Crystallinity of Freeze/Thaw Poly(vinyl alcohol) Hydrogels by Different Techniques’, *Macromolecules*, vol. 37, no. 25, pp. 9510–9516, Dec. 2004, doi: 10.1021/ma048418v.

[150] R. de Castro Ramos and M. Nosti Vega, ‘The caper (Capparis spinosa L.)’, *Grasas Aceites Spain*, vol. 38, no. 3, 1987, Accessed: Nov. 22, 2024. [Online]. Available: https://agris.fao.org/search/en/providers/122599/records/6471c2fc2a40512c710e25ff

[151] E. P. Judge, J. M. L. Hughes, J. J. Egan, M. Maguire, E. L. Molloy, and S. O’Dea, ‘Anatomy and Bronchoscopy of the Porcine Lung. A Model for Translational Respiratory Medicine’, *Am. J. Respir. Cell Mol. Biol.*, vol. 51, no. 3, pp. 334–343, Sep. 2014, doi: 10.1165/rcmb.2013-0453TR.

[152] K. Kazimierska-Drobny, M. El Fray, and M. Kaczmarek, ‘Determination of mechanical and hydraulic properties of PVA hydrogels’, *Mater. Sci. Eng. C*, vol. 48, pp. 48–54, Mar. 2015, doi: 10.1016/j.msec.2014.11.034.

[153] ‘Compressive Mechanical Behavior of Partially Oxidized Polyvinyl Alcohol Hydrogels for Cartilage Tissue Repair - PMC’. Accessed: May 24, 2026. [Online]. Available: https://pmc.ncbi.nlm.nih.gov/articles/PMC9774902/?utm_source=chatgpt.com

[154] A. S. Oliveira, O. Seidi, N. Ribeiro, R. Colaço, and A. P. Serro, ‘Tribomechanical comparison between PVA hydrogels obtained using different processing conditions and human cartilage’, *Materials*, vol. 12, no. 20, p. 3413, 2019.

[155] M. L. Oyen, ‘Mechanical characterisation of hydrogel materials’, *Int. Mater. Rev.*, vol. 59, no. 1, pp. 44–59, Jan. 2014, doi: 10.1179/1743280413Y.0000000022.

[156] O. Comas, ‘Real-time Soft Tissue Modelling on GPU for Medical Simulation’, PhD Thesis, Université des Sciences et Technologie de Lille-Lille I, 2010. Accessed: Jun. 02, 2024. [Online]. Available: https://theses.hal.science/tel-00561299/

[157] T. Siwowski, H. Zobel, T. Al-Khafaji, and W. Karwowski, ‘1 FRP bridges in Poland: state of practice’, *Arch. Civ. Eng.*, vol. 67, no. 3, pp. 5–27, 2021.

[158] ‘ABAQUS Vs ANSYS : Difference Between Ansys And Abaqus ✔- CAE Assistant’. Accessed: Jun. 02, 2024. [Online]. Available: https://caeassistant.com/abaqus/

[159] S. F. Gibson and B. Mirtich, ‘A survey of deformable modeling in computer graphics’, Technical report, Mitsubishi Electric Research Laboratories, 1997. Accessed: Jun. 02, 2024. [Online]. Available: https://www.merl.com/publications/docs/TR97-19.pdf

[160] G. S. P. Miller, ‘The motion dynamics of snakes and worms’, in *Proceedings of the 15th annual conference on Computer graphics and interactive techniques*, ACM, Jun. 1988, pp. 169–173. doi: 10.1145/54852.378508.

[161] K. Golec, ‘Hybrid 3D mass spring system for soft tissue simulation’, PhD Thesis, Université de Lyon, 2018. Accessed: Jun. 02, 2024. [Online]. Available: https://theses.hal.science/tel-01761851/

[162] B. Lloyd, G. Székely, and M. Harders, ‘Identification of spring parameters for deformable object simulation’, *IEEE Trans. Vis. Comput. Graph.*, vol. 13, no. 5, pp. 1081–1094, 2007.

[163] B. J. Mac Donald, *Practical stress analysis with finite elements*. Glasnevin publishing, 2007. Accessed: Jun. 02, 2024. [Online]. Available: https://dl.acm.org/doi/abs/10.5555/1543305

[164] D. Terzopoulos, J. Platt, and K. Fleischer, ‘Heating and melting deformable models’, *J. Vis. Comput. Animat.*, vol. 2, no. 2, pp. 68–73, Apr. 1991, doi: 10.1002/vis.4340020208.

[165] H. N. Onah, ‘Different element methods in engineering practice’, *Niger. J. Technol.*, vol. 31, no. 3, pp. 288–292, 2012.

[166] C. A. Brebbia, D. Howard, and A. Peters, *Applications of supercomputers in engineering II*. Springer Science & Business Media, 2012. Accessed: Jun. 02, 2024. [Online]. Available: https://books.google.com/books?hl=en&lr=&id=bU-qCAAAQBAJ&oi=fnd&pg=PA3&dq=.+Brebbia,+C.A.,+Honard,+D.+and+Peters+A.+Applications+of+super+computers+in+Engineering+II.+Computational+Mechanics+Publications,+Boston+USA,+1991.&ots=rIppH0ISOd&sig=YWfL61uJ3LIR_1HEvkpiVG2qj7U

[167] A. Harish, 'Implicit vs. Explicit FEM: What Is the Difference?', SimScale. Accessed: Jun. 02, 2024. [Online]. Available: https://www.simscale.com/blog/implicit-vs-explicit-fem/

[168] N. Rebelo, J. C. Nagtegaal, and L. M. Taylor, 'Comparison of implicit and explicit finite element methods in the simulation of metal forming processes', ABAQUS USERS CONFERENCE, 1992. Accessed: Jun. 02, 2024. [Online]. Available: https://www.sid.ir/paper/596501/en

[169] TheAlmightyBeak, 'Euler's Equations Simulation by TheAlmightyBeak | SimScale'. Accessed: Jun. 02, 2024. [Online]. Available: https://www.simscale.com/projects/TheAlmightyBeak/euler-s_equations_simulation/

[170] M. Zohrevand, 'A Comparison of Different Solvers in ABAQUS', HyperLyceum. Accessed: Jun. 02, 2024. [Online]. Available: https://hyperlyceum.com/a-comparison-of-different-solvers-in-abaqus/

[171] DOCAN, 'Explicit vs implicit FEA: What's the difference?', DOCAN. Accessed: Jun. 02, 2024. [Online]. Available: https://docanco.com/explicit-vs-implicit-fea/

[172] Ł. S. Ph.D, 'Difference Between Implicit vs Explicit Analysis', Enterfea. Accessed: Jun. 02, 2024. [Online]. Available: https://enterfea.com/implicit-vs-explicit/

[173] P. Han, D. Che, K. Pallav, and K. Ehmann, 'Models of the cutting edge geometry of medical needles with applications to needle design', *Int. J. Mech. Sci.*, vol. 65, no. 1, pp. 157–167, 2012.

[174] Z. F. Rad, P. D. Prewett, and G. J. Davies, 'An overview of microneedle applications, materials, and fabrication methods', *Beilstein J. Nanotechnol.*, vol. 12, no. 1, pp. 1034–1046, 2021.

[175] R. Krithiga and P. Geetha, 'Breast Cancer Detection, Segmentation and Classification on Histopathology Images Analysis: A Systematic Review', *Arch. Comput. Methods Eng.*, vol. 28, no. 4, pp. 2607–2619, Jun. 2021, doi: 10.1007/s11831-020-09470-w.

[176] E. Peña, A. Pérez Del Palomar, B. Calvo, M. A. Martínez, and M. Doblaré, 'Computational Modelling of Diarthrodial Joints. Physiological, Pathological and Pos-Surgery Simulations', *Arch. Comput. Methods Eng.*, vol. 14, no. 1, pp. 47–91, Mar. 2007, doi: 10.1007/s11831-006-9001-3.

[177] P. Dixit and G. R. Liu, 'A Review on Recent Development of Finite Element Models for Head Injury Simulations', *Arch. Comput. Methods Eng.*, vol. 24, no. 4, pp. 979–1031, Nov. 2017, doi: 10.1007/s11831-016-9196-x.

[178] F. Casanova, P. R. Carney, and M. Sarntinoranont, 'In vivo evaluation of needle force and friction stress during insertion at varying insertion speed into the brain', *J. Neurosci. Methods*, vol. 237, pp. 79–89, 2014.

[179] T. L. de Jong, L. H. Pluymen, D. J. van Gerwen, G.-J. Kleinrensink, J. Dankelman, and J. J. van den Dobbelsteen, 'PVA matches human liver in needle-tissue interaction', *J. Mech. Behav. Biomed. Mater.*, vol. 69, pp. 223–228, 2017.

[180] H. Mohammadi, A. Ebrahimian, and N. Maftoon, 'Finite-Element Modelling of Needle-Tissue Interactions', *Arch. Comput. Methods Eng.*, vol. 31, no. 3, pp. 1363–1404, 2024.

[181] C. Gokgol, C. Basdogan, and D. Canadinc, 'Estimation of fracture toughness of liver tissue: Experiments and validation', *Med. Eng. Phys.*, vol. 34, no. 7, pp. 882–891, 2012.

[182] L. Jiang *et al.*, 'Research on insertion process of medical needle', in *2016 3rd International Conference on Materials Engineering, Manufacturing Technology and Control*, Atlantis Press, 2016, pp. 779–785. Accessed: May 10, 2024. [Online]. Available: https://www.atlantis-press.com/proceedings/icmemtc-16/25852256

[183] M. Shakoor, V. M. Trejo Navas, D. Pino Munõz, M. Bernacki, and P.-O. Bouchard, 'Computational methods for ductile fracture modeling at the microscale', *Arch. Comput. Methods Eng.*, vol. 26, pp. 1153–1192, 2019.

[184] R. De Borst, 'Numerical aspects of cohesive-zone models', *Eng. Fract. Mech.*, vol. 70, no. 14, pp. 1743–1757, 2003.

[185] L. A. de Oliveira and M. V. Donadon, 'Delamination analysis using cohesive zone model: A discussion on traction-separation law and mixed-mode criteria', *Eng. Fract. Mech.*, vol. 228, p. 106922, 2020.

[186] M. Oldfield, D. Dini, G. Giordano, and F. Rodriguez Y Baena, 'Detailed finite element modelling of deep needle insertions into a soft tissue phantom using a cohesive approach', *Comput. Methods Biomech. Biomed. Engin.*, vol. 16, no. 5, pp. 530–543, May 2013, doi: 10.1080/10255842.2011.628448.

[187] A. M. Habraken and S. Cescotto, 'An automatic remeshing technique for finite element simulation of forming processes', *Int. J. Numer. Methods Eng.*, vol. 30, no. 8, pp. 1503–1525, Dec. 1990, doi: 10.1002/nme.1620300811.

[188] W. Boscheri, 'High order direct Arbitrary-Lagrangian–Eulerian (ALE) finite volume schemes for hyperbolic systems on unstructured meshes', *Arch. Comput. Methods Eng.*, vol. 24, no. 4, pp. 751–801, 2017.

[189] M. Movahhedy, M. S. Gadala, and Y. Altintas, 'Simulation of the orthogonal metal cutting process using an arbitrary Lagrangian–Eulerian finite-element method', *J. Mater. Process. Technol.*, vol. 103, no. 2, pp. 267–275, 2000.

[190] M. Bakroon, R. Daryaei, D. Aubram, and F. Rackwitz, 'Multi-material arbitrary Lagrangian-Eulerian and coupled Eulerian-Lagrangian methods for large deformation geotechnical problems', in *Numerical Methods in Geotechnical Engineering IX, Volume 1*, CRC Press, 2018, pp. 673–681. Accessed: May 11, 2024. [Online]. Available: https://www.taylorfrancis.com/chapters/edit/10.1201/9780429446931-84/multi-

material-arbitrary-lagrangian-eulerian-coupled-eulerian-lagrangian-methods-large-deformation-geotechnical-problems-bakroon-daryaei-aubram-rackwitz

[191] S. Yamaguchi, K. Tsutsui, K. Satake, S. Morikawa, Y. Shirai, and H. T. Tanaka, 'Dynamic analysis of a needle insertion for soft materials: Arbitrary Lagrangian–Eulerian-based three-dimensional finite element analysis', *Comput. Biol. Med.*, vol. 53, pp. 42–47, 2014.

[192] F. Ducobu, E. Rivière-Lorphèvre, and E. Filippi, 'Application of the Coupled Eulerian-Lagrangian (CEL) method to the modeling of orthogonal cutting', *Eur. J. Mech.-ASolids*, vol. 59, pp. 58–66, 2016.

[193] M. G. Jushiddi *et al.*, 'Simulation of biopsy bevel-tipped needle insertion into soft-gel', *Comput. Biol. Med.*, vol. 111, p. 103337, 2019.

[194] G. Qiu, S. Henke, and J. Grabe, 'Applications of Coupled Eulerian-Lagrangian method to geotechnical problems with large deformations', in *Proceeding of SIMULIA customer conference*, 2009, pp. 420–435. Accessed: May 12, 2024. [Online]. Available: https://www.academia.edu/download/90620191/Qiu_SCC2009.pdf

[195] B. N. A. Sowah, 'Mechanical characterization of the human atria based on patient-specific FEM models', 2017, Accessed: May 12, 2024. [Online]. Available: https://repositorio-aberto.up.pt/bitstream/10216/105219/2/199582.pdf

[196] G. Qiu, S. Henke, and J. Grabe, 'Application of a Coupled Eulerian–Lagrangian approach on geomechanical problems involving large deformations', *Comput. Geotech.*, vol. 38, no. 1, pp. 30–39, 2011.

[197] A. Aryal, 'A coupled Eulerian-Lagrangian extended finite element formulation for moving interface problems and damage transport in hyperelastic media', PhD Thesis, 2014. Accessed: May 12, 2024. [Online]. Available: https://ir.vanderbilt.edu/handle/1803/12841

[198] A. Sillem, 'Feasibility study of a tire hydroplaning simulation in a monolithic finite element code using a coupled Eulerian-Lagrangian method', *Delft Univ. Technol.*, 2008,

Accessed: May 12, 2024. [Online]. Available: https://citeseerx.ist.psu.edu/document?repid=rep1&type=pdf&doi=442a44725aa9626467bbd68bfbd695c2bc4440b3

[199] Y. Pan and D. Xiong, 'Study on compressive mechanical properties of nanohydroxyapatite reinforced poly(vinyl alcohol) gel composites as biomaterial', *J. Mater. Sci. Mater. Med.*, vol. 20, no. 6, pp. 1291–1297, Jun. 2009, doi: 10.1007/s10856-008-3679-8.

[200] H. Xu, X. He, F. Shan, G. Niu, and D. Sheng, '3D Simulation of Debris Flows with the Coupled Eulerian–Lagrangian Method and an Investigation of the Runout', *Mathematics*, vol. 11, no. 16, p. 3493, 2023.

[201] M. Mahvash and V. Hayward, 'Haptic rendering of cutting: A fracture mechanics approach', 2001, Accessed: Nov. 29, 2024. [Online]. Available: https://digital.lib.washington.edu/researchworks/handle/1773/34885

[202] A. Lathrop, R. Smith, and R. Webster, 'Needle-membrane puncture mechanics', in *Needle Steering Workshop, MICCAI*, 2008.

[203] A. G. Atkins and Y.-W. Mai, 'Elastic and plastic fracture: metals, polymers, ceramics, composites, biological materials', 1985, Accessed: Nov. 29, 2024. [Online]. Available: https://www.sidalc.net/search/Record/cat-unco-ar-770/Description

[204] J. Z. Moore, P. W. McLaughlin, and A. J. Shih, 'Novel needle cutting edge geometry for end-cut biopsy', *Med. Phys.*, vol. 39, no. 1, pp. 99–108, Jan. 2012, doi: 10.1118/1.3665253.

[205] T. Duerig, A. Pelton, and D. Stöckel, 'An overview of nitinol medical applications', *Mater. Sci. Eng. A*, vol. 273, pp. 149–160, 1999.

[206] W. Li *et al.*, 'Effects of needle inner surface topography on friction and biopsy length', *Int. J. Mech. Sci.*, vol. 119, pp. 412–418, 2016.

[207] W. Li, Y. Wang, V. Nteziyaremye, H. Yamaguchi, and A. J. Shih, 'Measurement of the friction force inside the needle in biopsy', *J. Manuf. Sci. Eng.*, vol. 138, no. 3, p. 031003, 2016.

[208] I. Elishakoff, 'Who developed the so-called Timoshenko beam theory?', *Math. Mech. Solids*, vol. 25, no. 1, pp. 97–116, Jan. 2020, doi: 10.1177/1081286519856931.

[209] N. Abolhassani, R. Patel, and M. Moallem, 'Needle insertion into soft tissue: A survey', *Med. Eng. Phys.*, vol. 29, no. 4, pp. 413–431, 2007.

[210] H. Heers *et al.*, 'The True Ablation Effect of Holmium YAG Laser on Soft Tissue', *J. Endourol.*, vol. 32, no. 3, pp. 245–251, 2018.

[211] T. Kim *et al.*, 'Regional biases in mutation screening due to intratumoural heterogeneity of prostate cancer', *J. Pathol.*, vol. 233, no. 4, pp. 425–435, Aug. 2014, doi: 10.1002/path.4380.

[212] S. P. DiMaio *et al.*, 'A system for MRI-guided prostate interventions', in *The First IEEE/RAS-EMBS International Conference on Biomedical Robotics and Biomechatronics, 2006. BioRob 2006.*, IEEE, 2006, pp. 68–73. Accessed: Dec. 12, 2024. [Online]. Available: https://ieeexplore.ieee.org/abstract/document/1639062/

[213] P. C. Mozer, A. W. Partin, and D. Stoianovici, 'Robotic image-guided needle interventions of the prostate', *Rev. Urol.*, vol. 11, no. 1, p. 7, 2009.

Appendices

Chapter 4 Appendix

Appendix 4.1: Complete calibration process.

The different steps of a complete calibration process are as follows:

- First, install the calibration holder (a) and click the "Calibrate" button to begin load cell calibration. This will open a window, as shown in (b), where the calibration weight (500 g-MA337) can be selected.
- A window will appear, as shown in (c) and (d). The calibration sample should be installed in the centre of the calibration holder.
- After the system acquires the calibration sample's weight, a window will appear in the form shown in (e), and the calibration weight can then be removed.
- Once the calibration weight is removed, the system will automatically update the calibration factor (f).

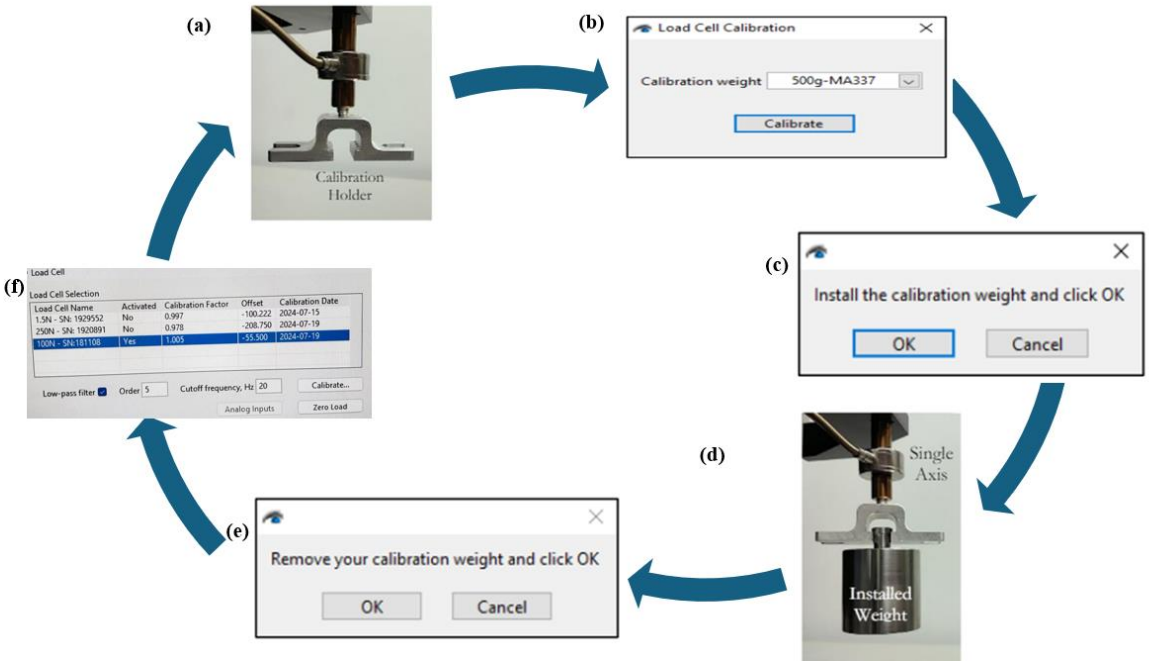

Appendix 4.2: Detailed PVA Hydrogel Preparation

Ingredients	6% crystalline PVA. 200 ml distilled, degassed water. 0.01%/ 0.021g of benzalkonium chloride.
Tools	Magnetic mixer. Temperature control heater. Pipette. Glass rod Temperature meter with wire sensor. 250ml Beaker. Glass conical flask. Cubic mold. Aluminium foil
PPE	Gloves.
Procedures	Weigh PVA crystals according to Table 5.1 or use formula 5.1 shown above to determine the required concentration. Weight the water and pour it into the glass beaker. Use a pipette to add benzalkonium chloride to the water. Add PVA crystals to the beaker and mix it with a glass rod. Place the magnetic mixer inside the beaker. Cover the beaker with an aluminium foil to prevent evaporation, putting the temperature sensor wire inside first. The wire needs to be close to the bottom of the beaker. Place the beaker on the heater. Set the temperature to 50^0C initially and slowly ramp up to around 100-150^0C. Mixer setting should be at about 1-2, making sure the PVA is getting mixed properly. Once 80^0C is reached, which could take about an hour, keep the temperature constant for about 2 hours, adjusting the heater temperature accordingly.

	Higher concentrations of PVA will be a lot thicker and harder to mix, they might require occasional manual mixing to ensure temperature remains consistent throughout. After about 2 hours, the PVA can be taken off the heat and allowed to cool down. This can be safely placed in the fridge while covered to ensure it does not evaporate. The mixture can be poured into a cubic mould and subsequently placed in the freezer for at least 12h, ensuring it is covered. After taking it out and allowing it the thaw for 12h more, usually in the fridge, the first cycle is complete. Repeat the freeze process to achieve the desired cycle.

Appendix 4.3: Complete Compression/Indentation Test Plan

Author: Lyne Raissa Mkoh

Test: Indentation / Compression test plan

Aims: Stress-strain response and mechanical characterisation of different soft materials (PVA hydrogel, large-pickled capers, chicken breast and porcine lymph node of the lung).

1: Test tools

Equipment	➢ Mechanical tester model Mach-1 v500c ➢ Sample holder ➢ 250 N load cell and 500g calibration weight ➢ 1.5 N load cell and 100g calibration weight ➢ Calibration holder ➢ Indenter adaptor. ➢ Indenter tips of 2 mm and 5 mm diameter ➢ 12.5 mm and 31.75 mm Compression flat indenter
Tools	➢ Cutting board ➢ Scalpel knife ➢ Sterile disposable 8 mm biopsy punch (for large, pickled capers). ➢ Digital calliper ➢ Tweezer
PPE	➢ Bluecoat ➢ gloves

2 Sample Preparation

- Cut the chicken breast and the PVA into a 20 mm x 20 mm square in the longitudinal direction.

- Using the 10 mm biopsy punch to sample the large pickled capers.

- 20 samples should be collected for each type of soft tissue.

- Using a digital calliper, measure and record your sample twice on each side: two measurements for the length and two for the width.

3 Choice of Indenter Tip Size

- Indenter diameter (mm): The indenter tip diameter should be $\leq$ 5x the sample thickness for a proper model fit and $\leq 1/5^{th}$ of the sample width to avoid edge effects.

- Indentation amplitude (mm): Indentation should be performed only within the elastic region ($\leq$ 15-20% of sample thickness). The indentation amplitude must be $<$ indenter radius.

4 Calibration

Before performing any type of test on the bio-momentum Mach-1 V500C, calibration is required.

- Turn on the Mach-1 controller and wait until it is initialised.

- Click on the load cell bottom. It will open a window that allows the selection and calibration of a load cell, as well as the selection of a low-pass filter to reduce noise in the load signal.

- All available load cells will be listed, and the activated column will indicate which load cell is active.

- Double-clicking any load cell will activate it, and only one can be active at a time.

- The other 3 columns are generated automatically after the calibration procedure.

- To calibrate a load cell, click the calibrate button. This will open a new window where a calibration weight can be selected from a drop-down list (the name of the calibration weight is usually written on the weight itself or on the bag it came in).

- Click the calibration button and follow the on-screen instructions (first install the calibration holder, being careful not to overload the load cell, then place the calibration weight in the middle portion).

- The calibration factor is always supposed to be within 5% of 1.00, i.e., between 0.95 and 1.05.

5 Thickness Measurement

The thickness of a sample is measured using the 'Find contact' function of the bio-momentum.

a- ''Find Contact".

- The find contact function moves the stage until the available load cells are listed, and the activated column indicates which load cell is active. It then repositions the stage based on the selected stage repositioning option.

- The find contact can be used to measure the exact location of a sample surface or the bottom of the testing chamber, or simply to place an indenter in contact with a sample.

- The stage should move very slowly to avoid overloading the load cell.

- The direction specified indicates whether the stage will move in the positive or negative direction.

- In a positive-displacement system, the vertical stage will move downwards under compression.

- The stage velocity specifies the speed at which the stage will move, and this speed is always given as an absolute value, without a negative sign.

- The contact criteria correspond to the variation in load relative to the current load, not to the absolute load value.

- The stage limit corresponds to the maximum relative displacement for the 'Find contact'. This serves as a safety precaution for the load cell.

- Stage repositioning has three options: the first is 'none', which keeps the stage at the position where it stopped; the second is the stop 'criteria + offset', which repositions the stage to the point where the load variation first meets the stop criteria; and the last is '2X load resolution', which repositions the stage to the point where the load variation first meets twice the load cell resolution. This is a surface detection function.

b- Step-by-Step Thickness Measurements

- Screw the sample holder onto the testing chamber.

- Using the manual controls, lower the stage at medium speed to approximately 20 mm above the sample holder.

- Lower the stage at low speed to approximately 2 mm above the sample holder.

- Find the vertical position of the bottom platen and set it as the reference by running the test sequence.

Table 1: Setting to measure the reference position.

Functions	Parameters
Zero load	No parameters
Find contact	Stage axis: position (z) Load cell Axis: Fz Direction: Positive Velocity: 0.001 mm / s Contact criteria: 3.75 gf. Stage limit: 3 mm Stage repositioning: 2X load resolution
Zero position	Stage axis: Position (z)

- Using manual control, raise the stage by at least 50 mm above the sample holder.
- Using tweezers, place your sample in the centre of the sample.
- Using the manual controls, lower the stage at medium speed to approximately 20 mm above the sample.
- Lower the stage at a low speed to approximately 2 mm above the sample.
- Perform the following test sequence to measure the thickness L_0 of the sample.

Table 2: Thickness measurement

Functions	Parameters
Zero load	No parameters
Find contact	Stage axis: position (z) Load cell Axis: Fz Direction: Positive Velocity: 0.001 mm / s Contact criteria: 3.75 gf. Stage limit: 3 mm Stage repositioning: 2X load resolution

6 Indentation / Compression Testing

Indentation testing on the bio-momentum is performed using the 'Stress Relaxation' function.

a- Relaxation Function.

- The 'stress relaxation' function allows the generation of sequences of ramp-and-hold displacement.
- A sequence of ramp displacements is specified by determining the number of ramps, amplitude and velocity.
- The ramp amplitude is the relative amplitude the stage will reach.
- The velocity determines the speed at which the stage performs the ramp.
- The number of ramps corresponds to the number of identical displacement-and-hold cycles that will be executed.

- There are two ways to determine the end of each relaxation-type cycle. The first is the fixed relaxation time, the duration of each relaxation period, expressed in seconds. The second is the relaxation rate, expressed in gf/min.

b- Indentation / Compression Parameters

- The indentation tests will be conducted under displacement control at 4 strains: 5%, 10%, 15%, and 20%.

- For each soft tissue, 5 samples should be tested at each indentation strain (5 samples for 5%, 5 for 10%, 5 for 15%, and 5 for 20%).

- The indentation test should follow immediately after the thickness measurement (using the 'find contact' function).

Table 3: Indentation testing parameters

Functions	Parameters
Zero load	No parameters
Stress relaxation ()	Stage axis: position (z) Load cell axis: Fz Ramp amplitude: % strain * L_0 Ramp velocity: 0.01 mm/ s Number of ramps: 1 Stop based on: Fixed relaxation time. Fixed relaxation time: 30s

7 Data Storage

- Create one folder titled ‘Indentation testing’.

- Create three subfolders for each soft tissue being tested (large pickled capers, chicken breast, and PVA hydrogel).

- In each subfolder, create 5 additional subfolders corresponding to your 5 samples.

- In each of the 5 subfolders, create a subfolder named ‘images’ (this is where you will save pictures from the sample preparation and during the procedure).

Appendix 4.4: Sample Preparation

Figure 4.4.1: Compression (a, b, c, and d) and indentation (e, f, g, and h) of PVA hydrogel samples at 20%, 15%, 10%, and 5% strain.

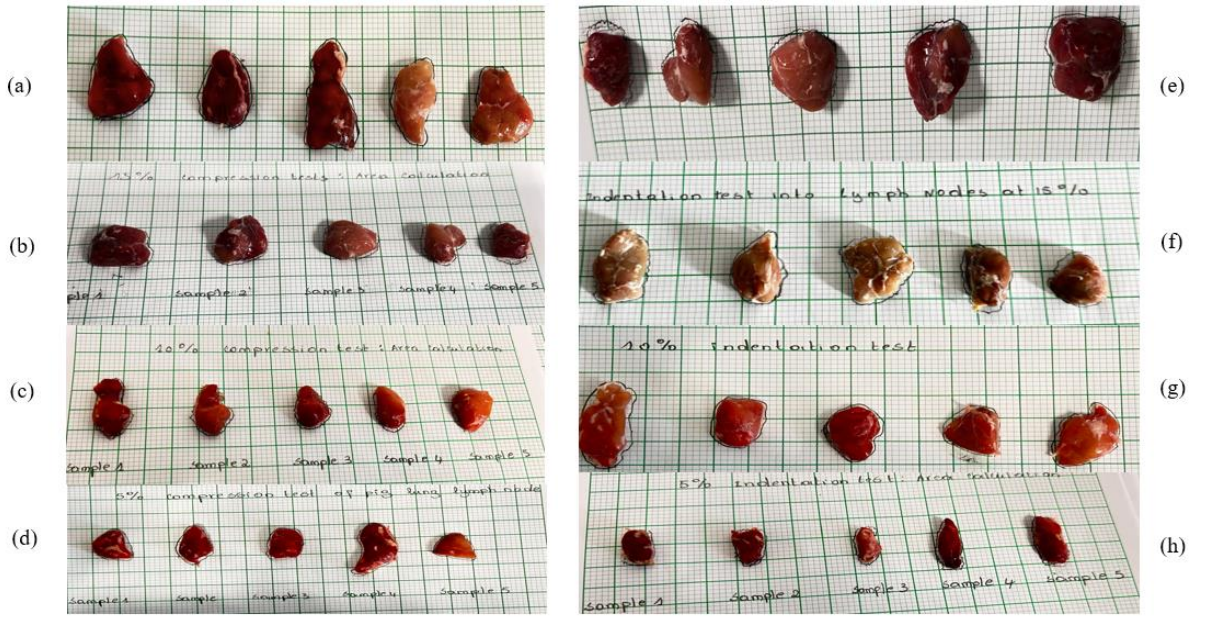

Figure 4.4.2: Compression (a, b, c, and d) and indentation (e, f, g, and h) of porcine lung lymph node samples at 20%, 15%, 10%, and 5% strain.

Appendix 4.5: Compression and Indentation Stress-Strain Curves of various Soft Materials.

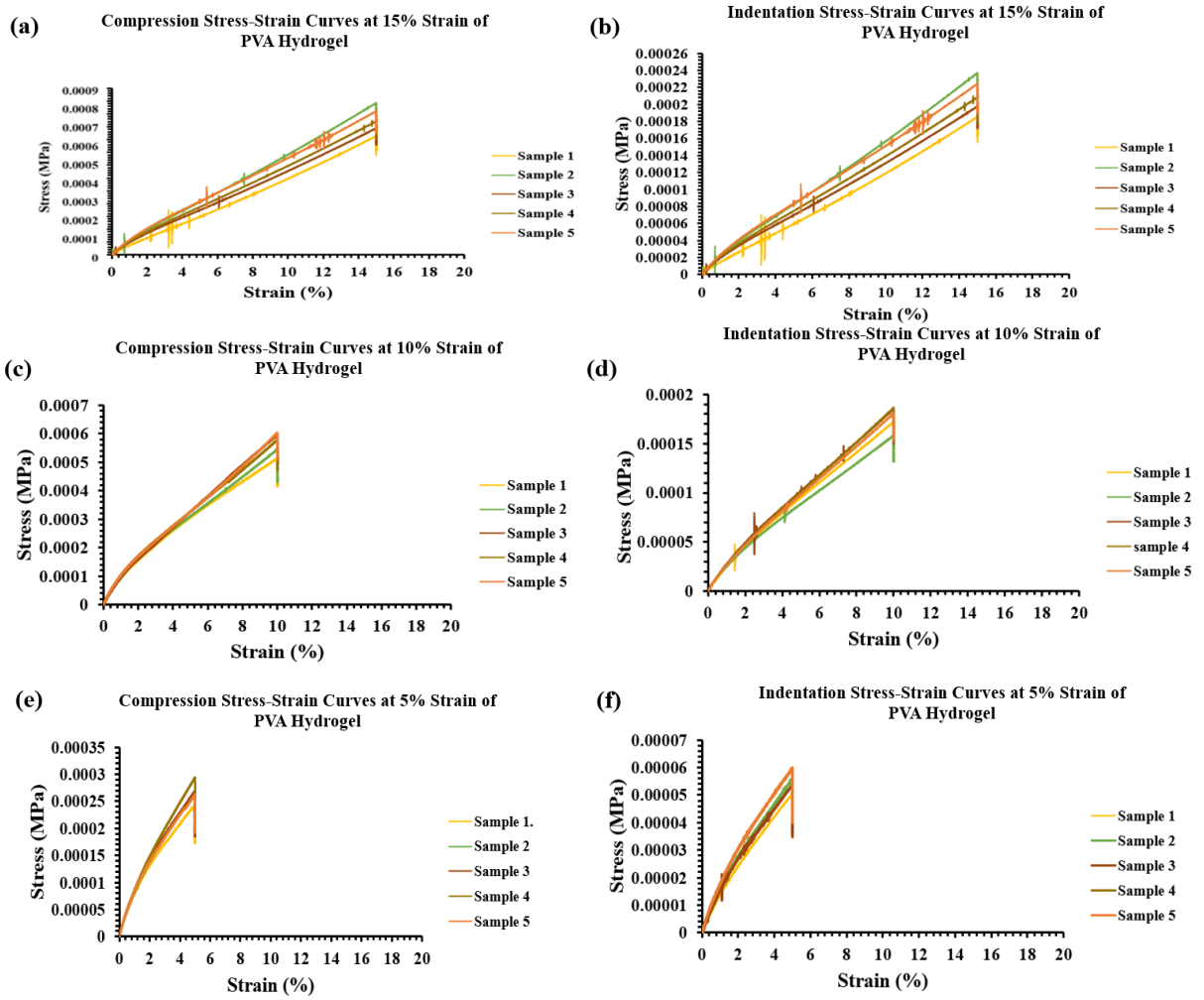

Figure 4.5.1: Compression and indentation stress-strain curves of PVA Hydrogel at different strains: (a) & (b) compression and indentation test results at 15% strain; (c) & (d) compression and indentation test results at 10% strain; (e) & (f) compression and indentation test results at 5% strain.

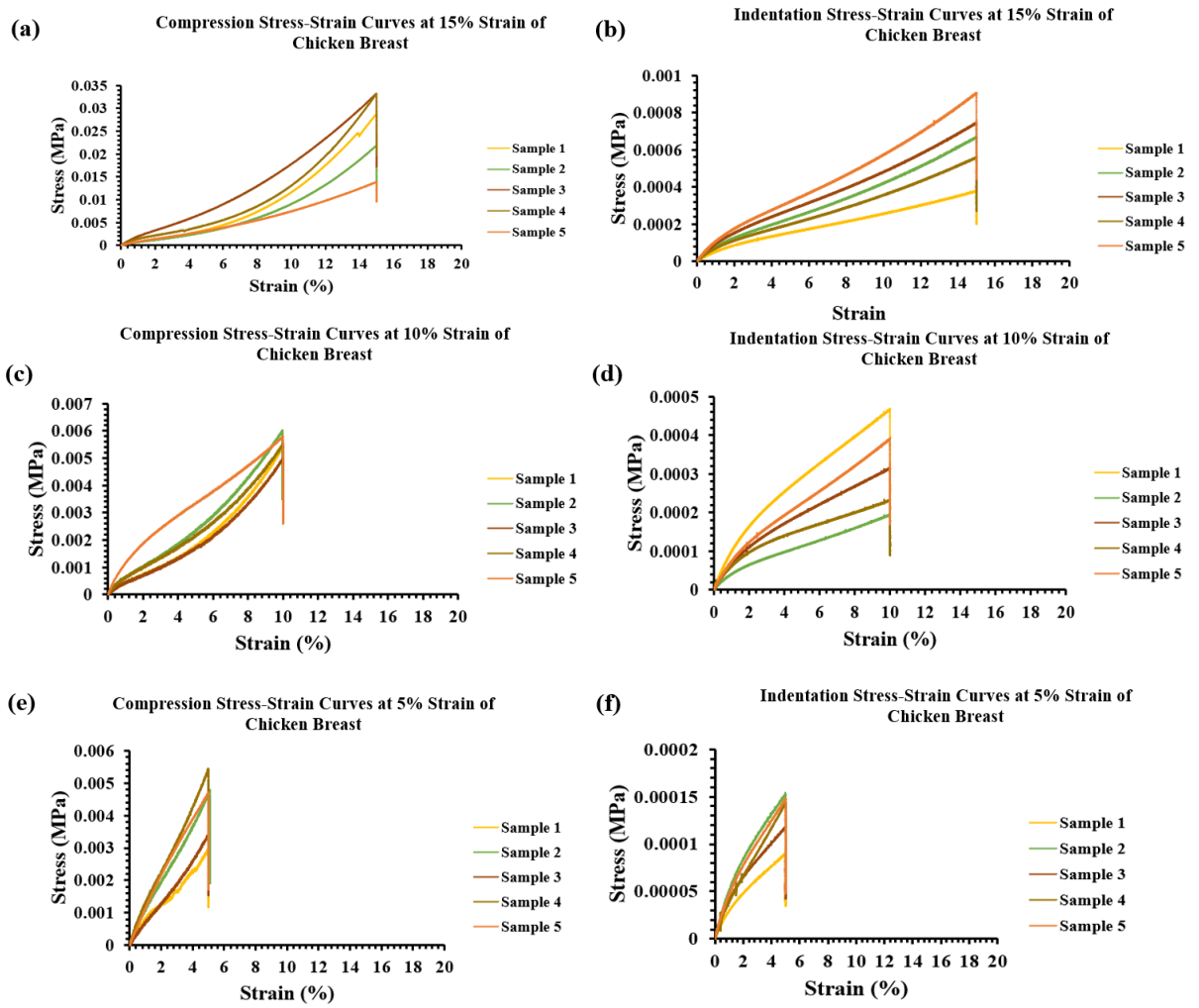

Figure 4.5.2: Compression and indentation stress-strain curves of chicken breast at different strains: (a) & (b) compression and indentation test results at 15% strain; (c) & (d) compression and indentation test results at 10% strain; (e) & (f) compression and indentation test results at 5% strain.

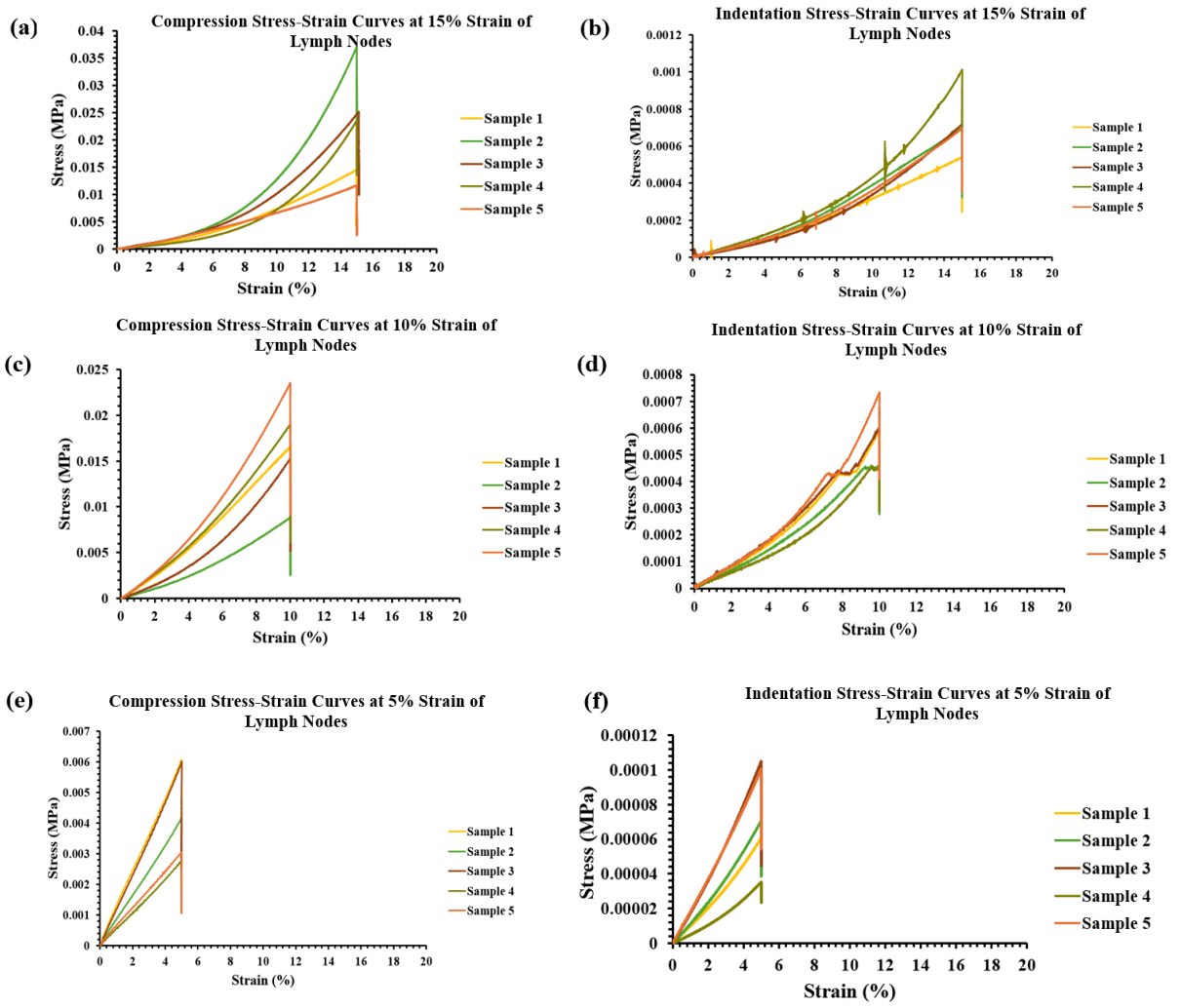

Figure 4.5.3: Compression and indentation stress-strain curves of lung lymph node at different strains: (a) & (b) compression and indentation test results at 15% strain; (c) & (d) compression and indentation test results at 10% strain; (e) & (f) compression and indentation test results at 5% strain.

Appendix 4.6: Curve Fitting in Abaqus

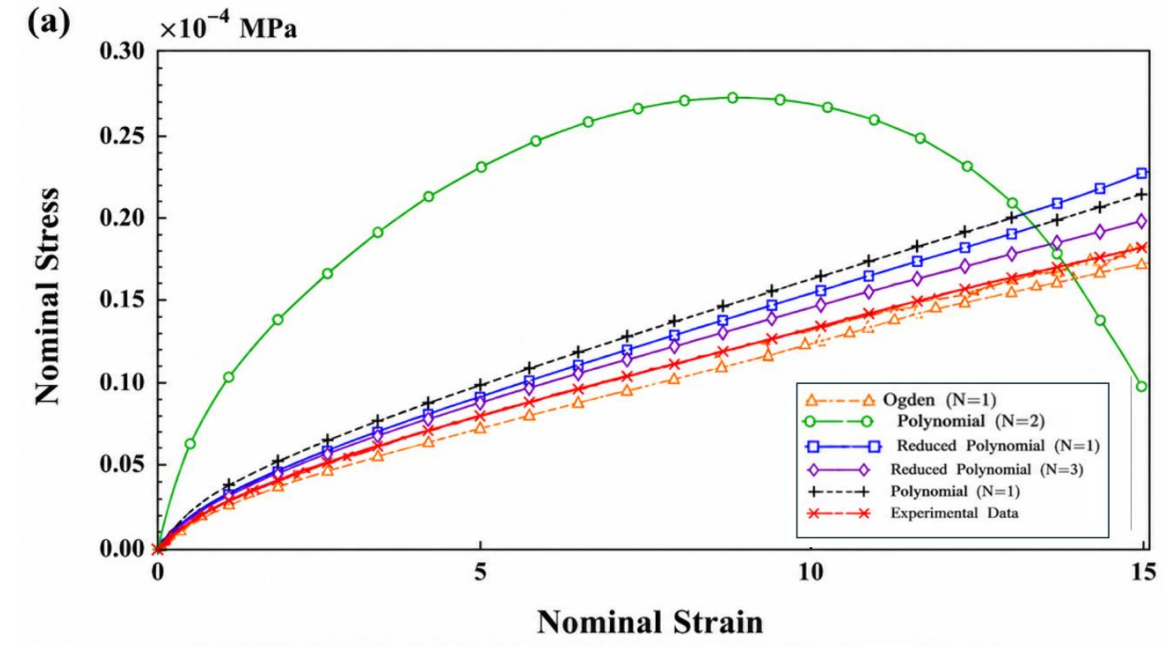
(a)
×10⁻⁴ MPa
Nominal Stress
Nominal Strain
Ogden (N=1)
Polynomial (N=2)
Reduced Polynomial (N=1)
Reduced Polynomial (N=3)
Polynomial (N=1)
Experimental Data

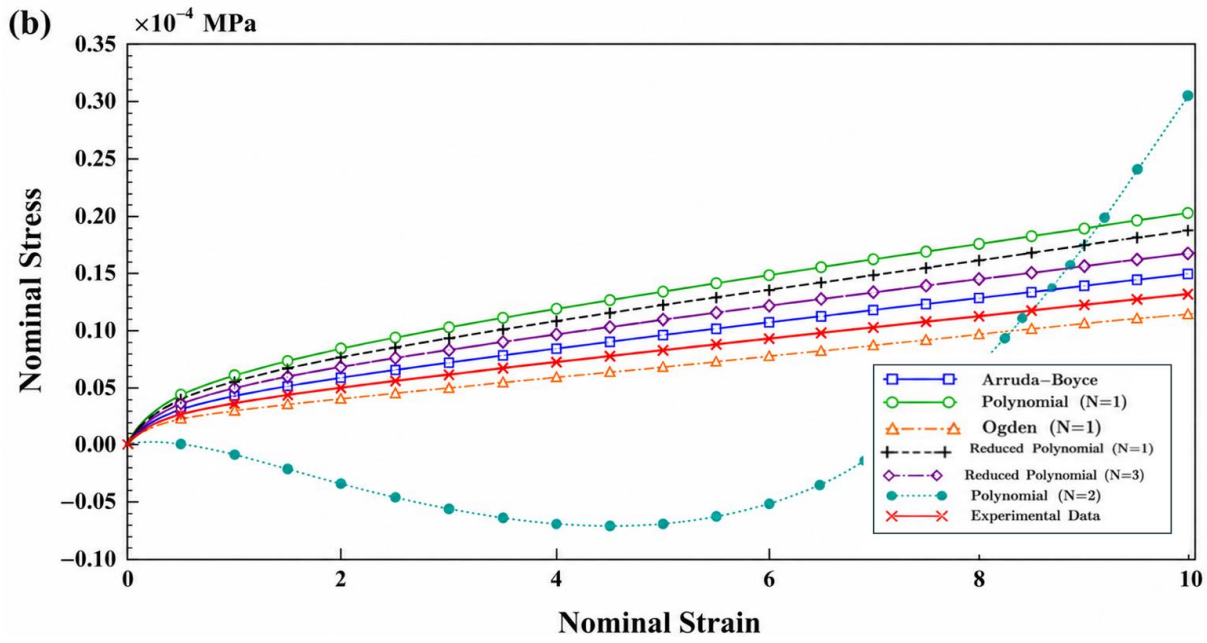
(b)
×10⁻⁴ MPa
Nominal Stress
Nominal Strain
Arruda–Boyce
Polynomial (N=1)
Ogden (N=1)
Reduced Polynomial (N=1)
Reduced Polynomial (N=3)
Polynomial (N=2)
Experimental Data

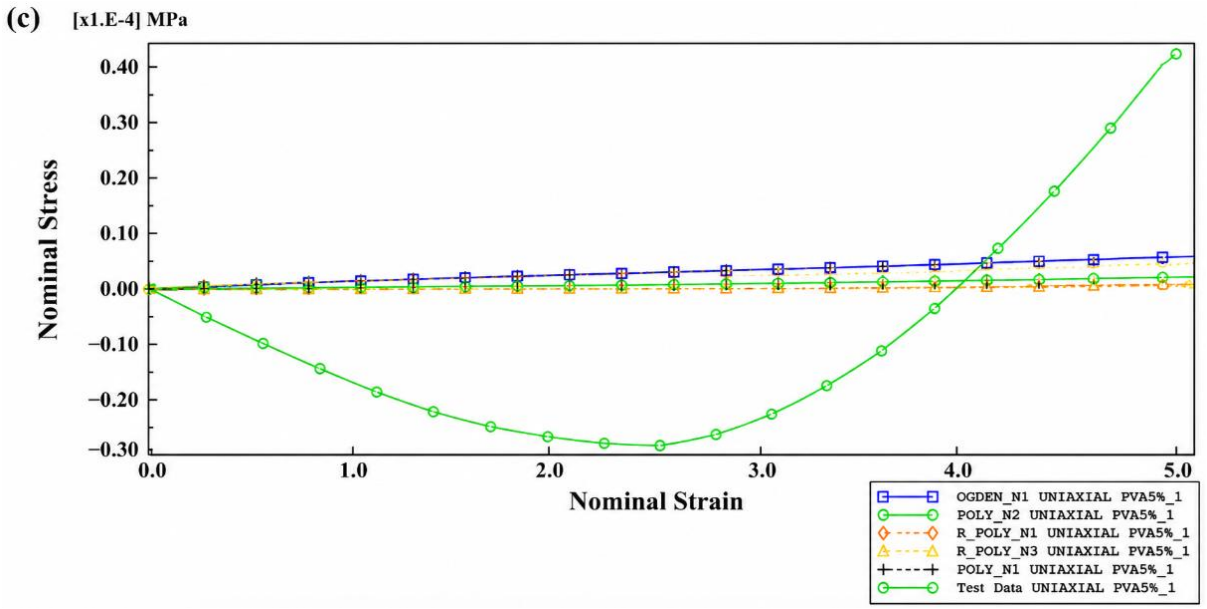

Figure 4.6.1: PVA hydrogel stability evaluated by curve-fitting the test data (red) to different hyperelastic models at various strains; Ogden model N=1 (blue); polynomial N=2 (green); reduced polynomial N=1 Neo-Hooke model (yellow); reduced polynomial N=3 Yeoh model (orange); polynomial N=1 Mooney-Rivlin model (black). The results indicate that the Ogden model N=1 (blue) provides the best fit. (a) 15% strain, (b) 10% strain, (c) 5% strain.

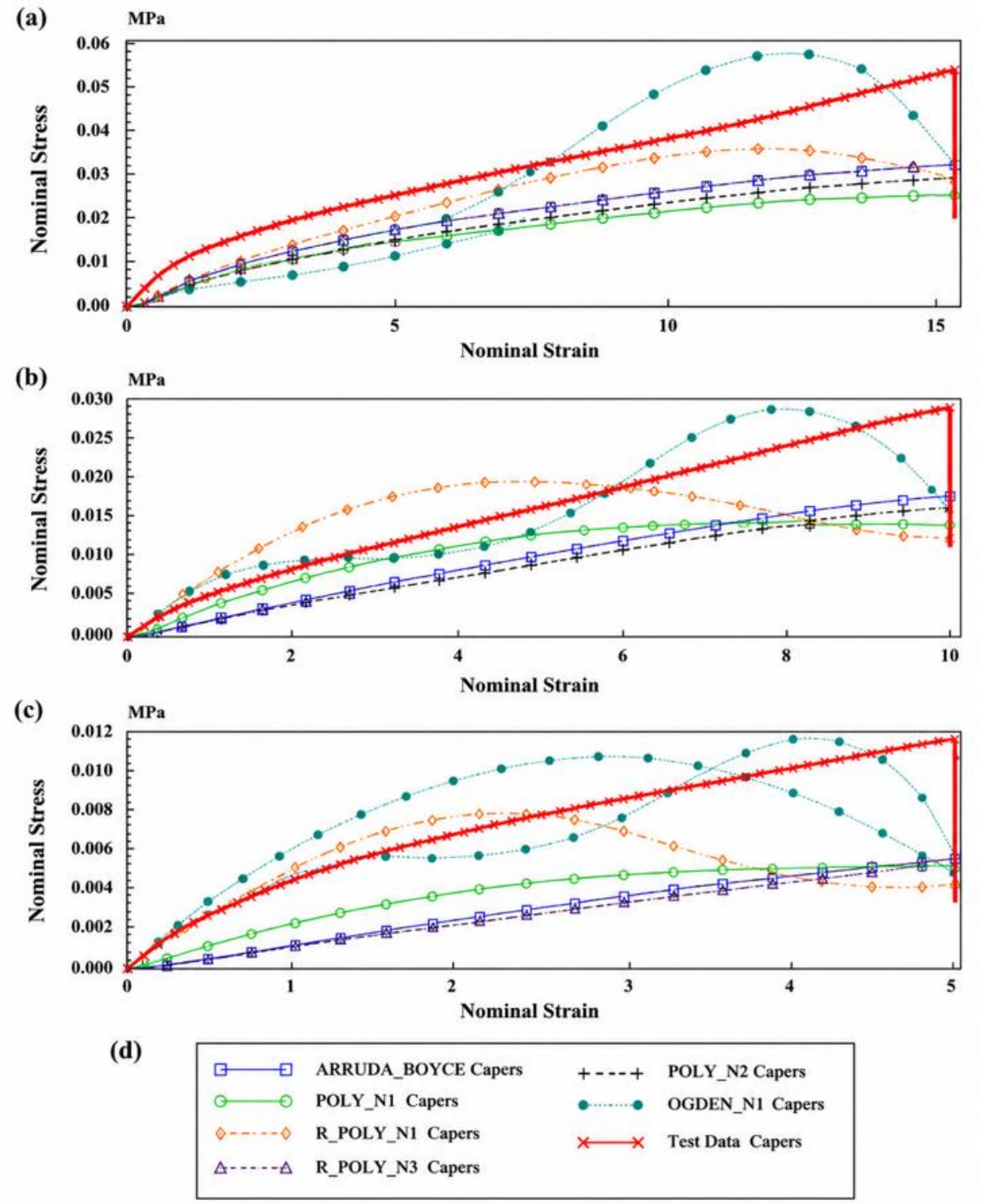

Figure 4.6.2: Stability evaluation of large-pickled capers using curve fitting between the test data (red) and different hyperelastic models at various strains; (a) 15% strain, (b) 10% strain, (c) 5% strain, (d) hyperelastic models, Arruda-Boyce (blue); polynomial N = 1 Mooney-Rivlin

model (light green); reduced polynomial N = 1 Neo-Hooke model (yellow); polynomial N = 2 (black); Ogden model N = 1 (green); experimental test data (red). The results indicate that the Ogden model N = 1 (green) provides the best fit.

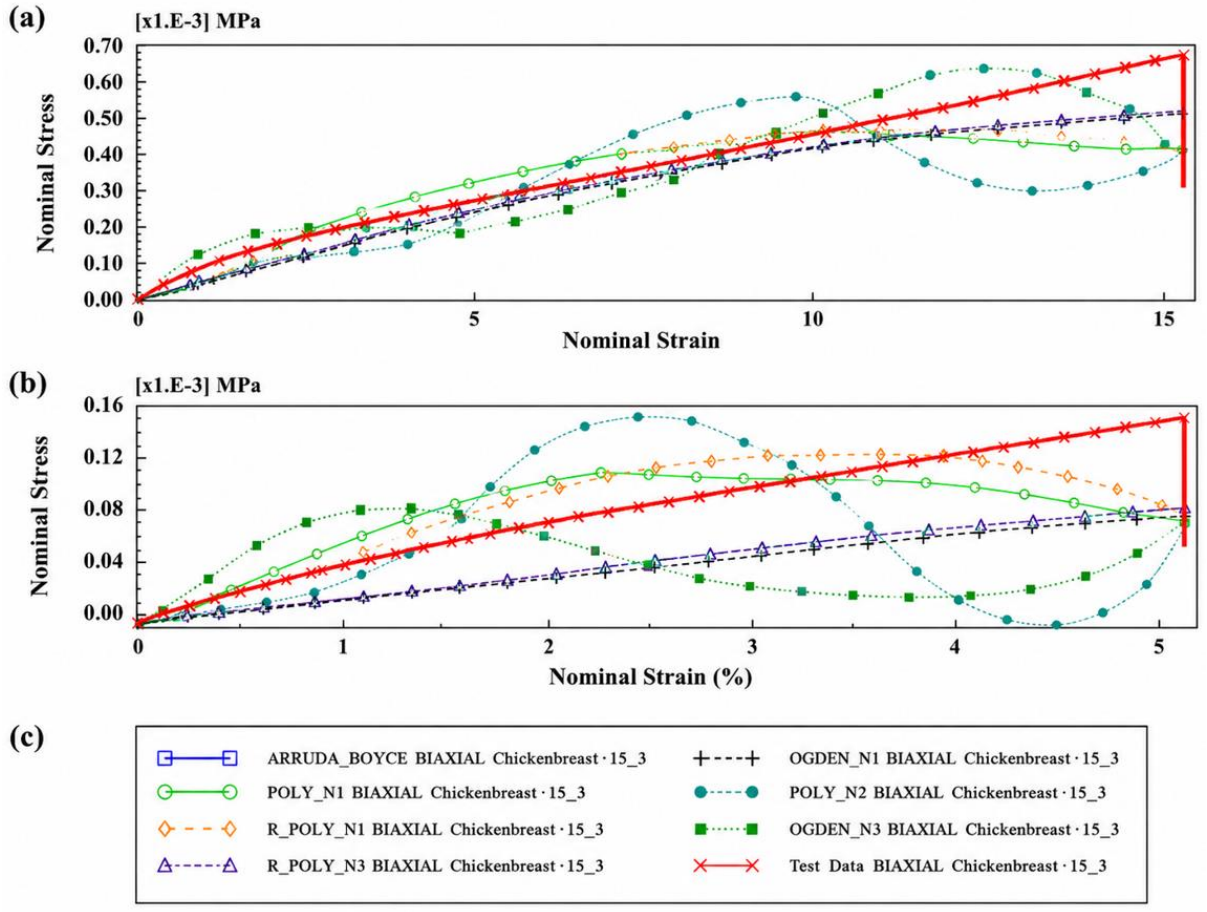

Figure 4.6.3: Chicken breast stability evaluation by curve fitting between the test data (red) and different hyperelastic models at various strains; (a) 15% strain, (b) 5% strain, (c) hyperelastic models, Arruda-Boyce (blue); polynomial N = 1 Mooney-Rivlin model (light green); reduced polynomial N = 1 Neo-Hooke model (yellow); polynomial N = 2 (green); Ogden model N = 1 (black); experimental test data (red). The results show the Ogden model N = 1 (black) as the best fit.

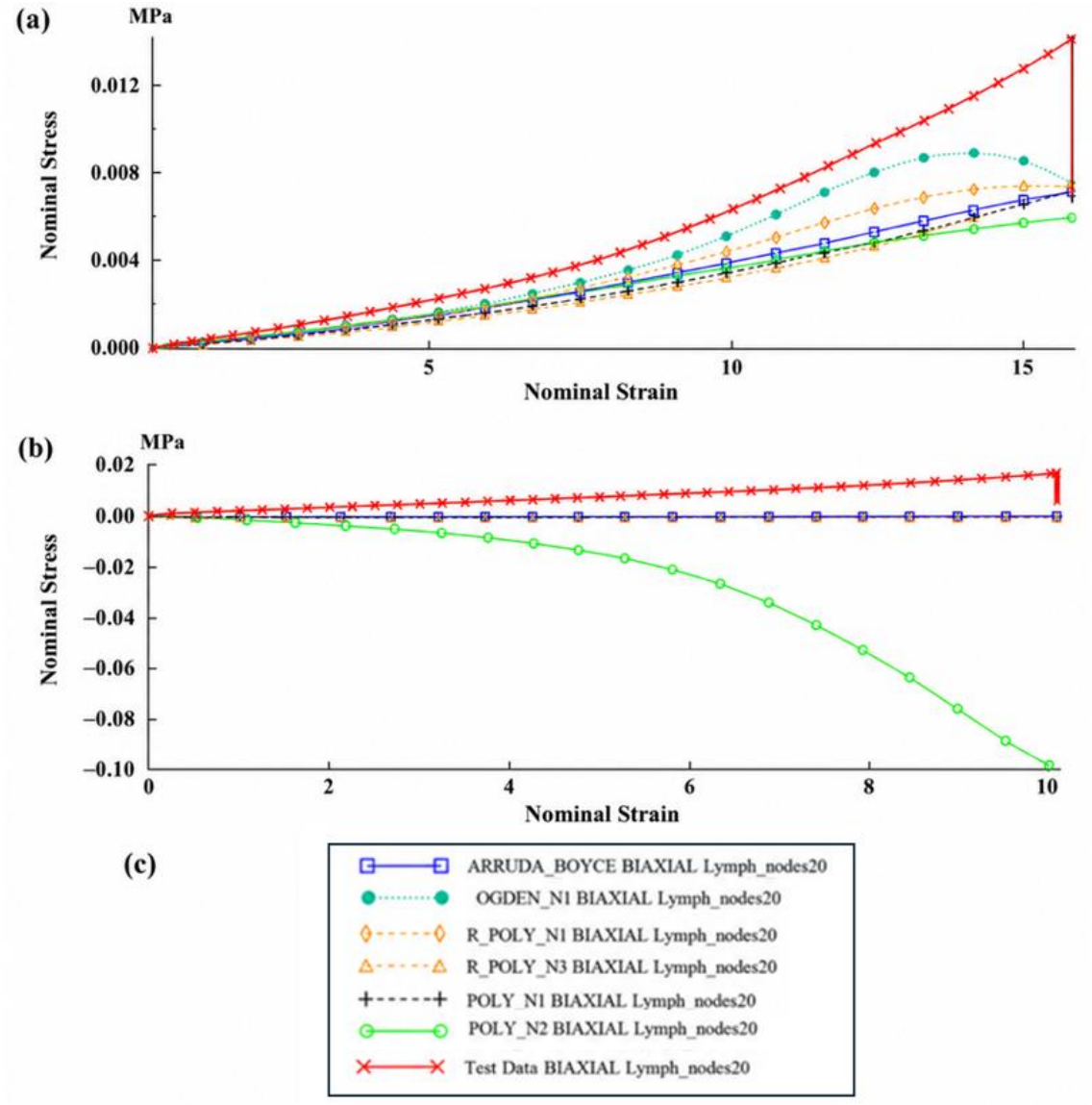

Figure 4.6.4: Stability evaluation of lung lymph nodes by curve fitting between the test data (red) and different hyperelastic models at various strains; (a) 15% strain, (b) 5% strain, (c) hyperelastic models, Arruda-Boyce (blue); polynomial N = 1 Mooney-Rivlin model (black); reduced polynomial N = 1 Neo-Hooke model (yellow); polynomial N = 2 (green); Ogden model N = 1 (light green); experimental test data (red). The results indicate that the Ogden model N = 1 (light green) provides the best fit.

Chapter 6 Appendix

Appendix 6.1: Needle Insertion into Soft Material Code

19 mm (0.75") DIAMETER SUBMINIATURE TENSION OR COMPRESSION LOAD CELLS

STANDARD AND METRIC MODELS

Tension/Compression
Calibrated in Tension
0-25 lb to 0-300 lb
0-100 to 0-500 N

1 Newton = 0.2248 lb
1 daNewton = 10 Newtons
1 lb = 454 g
1 t = 1000 kg = 2204 lb

LC201/LCM201 Series

NIST RoHS
Standard

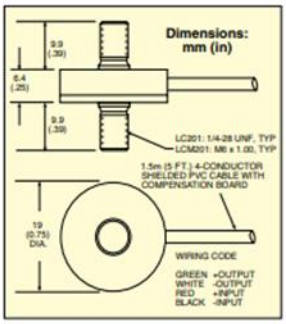

- **Subminiature Package for Robotic Applications, 19 mm (0.75") Diameter**
- **Dual Mounting Studs for Easy Installation**
- **5-Point Calibration Provided**

Thermal Effects:
Zero: 0.018% FSO/°C
Span: 0.018% FSO/°C
Safe Overload: 150% of capacity
Ultimate Overload: 300% of capacity
Input Resistance: 360 Ω minimum
Output Resistance: 350 ±10 Ω
Construction: Stainless steel
Electrical: 1.5 m (5') 4-conductor shielded cable with compensation board

OMEGA's LC201/LCM201 Series subminiature load cells are designed for the demanding environment of industrial automation and robotics. With a diameter of only 19 mm (0.75") and all stainless steel construction, they can fit into small systems. They deliver high accuracy and long-term reliability in a subminiature package.

SPECIFICATIONS

Excitation: 10 Vdc, 15 Vdc max
Output: 2 mV/V nominal
Accuracy: ±1.0% FSO linearity, hysteresis, repeatability combined
5-Point Calibration (in Tension): 0%, 50%, 100%, 50%, 0%
Zero Balance: ±2% FSO
Operating Temp Range: -54 to 121°C (-65 to 250°F)
Compensated Temp Range: 16 to 71°C (60 to 160°F)
Protection Class: IP54

STANDARD MODELS

To Order

CAPACITY lb	CAPACITY N	MODEL NO.	COMPATIBLE METERS	ROD END
25	111	LC201-25	DP41-S, DP25B-S	REC-014F
50	222	LC201-50	DP41-S, DP25B-S	REC-014F
75	334	LC201-75	DP41-S, DP25B-S	REC-014F
100	445	LC201-100	DP41-S, DP25B-S	REC-014F
300	1334	LC201-300	DP41-S, DP25B-S	REC-014F

METRIC MODELS

CAPACITY N	CAPACITY lb	MODEL NO.	COMPATIBLE METERS	ROD END
100	22	LCM201-100N	DP41-S, DP25B-S	MREC-M6F
200	45	LCM201-200N	DP41-S, DP25B-S	MREC-M6F
300	67	LCM201-300N	DP41-S, DP25B-S	MREC-M6F
500	112	LCM201-500N	DP41-S, DP25B-S	MREC-M6F

Comes complete with 5-point NIST traceable calibration and 59 kΩ shunt data.
Ordering Examples: LC201-25, *25 lb capacity subminiature universal load cell.*
LCM201-500N, *500 N capacity subminiature universal load cell.*

F-38

LOAD CELLS F

Figure 6.1.1: Compression Load Cell Specification.

```
Author: Lyne Mkoh

This is the calibration sketch. Use it to determine the calibration_factor.. It also
outputs the zero_factor useful for projects that have a permanent mass on the scale in between power cycles.

Setup your scale and start the sketch WITHOUT a weight on the scale
Once readings are displayed place the weight on the scale
Press +/- or a/z to adjust the calibration_factor until the output readings match the known weight
Use this calibration_factor on the example sketch
Arduino pin 2 -> HX711 CLK
3 -> DOUT
5V -> VCC
GND -> GND

Most any pin on the Arduino Uno will be compatible with DOUT/CLK.

The HX711 board can be powered from 2.7V to 5V so the Arduino 5V power should be fine.

*/

#include "HX711.h"

#define DOUT  5
#define CLK  2

HX711 scale;

float calibration_factor =-59500; //-7050 worked for my 440lb max scale setup

void setup() {
  Serial.begin(9600);
  Serial.println("HX711 calibration sketch");
  Serial.println("Remove all weight from scale");
  Serial.println("After readings begin, place known weight on scale");
  Serial.println("Press + or a to increase calibration factor");
  Serial.println("Press - or z to decrease calibration factor");

  scale.begin(DOUT, CLK);
  scale.set_scale();
  scale.tare(); //Reset the scale to 0

  long zero_factor = scale.read_average(); //Get a baseline reading
  Serial.print("Zero factor: "); //This can be used to remove the need to tare the scale. Useful in permanent scale projects.
  Serial.println(zero_factor);
}

void loop() {

  scale.set_scale(calibration_factor); //Adjust to this calibration factor

  Serial.print("Reading: ");
  Serial.print(scale.get_units(), 2);
  Serial.print(" N"); //Change this to kg and re-adjust the calibration factor if you follow SI units like a sane person
  Serial.print(" calibration_factor: ");

  Serial.print(calibration_factor);
  Serial.println();

  if(Serial.available())
  {
    char temp = Serial.read();
    if(temp == '+' || temp == 'a')
      calibration_factor += 100;
    else if(temp == '-' || temp == 'z')
      calibration_factor -= 100;
  }
}
```

Figure 6.1.2: Calibration Code for Needle Insertion Experiment.

```
// Author: Dr Kevin Worall
// Modified: Lyne Raissa Mkoh


// This code is used to find out the speed.

#include <HX711.h>
#include <PID_v2.h>
#define calibration_factor -61700 //This value is obtained using the SparkFun_HX711_Calibration sketch
#define DOUT 5
#define CLK 2
HX711 scale;

int actSpeed = 3; //actuator speed 0-255
int actDirection = 12; //actuator direction. 1 = forward, 0 = backward

int actFB = A4; //actuator position FB. 0 = 0mm, 1023 = 100mm. Read from A2.
float actPos; //store and convert position to mm
int curSens = A0; //current drawn from linear actuator
float actCurrent; //store and convert current draw

float force; //convert and store force data.
float forceSetpointUpper = 4.5; //desired force value in N -- Upper Bound
float forceSetpointLower = 4.0; // desired force value in N -- Lower Bound
int comSpeed = 35; //initial commanded speed, this variable also stores commanded speed throughout

long runtime = 0, endtime = 0, starttime = 0;

float runspeed = 0.0;

int maxvalue = 0, minvalue = 0;

int dir = 1;

void setup() {
  pinMode(actSpeed, OUTPUT);
  pinMode(actDirection, OUTPUT);
  pinMode(actFB, INPUT);

  //set up  serial monitor and writing to excel file
  Serial.begin(9600);

  //begin ADC force sensing
  scale.begin(DOUT, CLK, 128);
  scale.set_scale(calibration_factor); //This value is obtained by using the SparkFun_HX711_Calibration sketch
  scale.tare();


 // Serial.println("CLEARDATA");
//  Serial.println("LABEL, Time, Timer, Commanded Speed, Actuator Extension, Actuator Current Draw, Force Reading");
//  Serial.print("RESETTIMER");

actPos = analogRead(actFB);
    actPos = (actPos/1023)*100;
    }

void loop() {
```

```
58
59      starttime = millis();
60      actPos = analogRead(actFB);
61      minvalue = actPos;
62      Serial.print(runspeed);
63      Serial.print(",");
64      analogWrite(actSpeed, 160); // <--- change here for different speeds
65      digitalWrite(actDirection,  dir);
66      endtime = millis();
67
68      actPos = analogRead(actFB);
69      maxvalue = actPos;
70      actPos = (actPos/1023)*10;
71      Serial.print(actPos);
72
73      runtime = endtime - starttime;
74
75      Serial.print(runtime);
76      Serial.print(",");
77      Serial.print(maxvalue);
78      Serial.print(",");
79       Serial.println(minvalue);
80
81       runspeed = (maxvalue - minvalue)/float(runtime);
82
83
84    if (actPos > 9)
85     dir = 0;
86
87    if (actPos < 3)
88     dir = 1;
```

Figure 6.1.3: Linear Speed Code for Needle Insertion Experiment

```
Author: Lyne Mkoh

This is the calibration sketch. Use it to determine the calibration_factor.. It also
outputs the zero_factor useful for projects that have a permanent mass on the scale in between power cycles.

Setup your scale and start the sketch WITHOUT a weight on the scale
Once readings are displayed place the weight on the scale
Press +/- or a/z to adjust the calibration_factor until the output readings match the known weight
Use this calibration_factor on the example sketch
Arduino pin 2 -> HX711 CLK
3 -> DOUT
5V -> VCC
GND -> GND

Most any pin on the Arduino Uno will be compatible with DOUT/CLK.

The HX711 board can be powered from 2.7V to 5V so the Arduino 5V power should be fine.

*/

#include "HX711.h"

#define DOUT  5
#define CLK  2

HX711 scale;



int LinActSpeed = 150;
;
int LinActDir = 1;

HX711 scale;

void setup() {
  pinMode(actSpeed, OUTPUT);
  pinMode(actDirection, OUTPUT);
  pinMode(actFB, INPUT);

  //set up  serial monitor and writing to excel file
  Serial.begin(9600);

  scale.begin(DOUT, CLK,128);
  scale.tare();
}

void loop() {

  // Work out position
   actPos = analogRead(A4);
   actPos = (actPos/1023)*5;

   // Get additional sensing parameters
   actCurrent = analogRead(A0);
   reading = scale.get_units(3);
   force = reading; //divided by calibration factor
```

```
88
89      // Drive the Actuator
90      analogWrite(actSpeed, LinActSpeed);
91      digitalWrite(actDirection,  LinActDir);
92
93      // Work out position
94      actPos = analogRead(A4);
95      actPos = (actPos/1023)*5;
96
97      // Get additional sensing parameters
98      actCurrent = analogRead(A0);
99      reading = scale.get_units(3);
100     force = reading; //divided by calibration factor
101
102     //data aquisition
103     Serial.print(actPos);
104     Serial.print(",");
105     Serial.print(actCurrent);
106     Serial.print(",");
107     Serial.println(force);
108     delay(50);
109
110   }
111
112 // while(1) {
113     // Drive the Actuator
114    // analogWrite(actSpeed, 0);
115    // digitalWrite(actDirection,  LinActDir);
116     };
```

Figure 6.1.4: Needle insertion into Soft Material Code.

Appendix 6.2: Actuator speed: (a) conversion from analogue to digital; (b) linear relationship between the analogue speed and the digital readout.

(a)

Analogue Speed	Digital Speed (mm/s) ± SD
255	12.97 ± 0.037
250	12.4 ± 0.037
245	11.84 ± 0.037
240	11.28 ± 0.037
235	10.72 ± 0.037
230	10.2 ± 0.037
225	9.69 ± 0.037
220	9.1 ± 0.037
215	8.6 ± 0.037
210	8 ± 0.037
205	7.44 ± 0.037
200	6.95 ± 0.037
195	6.31 ± 0.037
190	5.71 ± 0.037
185	5.1 ± 0.037
180	4.54 ± 0.037
175	3.9 ± 0.037
170	3.2 ± 0.037
165	2.54 ± 0.037
160	2.02 ± 0.037
155	1.38 ± 0.037
150	0.5 ± 0.037

(b)

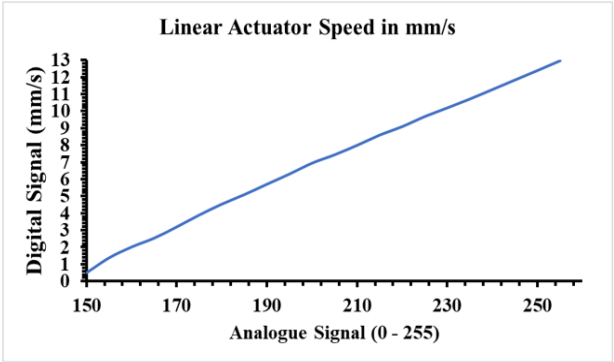

Appendix 6.3: Comparison of Forces Profile between the 21G and 22G needles insertion into various Soft Materials

Table 6.3.1: Comparison of force profiles for insertion of 21G and 22G needles into PVA hydrogel, chicken breast, large pickled capers, and porcine lung lymph node at 9 mm/s, showing higher peak force F_1 and outside friction force F_2 with the 22G needle, and higher inner friction F_i and cutting force F_c with the 21G needle.

Needles	Forces	PVA Hydrogel	Large Pickled Capers	Chicken Breast	Lymph Nodes
22G	**F_1 (N)**	4.081	16.105	5.550	5.727
	(STD)	[0.132]	[0.117]	[0.369]	[0.185]
	F_2 (N)	3.123	13.509	3.621	3.615
	(STD)	[0.622]	[0.201]	0.629]	[0.568]
	F_i (N/mm)	0.348	1.725	0.51	0.609
	(STD)	[0.212]	[0.014]	[0.176]	[0.253]
	F_c (N)	0.850	1.13	0.712	0.565
	(STD)	[0325]	[0.09]	[0.265]	[0.161]
21G	**F_1 (N)**	4.22	18.144	5.582	6.195
	(STD)	[0.04]	[0.12]	[0.272]	[0.153]
	F_2 (N)	3.272	17.461	4.381	4.802
	(STD)	[0.383]	[0.07]	[0.595]	[1.189]
	F_i (N/mm)	0.571	3.33	0.724	0.847
	(STD)	[0.413]	[0.325]	[0.342]	[0.231]
	F_c (N)	1.027	1.79	0.914	0.551
	(STD)	[0.760]	[0.17]	[0.634]	[0.296]

Table 6.3.2: Comparison of force profiles for insertion of 21G and 22G needles into PVA hydrogel, chicken breast, large pickled capers, and porcine lung lymph node at 3 mm/s, showing higher peak force F_1 and outside friction force F_2 with the 22G needle, and higher inner friction F_i and cutting force F_c with the 21G needle.

Needles	Forces	PVA Hydrogel	Large Pickled Capers	Chicken Breast	Lymph Nodes
22G	**F_1 (N)**	4.644	23.529	7.199	6.338
	(STD)	[0.124]	[0.14]	[0.391]	[0.183]
	F_2 (N)	3.289	18.261	5.276	4.915
	(STD)	[0.962]	[0.35]	[0.921]	[0.293]
	F_i (N/mm)	0.241	0.95	0.452	0.582
	(STD)	[0.079]	[0.085]	[0.212]	[0.498]
	F_c (N)	0305	1.871	0.509	0.279
	(STD)	[0.126]	[0.093]	[0.429]	[0.145]
21G	**F_1 (N)**	5.081	21.235	7.327	6.878
	(STD)	[0.052]	[0.204]	[0.668]	[0.638]
	F_2 (N)	4.484	17.737	5.452	5.388
	(STD)	[0.196]	[0.108]	[0.949]	[1.378]
	F_i (N/mm)	0.335	3.129	0.687	0.778
	(STD)	[0.452]	[0.21]	[0.140]	[0.118]
	F_c (N)	0.814	2.335	0.907	0.531
	(STD)	[0.682]	[0.22]	[0.186]	[0.58]

Table 6.3.3: Comparison of force profiles for inserting 21G and 22G needles into PVA hydrogel, chicken breast, large pickled capers, and porcine lung lymph node at 0.5 mm/s, showing higher peak force F_1 and outside friction force F_2 with the 22G needle, and higher inner friction F_i and cutting force F_c with the 21G needle.

Needles	Forces	PVA Hydrogel	Large Pickled Capers	Chicken Breast	Lymph Nodes
22G	**F_1 (N)**	5.746	27.165	8.333	7.682
	(STD)	[0.087]	[0.629]	[0.446]	[0.315]
	F_2 (N)	4.467	26.673	7.037	6.136
	(STD)	[0.697]	[0.767]	[0.633]	[0.964]
	F_i (N/mm)	0.204	0.9	0.408	0.456
	(STD)	[0.152]	[0.09]	[0.435]	[0.318]
	F_c (N)	0.189	2.05	0.317	0.565
	(STD)	[0.09]	[0.11]	[0.626]	[0.161]
21G	**F_1 (N)**	6.117	27.043	8.526	7.760
	(STD)	[0.251]	[0.207]	[0.350]	[0732]
	F_2 (N)	5.277	26.84	6.809	6.444
	(STD)	[0.461]	[0.39]	[0.627]	[0.703]
	F_i (N/mm)	0.340	2.12	0.587	0.464
	(STD)	[0.345]	[0.174]	[0.200]	[0.247]
	F_c (N)	0.454	1.483	0.592	0.427
	(STD)	[0.494]	[0.145]	[0.453]	[0.138]

Chapter 7 Appendix

Appendix 7.1: 21G needle insertion into PVA hydrogel, showing the stress changes and tissue yield at depths of (a) 4 mm, (b) 8.5 mm, and (c) 9.5 mm, and at insertion speeds of (I) 13 mm/s, (II) 9 mm/s, and (III) 3 mm/s.

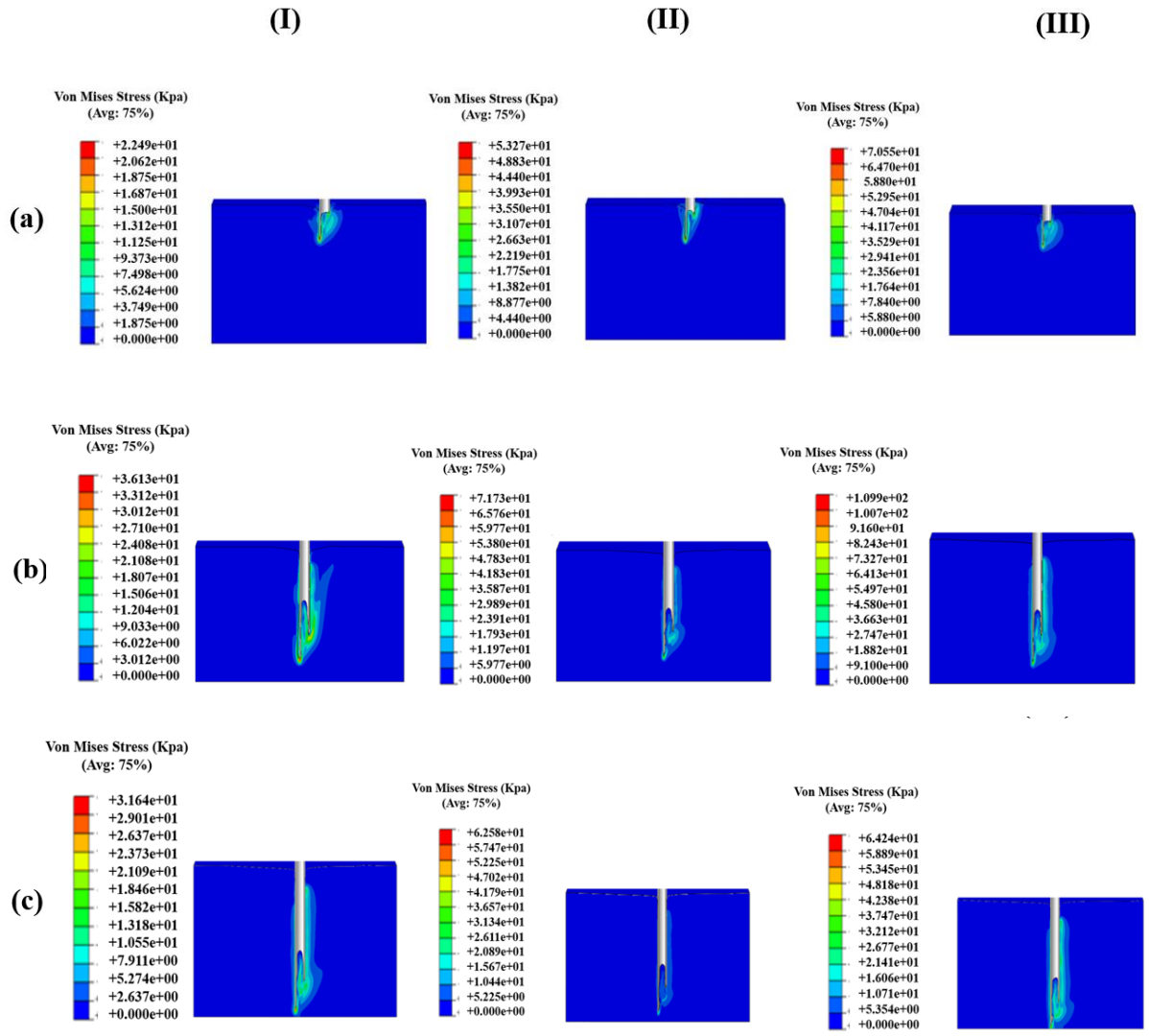

Appendix 7.2: 21G needle insertion into chicken breast, showing stress changes and tissue yield at depths of (a) 4 mm, (b) 8.5 mm, and (c) 9.5 mm, and at insertion speeds of (I) 13 mm/s, (II) 9 mm/s, and (III) 3 mm/s.

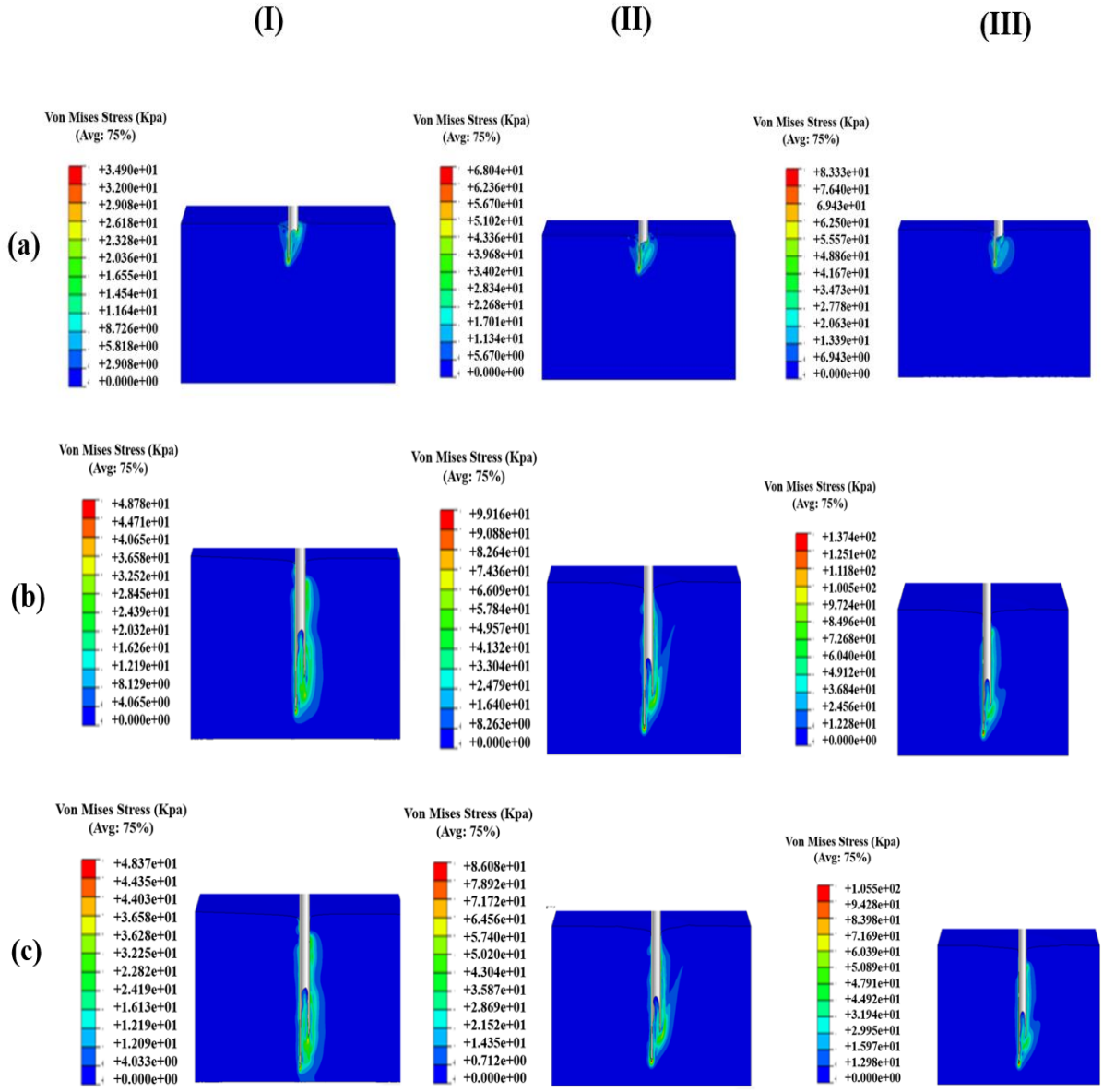

Appendix 7.3: 21G single-bevel needle insertion into PVA hydrogel at (a) 13 mm/s, (b) 9 mm/s, and (c) 3 mm/s: Comparison of FEA and experimental test results.